DISSERTATION

EXPLORING GAS-PHASE PLASMA CHEMISTRY AND PLASMA-SURFACE INTERACTIONS: PROGRESS IN PLASMA-ASSISTED CATALYSIS

Submitted by

Angela R. Hanna

Department of Chemistry

In partial fulfilment of the requirements

For the Degree of Doctor of Philosophy

Colorado State University

Fort Collins, Colorado

Spring 2020

Doctoral Committee:

Advisor: Ellen R. Fisher

Nancy E. Levinger
Anthony Rappe
R. Mark Bradley

ABSTRACT

EXPLORING GAS-PHASE PLASMA CHEMISTRY AND PLASMA-SURFACE INTERACTIONS: PROGRESS IN PLAMSA-ASSISTED CATALYSIS

The fundamental aspects of inductively coupled plasma chemistry was investigated, focusing on the interdependence of gas-phase and surface reactions for process improvement. Different project aspects included (1) gas-phase energetics and kinetics determination with and without substrates (i.e., catalysts) via spectroscopy; (2) material characterization before and after plasma modification; and (3) elucidation of gas-surface relationships whereby both the substrate and plasma are impacted by their interaction. The research presented herein focused on a holistic approach to plasma diagnostics, specifically addressing current limitations in pollution abatement strategies.

To enhance our understanding of plasma phenomena, optical spectroscopy was employed to provide insight into foundational plasma properties. This dissertation begins with a review of the applicability of optical spectroscopy as a non-intrusive, versatile diagnostic tool to explore non-thermal discharges. Specifically, time-resolved optical emission spectroscopy (TR-OES) was utilized to provide kinetic information about excited-state species formation, ultimately lending mechanistic insight into a range of plasma reactions. In addition, optical emission and broadband absorption spectroscopies (OES and BAS, respectively) were combined for the determination of rotational and vibrational temperatures (T_R and T_V, respectively) for both excited and ground state species. This comprehensive approach can and should be applied globally, across a wide range of plasma systems (i.e., clean gas, etching, depositing) and

materials (i.e., semiconductors, catalysts, polymers). The two platforms explored here were plasma-assisted catalysis systems containing N_xO_y species and fluorocarbon (FC) plasmas, utilizing a range of precursors to evoke either etching or depositing conditions.

An understanding of how energy is dispersed into rotational, vibrational, and translational modes of a gas-phase molecule by means of plasma-stimulated decomposition of a precursor lends critical insight into molecule formation mechanisms, decomposition pathways, and overall plasma chemistry. Specifically, energetic distributions for excited and ground state CF_x (x = 1, 2) radicals within fluorinated plasma systems were measured via OES and BAS. Elevated excited state T_V for CF radicals within C_xF_y discharges suggest that vibrational modes are preferentially excited over other degrees of freedom. In C_xF_y plasma systems, T_R for the radicals equilibrate to the plasma gas temperature and remain independent of changing plasma parameters.

Generally, C_xF_y precursors with lower fluorine-to-carbon (F/C) ratios tend to deposit FC films, where higher F/C ratios tend to etch surfaces. Here, zeolite modification via C_xF_y and $H_2O_{(v)}$ plasmas was investigated, along with the fabrication of various zeolite constructs (i.e., native, pellets, and electronspun fibers). Inductively coupled plasmas tuned the wettability of microporous zeolites, evaluated by static and dynamic water contact angle goniometry. Zeolite modification, such as the formation of fluorocarbon films or surface functionalization, was verified via X-ray photoelectron spectroscopy and scanning electron microscopy. OES was used to probe gas-phase species, gleaning how the material intrinsically changes the plasma environment. Our studies revealed correlations between gas-phase spectroscopic analyses, the gas-surface interface, and the resulting plasma modified surface properties.

A current area of interest to the plasma community, plasma-assisted catalysis (PAC), seeks to understand the synergistic coupling of a plasma with a catalyst for improved pollution abatement. Prior to probing the plasma-material interface within PAC systems, energetic and kinetic processes in N_xO_y plasmas were elucidated. Energy partitioning between degrees of freedom and multiple molecules (i.e., N_2 and NO) formed within N_xO_y plasma systems (N_2, N_2O, N_2/O_2) was investigated at various applied rf powers and system pressures. T_R and T_V for both molecules (regardless of state) showed a strong positive correlation with applied plasma power, as well as a negative correlation with system pressure. Analogous to the excited state CF radical study, in all cases, T_V values are significantly higher than T_R for NO and N_2 species. These studies characterized the gas-phase plasma chemistry without the added complexity of a material.

The impact of adding a catalyst (i.e., zeolites) on plasma energetics within an N_2 low-temperature, radio frequency plasma was investigated, where OES-related studies entailed *in situ* measurements of steady-state plasma-substrate interactions through the determination of N_2 T_R and T_V. N_2 plasmas were selected for this study to minimize system intricacy and number of plasma species. The presence of micro-structured zeolites within the plasma significantly decreases $N_{2(g)}$ vibrational temperature, suggesting these materials promote vibrational relaxation within the discharge upon interaction with a catalytic substrate. In addition to evaluating the spectroscopic characteristics of the N_2 discharge, material morphology and chemical composition were assessed before and after plasma exposure. Zeolite substrates maintained a porous, interconnected network, although small amounts of surface nitrogen incorporation occurred at high applied powers.

Building upon this foundation, OES was utilized to examine the impact of Pt and zeolite

catalysts on gas-phase species densities, plasma energetics, reaction kinetics, and plasma-catalyst configurations within an N_2O plasma. By studying Pt materials with two different morphologies and size scaling (i.e., foil and nanopowder), the role of material structure on resulting plasma chemistry was revealed. The concentration of excited state NO substantially decreased at high powers in the presence of Pt nanopowder and micro-structured zeolites. All catalytic materials studied herein significantly decreased N_2 T_V in the plasma, with little impact on rotational thermalization pathways. Pt nanopowder further enhanced NO decomposition within a two-stage configuration (i.e., plasma and substrate are physically separate), compared to the single-stage system. Material characterization conducted after N_2O plasma exposure revealed the plasma effectively poisons both Pt materials through oxidation, resulting in poorer performance in the single-stage system. Alternatively, zeolites, remained relatively unchanged by N_2O plasma exposure, hence further decomposed NO within the single-stage system. These studies exemplify the need for a holistic approach to solving challenges presented in the plasma-catalysis and fluorocarbon plasma community.

TABLE OF CONTENTS

LIST OF TABLES

LIST OF FIGURES

CHAPTER 1

INTRODUCTION

Presented herein is an introductory chapter, providing an overview of the fundamentals of plasma chemistry and plasma processing of materials. An essential portion of this dissertation work focuses on the use of various diagnostic tools to holistically study the gas-phase and resulting plasma-surface interface upon addition of a substrate. These topics are also introduced, along with an overview of the specific research to be found in subsequent chapters of this work.

1.1. Plasma Chemistry Fundamentals

Plasmas, the fourth state of matter, are partially ionized gases containing a heterogenous variety of energetic components. Plasmas generally fall into two main classifications: thermal or non-thermal. Thermal plasma systems are characterized by the existence of thermodynamic equilibrium, where the ion and electron temperatures (T_i and T_e, respectively) equilibrate.[1] Chemical reactions within these systems take place near the thermal equilibrium, characterized by a common temperature of all species. High-temperature thermal plasmas are often employed in industrial applications (e.g., welding, metallurgical and steel-making),[2] as well as the formation and growth of nanomaterials.[3,4] Non-thermal plasmas, however, contain electrons with higher energies than those found in thermal systems, resulting in T_e values up to two orders of magnitude greater than T_i.[1] In addition to high energy electrons, non-thermal plasmas have relatively low gas temperatures ($T_g < 10^3$ K), often thermalizing to room temperature (~300 K).[1] The differences between thermal and non-thermal discharges are explained, in part, by increased Brownian motion in the non-thermal system, caused by the movement of electrons in response to

an external applied electric field.[1,5] Thus, non-thermal plasmas consist of more electron-based collisions with other gas species compared to thermal plasmas, discussed below.

A plasma is ignited when a free electron is accelerated across an applied electric potential and collides with another species. For the work herein, radio frequency (rf) at 13.56 MHz is driven through an induction coil, generating an applied electric field, where a resulting cascade of electron-mediated collisions produces a plasma. Electrons can ionize atoms or molecules present in the gas phase, generate excited species, and promote molecular dissociation. Thus, the plasma bulk nominally comprises free electrons, ions, metastables, as well as ground- and excited-state atoms and molecules. The presence of both electrons and positive ions generally renders the bulk of the plasma gas quasi-neutral. Due to the multitude of gas-phase species produced in a plasma, plasma chemistry and species interactions are complex and multi-faceted, even in relatively simple atomic and molecular systems (e.g., Ar and N_2). The discharge chemistry becomes increasingly convoluted when studying larger precursors and feed gas mixtures, as the number of breakdown products nominally increases with more complex precursors.

Several characteristic and distinct temperatures arise within non-thermal plasmas due to the lack of thermodynamic equilibrium, such as rotational (T_R) and vibrational (T_V) temperatures for individual plasma species.[6] Determining energy partitioning trends within a discharge can elucidate the underlying chemistry leading to macroscopic plasma behavior and provide a molecular-level understanding of plasma processes. Therefore, these studies sought to gain a fundamental, molecular-level understanding of rf plasma systems, including the energetic implications of species' interactions, using a combination of spectroscopic techniques [e.g., optical emission spectroscopy (OES) and broadband absorption spectroscopy (BAS)] to

holistically probe the discharge.[7] This requires knowledge of discharge operation parameters (i.e., applied power, system pressure, gas mixture) and its interconnection with fundamental plasma parameters [i.e., gas temperature (T_g), electron density (n_e), electron temperature (T_e), and electron energy distributions]. A literature review for the applicability of spectroscopy-based diagnostics to study plasmas is provided in Chapter 3. Many studies have focused on homonuclear N_2[8-10] and other diatomic molecules (i.e., H_2, OH, NO),[11-14] yet a vast data gap exits for energy partitioning information for a majority of species found in technologically and environmentally relevant plasma systems. Moreover, there are substantially fewer experimental studies measuring plasma kinetics. Plasma dynamics can be quantitatively probed with time-resolved (TR) OES to gain mechanistic insight into formation and decomposition pathways. Here, a systematic approach was implemented to study non-thermal discharges with incremental increases in system complexity to build a comprehensive library of knowledge pertaining to plasma energetics and kinetics.

Non-thermal plasmas are widely employed to modify materials via surface etching (removal of material), thin film formation, or functionalization processes.[1] This versatility has led to plasmas being incredibly useful in semiconductor processing, creation of protective coatings, biomaterial fabrication and modification, and more recently, pollution abatement strategies.[15] Often, plasma modification studies focus on characterizing the material after plasma processing, with little to no description of the gas-phase chemistry (i.e., energy partitioning and kinetic distributions). Ultimately, a thorough understanding of interactions occurring at the plasma-surface interface is necessary to improve plasma processes. Therefore, a significant portion of this dissertation work sought to quantify how the addition of two- and three-dimensional (2D and

3D, respectively) substrates impact plasma species densities, energetics, and kinetics via optical spectroscopy.

1.2. Motivations for Fluorocarbon Investigations

Fluorocarbon (FC) plasmas are extensively employed in a variety of surface modification strategies, where plasmas are used to deposit conformal films or fluorinate inorganic and organic substrates,[16-18] create surfaces with relatively low surface energy and dielectric constants,[19] as well as for applications requiring biocompatibility.[20] d'Agostino *et al.* identified the formation and interactions of reactive F atoms and CF_x (x = 1, 2) radicals generated from a FC plasma with a substrate leads to an inherent dualistic behavior, where FC plasma can readily etch or deposit films.[21] Generally, as the fluorine-to-carbon (F/C) ratio of the precursor increases, surface etching is likely to dominate over film deposition. These processes are, however, occurring simultaneously and competitively within the discharge. Therefore, the role of gas-phase CF_x and F species as contributing factors on the net effect of substrate exposure warrants further investigation.

The seminal work by Coburn and Winters explored plasma-assisted etching of materials using halogenated systems, discovering a synergy between ions (Ar^+) and reactive plasma ($XeF_{2(g)}$) radicals for enhanced etch rates.[22] Millard and Kay were among the first to report strong correlations between the amount of CF_2 in the gas phase and the rate of FC deposition, utilizing *in situ* optical spectroscopy as a diagnostic tool for the polymerization process.[23] The Fisher Group has employed a three-tier diagnostic strategy to investigate a range of FC plasmas: (1) gas-phase diagnostics (i.e., emitting species densities, kinetics, and ion energies), (2) study of the gas-surface interface via our unique Imaging Radicals Interacting with Surfaces (IRIS) technique, and (3) robust surface characterization of plasma-processed materials.[24-29]

Specifically, Cuddy and Fisher used OES to measure relative CF_2 and F species densities during plasma processing of Si and ZrO_2 wafers, where greater amounts of CF_2 compared to F were measured with both substrates and at all applied powers.[25] Cuddy and Fisher also investigated the contributions of CF and CF_2 radicals to the formation of FC films, determining rate constants via TR-OES, as well as the propensity of CF and CF_2 radials to scatter from Si substrates within a variety of C_xF_y precursors via IRIS.[26] Their results demonstrated precursors with high F/C ratios (e.g., CF_4) did not readily deposit FC films on Si wafers, agreeing with the work by d'Agostino *et al.*.[21] Interestingly, TR-OES revealed rate constants of formation (k_f) for CF radicals were elevated and k_f (CF_2) values were significantly lowered within CF_4 discharges, compared to the depositing C_xF_y precursors ($F/C \leq 3$).[26] CF_2 species are hypothesized to promote surface passivation and FC film growth,[26] therefore the delayed formation of excited-state CF_2 may contribute to the absence of FC moieties on the material surface (detected via X-ray photoelectron spectroscopy) after CF_4 processing.

Additionally, as the F/C ratio within C_xF_y precursors decreased, the propensity of CF_x radicals to scatter from Si wafers also decreased.[26] Despite the extensive amount of literature investigating FC plasmas, a lack of understanding concerning energetic distributions of excited and ground state CF_x species and the ultimate mechanisms that drive C_xF_y plasma processing persists. Therefore, OES and BAS was used to determine T_R (CF and CF_2) and T_V (CF) values for a range of operating conditions and FC precursors. Studies on FC plasma deposition have largely focused on traditional, 2D substrates, such as wafers. Hawker *et al.* sought to deposit hydrophobic coatings on biopolymeric substrates with C_3F_8 and hexafluoropropylene oxide (HFPO) discharges.[20] Here, efficacy of FC film deposition or substrate etching was also investigated for 3D, microporous aluminosilicate zeolite materials.

Zeolites are commonly used in catalysis, wastewater treatments, and gas separations because of stable, micro- and nano-sized porous frameworks,[30-32] yet functionality is limited by surface effects. Therefore, plasma modification strategies were used to tailor surface chemistries while maintaining bulk crystallinity and morphology of zeolite constructs. The catalytic properties and potential for microporous zeolites are further discussion in Section 1.3.

1.3. Motivations for Plasma-Assisted Catalysis Studies

Plasma-assisted catalysis (PAC), the coupling of a discharge with a catalyst, has gained increasing attention in recent years as a possibly route to enhanced pollution abatement.[15,33] PAC has been investigated for a wide variety of applications, including volatile organic compound (VOC) removal,[34,35] CO_2 capture,[36] and treatment of exhaust gases.[37] Nitrogen oxides are a major pollutant in the atmosphere, especially N_2O, a greenhouse gas[38] and nitric oxide (NO). Morgan *et al*. studied the potential of rf ICPs to remove NO emissions from a variety of gas mixtures, containing NO, N_2, O_2, H_2O, and CH_4 precursors.[39] The authors observed a decrease in NO density as a function of power in NO and N_2/O_2 system. The decomposition of NO within a $NO/CH_4/Ar$ system was impacted by the addition of 2D substrates [e.g., Si wafers (as-received and Au-coated) and Pt foil].[39] The coupling of nano- and micro-structured 3D catalysts with N_xO_y discharges represents a large portion of the work presented in this dissertation. Specifically, microporous zeolite and nanostructured Pt catalysts were employed to study the plasma-catalytic decomposition of N_2O, Chapter 8.

Within the PAC community, three plasma-catalyst configurations are nominally investigated, studying system characterization and optimization.[40] Illustrated in Figure 1.1, two-stage systems require physical separation of the plasma and catalyst; where the exhaust gas decomposition is catalyzed by the material and those reaction products are subsequently exposed to the discharge

(pre-plasma catalysis) or the plasma alters the gas-phase composition prior to interaction with the catalyst (post-plasma catalysis).[40] Within single-stage systems, the plasma components can directly interact with the catalyst, ultimately resulting in complex and entangled chemistries. Active plasma species can influence the electronic, chemical, and physical properties of the catalysts, thus thorough material characterization is necessary to assess catalyst properties after plasma exposure. Conceivably, a catalyst that degrades or is damaged by the plasma is non-ideal for single-stage PAC systems. Subsequently, the material within the discharge can influence the electric field, electron energy distribution function (EEDF), adsorption of pollutants on the surface, and residence times in the discharge. Moreover, microdischarges can be formed within the pores of a material, illustrated in Figure 1.2, which can significantly impact the overall plasma character. Strong electric fields inside pores can lead to different electron energy distributions, giving rise to modified electron impact reaction rates and changes in the plasma chemistry.[41] The generation of a stable plasma inside catalyst pores is an important factor for PAC, as it can increase the active surface area of the catalyst that is available for waste treatment. Additionally, after plasma ignition, electrons rapidly move toward surfaces (i.e., reactor walls and substrates) in response to the external electric field,[1] depicted in Figure 1.2, creating a sheath around boundaries within the discharge. Sheath and ion effects at the surface of these catalytic materials are, therefore, important to consider and may contribute to the effectiveness of PAC technologies.

Therefore, a significant portion of this work was dedicated to investigating the impact on kinetics and energetics of gas-phase species when materials were added to PAC-relevant discharges.

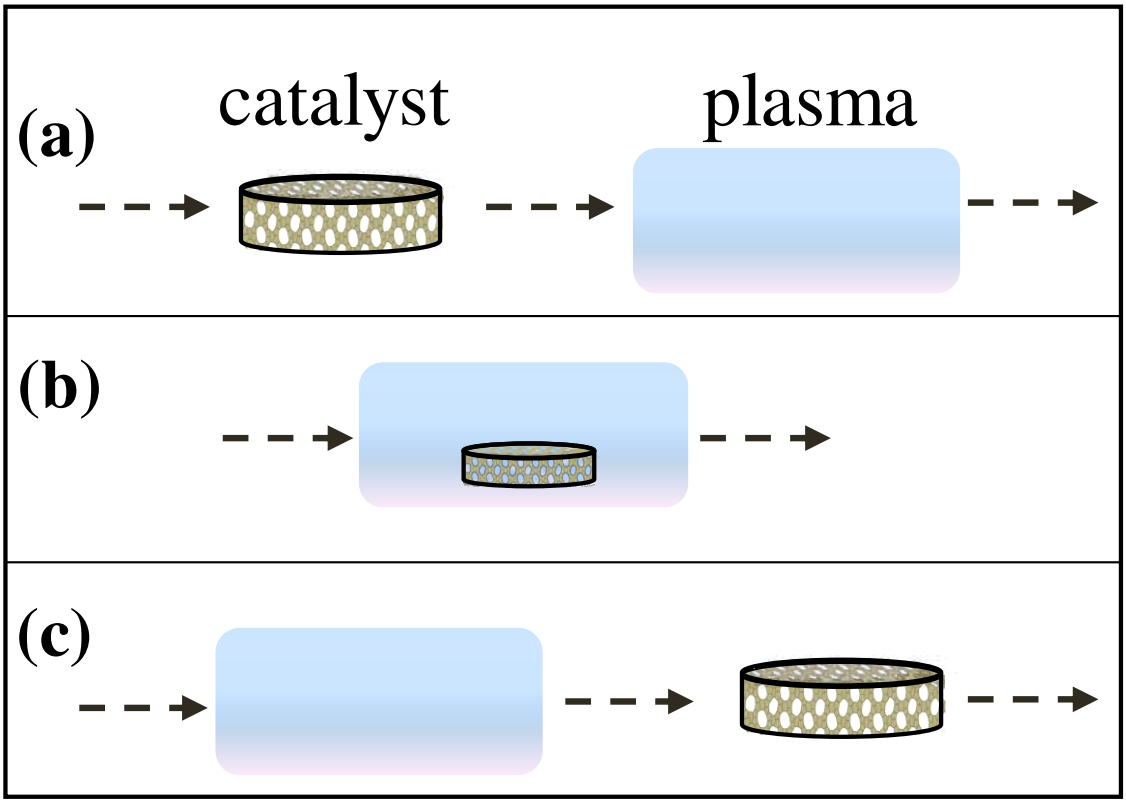

Figure 1.1. Representation of plasma-catalyst configurations, depicting (a) pre-plasma (or two-stage), (b) single-stage, in-plasma, and (c) post-plasma catalysis.

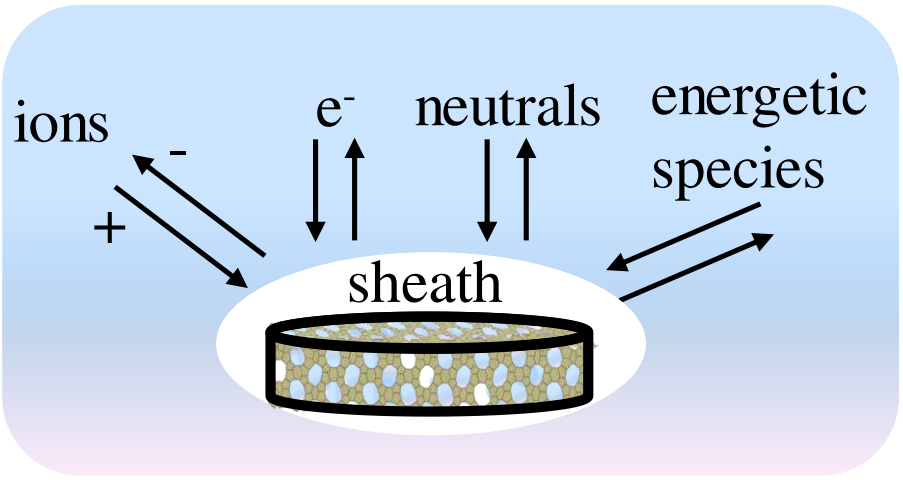

Figure 1.2. Schematic representation of some of the potential interactions occurring at the plasma-surface interface.

Specifically, formation and destruction mechanisms of key excited state species have been examined to provide mechanistic insight that could be correlated with system energetics. An overview of the work presented here is provided below in Section 1.4.

1.4.Overview of Research

Research efforts in this dissertation focus on linking the gas-phase, gas-surface interface, and material properties. All components represent a larger effort to elucidate potential plasma-material synergisms, where a fundamental understanding of these systems is essential to the continued development and application of plasma technologies. Chapter 2 provides detailed descriptions of the plasmas and materials studied herein; as well as the techniques, instruments, and methods used to characterize and explore those systems.

Chapter 3 provides a literature review of the development of optical diagnostic techniques to study non-thermal plasma discharges. Opportunities to elucidate fundamental plasma properties (i.e., electron temperatures and densities) within noble gases are discussed and demonstrated. This study illustrates the value of using temporally- and spatially-resolved optical spectroscopies to probe complex environmentally and technologically relevant discharges.

Although Chapter 4 may seem like a departure from the theme of other chapters, it extends our studies of plasma-surface interactions for a variety of fluorocarbon (FC) systems. Indeed, Chapter 4 focuses on the plasma energetics, primarily for CF and CF_2 species, including their ability to influence surface scatter properties. This fundamental FC work was applied to the surface modification of microstructured materials, detailed in Chapter 5.

Zeolites are a versatile class of materials, with widespread utility in catalysis, wastewater treatments, and gas separations.[30] The work presented in Chapter 5 focuses on customizing zeolite surface properties via plasma modification, while maintaining morphology and bulk

characteristics of the materials. The dynamic balance between etching and depositing regimes with differing F/C ratios in the precursors gas was studied, as well as how the addition of H_2 or O_2 promotes deposition and etching, respectively. Using $H_2O_{(v)}$ plasmas, the wettability of the zeolite materials was significantly enhanced and examined as a function of plasma operating conditions (i.e., power and time) and placement of material in the reactor. In addition to surface modification of these materials, the potential of zeolites to be employed in plasma-assisted catalysis was also explored.

Prior to adding a substrate to the discharge, a detailed characterization of the internal energetics and reaction kinetics of N_2 and NO molecules within N_XO_Y precursors is presented in Chapter 6. Rotational and vibrational temperatures were determined as a function of pressure and power for both absorbing and emitting species in the discharge. Rate constants of formation and destruction for excited state species, measured by former Fisher group member, Dr. J.M. Blechle, are also included. Chapter 7 expands upon the results detailed in Chapter 6 and focuses on the deciphering plasma-catalyst interactions.

Chapter 7 reports on our initial PAC studies with the precursor N_2: a simple, homonuclear diatomic molecule. With the addition of a single zeolite pellet in the coil region of an inductively-coupled plasma, a drastic decrease (~800 K) in $T_V(N_2)$ was documented at applied rf powers above 100 W. This vibrational cooling was further enhanced upon the addition of multiple zeolites throughout the reactor, where a decrease of ~1500 K (from the plasma system with no substrate present) was documented. PAC is thought to be a viable technology for pollution abatement, therefore we increased the complexity of the gaseous precursor to a more environmentally relevant gas, such as N_2O. Chapter 8 examines plasma energetics, reaction

kinetics, and plasma-catalyst configuration for both platinum and zeolite materials within an N_2O plasma.

Finally, Chapter 9 provides a brief summary of the entire dissertation and conveys the potential for further extension and application of this research. These studies exemplify the need for a holistic, well-rounded approach to solving challenges presented in the plasma community.

REFERENCES

1. Grill, A., *Cold Plasma Materials Fabrications: From Fundamentals to Applications*. IEEE Press: Piscataway, NJ, 1994.
2. Szente, R. N., Industrial Applications of Thermal Plasmas. *AIP Conf. Proc.* **1995**, *345*, 487-494.
3. Kodas, T., Vapor Synthesis. In *Encyclopedia of Materials: Science and Technology*, Buschow, K. H. J.; Cahn, R. W.; Flemings, M. C.; Ilschner, B.; Kramer, E. J.; Mahajan, S.; Veyssière, P., Eds. Elsevier: Oxford, 2001; pp 9497-9505.
4. Park, Y.-T.; Park, D.-W., Preparation of Nitrogen-Doped TiO_2 Powder by Plasma Jet. In *Stud. Surf. Sci. Catal.*, Rhee, H.-K.; Nam, I.-S.; Park, J. M., Eds. Elsevier: 2006; Vol. 159, pp 769-772.
5. Fridman, A., *Plasma Chemistry*. Cambridge University Press: 2008.
6. Penetrante, B.; Brusasco, R.; Merritt, B.; Vogtlin, G., Environmental Applications of Low-Temperature Plasmas. *Pure Appl. Chem.* **1999**, *71*, 1829-1835.
7. Stillahn, J. A.; Trevino, K. J.; Fisher, E. R., Plasma Diagnostics for Unraveling Process Chemistry. *Annu. Rev. Anal. Chem.* **2008**, *1*, 261-291.
8. Britun, N.; Gaillard, M.; Ricard, A.; Kim, Y. M.; Kim, K. S.; Han, J. G., Determination of the Vibrational, Rotational and Electron Temperatures in N_2 and Ar–N_2 rf Discharge. *J. Phys. D: Appl. Phys.* **2007**, *40*, 1022.
9. Ambrico, P. F.; Bektursunova, R.; Dilecce, G.; De Benedictis, S., Nitrogen Vibrational Excitation in a N_2/He Pulsed Planar-ICP RF Discharge. *Plasma Sources Sci. Technol.* **2005**, *14*, 676-685.
10. Shakhatov, V. A.; Mavlyudov, N. B.; Lebedev, Y. A., Studies of the Distribution Functions of Molecular Nitrogen and its Ion over the Vibrational and Rotational Levels in the DC Glow Discharge and the Microwave Discharge in a Nitrogen-Hydrogen Mixture by the Emission Spectroscopy Technique. *High Temp.* **2013**, *51*, 551-565.
11. Blechle, J. M.; Hanna, A. R.; Fisher, E. R., Determination of Internal Temperatures Within Nitric Oxide Inductively Coupled Plasmas. *Plasma Process. Polym.* **2017**, *14*, 1700041.
12. Hollmann, E. M.; Pigarov, A. Y.; Taylor, K., Measurement and Modeling of H_2 Vibrational and Rotational Temperatures in Weakly Ionized Hydrogen discharges. *J. Nucl. Mater.* **2005**, *337*, 451-455.
13. Bruggeman, P.; Cunge, G.; Sadeghi, N., Absolute OH Density Measurements by Broadband UV Absorption in Diffuse Atmospheric Pressure He-H_2O RF Glow Discharges. *Plasma Sources Sci. Technol.* **2012**, *21*, 035019.
14. Stuckert, E. P.; Miller, C. J.; Fisher, E. R., Gas-phase Diagnostics during H_2 and H_2O Plasma Treatment of SnO_2 Nanomaterials: Implications for Surface Modification. *J. Vac. Sci. Technol., B* **2017**, *35*, 021802.
15. Adamovich, I.; Baalrud, S. D.; Bogaerts, A.; Bruggeman, P. J.; Cappelli, M.; Colombo, V.; Czarnetzki, U.; Ebert, U.; Eden, J. G.; Favia, P.; Graves, D. B.; Hamaguchi, S.; Hieftje, G.; Hori, M.; Kaganovich, I. D.; Kortshagen, U.; Kushner, M. J.; Mason, N. J.; Mazouffre, S.; Thagard, S. M.; Metelmann, H. R.; Mizuno, A.; Moreau, E.; Murphy, A. B.; Niemira, B. A.; Oehrlein, G. S.; Petrovic, Z. L.; Pitchford, L. C.; Pu, Y. K.; Rauf, S.; Sakai, O.; Samukawa, S.; Starikovskaia, S.; Tennyson, J.; Terashima, K.; Turner, M. M.; Sanden, M. C. M. v. d.; Vardelle, A., The 2017 Plasma Roadmap: Low Temperature Plasma Science and Technology. *J. Phys. D: Appl. Phys.* **2017**, *50*, 323001.

16. Strobel, M.; Corn, S.; Lyons, C. S.; Korba, G. A., Plasma Fluorination of Polyolefins. *J. Polym. Sci., Part A: Polym. Chem.* **1987**, *25*, 1295-1307.
17. Vaswani, S.; Koskinen, J.; Hess, D. W., Surface Modification of Paper and Cellulose by Plasma-Assisted Deposition of Fluorocarbon Films. *Surf. Coat. Technol.* **2005**, *195*, 121-129.
18. Kylián, O.; Petr, M.; Serov, A.; Solař, P.; Polonskyi, O.; Hanuš, J.; Choukourov, A.; Biederman, H., Hydrophobic and Super-hydrophobic Coatings Based on Nanoparticles Overcoated by Fluorocarbon Plasma Polymer. *Vacuum* **2014**, *100*, 57-60.
19. Jin, Y.; Ajmera, P. K.; Lee, G. S.; Singh, V., Ultralow-k Silicon Containing Fluorocarbon Films Prepared by Plasma-Enhanced Chemical Vapor Deposition. *J. Electron. Mater.* **2005**, *34*, 1193-1205.
20. Hawker, M.; Pegalajar-Jurado, A.; Fisher, E., Conformal Encapsulation of Three-Dimensional, Bioresorbable Polymeric Scaffolds Using Plasma-Enhanced Chemical Vapor Deposition. *Langmuir* **2014**, *30*.
21. d'Agostino, R.; Cramarossa, F.; Fracassi, F.; Illuzzi, F., 2 - Plasma Polymerization of Fluorocarbons. In *Plasma Deposition, Treatment, and Etching of Polymers*, d'Agostino, R., Ed. Academic Press: San Diego, 1990; pp 95-162.
22. Coburn, J. W.; Winters, H. F., Ion-and Electron-Assisted Gas-Surface Chemistry - An Important Effect in Plasma Etching. *J. Appl. Phys.* **1979**, *50*, 3189-3196.
23. Millard, M. M.; Kay, E., Difluorocarbene Emission Spectra from Fluorocarbon Plasmas and Its Relationship to Fluorocarbon Polymer Formation. *J. Electrochem. Soc.* **1982**, *129*, 160.
24. Cuddy, M. F. Contributions of Gas-Phase Plasma Chemisry to Surface Modifications and Gas-Surface Interations: Investigations of Fluorocarbon rf Plasmas. Colorado State University, ProQuest Dissertations Publishing, 2012.
25. Cuddy, M. F.; Fisher, E. R., Investigation of the Roles of Gas Phase CF_2 and F During FC Processing of Si and ZrO_2 *J. Appl. Phys.* **2010**, *108*, 033303.
26. Cuddy, M. F.; Fisher, E. R., Contributions of CF and CF_2 Species to Fluorocarbon Film Composition and Properties for C_xF_y Plasma-Enhanced Chemical Vapor Deposition. *ACS Appl. Mater. Interfaces* **2012**, *4*, 1733-1741.
27. Liu, D.; Martin, I. T.; Fisher, E. R., CF_2 Surface Reactivity During Hot Filament and Plasma-Enhanced Chemical Vapor Deposition of Fluorocarbon Films. *Chem. Phys. Lett.* **2006**, *430*, 113-116.
28. Martin, I. T.; Zhou, J.; Fisher, E. R., Correlating Ion Energies and CF_2 Surface Production During Fluorocarbon Plasma Processing of Silicon. *J. Appl. Phys.* **2006**, *100*, 013301.
29. Martin, I. T.; Fisher, E. R., Ion Effects on CF_2 Surface Interactions During C_3F_8 and C_4F_8 Plasma Processing of Si. *J. Vac. Sci. Technol., A* **2004**, *22*, 2168-2176.
30. Shi, J.; Yang, Z.; Dai, H.; Lu, X.; Peng, L.; Tan, X.; Shi, L.; Fahim, R., Preparation and Application of Modified Zeolites as Adsorbents in Wastewater Treatment. *Water Sci. Technol.* **2018**, *2017*, 621-635.
31. Liu, J.; Jiang, G.; Liu, Y.; Di, J.; Wang, Y.; Zhao, Z.; Sun, Q.; Xu, C.; Gao, J.; Duan, A.; Liu, J.; Wei, Y.; Zhao, Y.; Jiang, L., Hierarchical Macro-meso-microporous ZSM-5 Zeolite Hollow Fibers With Highly Efficient Catalytic Cracking Capability. *Sci. Rep.* **2014**, *4*, 7276.
32. Bastani, D.; Esmaeili, N.; Asadollahi, M., Polymeric Mixed Matrix Membranes Containing Zeolites as a Filler for Gas Separation Applications: A Review. *J. Ind. Eng. Chem.* **2013**, *19*, 375-393.

33. Whitehead, J. C., Plasma Catalysis: A Solution for Environmental Problems. *Pure Appl. Chem.* **2010**, *82*, 1329.
34. Chen, H. L.; Lee, H. M.; Chen, S. H.; Chang, M. B.; Yu, S. J.; Li, S. N., Removal of Volatile Organic Compounds by Single-Stage and Two-Stage Plasma Catalysis Systems: A Review of the Performance Enhancement Mechanisms, Current Status, and Suitable Applications. *Environ. Sci. Technol.* **2009**, *43*, 2216-2227.
35. Feng, X.; Liu, H.; Hi, C.; Shen, Z.; Wang, T., Synergistic Effects and Mechanism of a Non-Thermal Plasma Catalysis System in Volatile Organic Compound Removal: A Review. *Catal. Sci. Technol.* **2018**, *8*, 936-954.
36. Chen, G.; Britun, N.; Godfroid, T.; Georgieva, V.; Snyders, R.; Delplancke-Ogletree, M.-P., An Overview of CO_2 Conversion in a Microwave Discharge: The Role of Plasma-Catalysis. *J. Phys. D: Appl. Phys.* **2017**, *50*, 084001.
37. Kim, H.-H.; Teramoto, Y.; Ogata, A.; Takagi, H.; Nanba, T., Plasma Catalysis for Environmental Treatment and Energy Applications. *Plasma Chem. Plasma Process.* **2016**, *36*, 45-72.
38. Understanding Global Warming Potentials. https://www.epa.gov/ghgemissions/understanding-global-warming-potentials (accessed June 3 2019).
39. Morgan, M. M.; Cuddy, M. F.; Fisher, E. R., Gas-Phase Chemistry in Inductively Coupled Plasmas for NO Removal from Mixed Gas Systems. *J. Phys. Chem. A* **2010**, *114*, 1722-1733.
40. Whitehead, J. C., Plasma-Catalysis: The Known Knowns, the Known Unknowns, and the Unknown Unknowns. *J. Phys. D: Appl. Phys.* **2016**, *49*, 243001.
41. Yu-Ru, Z.; Erik, C. N.; Annemie, B., Enhancement of Plasma Generation in Catalyst Pores with Different Shapes. *Plasma Sources Sci. Technol.* **2018**, *27*, 055008.

CHAPTER 2

EXPERIMENTAL METHODS

This chapter contains a detailed description of experimental apparatus, instruments, materials, fabrication techniques, and methods used to perform the research discussed in this dissertation. These experimental details are also presented in publications that are the basis for Chapters 3 – 8.[1-5] This chapter includes five main sections: Section 2.1 provides an overview of the plasma systems and treatment conditions used herein; gas-phase diagnostics (2.2); the IRIS technique (2.3); substrate preparation and fabrication (2.4); and material characterization (2.5). All IRIS data were collected by previous Fisher Group members, specifically Dr. C.I Butoi, Dr. K. L. Williams, Dr. J. Zhang, Dr. M. F. Cuddy, and Dr. J. M. Blechle. I would like to thank all members of the Central Instrument Facility at CSU, without their guidance and technical expertise, this work would have not been possible. Additionally, Michael Olsen, Ron Costello, and Tom Frederick within the CSU Chemistry Department have all played essential roles in the work presented herein, particularly with system design and maintenance.

2.1 General Information

Plasma reactor. The majority of plasma treatments were performed in a home-constructed glass tubular reactor, inductively coupled via an eight-turn Ni-plated Cu coil, described in detail previously and shown in Figure 2.1a.[3,6] Slightly different reactor configurations were employed throughout this dissertation work; the reactor shown in Figure 2.1a was used to collect the spectroscopy data presented in Chapters 3 – 8. The reactor utilized for zeolite material modification (Figure 2.1b) has a central O-ring joint to enable efficient sample introduction and

is elongated to probe downstream plasma species. The reactor in Figure 2.1a was lined with zeolite pellets to create a multi-substrate reactor, discussed in Chapter 7 (Figure 2.2a). For two-stage studies, a pre-plasma catalysis system was constructed (Figure 2.2b) that included a stainless-steel vacuum chamber mated upstream to the plasma reactor.[5] Catalytic substrates were placed in the center of this chamber, feed gas flowed over the substrate, entered the glass reactor, and a plasma was subsequently ignited. Regardless of reactor configuration, radio frequency (rf) at 13.56 MHz was applied through a matching network; applied rf power (P) ranged from 5 – 200 W in the work presented in this dissertation. For some experiments, a pulsed plasma was employed. For these experiments, pulsed power is reported in the form of duty cycle (d.c.), defined here as the ratio of pulse on time to total cycle time, where a d.c. of 100% is equivalent to continuous wave (CW) plasma condition. For comparison to CW plasmas, when the power was pulsed, the equivalent power (P_{eq}), defined as the product of the d.c. and the peak power, was reported. Here, 20 ms and 10 ms pulse widths were used to study pulsed Ar (Chapter 3) and N_2 (Chapter 7) discharges, respectively. Vacuum was maintained using a mechanical rotary vane pump, reactor pressure (p) was monitored using a Baratron® capacitance manometer. The reactor stabilized at base pressure (< 1 mTorr) before introduction of plasma precursors, where system p ranged from 25 – 200 mTorr. After introduction of gaseous or liquid precursors to the reactor, pressure stabilized for a minimum of 5 min prior to plasma ignition and for at least 5 min after plasma treatment to quench possible surface active sites, further discussed in Chapter 5.

Gaseous precursors were used as-received and introduced into the reactor with flow rates regulated through mass flow controllers (MKS Instruments Inc.) or a series of needle values, depending on the experiment. Liquid precursors (i.e., $H_2O_{(v)}$) were subject to a minimum of three freeze-pump-thaw cycles to remove trapped atmospheric gases before use.

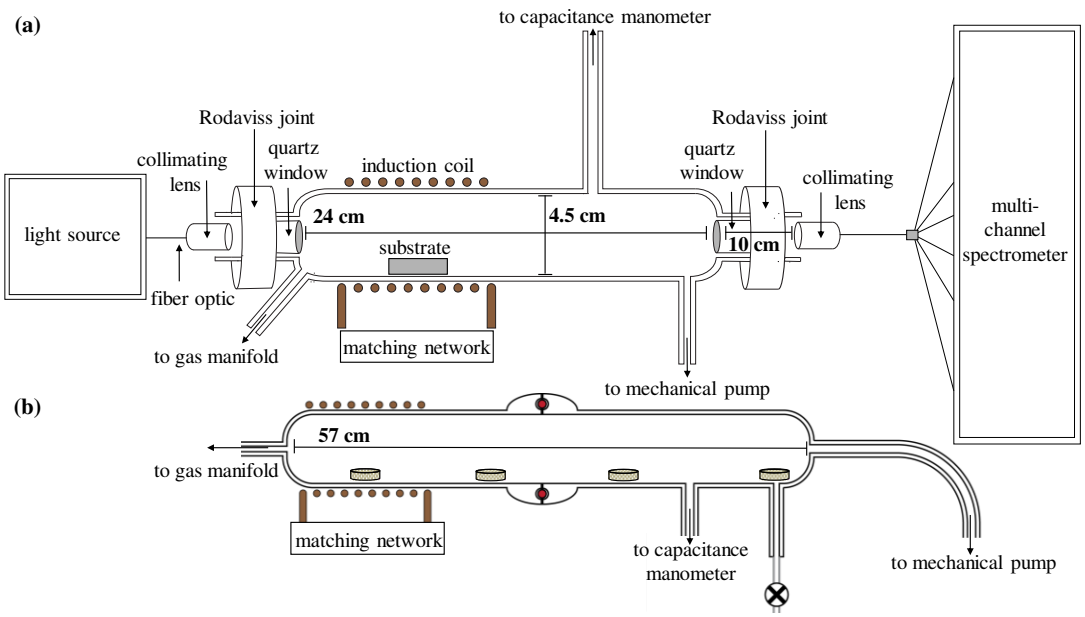

Figure 2.1. (a) Detailed schematic of OES/BAS apparatus used in spectroscopic investigations of low-temperature ICP discharges. Both collimating lenses are equidistant from quartz windows. (b) ICP reactor utilized to modify zeolites (Chapter 5), illustrating the range of substrate positions within the reactor.

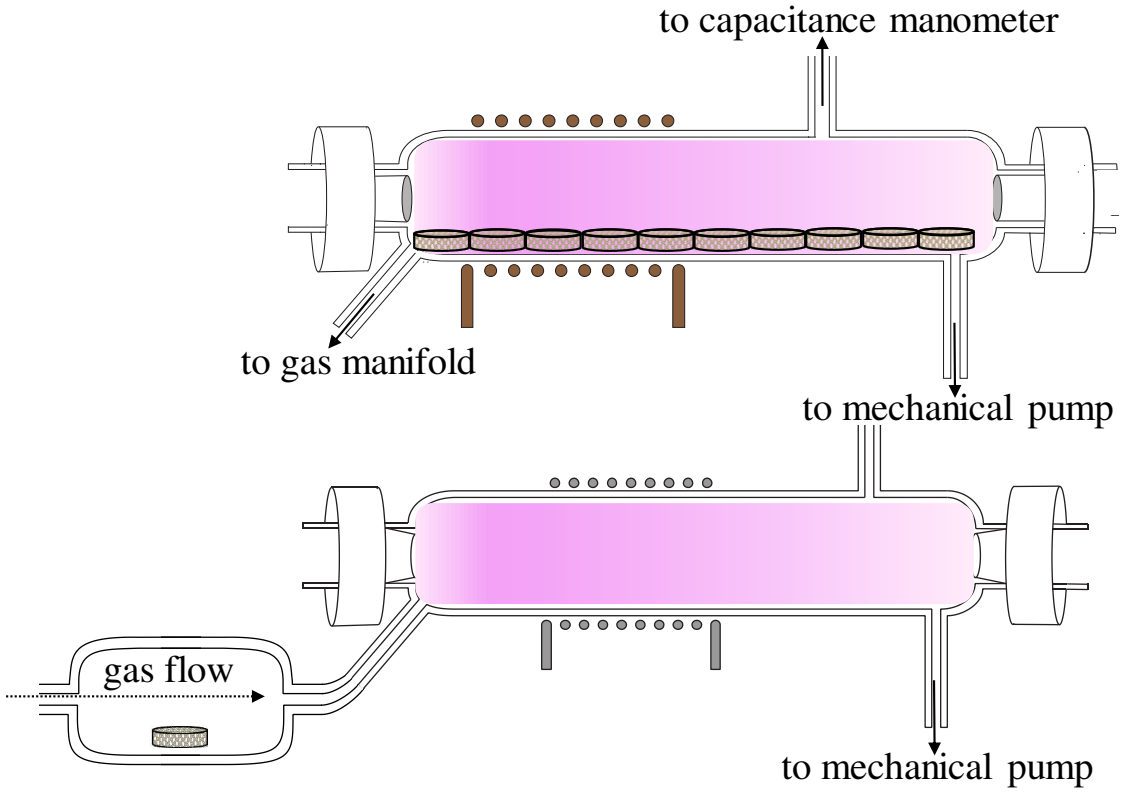

Figure 2.2. Schematic representation of (a) zeolite pellet, packed-bed system (Chapter 7) and (b) two-stage, pre-plasma catalysis configuration (Chapter 8).

Additionally, liquid precursors were stored in a 50 mL Pyrex sidearm vacuum flask with a Teflon stopcock and introduced to the reactor via needle valves. Table 2.1 lists the purity and manufacturer information for gaseous and liquid precursors used in this dissertation.

2.2 Gas – Phase Diagnostics

Optical Emission Spectroscopy (OES). All steady-state spectra were collected by an AvaSpec-2048L-USB2-RM multichannel spectrometer over a wavelength range of 197 – 1061 nm. Briefly, quartz windows are secured to the up and downstream ends of the reactor using RODAVISS® joints, enabling maximal signal intensities via the coaxial collection of plasma emission. The spectrometer houses six gratings, each synchronized for simultaneous data collection with 2048-pixel linear array charged couple device detectors with a spectral resolution of ~0.1 nm, determined from the full width half maximum (FWHM) of a HeNe laser. A second spectrometer (AvaSpec-ULS4096CL-EVO) was employed in time-resolved studies (Chapter 8) for enhanced temporal resolution (i.e., μs time scale), with a spectral resolution of 0.5 nm. A Faraday cage was constructed around the plasma reactor and spectrometer(s) to minimize potential rf coupling between the discharge and electronics of the spectrometer.

Actinometry was used in specified OES experiments, where the ratio of emission intensity for each excited state species of interest to that of an actinometric species is taken as a relative species density.[7,8] Using Ar as an actinometer, small amounts (~5-10% by pressure) were added to the feed gas to provide a reference to determine relative number density. The inherent assumptions with inert gas actinometry are discussed at length in Chapter 3. A concise list of species analyzed via actinometry and discussed in this dissertation is provided in Table 2.2.

Table 2.1. Summary of plasma precursors used for work presented in this dissertation

Precursor	Chemical Formula	Purity (%)	Manufacturer	Chapter(s)
argon	Ar	>99.999	Airgas	3-8
ultrapure ionized water	H_2O	--	Millipore	5
nitric oxide	NO	>95	American Gas Group	6
nitrogen	N_2	>99.99	Airgas	6,7
oxygen	O_2	99.5	Airgas	5,6
nitrous oxide	N_2O	>99	Airgas	5, 6, 8
tetrafluoromethane	CF_4	>95	Airgas	4, 5
hexafluoroethane	C_2F_6	>95	Airgas	4, 5
hexafluoropropylene	C_3F_6	>95	Airgas	4, 5
octofluoropropane	C_3F_8	>95	Airgas	4, 5
hexafluoropropylene oxide	HFPO	98	Sigma-Aldrich	4
hydrogen	H_2	99	Airgas	5

Table 2.2. Transitions and corresponding wavelengths used in actinometry studies

Emitting species	Transition	Wavelength (nm)
Ar	$2p_1 \rightarrow 1s_2$	750.4
NO	$A^2\Sigma^+ \rightarrow X^2\Pi$	235.9
N_2	$B^3\Pi_g \rightarrow C^3\Pi_u$	337.0
O	$^3S^0 \rightarrow {}^3P$	777.2
OH	$A^2\Sigma^+ \rightarrow X^2\Pi$	309.0
H_α	$^2P^0 \rightarrow {}^2D$	656.3
CF	$B^2\Delta \rightarrow X^2\Pi$	202.4
CF_2	$A^1B_1 \rightarrow X^1A_1$	251.9
F	$2p^43p^1 \rightarrow 2p^43s^1$	703.7

Broadband Absorption Spectroscopy (BAS). Depicted in Figure 2.1a, the experimental apparatus for BAS measurements consists of an AvaLight-DHS deuterium-halogen light source interfaced to the ICP reactor via a fiber optic cable and collimating lens (Avantes DCL-UV/VIS-200). Optics were aligned with the light source prior to any spectroscopic measurement. Three measurements were collected during each BAS experiment: emission from the light source (I_S), emission from the plasma (I_P), and emission from the plasma and source together (I_{PS}). An absorbance spectrum was determined via Equation (2.1).[9]

$$A = -\left(\frac{I_{PS}-(I_P+I_S)}{I_S}\right) \qquad (2.1)$$

A range of integration times (25 – 200 ms) and number of averages (25 – 150) were explored to examine the steady state of each plasma system with optimized signal-to-noise ratios, where discharge run times were several minutes. Within steady-state measurements, these plasma interactions are examined on the millisecond to minute time scales, therefore rf periods are not thought to play a major role in the final evaluation of the resulting data.[10]

Time Resolved Gas-Phase Analyses. Time resolved (TR)- OES data were collected to study formation and decomposition mechanisms within atomic and molecular plasma systems. Data collection began before plasma ignition and lasted for ~ 5 – 15 seconds after ignition; integration times for TR-OES varied from 75 μs to 25 ms, depending on the experiment.

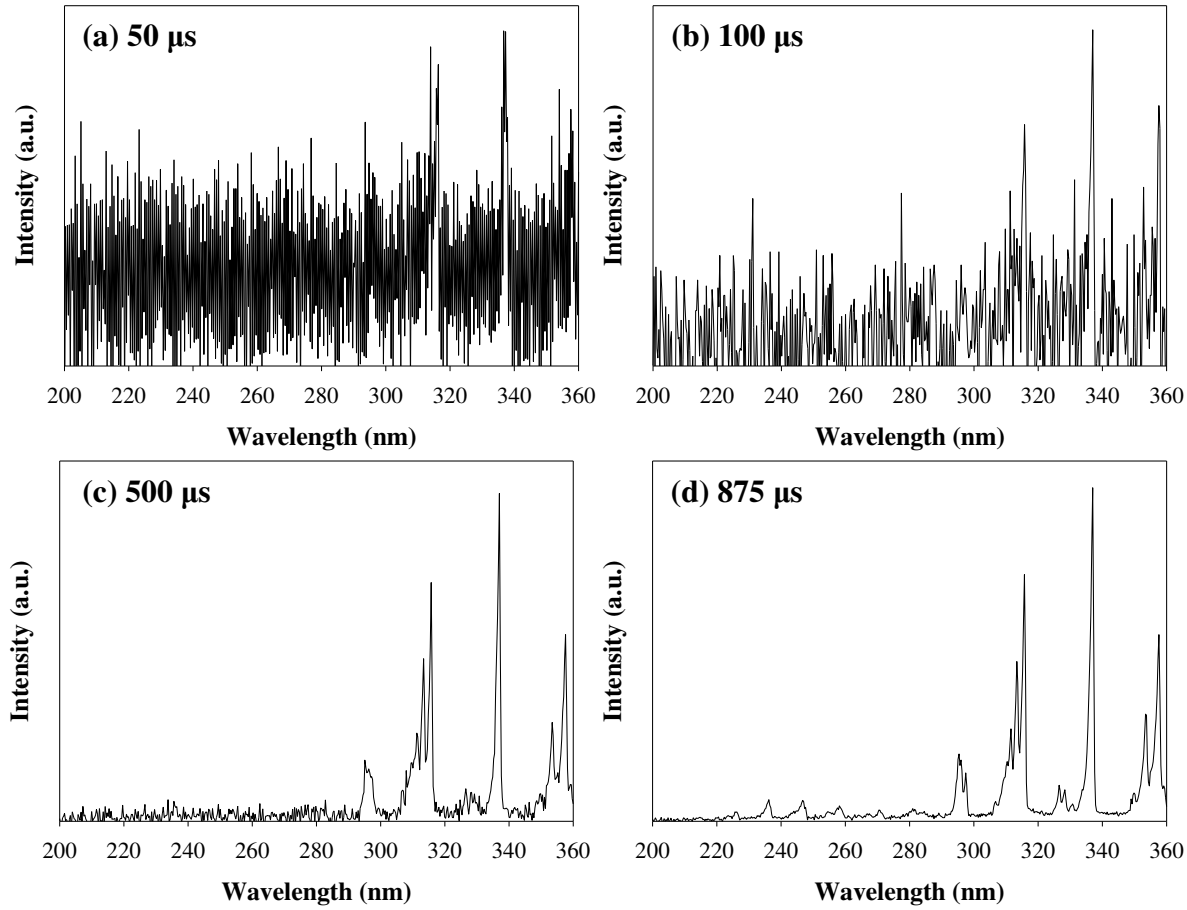

Figure 2.3. N_2O plasma emission (p = 100 mTorr, P = 150 W) collected at various integration times.

Integration time determination is heavily influenced by the system of study, highlighted in Figure 2.3. Emission arising from an N_2O plasma (p = 100 mTorr, P = 150 W) was collected at four integration times with one average, ranging from 50 μs up to 875 μs. Steady-state N_2O spectroscopy was previously collected at this experimental condition,[3] revealing strong emission bands from N_2 second positive ($C^3\Pi_g \rightarrow B^3\Pi_u$) and NO γ ($A^2\Sigma^+u \rightarrow X^2\Pi$) transitions. As can be seen in the Figure 2.3 spectra, at the fastest integration times, virtually no signal is observed for NO emissions and the N_2 signal is barely above the noise. As the integration time is increased slightly, emission bands from both molecules can clearly be seen in the spectra. This exemplifies the notion that the fastest integration time is not always optimal as emission from molecular species could get suppressed underneath poor signal-to-noise ratios. Therefore, selection of an integration time for a time-resolved study should be based on steady-state emission measurements to accurately include and assess species within a discharge. TR-OES data were collected with an AvaSpec-2048L-USB2-RM multichannel and an AvaSpec-ULS4096CL-EVO spectrometer. The TR-OES data presented in Chapter 6 were collected by Dr. J.M. Blechle with a 5 ms integration time and at an interval of 25.5 ms (AvaSpec-2048L-USB2-RM multichannel) with small amounts of Ar added as an actinometer.[11] The data presented in Chapter 7 were collected with a 25 ms integration time and one average, TR-OES data included in Chapter 8 were collected with a 1.5 ms integration time (AvaSpec-ULS4096CL-EVO). Actinometry (i.e., Ar dilution) was not used in the TR-OES data presented in Chapters 7 and 8. Regardless of spectrometer or integration time, data collection began before plasma ignition; the first non-zero data point was set at time (t) = 0.0 s and time points for all subsequent data points were adjusted accordingly. The intensity of signals arising from excited-state NO (235.9 nm) and N_2 (337.0 nm) were monitored as a function of time, shown in Figure 2.4a and

2.4b, respectively. The data presented in Figure 2.4 were collected with the AvaSpec-ULS4096CL-EVO spectrometer with a 1.5 ms integration time. The point(s) of highest intensity was identified; where the rise to maximum intensity was denoted as the rate constant of formation (k_f). The subsequent decrease in intensity marked the end of species formation and the start of signal decay, denoted as the rate constant of destruction (k_d). It is important to note that "destruction" here does not refer to complete decomposition or removal of the species, but rather a decrease in intensity resulting from several decay pathways available to the species of interest. In some cases, no specific formation and destruction of species were detected on the time scale of our system, further discussed in Chapter 6.

Characteristic Temperature Determination. The atomic emission intensity (I_{jk}) of the transition from level j to k depends on the Einstein coefficient of spontaneous emission (A_{jk}) and absolute population of the atomic level (n_j), shown in Equation 2.2

$$I_{jk} = n_j A_{jk} h\nu \tag{2.2}$$

where h is the Planck constant and ν is the frequency corresponding to the transition. Assuming the atomic level populations follow a Boltzmann distribution, I_{jk} is given by Equation 2.3:

$$I_{jk} = h\nu \left(\frac{A_{jk} g_j n}{U(T_{exc})}\right) exp\left(\frac{-E_j}{k_B T_{exc}}\right) \tag{2.3}$$

where g_j is the statistical weight of level j, n is the number density of bound electrons (not to be confused with n_e pertaining to free electrons in the plasma), $U(T_{exc})$ is the partition function, k_B is the Boltzmann constant, and E_j is the energy of the upper level, j. Equations 2.2 and 2.3 represent relationships for emitting species within ideal systems, not accounting for radiation trapping or electron distributions that deviate from a Boltzmann distribution. A representative emission spectrum of an Ar plasma (p = 100 mTorr, P = 20 W) is provided in Figure 2.5a.

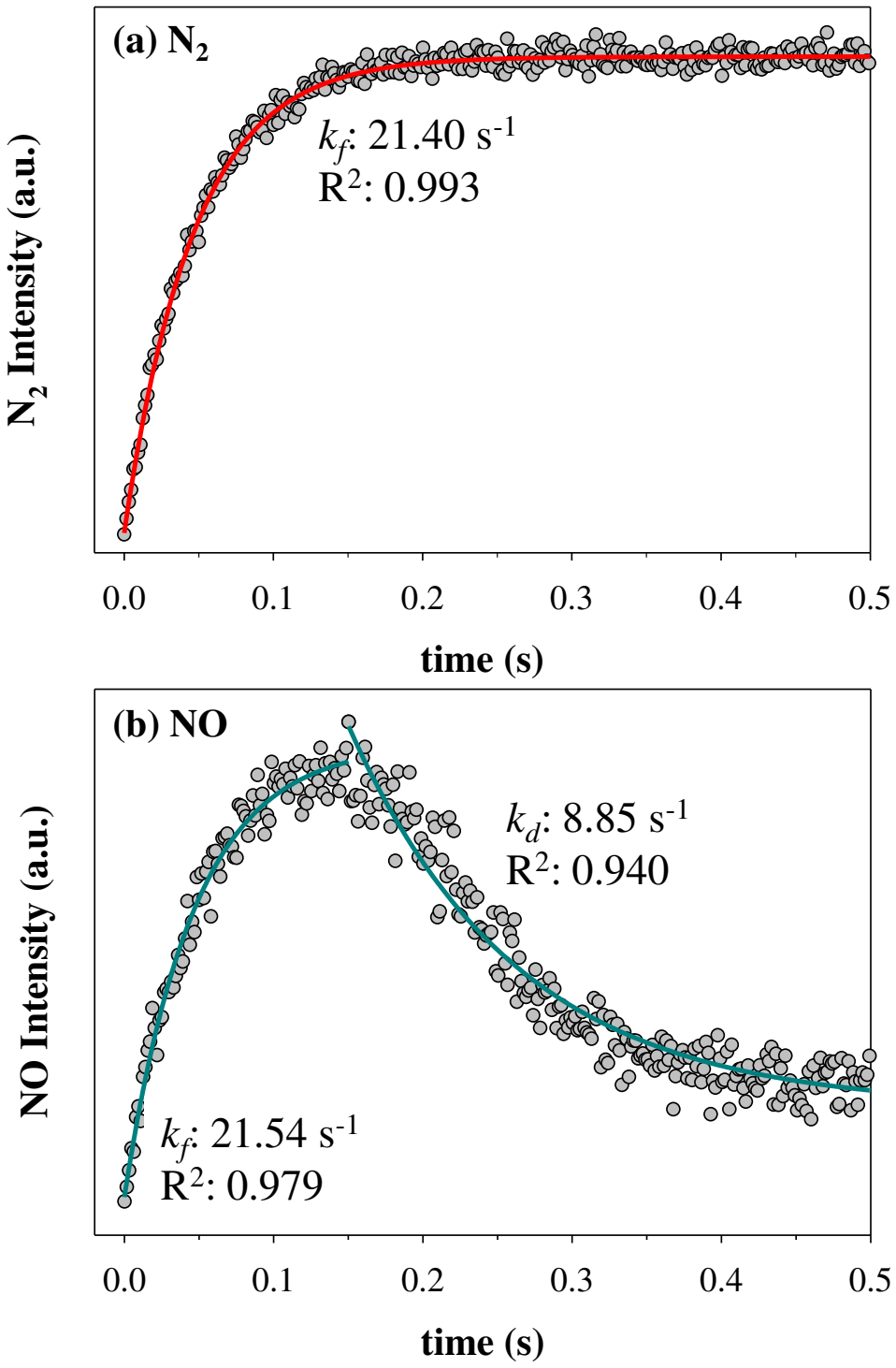

Figure 2.4. Intensity from (a) N_2 and (b) NO emission as a function of time, where first order exponentials were used to determine rate constants (P = 150 W, Pt powder substrate present).

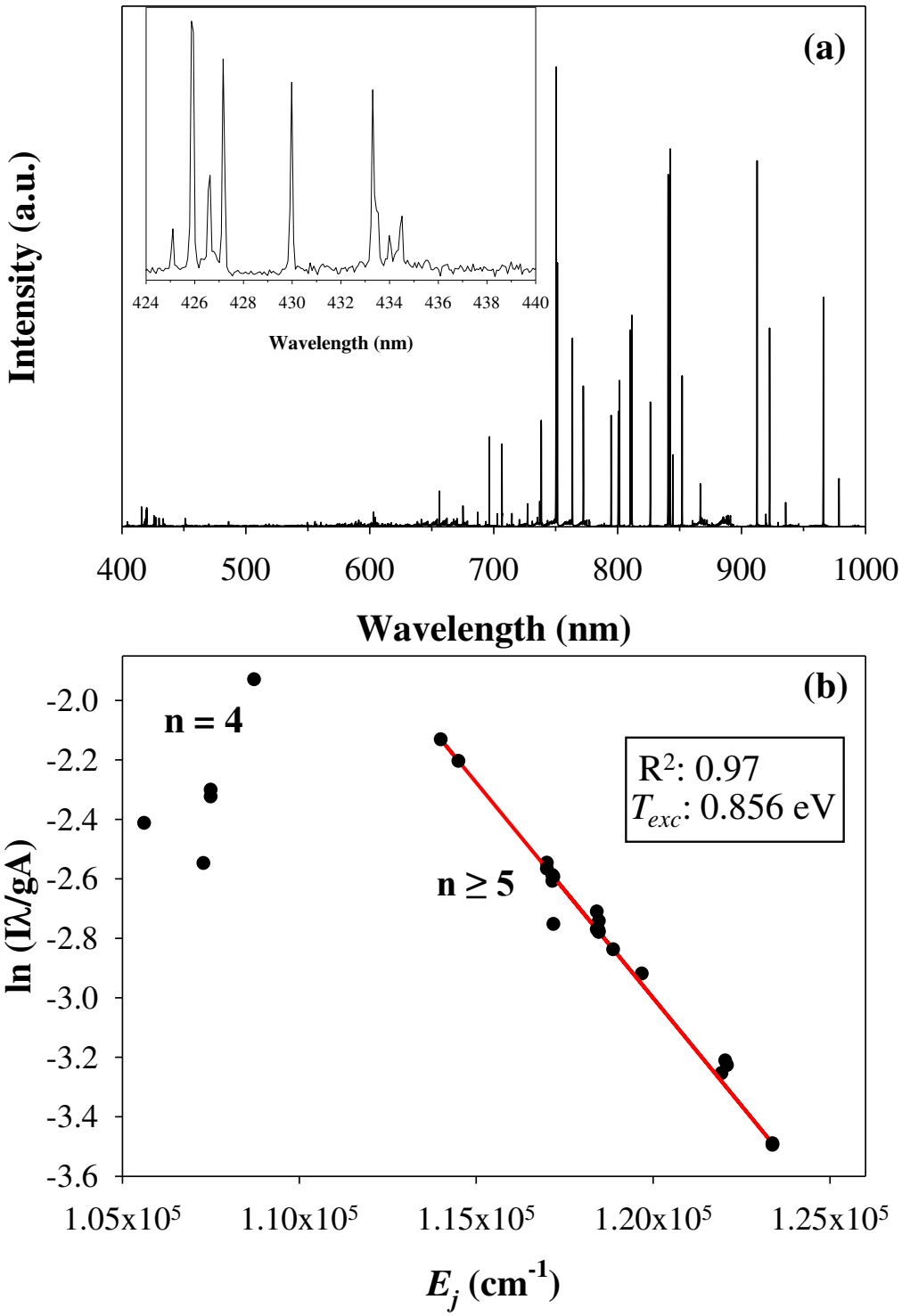

Figure 2.5. (a) Representative Ar emission spectrum and resulting (b) T_{exc} Boltzmann plot of Ar plasma (p = 150 mTorr, P = 10 W).

Table 2.3. Ar emission lines used in Boltzmann plotting procedure to determine T_{exc}

Transition	λ (nm)	A_{jk} (10^5 s^{-1})	g
$1s_4 - 3p_6$	426.6	3.33	5
$1s_4 - 3p_7$	427.2	8.40	3
$1s_4 - 3p_8$	430.0	3.94	5
$1s_2 - 3p_3$	433.3	6.00	5
$1s_2 - 3p_2$	433.5	3.80	3
$1s_2 - 3p_4$	434.5	3.13	3
$2p_{10} - 5s_1$"	518.7	13.8	5
$2p_9 - 7d_4$'	522.0	9.20	9
$2p_9 - 6d_4$'	549.5	17.6	9
$2p_{10} - 5d_3$	555.8	14.8	5
$2p_{10} - 5d_4$	560.6	22.9	3
$2p_9 - 5d_4$'	603.2	24.6	9
$2p_{10} - 3s_5$	641.6	12.1	5

Excitation temperature (T_{exc}) was determined via a Boltzmann method, where $\ln(I_{ij}\lambda/g_jA_{jk})$ was plotted as a function of the upper level energy E_j, the slope of which is equal to $-1/k_BT_{exc}$. Shown in Figure 2.5b, the experimental data for the higher Ar levels (quantum number $n \geq 5$) are linear with E_j, whereas lower lying levels (quantum number $n < 4$) deviate. This underpopulation of the lower energy state is a deviation from local thermodynamic equilibrium (LTE), most likely resulting from plasma relaxation processes, rather than only through electron-impact excitation from the ground state followed by de-excitation. This concept is further discussed in Chapter 3. Only the $n \geq 5$ Ar emission lines were utilized in the determination of T_{exc}, transitions (Paschen's notation) and relevant constants are listed in Table 2.3.

Plasma mean electron temperature (T_e) values were also determined via analysis of Ar emission lines in more complex gas systems (Chapters 4 and 6). This process involved iterative comparison of the intensities of four Ar transitions, summarized in Table 2.4, with the emission line of Ar^+ ($\lambda = 617.2$ nm). Specifically, T_e is calculated from emission intensities via Equation 2.4:[12]

$$\frac{(E_n - E_1)}{kT_e} = \ln\left[\frac{I_1 \nu_n A_n (E_n + 2kT_e)}{I_n \nu_1 A_1 (E_1 + 2kT_e)}\right] \qquad (2.4)$$

where E_n represents the excitation energy of arbitrarily defined transition n. I_n is the emission intensity obtained from the OES spectrum, ν_n is the frequency of the transition, and A_n is the transition probability. This calculation yielded three T_e values for each OES spectrum collected, which were then averaged and reported with one standard deviation from the mean. Although T_{exc} and T_e have been determined using analysis of Ar atomic lines, several studies have combined computational (CR models) and experimental (Langmuir probes) results to select emission line-ratios with a high sensitivity to T_e and n_e, shown in Equations 2.5 and 2.6, respectively.

Table 2.4. Emission parameters for used in T_e determination

Transition[a]	**λ (nm)**	**ν x 10^{14} (s^{-1})**	**A (s^{-1})**	**Excitation Energy (eV)**
--	617.2	4.86	2.00 x 10^7	21.127
$2p_{10} - 3s_2$	641.6	4.68	1.16 x 10^6	14.839
$2p_{10} - 3s_4$	638.5	4.70	4.21 x 10^5	14.848
$2p_{10} - 4d_3$	675.3	4.44	1.93 x 10^6	14.743

[a] Transitions are denoted in Paschen's notation for excited state Ar.

$$T_e\ sensitive\ ratio = \left(\frac{I(763.5\ nm)}{I\ (738.3\ nm)}\right) \quad (2.5)$$

$$n_e\ sensitive\ ratio = \left(\frac{I(706.7\ nm)}{I\ (750.4\ nm)}\right) \quad (2.6)$$

Results from the T_e sensitive ratio (Equation 2.5) are compared to the T_{exc} values obtained via the Boltzmann plotting method for a range of system pressures (50 – 150 mTorr) and applied rf powers (5 – 50 W) in Chapter 3.

Emission and absorbance spectra were analyzed using LIFBASE 2.1.1[13] simulations of the radiative transitions NO gamma ($A^2\Sigma^+ \leftrightarrow X^2\Pi$), OH ($A^2\Sigma^+ \leftrightarrow X^2\Pi$), and CF ($B^2\Delta \leftrightarrow X^2\Pi$) within N_xO_y, H_2O, and FC (fluorocarbon) plasma systems, respectively. After importing experimental spectra and specifying the parameter space, the simulated vibrational histogram was manually manipulated to best represent experimental peak heights, yielding non-equilibrium distributions. Using these vibrational state populations, we determined T_V via Equation 2.7:

$$T_V = \frac{\sum_{v_i}^{v_f} n(\hbar\omega)(v + ½)}{k_B} \quad (2.7)$$

where n represents the fractional population of an individual vibrational state, ω is the vibrational constant (ω = 1904 cm^{-1} for NO $X^2\Pi$, ω =2374 cm^{-1} for NO $A^2\Sigma^+$)[13], v is the numeric vibrational state, and k_B is Boltzmann's constant. Determination of T_R was achieved by adjusting the rotational temperature within LIFBASE to match peak FWHM, assuming a thermalized distribution. Using LIFBASE to determine vibrational populations and rotational temperatures, we sought to maximize peak correlation (>90%), as reported within the program.

Specair, a commercially available spectral fitting program, was utilized to determine N_2 plasma temperatures. All $T_R(N_2)$ values for the $C^3\Pi_u \leftrightarrow B^3\Pi_g$ transition were determined from simulated fits of experimental spectral data using Specair.[14] $T_V(N_2)$ values reported in Chapter 6 were determined via the "Temperature Loop" function within Specair.[3] A Boltzmann plot of

$\ln(I\lambda/A)$ as a function of vibrational energy (E) was used to calculate $T_V(N_2)$ in Chapters 7[4] and 8,[5] where I and λ are the intensity (a.u.) and wavelength (nm) of a specific emission line and A (s^{-1}) is the corresponding Einstein transition probability coefficient for the transition. Table 2.5 lists the N_2 vibrational transitions, corresponding wavelengths, and A values used herein.[15,16] The differences between these temperature determination methods is discussed in Chapter 7. Figure 2.6 shows a representative Boltzmann plot for a 100% N_2O plasma (with a zeolite substrate) created from Specair fits of T_R and the Table 2.5 data. The slope of the linear regression is inversely proportional to T_V, yielding $T_V = 2300$ K. pGopher[17] was used to determine T_R values CF_2 molecules, described in Chapter 4.[2] To simulate the CF_2 ($\tilde{A}^1B_1 - \tilde{X}^1B_1$) transition at wavelengths 240 – 260 nm, the rotational constants described by Blucourt and coworkers were utilized.[18] For all rotational and vibrational temperatures determined within this dissertation work, error was determined from a standard deviation of $n \geq 3$ trials.

Discussed in detail below, the application of spectroscopy to elucidate fundamental plasma properties is inherently dependent on the spectral resolution, quantum efficiency, and grating efficiency of the spectrometer. The wavelength-dependent quantum and grating efficiencies should be calibrated and corrected before the fit of measured spectra can be used for the determination of plasma temperatures.[1] The quantum efficiency of these detectors varied by ~5% and therefore, was not considered in the work presented herein. All spectra collected herein are irradiance-calibrated across the wavelength range 200 – 1000 nm; however, the grating efficiency reported by Avantes ranged from ~35% to ~65%, depending on the spectrometer channel. As may be expected, applying a correction for grating efficiency has no measurable effect on measured T_R values, as these are nominally determined by fitting the FWHM of the vibrational peaks.

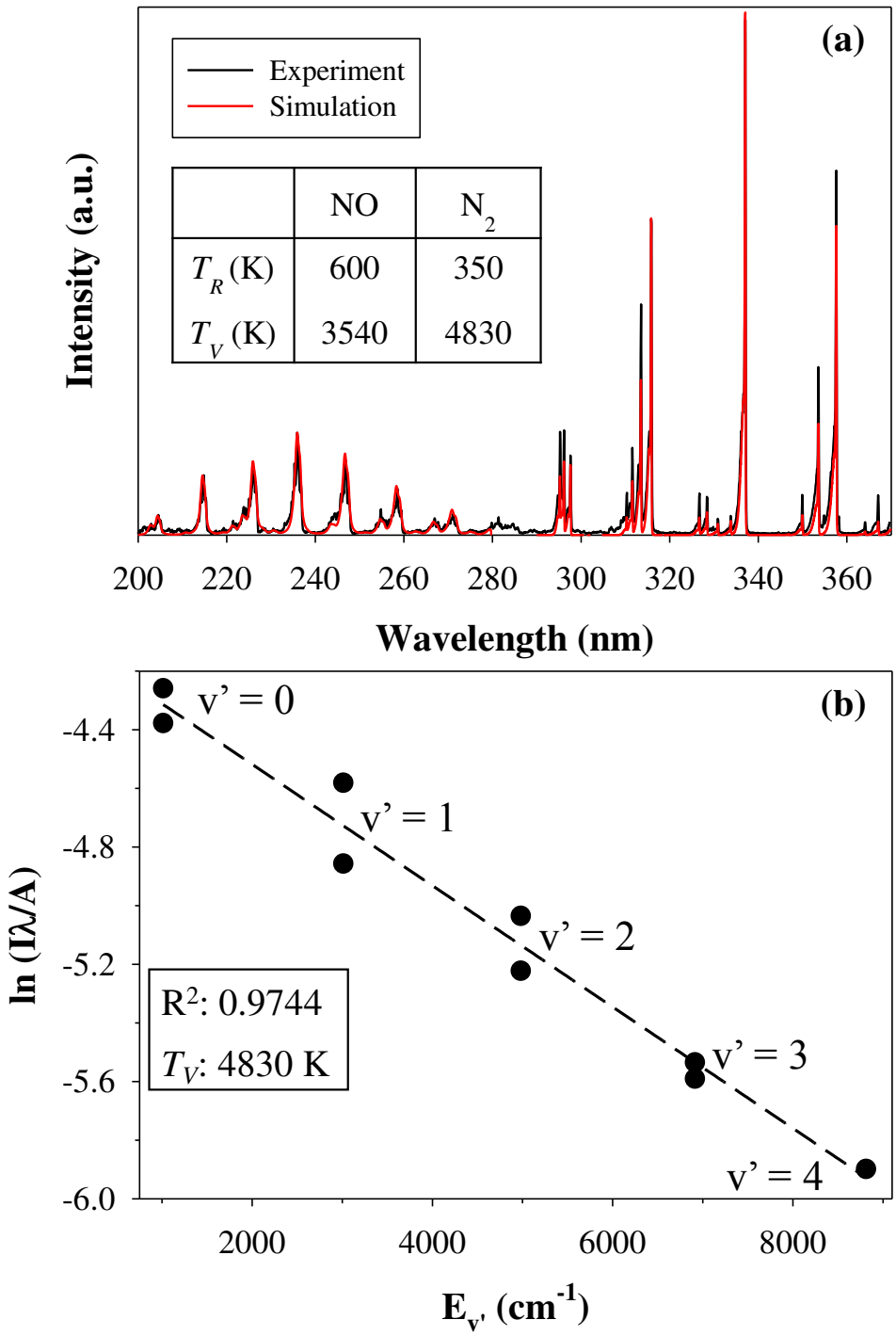

Figure 2.6. (a) Representative N_2O emission spectrum (100 mTorr, 125 W, zeolite pellet present), with both NO and N_2 bands fit. Internal temperatures are reported within inset table. (b) Boltzmann plot corresponding to the determination of N_2 T_V(K) at the above conditions.

Table 2.5. Parameters for the vibrational bands in N_2 used to determine T_V (K) using a Boltzmann plot.

vibrational transition	**λ (nm)**	**$A_{v'-v''}$ (10^6 s^{-1})**
4 → 2	295.3	8.84
3 → 1	262.2	6.61
2 → 0	297.6	3.49
3 → 2	311.6	5.48
2 → 1	313.5	8.84
1 → 0	315.9	10.2
0 → 0	337.1	11
1 → 2	353.6	4.61
0 → 1	375.6	7.33

In contrast, the grating efficiency can impact determined T_V values. The differences in the resulting T_V(NO) values obtained with a grating efficiency correction compared to those obtained without a correction were, however, within the overall experimental error.[6] This can be rationalized by considering the methodology used to obtain T_V(NO) from emission spectra, which includes the entire vibrational band corresponding to the $A^2\Sigma^+ \rightarrow X^2\Pi$ transition in the simulated spectra (Figure 2.6a). As a consequence, small differences in grating efficiency are likely accounted for within the fit of this relatively wide wavelength range (200 – 280 nm). For comparison, in the determination of T_V(CH) within CH_4 plasmas, Van Surksum and Fisher found the grating efficiency did have a significant impact on the resulting temperature.[19] These data were, however, collected on a different, four-channel Avantes AvaSpec-3648-USBS spectrometer.[19] In addition, the wavelength range for the CH ($A^2\Delta \rightarrow X^2\Pi$) molecule is significantly smaller (425 – 437 nm) and the v' = 0 and v'= 1 vibrational states significantly overlap in the CH vibrational band. By comparison, the NO emission band is characterized by distinctively separate vibrational peaks (shown in Figure 2.6a). Thus, small fluctuations in the grating efficiency within this smaller, more conflated wavelength range impacted the determined T_V(CH) values. These examples clearly demonstrate that the potential influence of quantum and grating efficiencies, spectral resolution, and calibration technique should all be carefully considered when employing spectral techniques in plasma temperature determination.

2.3 Gas-Surface Interface

Imaging Radicals Interacting with Surfaces (IRIS). Laser induced fluorescence (LIF) spectra were acquired for SiF, CF, rand NO radicals for the $A^2\Sigma^+ \leftarrow X^2\Pi$ transition, as well as CF_2 ($A^1B_1 \leftarrow X^1A_1$) by previous Fisher Group members.[2,6] For these studies, an rf inductively coupled plasma (ICP) reactor was mated to the IRIS chamber, described in detail previously.[20-22]

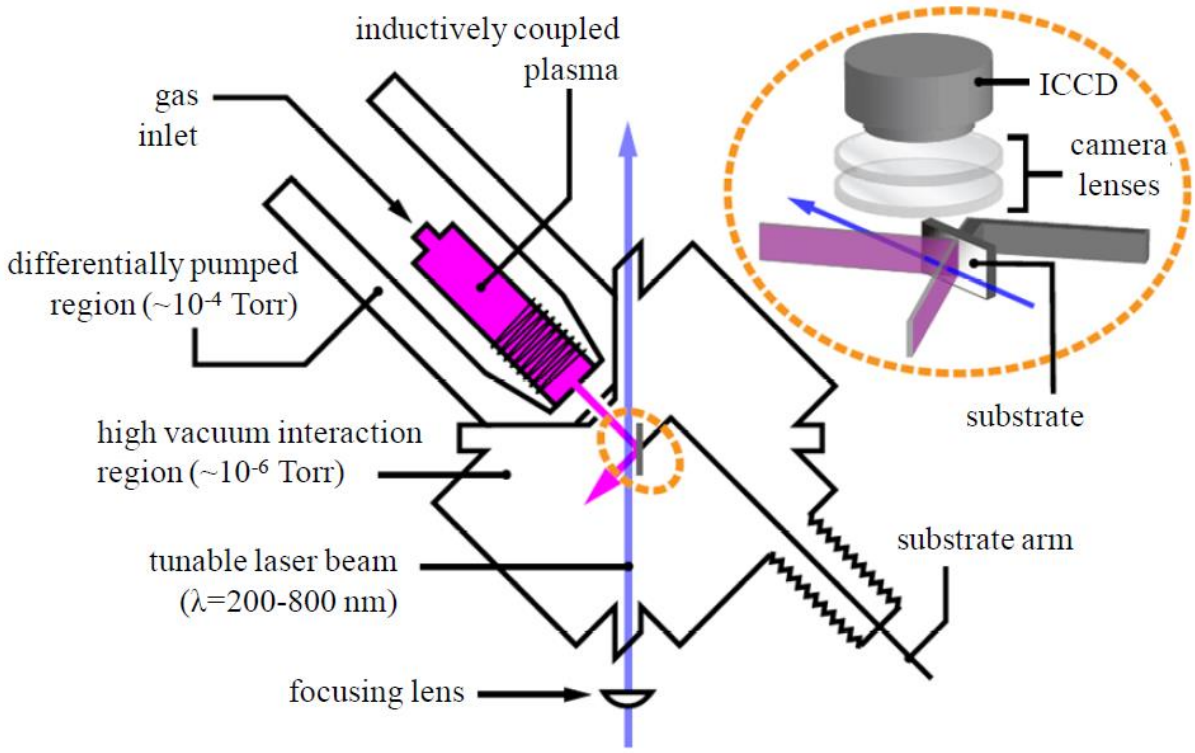

Figure 2.7. Schematic of imaging of radical interacting with surfaces (IRIS) apparatus. Detail of the interaction region shows the spatial orientation of the optics and detector relative to the molecular and laser beam.

Plasma afterglow from the reactor expands through a series of collimating slits into a differentially pumped region (base pressure ~10^{-6} Torr) to generate a molecular beam, consisting of virtually all species present in the plasma. Tunable laser light generated from an excimer-pumped (Lambda Physik LPX210i, XeCl 180 mJ/pulse, 25 Hz) dye laser intersected the plasma molecular beam at a 45° angle. For LIF studies requiring UV radiation, the output of the laser was frequency doubled using BBO I crystals. Total fluorescence was imaged through two focusing lenses onto a 512 x 512 pixel array of an intensified charge-coupled device (ICCD) located directly above the region of intersection and perpendicular to the laser and plasma molecular beam. Individual images were pixel averaged for a 20 x 12 region around the center of the most intense fluorescence and these averages were plotted as a function of the corresponding laser wavelength to generate the excitation spectrum.

Radical surface reactivities for SiF, CF and CF_2 were measured using the IRIS technique, described previously.[2] Briefly, IRIS employs analysis of spatially-resolved LIF excitation of plasma species in the molecular beam as they interact with a substrate mounted on a rotatable arm. Fluorescence signals were collected at specific excitation wavelengths (SiF: 437.348 nm, CF: 223.838 nm, CF_2: 234.278 nm, NO: 226.199 nm) for the molecular beam alone ("beam only") and the beam interacting with a substrate ("beam + scatter"). Background subtractions were performed for each image by turning the laser off. The difference between the "beam + scatter" and "beam only" images provides a measure of the signal arising from molecules scattered from the surface during plasma processing ("scatter"). Cross-sections along the laser propagation axis were taken in 20 - pixel wide swaths around the center of most intense fluorescence for both the "beam only" and "scatter" images. These cross-sections were fit with a geometrical model to derive scatter coefficients, *S*. Briefly, *S* represents the fraction of incident

radicals scattered from the surface. *S* values greater than unity indicate radicals are generated at a surface, where $S < 1$ represent radicals disappearing from the gas-phase upon interaction with the substrate. Surface generation can occur via a number of mechanisms, including fragmentation and desorption of a deposited film, discussed further in Chapter 4 and Appendix B.

2.4 Substrate Preparation and Fabrication

Zeolite construct fabrication. Three types of molecular sieve constructs were utilized in this work: native, pressed pellets, and electrospun fibers, Figure 2.8. Molecular sieves (Sigma-Aldrich, 13x, 45/60 mesh) were used as received and secured to glass slides (VWR) with double-sided carbon tape (VWR), referred to as "native zeolite" throughout this work. The received 13x zeolites were crushed into a fine powder using a mortar and pestle, then pressed in 0.3 g pellets using a pellet die at 18k pounds per square inch (Carver), as depicted in Figure 2.8a. Electrospun fibers were fabricated using polyvinylpyrrolidone [PVP (MW – 1,300,000)] and ground zeolites. An overview of the electrospinning process is displayed in Figure 2.8b, specific parameters are detailed in Appendix A. Briefly, zeolite solutions were prepared by fully dissolving the zeolites in 200 proof ethanol [EtOH, (PHAMCO-APPER, absolute anhydrous, ACS grade)] and bath sonicated for seven hours to achieve uniform dispersion; zeolite: EtOH solutions were then stirred magnetically overnight. PVP was added to the zeolite solution and magnetically stirred for at least six hours to obtain a homogeneous suspension to be loaded into a 5 mL syringe equipped with a 20-gauge needle. The syringe was placed in a Kent Scientific syringe pump with a constant 0.5 mL/hour or 5 mL/hour dispensing rate and the pump was oriented such that the tip of the needle was 15 cm away from a conductive disk wrapped in heavy-duty Al foil.

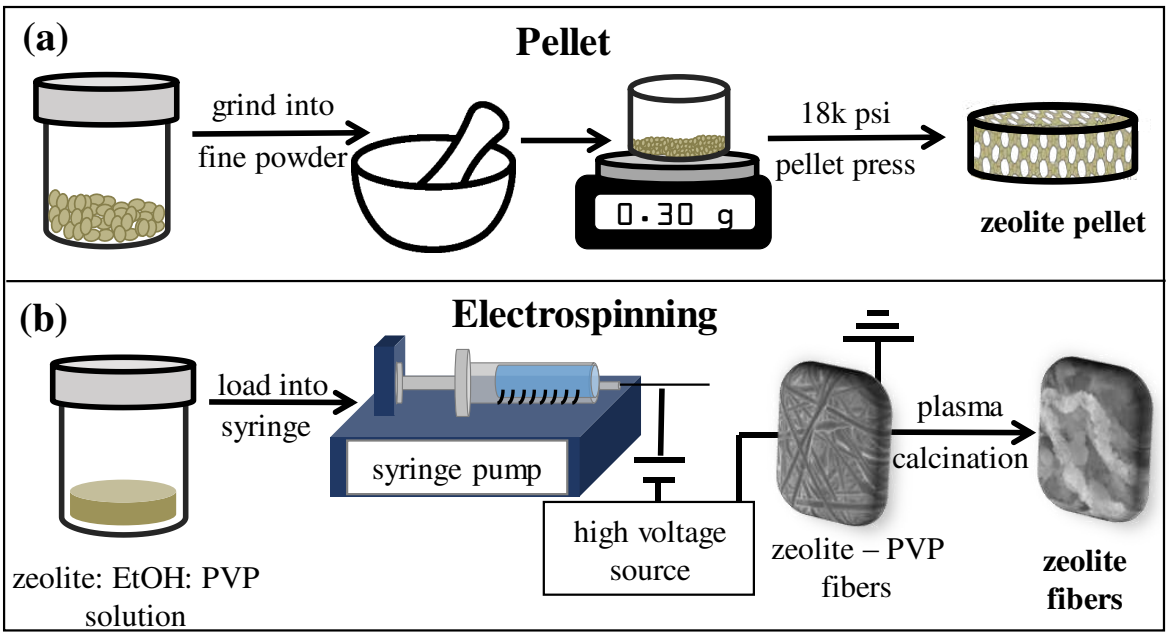

Figure 2.8. Overview of in-house zeolite fabrication methodologies including (a) pressed zeolite pellets and (b) electrospinning fiber mats**.**

Electrodes were connected to the needle tip and conductive disk, where a constant voltage ranging from 12 to 24 kV was applied for the entirety of the electrospinning process using a high voltage power supply (Gamma High Voltage Research). The as-spun fiber mats were removed from the Al foil prior to calcination to remove the polymeric phase. Here, the PVP-zeolite fibers were calcinated in a furnace (Thermolyne 1300) at 550° C for 2 hours. Additionally, the potential utility of using Ar and O_2 rf ICPs to remove the polymeric phase was examined, discussed in Chapter 5 and Appendix A.

Platinum substrate preparation. Platinum foil (Alfa Aesar, 99.99 %, 0.025 mm) was used as received. Commercial Pt powder (Alfa Aesar 99.99%, 9-19 m^2/g) was secured to glass slides (VWR) with double-sided carbon tape. Pt powder was suspended in both ethanol and hexane to crease a suspension of particles, which was drop cast onto glass slides and left to dry overnight in ambient laboratory conditions. These fabrication processes, however, resulted in the oxidation of the Pt nanoparticles (EtOH) and poor adhesion to the glass slides (hexanes), therefore were these fabrication methodologies were not employed for plasma-assisted catalysis studies, Chapter 8.

2.5 Material Characterization

Composition analysis. Powder X-ray diffraction (PXRD) data (Bruker D8 Discover DaVinci Powder X-ray Diffractometer, Cu K_α radiation source using 2θ from 5° to 80° at intervals of 0.02° with scans of 0.25 – 0.5 step/s) was collected on catalytic substrates to elucidate any changes to bulk crystallinity of the material after plasma exposure.

X-ray photoelectron spectroscopy (XPS) was performed on a Physical Electronics PE5800 ESCA/AES system equipped with an Al K monochromatic X-ray source (1486.6 eV), hemispherical electron analyzer, and multichannel detector to elucidate surface composition.

Spectra were collected using a 45° angle and a low energy electron flood gun (15 eV). A minimum of three spots on three samples (n = 9) was collected to analyze surface and sample reproducibility, where a mean value and its standard deviation are reported. CasaXPS software was used to process all high-resolution spectra with Gaussian-Lorentzian (30:70) fits and FWHM of each component was constrained to ≤ 2.0 eV. High-resolution C_{1s} spectra were charge corrected by setting the aliphatic carbon component (-C-C/C-H) to 284.8 eV. Fluorocarbon peaks were generally shifted to the F-C binding environment at 689.0 eV. For high-resolution Si_{2p} XPS spectra, Alexander *et al.* have assigned the binding energies for Si(-O), $Si(-O)_2$, $Si(-O)_3$, and $Si(-O)_4$ to 101.5, 102.1, 102.8 and 103.5 eV, respectively.[23]

Morphological analysis. Scanning electron microscopy (SEM) images were collected using a JEOL JSM-6500F field emission microscope, operating with an accelerating voltage of 5 – 15.0 kV and a working distance of 10 mm. Energy dispersive spectroscopy (EDS) was collected in conjunction with SEM to obtain elemental composition maps of untreated and plasma modified materials. Multipoint Brunauer-Emmett-Teller (BET) measurements were performed to elucidate the surface area of the ground zeolite powder, Figure 2.9. Figure 2.9a shows the obtained signal intensity as a function of time as N_2 is desorbed and adsorbed to the ground zeolite powder, where 2 mL of N_2 gas was injected as an internal calibration. Utilizing different ratios of He and N_2 gas, a multipoint BET plot was generated, Figure 2.9b. A specific surface area of 930 m^2/g for the ground zeolite material was obtained using this plot.

Wettability analysis. Water contact angles (WCA) experiments were performed using a Krüss DSA30 goniometer. Substrates did not require further sample preparation for WCA. Static and dynamic WCA data were collected depending on the wettability of the substrate (i.e. hydrophobic or hydrophilic).

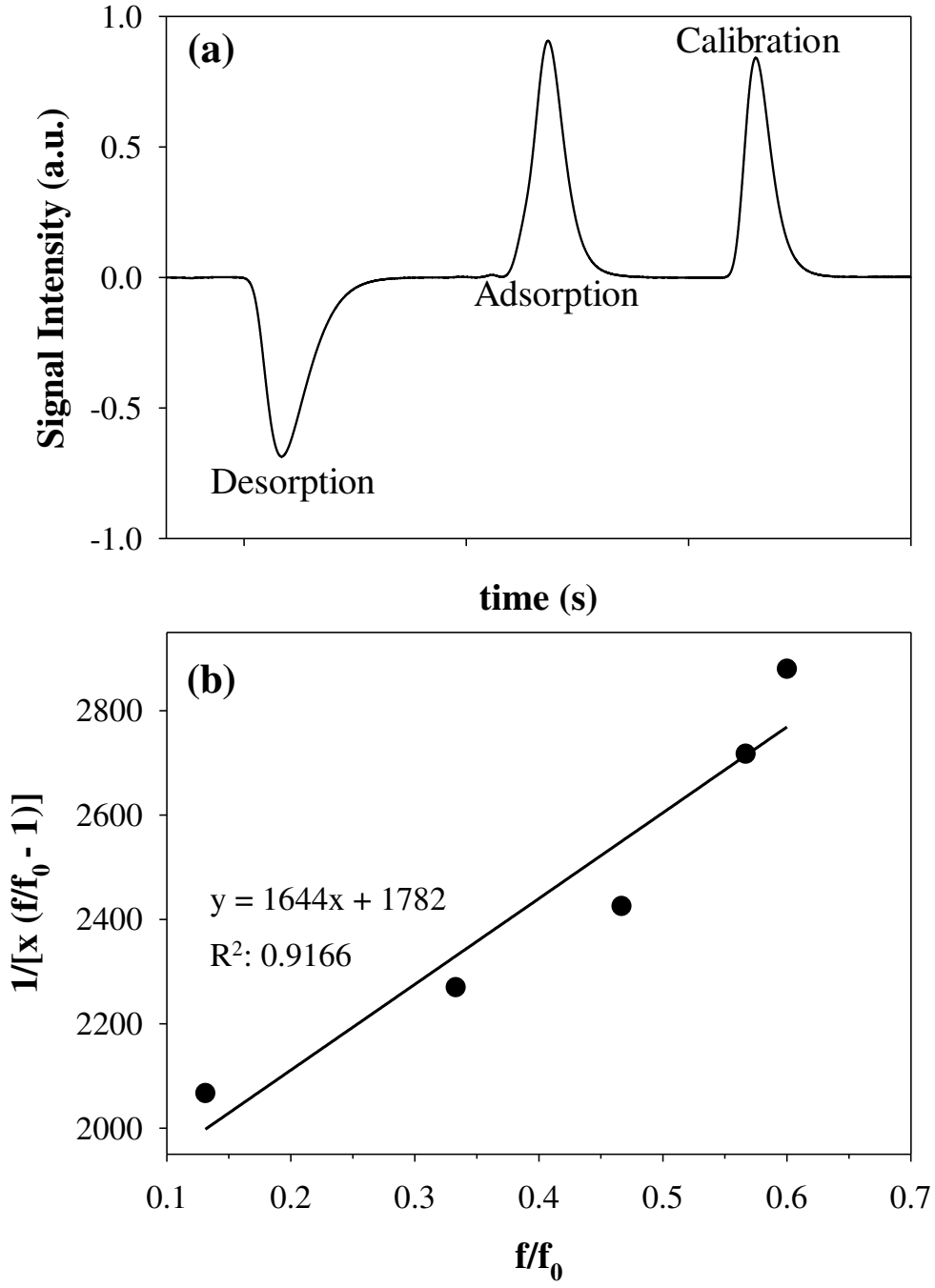

Figure 2.9. (a) Signal intensity plotted as a function of time during while performing a multipoint BET experiment, where 2 mL of N_2 was injected during the calibration. (b) Multipoint BET curve used to determine specific surface area of ground zeolite powder.

Regardless of substrate, deionized ultrapure water (Millipore, 18 mΩ) was used at ambient laboratory conditions for all data collection. The probe liquid parameters (density 0.9970 g/mL, viscosity = 0.010 P, surface tension = 72.16 mN/m) were programmed into the onboard software and utilized when performing all WCA fitting. For non-wettable materials, static WCA values were collected using a 2 uL drop volumes, where drops stabilized in < 1 s. When WCA values were less than twenty degrees, the circle method was employed, otherwise tangent methods were used (assuming elliptical drop profiles). Water adsorption rates were determined via video analysis, $t = 0$ s is defined as the time the water droplet first contacts the material surface. An adsorption rate was calculated by dividing the drop volume by the time it took for the drop to be fully adsorbed. Video data were acquired at 25 and 75 frames/s over 15 s to measure water sorption behavior on zeolite constructs, discussed in Chapter 5.

REFERENCES

1. Hanna, A. R.; Fisher, E. R., Investigating Recent Developments and Applications of Optical Plasma Spectroscopy: A Review. *J. Vac. Sci. Technol., A* **2020**, *38*, 020806.
2. Hanna, A. R.; Cuddy, M. F.; Fisher, E. R., Energy Partitioning and its Influence on Surface Scatter Coefficients within Fluorinated Inductively Coupled Plasmas. *J. Vac. Sci. Technol., A* **2017**, *35*, 05C308.
3. Hanna, A. R.; Blechle, J. M.; Fisher, E. R., Using Fundamental Spectroscopy to Elucidate Kinetic and Energetic Mechanisms within Environmentally Relevant Inductively Coupled Plasma Systems. *J. Phys. Chem. A* **2017**, *121*, 7627-7640.
4. Hanna, A. R.; Van Surksum, T. L.; Fisher, E. R., Investigating the Impact of Catalysts on N_2 Rotational and Vibrational Temperatures in Low Pressure Plasmas. *J. Phys. D: Appl. Phys.* **2019**, *52*, 345202.
5. Hanna, A. R.; Fisher, E. R., Efforts Towards Unraveling Plamsa-Assisted Catalysis: Determination of Kinetics and Molecular Temperatures Within N_2O Discharges *ACS Catalysis* **2020**, *manuscript submitted*.
6. Blechle, J. M.; Hanna, A. R.; Fisher, E. R., Determination of Internal Temperatures Within Nitric Oxide Inductively Coupled Plasmas. *Plasma Process. Polym.* **2017**, *14*, 1700041.
7. Coburn, J. W.; Chen, M., Optical Emission Spectroscopy of Reactive Plasmas: A Method for Correlating Emission Intensities to Reactive Particle Density. *J. Appl. Phys.* **1980**, *51*, 3134-3136.
8. Gottscho, R. A.; Donnelly, V. M., Optical Emission Actinometry and Spectral Line Shapes in rf Glow Discharges. *J. Appl. Phys.* **1984**, *56*, 245-250.
9. Bruggeman, P.; Cunge, G.; Sadeghi, N., Absolute OH Density Measurements by Broadband UV Absorption in Diffuse Atmospheric Pressure He-H_2O RF Glow Discharges. *Plasma Sources Sci. Technol.* **2012**, *21*, 035019.
10. Abdel-Rahman, M.; Gans, T.; Gathen, V. S.-v. d.; Döbele, H. F., Space and Time Resolved Rotational State Populations and Gas Temperatures in an Inductively Coupled Hydrogen RF Discharge. *Plasma Sources Sci. Technol.* **2005**, *14*, 51.
11. Blechle, J. M. Investigations of Nitrogen Oxide Plasmas : Fundamental Chemistry and Surface Reactivity and Monitoring Student Perceptions in a General Chemistry Recitation. Colorado State University, ProQuest Dissertations Publishing, 2016.
12. Boogaard, A.; Kovalgin, A. Y.; Aarnink, A. A. I.; Wolters, R. A. M.; Holleman, J.; Brunets, I.; Schmitz, J. In *Measurement of Electron Temperatures of Argon Plasmas in a High-Density Inductively-Coupled Remote Plasma System by Langmuir Probe and Optical-Emission Spectroscopy*, Proceedings of the 9th annual workshop on Semiconductor Advances for Future Electronics and Sensors 2006, Utrecht, The Netherlands, 2006/11/23/; Technology Foundation STW: Utrecht, The Netherlands, pp 412-418.
13. Crosley, J. L. D. R. *LIFBASE: Database and Spectral Simulation Program (Version 1.5)*; 1999.
14. Laux, C. O. In *Radiation and Nonequilibrium Collisional-Radiative Models*, von Karman Institute Lecture Series, Physico-Chemical Modeling of High Enthalpy and Plasma Flows, Rhode-Saint-Gense, Belgium), Fletcher, D.; Charbonnier, J.-M.; Sarma, G. S. R.; Magin, T., Eds. Rhode-Saint-Gense, Belgium), 2002.

15. NIST. *NIST Chemistry WebBook*. http://webbook.nist.gov/chemistry (accessed October 12, 2018).
16. Wu, A. J.; Zhang, H.; Li, X. D.; Lu, S. Y.; Du, C. M.; Yan, J. H., Determination of Spectroscopic Temperatures and Electron Density in Rotating Gliding Arc Discharge *IEEE Trans. Plasma Sci.* **2015**, *43*, 836-845.
17. Western, C. M., PGOPHER: A Program for Simulating Rotational, Vibrational and Electronic Spectra. *J. Quant. Spectrosc. Radiat. Transfer* **2017**, *186*, 221-242.
18. Bulcourt, N.; Booth, J.-P.; Hudson, E. A.; Luque, J.; Mok, D. K. W.; Lee, E. P.; Chau, F.-T.; Dyke, J. M., Use of the Ultraviolet Absorption Spectrum of CF_2 to Determine the Spatially Resolved Absolute CF_2 Density, Rotational Temperature, and Vibrational Distribution in a Plasma Etching Reactor. *J. Chem. Phys.* **2004**, *120*, 9499-9508.
19. Van Surksum, T. L.; Blechle, J. M.; Fisher, E. R., Determination of Rotational and Vibrational Temperatures of CH in CH_4 plasmas. *J. Vac. Sci. Technol., A* **2018**, *36*, 041302.
20. McCurdy, P. R.; Bogart, K. H. A.; Dalleska, N. F.; Fisher, E. R., A Modified Molecular Beam Instrument for the Imaging of Radicals Interacting with Surfaces During Plasma Processing. *Rev. Sci. Instrum.* **1997**, *68*, 1684-1693.
21. Liu, D.; Martin, I. T.; Zhou, J.; Fisher, E. R., Radical-Surface Interactions During Film Deposition: A Sticky Situation? *Pure Appl. Chem.* **2006**, *78*, 1187-1202.
22. Mackie, N. M.; Venturo, V. A.; Fisher, E. R., Surface Reactivity of CF_2 Radicals Measured Using Laser-Induced Fluorescence and C_2F_6 Plasma Molecular Beams. *J. Phys. Chem. B* **1997**, *101*, 9425-9428.
23. Alexander, M. R.; Short, R. D.; Jones, F. R.; Michaeli, W.; Blomfield, C. J., A Study of HMDSO/O_2 Plasma Deposits Using a High-Sensitivity and -Energy Resolution XPS Instrument: Curve Fitting of the Si_{2p} Core Level. *Appl. Surf. Sci.* **1999**, *137*, 179-183.

CHAPTER 3

INVESTIGATING RECENT DEVELOPMENTS AND APPLICATIONS OF OPTICAL PLASMA SPECTROSCOPY: A REVIEW[a]

A key portion of this dissertation work employs various diagnostic tools to holistically study the gas-phase and resulting plasma-surface interface upon addition of a substrate. This chapter comprises a review of literature using optical spectroscopies to study plasma discharges, focusing on the elucidation of fundamental plasma properties, specifically electron temperature and electron density, using optical emission spectroscopy. The potential to use spectroscopy for kinetic and thermodynamic insights are discussed here, as well as subsequent chapters (Chapters 6 – 8).

[a] Adapted from an invited review published in the *Journal of Vacuum Science and Technology A* Special Topic Collection: 30 years of the Nellie Yeoh Whetten Award – Celebrating the Women of the AVS, written by Angela R. Hanna and Ellen R. Fisher.

3.1 Introduction

Described in Chapter 1, OES is a widely used, relatively simple diagnostic tool for non-thermal plasmas, at both low– and atmospheric– pressure. In the most straightforward configuration, OES only requires a means of collecting light emitted, a dispersing element, and a detector.[1] Recent technological advances have, however, enhanced both the spatial and temporal resolution of spectrometers, leading to new applications and robust characterization of plasma processing. Indeed, the body of literature using OES to study plasmas has increased exponentially over the past decade, shown by the steadily increasing number of publications and citations in Figure 3.1a and 3.1b, respectively. This powerful technique can be employed to identify species, elucidate fundamental plasma properties, and monitor end-product formation in discharges. The most common use of OES by far, however, is species identification. Consequently, there are several noticeable gaps in the literature. For example, although plasmas are universally applied for surface modification strategies (i.e., etching, deposition, modification), very few studies focus on how the presence of a substrate alters the gas phase of the plasma. Considering that the substrates being subjected to modification often have substantive electrical and/or catalytic properties, it is not difficult to imagine that the plasma properties could be substantially different with and without a substrate. The data in Figure 3.1 also demonstrate the increased efforts of the plasma community in recent years to measure plasma temperatures and kinetics via optical spectroscopy. This approach can afford tremendous insight into the underlying mechanisms at work within the dynamic environment of a plasma. Furthermore, the types of data revealed from such studies are critical to the development of more accurate computational models of plasma systems, thereby increasing their predictive power.

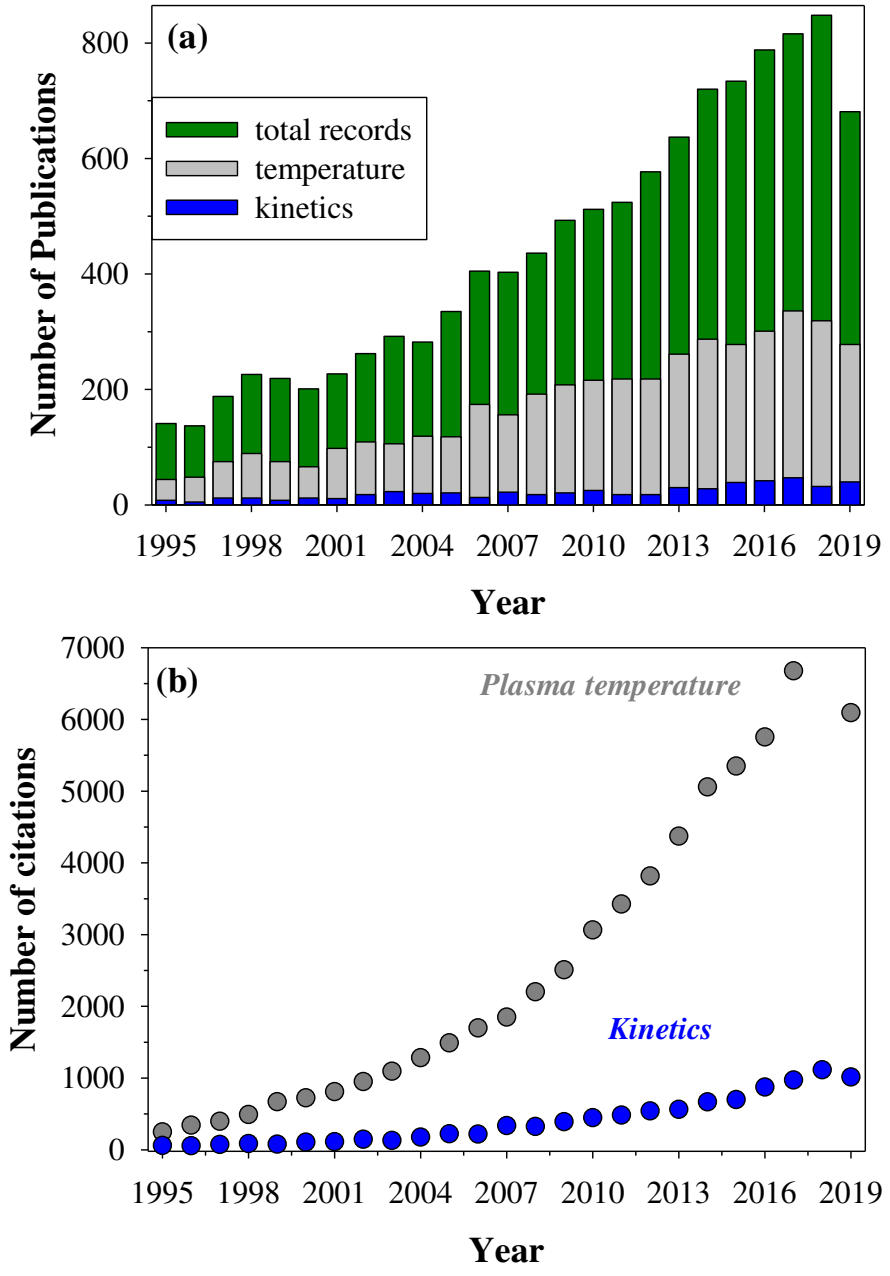

Figure 3.1. History of research interest in plasmas investigated by optical emission spectroscopy, detailing (a) total publications and (b) sum of times cited per year for plasma temperature and kinetic studies since 1995 (Web of Science search on October 3, 2019).

Thus, the primary focus of this chapter will be on demonstrating how optical spectroscopy tools can be used, either alone or in combination, to provide valuable, formative data on the kinetics and thermodynamics of low temperature plasmas. An additional aim of the current work is to highlight the contributions of women scientists to the plasma community within this Special Topic Collection: 30 Years of the Nellie Whetten Award, Celebrating the Women of the AVS. As such, a significant fraction of the cited works herein represents contributions from female researchers.

In the sections below, we provide (1) a brief literature review and background covering recent context for (2) the remainder of this dissertation work, which focuses on specific examples of how the Fisher group has further explored the use of optical spectroscopy techniques to understand underlying plasma chemistry. We begin these studies by characterizing fundamental properties within noble gas plasmas, specifically Ar. As detailed in Section 1.1, non-thermal plasmas generally follow the empirical relationship wherein electron temperature (T_e) is significantly greater than the gas temperature (T_g) of the discharge.[2] Here, we discuss the application of OES to determine T_e, as well as electron density (n_e), exploring how these parameters change temporally and as a function of operating conditions. Studying these fundamental plasma properties via OES in noble gas discharges represents a small fraction of the world of plasma diagnostics. Here, a review and discussion of new data were provided to highlight the utility of spectroscopy as a diagnostic tool for deconstructing the complexity within non-thermal plasmas. Specifically, molecules partition energy through vibrational and rotational degrees of freedom, which can be determined through the analysis of spectral transitions. By coupling energetic insights with temporally-resolved kinetics, one can begin to unravel underlying mechanisms and chemistries in a variety of non-thermal plasma systems. Thus, we

explored the utility of optical spectroscopies with a focus on comprehensive plasma diagnostics. Potential plasma-material synergisms in the context of plasma-assisted catalysis (PAC) systems containing NO_x species were investigated (Chapters 6 – 8, Appendix B) as well as a several fluorocarbon (FC) discharges (Chapters 4 and 5). These two platforms were chosen because they demonstrate the wide range of environmental and technological applications that can be achieved with non-thermal plasmas, as well as provide useful exemplifying data for each of the techniques covered herein.

3.2 Literature Review and Background

This section provides a concise literature review of recent articles describing the use of optical diagnostic techniques with a focus on pushing the capabilities of OES beyond simple species identification. The literature review provided is purposefully limited in scope by focusing on the past ten to fifteen years of published, peer reviewed articles. It is not meant to be a fully comprehensive review but does include necessary background for the data presented in subsequent sections and chapters, as well as coverage of pivotal studies that could be considered seminal to the development of new directions in optical spectroscopy techniques.

3.2.1 Spectroscopic studies of inert gas plasmas

Ionization, excitation, dissociation, recombination, and relaxation processes can occur as electrons transfer energy from the external field to the discharge gas.[2,3] As such, electrons play a crucial role in governing the overall plasma chemistry; understanding their behavior in these interrelated processes is thus critical to accurate modelling and simulation of plasma systems.[4] Although n_e and T_e are key parameters, they are often difficult to measure spectroscopically; rather, electrostatic Langmuir probes are often employed. Unfortunately, these probes physically

perturb the plasma environment which can be problematic, especially for depositing systems.[5] A direct, non-intrusive measurement of T_e is challenging and many works have sought to establish a methodology based on the evaluation of OES emission lines in inert gas systems, with connection to detailed plasma collisional radiative (CR) modeling for verification.[6-11] Often explored within Ar plasmas, the CR technique uses a population density model determined by a system of rate equations, specifically considering collisional and radiative processes.[12] If one assumes a local thermodynamic equilibrium (LTE) environment, population and depopulation processes are dominated by collisions; therefore, rates and distributions are governed by Boltzmann statistics and Saha equations.[2,13] Excitation transitions are primarily dominated by electron collisions; thus, if the discharge is operating in LTE, determination of an excitation temperature (T_{exc}) is an approximation for T_e, assuming the population of atomic excited states follows a Boltzmann distribution.[14] The validity of LTE assumptions has been investigated for a variety of discharge types.[6,15,16] Avoiding the inclusion of complex equilibrium models and intrusive probes, T_{exc} can be determined through the analysis of atomic emission lines via a Boltzmann plotting method, described in Chapter 2. This technique, which naturally assumes a Boltzmann distribution, has been used for both low- and atmospheric-pressure plasmas, with comparison to traditional T_e determination methods (e.g., Langmuir probes).[3,17]

Plasma chemistry is largely governed by electron-mediated processes and thereby the electron energy distribution function (EEDF). Factors that influence the EEDF include discharge type, system pressure, and power.[18] Under equilibrium conditions, the EEDF follows a Maxwell-Boltzmann distribution, expressed via Equation 3.1;[2]

$$f^{MB}(\varepsilon) = 2\sqrt{\frac{\varepsilon}{\pi(k_B T_e)^3}}\, exp\left(-\frac{\varepsilon}{k_B T_e}\right) \qquad (3.1)$$

where ε is the electron energy and k_B is the Boltzmann constant. The EEDF of non-thermal discharges, however, can deviate from a Maxwellian distribution due to temporal or spatial variation of electromagnetic fields, presence of boundaries (e.g., reactor walls or substrates) and an absence of thermodynamic equilibrium (described in Section 3.2.3) [2,19] Often, despite these deviations, some portion of the EEDF is Maxwellian. As such, the practice of determining T_e assuming Maxwellian statistics is common, acknowledging the possibility of inherent errors in this simplification.[20] A Druyvesteyn EEDF, Equation 3.2, is also commonly used to describe low-pressure plasmas, with the assumptions that the electric field strength is low enough to neglect inelastic collisions, T_e is significantly greater than ion temperature (T_i), and the collisional frequency is independent of electron energy.[2]

$$f^D(\varepsilon) = \sqrt{\frac{\varepsilon}{\pi(kT_e)^3}}\, exp\left[-0.244\left(-\frac{\varepsilon}{kT_e}\right)^2\right] \qquad (3.2)$$

Druyvesteyn distributions are characterized by a shift toward higher electron energies, compared to a Maxwell distribution, depicted in Figure 3.2a.[2] Inelastic collisions of electrons with heavy particles can lend to a drop of the EEDF at higher electron energies, therefore is it generally accepted a Druyvesteyn distribution is present in plasmas with low ionization degrees. Rather than reporting EEDF curves, it is common in the plasma community to report the electron energy probability function (EEPF), determined via Equation 3.3.

$$f_p(\varepsilon) = f(\varepsilon)e^{-1/2} \qquad (3.3)$$

In the case of a Maxwellian distribution, this results in a straight line with the slope of ($-1/k_BT_e$), shown in Figure 3.2b. The sample EEDF and EEPF curves shown in Figure 3.2 were theoretically determined, however there are significant research efforts to determine these properties with electrostatic plasma probes and OES techniques.[18,19,21]

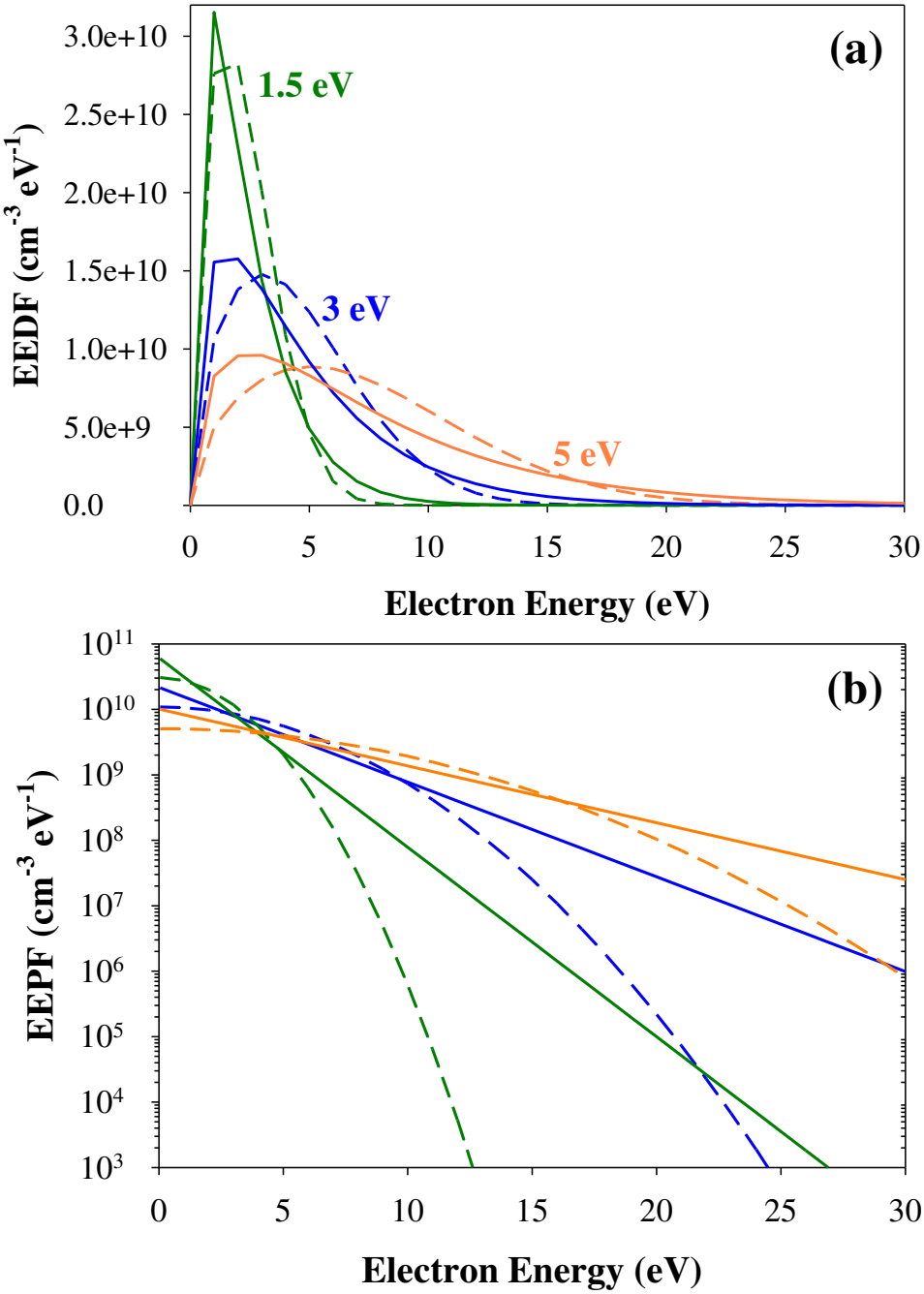

Figure 3.2. (a) EEDFs and (b) EEPFs for two distributions with three average electron energy [T_e = 1.5 (green), 3 (blue), and 5 (orange)] and the same electron density ($n_e = 10^{11}$ cm^{-3}). Solid and dashed traces represent Maxwell-Boltzmann and Druyvesteyn distributions, respectively.

Additionally, a bi-Maxwellian representation can be employed to model measured EEDFs, where a low energy or "bulk" electron population and the higher energy tail of the distribution are characterized by different temperatures.[22] The electrons in the high-energy tail of the distributions, though present in small concentrations, can have a significant impact on the overall reaction rates and plasma character.

Recently, several studies have implemented an emission line-ratio technique for the determination of T_e and n_e, with comparison to trends obtained from electrostatic probes.[23-27] These measurements assume excitation processes are dominated by direct electron impact and that subsequent depopulation from upper levels is either radiative or proceeds through collisional quenching. Both are reasonable assumptions for Ar plasmas operating at low pressure. Zhu and coworkers detailed a variety of methods to determine T_e and n_e by line-ratios for non-thermal Ar and N_2-containing plasmas, discussing the selection of appropriate line-ratio and the limitations of the technique.[26] Several fundamental noble gas plasma studies explore the interdependence of T_e, T_{exc}, n_e, and plasma conditions.[7,10,21,28-31] The effect of plasma operating parameters on Ar ion and metastable number densities has also been with explored with the OES line-ratio technique.[32,33] Although Ar is a widely studied plasma precursor and commonly used as an inert gas actinometer (see below), T_{exc} and line-ratio studies were also included in this review to provide context for OES as a technique to characterize fundamental plasma parameters.

We note that obtaining absolute species concentrations from optical emission data is possible; however, this requires knowledge of electron impact rate constants, electron density and energy distributions, as well as the absolute sensitivity of the spectrometer.[34] Coburn and Chen were among of the first to quantify the relationship between emission intensity and reactive particle density, thereby founding the technique of rare-gas actinometry in the plasma

community.[35] To be as accurate as possible, this technique requires the actinometer and the species of interest to have similar cross sections for excitation, excitation thresholds, and excitation pathways.[36] Following the landmark work of Coburn and Chen, relative and absolute species densities within many plasma systems have been studied with OES. A brief overview of these studies that explored the relationship between gas-phase chemistry and a resulting plasma process is provided here.

To better understand the mechanisms of plasma-surface processing, regardless of precursor or substrate, it is necessary to recognize the role of gas-phase species in gas-surface interactions. Donnelly and coworkers investigated the practice of adding traces of multiple rare gases (i.e., Ne, Ar, Kr, Xe) to a variety of etchant plasma systems to elucidate species density, T_e, as well as EEDFs via trace rare gases OES.[34,37,38] By examining T_e obtained from each individual gas, as well as various mixtures, the authors were able to differentiate and study different portions of the Maxwellian EEDF. Through the selection of emission lines primarily excited through electron impact of the ground state, electron temperatures were determined and differentiated for electrons within both the high-energy tail of the distribution and the lower energy, bulk electrons.[37] Fuller *et al.* measured absolute densities of Cl_2, Cl, Cl^+, and Ar^+ within inductively coupled (ICP) Cl_2-Ar plasmas, a system routinely utilized for the etching of semiconductor materials.[39] Absolute Cl atom densities have also been determined via actinometric OES in an ICP Cl_2 plasma, where a cylindrical substrate is rapidly rotated, creating a "spinning wall" effect.[40] Alshaltami and Daniels measured concentrations of oxygen and fluorine with OES and studied their impact on selective etching with SF_6-O_2 discharges.[41] Notably, in many industrial plasma processes, dry etch is performed without the addition of an inert gas as it can effect both etch rate and selectivity, hence inert gas actinometry is unavailable. To address this, Kang *et al.*

developed a "pseudo actinometry" technique for the normalization of species density in the absence of an inert gas.[42] A correction factor was experimentally determined by incrementally decreasing the number density of the inert gas within the discharge, eventually determining a convergence when the concentration of the inert gas was zero. The feasibility of the proposed technique was tested by the etching of Cr with a Cl_2/O_2 discharge, documenting strong correlation between Cl density distributions with Cr etch rate, determined via ellipsometry.[42] Thus, understanding species density within a plasma process can ultimately lead to process optimization, with and without an inert actinometer.

Another important consideration is how the relative concentrations of species are affected by the mere introduction of a substrate into the discharge. Cuddy *et al.* determined the density of CF and CF_2 species upon the addition of a substrate. Examining CF_4 and C_2F_6 plasma processing of Si and ZrO_2 wafers, they found the presence of a substrate could dramatically affect the species density, and furthermore, this finding was substrate dependent, further discussed in Chapters 1 and 5.[43] Stuckert and co-workers monitored gas-phase species upon the addition of SnO_2 nanomaterial gas-sensors in H_2 radio frequency (rf) ICPs, a known reducing environment. The formation of both excited state OH* and Sn* in H_2 plasmas was observed when SnO_2 nanomaterials were present. As neither species is formed in H_2 or H_2/Ar plasmas without a substrate, they must be formed via plasma-surface interactions.[44] This study also introduced an additional level of complexity; micro- and nano-structured materials are more likely to strongly influence the plasma as compared to the effects of traditional two-dimensional materials (e.g., thin films, wafers), further explored in Chapters 7 and 8. To better understand the mechanisms that govern plasma processes (i.e., modification through functionalization,

etching, or deposition) of a specified surface, we must gain quantitative information concerning the kinetics and energetics of these complex systems.

3.2.2 Temporally-resolved spectroscopy: kinetic insights

The intricate dynamics occurring within plasma systems can be systematically and quantitatively probed with time-resolved (TR) OES. By employing TR-OES with an intensified charge coupled device (ICCD) camera, spatially- and temporally-resolved images can be obtained to study mode shifts and ionization events in discharges.[45] Gherardi *et al.* provided a detailed experimental and theoretical discussion regarding the increased use of ICCDs to study both physical and chemical properties of non-thermal plasmas, focusing on atmospheric plasma jets.[46] ICCDs can provide time-resolution on the nanosecond scale, an important consideration of the study of streamers formed through nanosecond pulsed discharges.[47,48] Furthermore, TR-OES studies with ICCDs aid in the visualization of plasma dynamics,[49] where the temporal behavior of radiative species, T_g, T_e, and n_e have been investigated within a variety of continuous wave (CW) and pulsed plasma systems.[50,51]

Pulsed plasmas are often used in the processing of materials to reduce substrate temperatures and prevent substrate damage, with the goal to increase uniformity of the overall plasma process.[52] Within pulsed systems, once the plasma pulses off, an afterglow region can persist wherein energetic electrons recombine with ions to create neutral and excited-state species.[53,54] Within Ar plasmas, it is stipulated that higher excited states are more populated during plasma ignition and decay to a steady state through the pulse duration, whereas the afterglow is characterized by electron thermalization and plasma recombination.[55,56] This hypothesis is further tested below, where TR-OES is employed to characterize the properties of pulsed rf Ar plasmas.

Additional studies have measured the evolution of species in the plasma afterglow during magnetron sputter deposition of Al_2O_3 and TiO_2 materials in direct current (DC) plasmas.[57,58] During these processes, Lopez *et al.* observed different Ar emission lines decayed with different rate constants, where the emission decay times (1 to 4 μs) were significantly longer than the radiative lifetimes of the Ar emitting levels.[57] The authors argue these longer decay rates result from plasma dynamics and operating conditions, where the decay of fast electrons, Ar metastables, as well as Al and O atoms in the plasma afterglow (i.e., after plasma power is turned off) could be monitored via TR-OES. Within a pulsed DC magnetron Ar plasma, two decay times for different groups of Ar emissions lines were found. The authors attribute the fast decay time (1 μs) to the decline of fast beam electrons in the plasma afterglow and the slower decay time (3.2 μs) to the decrease in Ar metastable density.[57] Hioki *et al.* argue the decay of electron and ion densities, dissipation of electron energies, and metastable number density decrease will occur on different timescales.[59] Furthermore, the authors acknowledge the necessity to study low, moderate, and high energy electrons separately, as each may temporally-decay differently.[59] Salmon *et al.* coupled TR-OES with a detailed kinetic model to determine the quenching rates of $N(^2P)$ atoms in the afterglow of an N_2 atmospheric pressure discharge.[60] Aforementioned, gaining quantitative experimental information on fundamental plasma properties can assist in plasma computational simulations. Specifically, the determination of quenching rates within pulsed N_2 plasma systems can have substantial impact on the ability to build accurate models, with potential for process improvement.

Significant technological applications can benefit from the use of TR-OES, such as the sterilization and cleaning of plasma chambers post film deposition. Bišćan and co-workers studied the removal of amorphous carbon film deposits on reactor walls by an oxygen plasma,

where OES was employed for *in situ* monitoring of film deposition as well as O_2 plasma cleaning processes.[61] By measuring emissions from oxygen and hydrogen atoms, OH radicals, CH, and CO, alongside the documentation of plasma mode shifts during the cleaning of the plasma chamber, they were able to deduce when the system was free of impurities (i.e., hydrogen and carbon species) with improved accuracy over visual inspection.[61] This line of inquiry could easily be expanded to other film deposition systems, including the removal of fluorocarbon and chlorine contamination after plasma processing. Plasma cleaning studies are usually limited to searching for the disappearance or appearance (depending on experiment) of a given species in the gas-phase, an inherently qualitative process. Of burgeoning interest, TR-OES can be quantitively used to measure the initial production of plasma species, thus determining rate constants of formation through analysis of emission lines.[62] The ability to experimentally measure rate constants and reveal underlying plasma-surface mechanisms is presented in subsequent chapters.

3.2.3 Energy partitioning between molecules and electronic states

Within non-thermal plasma systems, T_g is an important plasma parameter, it strongly influences the underlying chemistry that drives most plasma processes. T_g studied via OES has been shown to be highly dependent on plasma parameters, leading to an increased necessity to understand trends in energy partitioning.[63,64] The distribution of energy into rotational and vibrational degrees of freedom (expressed as temperatures T_R and T_V, respectively) is also an important consideration. The second positive system of N_2 ($C^3\Pi_g \rightarrow B^3\Pi_u$) is commonly used to determine T_R and T_V in N_2 or N_2-containing plasma systems within low- and atmospheric-pressure discharges.[29,65-67] T_R values have long been employed as a measure of T_g,[68,69] with the assumption that rotational and collective translational temperatures (T_T) of the gas equilibrate

within the plasma. Bruggeman *et al.* demonstrated T_R only equilibrates with T_T when rotational energy transfer is relatively fast or nascent rotational distributions are thermalized.[63] Information gleaned from internal temperatures can elucidate the processes that dictate the overall character of the plasma, as the values are interrelated to species densities, T_e, formation reactions, and gas-phase and surface collisions of plasma species. Thus, elucidating energy partitioning trends (Figure 3.1b) for a variety of excited state species, ranging from homonuclear diatomics (H_2, N_2, O_2) to species formed through the decomposition of a more complex precursor (e.g., CF from C_xF_y discharges) is a growing area of study. Energy partitioning trends for technologically- and environmentally-relevant plasma systems are further discussed in Chapters 4, 6 – 8.

OES provides useful kinetics and energetics data for emitting species; however, it is unable to directly evaluate ground state species within the plasma. Nevertheless, the rate balance equations for emitting species within the discharge can be employed to indirectly assess ground state neutrals via OES. Laser-induced fluorescence (LIF) is commonly used to probe the ground state; however, this technique requires expensive laser equipment and is inherently limited to species that possess a fluorescing excited state.[1] Thus, broadband absorption spectroscopy (BAS), where a light source is interfaced with a high-resolution spectrometer, has recently found promise as an alternative technique for ground state species measurements, such as absolute species density and plasma energetics. Literature studies have used a range of light sources, including UV-enhanced Xe arc lamps,[70,71] deuterium-halogen lamps,[4,72,73] and light-emitting diodes (LED).[74-76] Compared to LIF, BAS is a viable strategy to determine absolute species density without intensive calibration procedures, discussed in depth in a recent review of atmospheric plasma characterization.[77] Liu and co-workers employed BAS to determine absolute density and rotational temperatures of CF_2 radicals in capacitively coupled CF_4/Ar

plasmas.[76] One of the difficulties with plasma absorbance measurements is the dual-reference nature of the system (i.e., both the light source and plasma are emitting), as well as poor signal-to-noise ratios. Wijaikhum *et al.* developed a two-beam ultraviolet-LED absorption technique, equipped with a probe and reference beam to improve the signal-to-noise ratio when measuring ozone densities.[75] In this dissertation, the utility of BAS to determine plasma temperatures in FC and N_xO_y discharges will be discussed (Chapters 4 and 6, respectively). Moreover, our unique imaging radicals interacting with surfaces (IRIS) technique, which employs LIF spectroscopy, can provide insights into the behavior of radicals near substrates *during* plasma processing. Coupled with the kinetic and energetic information gained through gas-phase spectroscopy diagnostics, a more holistic understanding of gas-surface interactions is gained.

3.3 Results and Discussion

Noble gas precursors have been widely used as model systems to study the behavior of electrons within plasma discharges, especially Ar due to its relatively simple gas-phase chemistry and availability of electron-impact cross section information.[20] Ar emission spectra are nominally dominated by the Ar I emissions, shown in Figure 2.4a in the wavelength range 650 – 1000 nm. As noted in the Introduction and Background section, dilute amounts of Ar are often added to more complex systems as an inert gas actinometer to probe T_e and n_e, as well as determine relative and absolute species densities, as a function of plasma operating conditions. Within non-thermal ICPs, it is generally recognized the primary effect of increasing rf P is to increase plasma density at a fixed pressure, where T_e is hypothesized to be relatively independent from plasma power.[2,13] Several works, however, have experimentally observed T_e fluctuations over a range of P in rf ICP discharges. Lee *et al.* measured changes in T_e as a function of power in Ar rf ICPs, ignited at 13.56 MHz via an antenna coil, with both Langmuir probe and laser

Rayleigh scattering measurements.[78] This study was performed at p = 50 mTorr, P = 100 – 900 W; where the authors claim T_e decreases as power increases from 100 – 500 W and then increases with P = 500 - 900 W. The measured T_e values, however, are within experimental error of each other at several P conditions, with all of the values falling in a narrow range of ~1.81– ~2.10 eV.[78] As such, it is challenging to understand whether the claims of a local minimum in T_e with power are valid or if it might be translatable to other systems. Consequently, we sought to perform a similar characterization of our rf Ar plasmas by using OES to examine our systems as a function of small changes in P (ΔP = 5 W) at three different plasma pressures.

Figure 3.3a shows calculated T_{exc} (eV) values as a function of plasma operating conditions, revealing several interesting trends regarding pressure, power, and discharge-mode. At $P \leq 15$ W, there is a clear pressure dependence: increasing the system pressure from 50 to 150 mTorr can increase the frequency of collisions, hence a quenching of T_{exc} is observed. Within the 150 mTorr system, as power increases from 15 to 20 W, the discharge visually changes, indicating a shift from operating in capacitive (E) to inductive (H) mode, and a corresponding sharp decrease in T_{exc} was also observed. Generally speaking, a discharge operating in E mode is sustained by the electrostatic field and is characterized by a low plasma density; H mode is sustained by applying more power or current, subsequently creating a system characterized by higher plasma density.[79] Above p = 150 mTorr and P = 40 W, emission from the plasma saturated the detector and no additional spectral data could be reliably collected. At lower pressures (50 and 100 mTorr), the visual mode change occurred at higher power, between 30 and 35 W. When the plasma is operating in E mode or H mode, regardless of pressure, small fluctuations in T_{exc} may be observed as a function of power; nevertheless, the majority of these data are within

experimental error. Notably, the largest changes in T_{exc} occur when the plasma shifts between modes.

A considerable number of studies have sought to use the intensity ratio of two OES lines to determine T_e and n_e trends as a function of plasma operating conditions. The sensitivity and potential accuracy of these measurements will, however, strongly depend on the choice of line-ratios.[25] The selection of emission line ratios is largely dependent on the major collisional-radiative processes within the discharge and are theoretically supported by a population model (e.g., Corona and collisional-radiative models).[26] Therefore, system pressure and ionization rate, as well as the EEDF, plasma dimension, and gas temperature can influence the population and depopulation processes and thereby selection of line-ratios. Discussed above, the plasma can shift between capacitive and indicative modes based on operating conditions, therefore plasma mode may also play a role in the determination of T_e via OES line – ratios. Boffard *et al.* studied rf ICP discharges at 13.56 MHz at p = 10 – 50 mTorr, P = 600 W, using the ratio of line intensities at 420.1 and 419.8 nm to measure the effective T_e in Ar-containing systems, finding temperatures obtained with this line pairing in ICPs are consistent with those determined via a Langmuir probe.[24] Siepa and co-workers studied 13.56 MHz rf driven, capacitively-coupled plasma (CCP) discharges, at p = 20 Pa (~150 mTorr) and 200 Pa (1.5 Torr) at P = 50 – 350 W, using the ratio of line intensities at 763.5 and 738.4 nm to examine T_e.[25] We also employed this line ratio to examine our Ar rf ICPs at p = 50 – 150 mTorr, P = 5 – 50 W, Figure 3.3b. Upon comparison to calculated T_{exc} values, a similar pressure trend emerges when the plasma is operating at low power (i.e., in E mode); however, there appears to be a stronger rf power dependence with the line-ratio method than with the T_{exc} values, determined via the Boltzmann plot (Figure 3.3a).

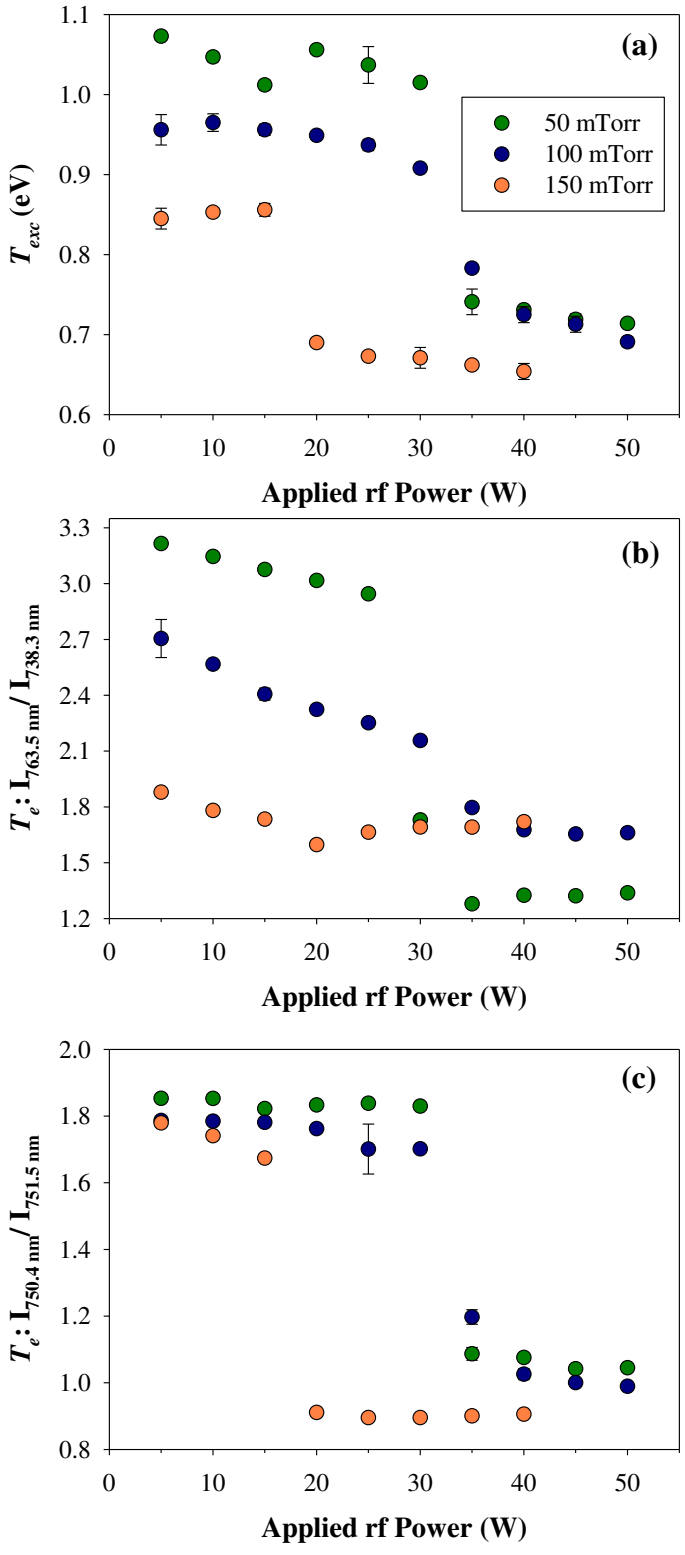

Figure 3.3. (a) Calculated T_{exc} values, T_e sensitive line-ratios (b) ($I_{763.5\ nm}/I_{738.3\ nm}$) and (c) ($I_{750.4\ nm}/I_{751.5\ nm}$) determined in Ar plasmas, plotted as a function of p and P.

Furthermore, a sharp drop in T_e (line-ratio method) corresponding to an E to H mode transition is not observed for the 150 mTorr system, although visually the plasma has switched operating modes. Furthermore, at P = 40 W, the T_e line-ratios suggest a lower T_e is obtained with a lower system pressure, which conflicts with expected ionization balance within a discharge and the T_{exc} trends shown in Figure 3.3a. Similarly, however, Chai and Kwon observed a drastic increase in the relative intensities of 811.5 and 763.5 nm emission lines with increasing Ar pressure within a CCP at 13.56 MHz.[7] The authors attribute this intensity increase to radiation trapping, an argument supported by the results of their CR modeling.[7] The potential susceptibility of the Ar $2p_6$ (763.5 nm) line to radiation trapping at increased pressures could further explain the discrepancies in Figure 3.3b. Ar $2p_1$ (750.4 nm) and $2p_5$ (751.5 nm) emissions are primarily produced by ground-state excitation, whereas other Ar (2p) levels are produced by both ground- and metastable-state excitations.[20] The $2p_1$ and $2p_5$ lines have shown sensitivity to T_e at p = 120 Pa (900 mTorr);[26] Donnelly employed these emission levels to determine high T_e (characterizing electrons in high-energy tail) in combination with additional Kr and Xe lines.[37] Figure 3.3c depicts the $2p_1/2p_5$ ratio as a function of system pressure and power. Here, pressure effects are diminished at lower powers (i.e., E mode) for this line-ratio compared to T_{exc} (Figure 3.3a) and results from $2p_6/2p_3$ ratio (Figure 3.3b). Notably, the trends in Figure 3.3a and 3.3c are better aligned at higher powers (i.e., H-mode). These data suggest that discharge mode should be an additional consideration when applying the line-ratio method to assess T_e trends within a discharge.

Additionally, the discrepancies presented in Figure 3.3 highlight the necessity for careful selection of line-ratios, as well as comparison to other computational and experimental techniques, such as population models and Langmuir probes. A previous Fisher group study

characterized Ar ICPs at p = 30 – 50 mTorr, P = 25 – 150 W with Langmuir probe and mass spectrometry measurements.[80] At 25 and 50 W, little to no pressure dependence is documented; however, at the highest P (150 W), T_e decreases from ~3.75 eV to ~3.0 eV as p increases from 30 to 50 mTorr. Although different operating conditions were employed, this same trend is reflected in Figure 3.3a and 3.3c; however, the values of T_{exc} are considerably lower compared to T_e measured with a Langmuir probe. Further comparison reveals that although the type of plasma was consistent between these studies (rf ICP), the plasma dimensions and discharge volume differed, which may contribute to the difference in T_{exc} and T_e. As described above, a bi-Maxwellian distribution can be used to describe plasmas that contain both a high T_e (electrons in the tail of the distribution) and a low T_e corresponding to bulk electrons. By assuming a Maxwell-Boltzmann distribution to determine T_{exc} in our current studies, it is likely we are primarily characterizing the bulk electrons, providing a lower-limit for T_e compared to the T_e values obtained directly with the Langmuir probe of a similar system.

Electron density (n_e) is an additional plasma parameter that can be characterized through the OES line-ratio method, Figure 3.4. At 50 and 100 mTorr, there is little power dependence when the plasma operates in E mode (5 – 30 W); at P = 35 W, however, a sharp increase by a factor of ~3 is documented. Revealed via a global model analysis, an increase in system pressure leads to a decrease in electron temperature and concomitant increase in plasm density, presented through n_e determination.[81] The 100 mTorr system continues to increase until 40 W, then little power dependence is observed in H mode operation at 50 or 100 mTorr. Although a similar trend is observed for the 150 mTorr system, the mode transition occurs at lower P (15 W → 20 W).

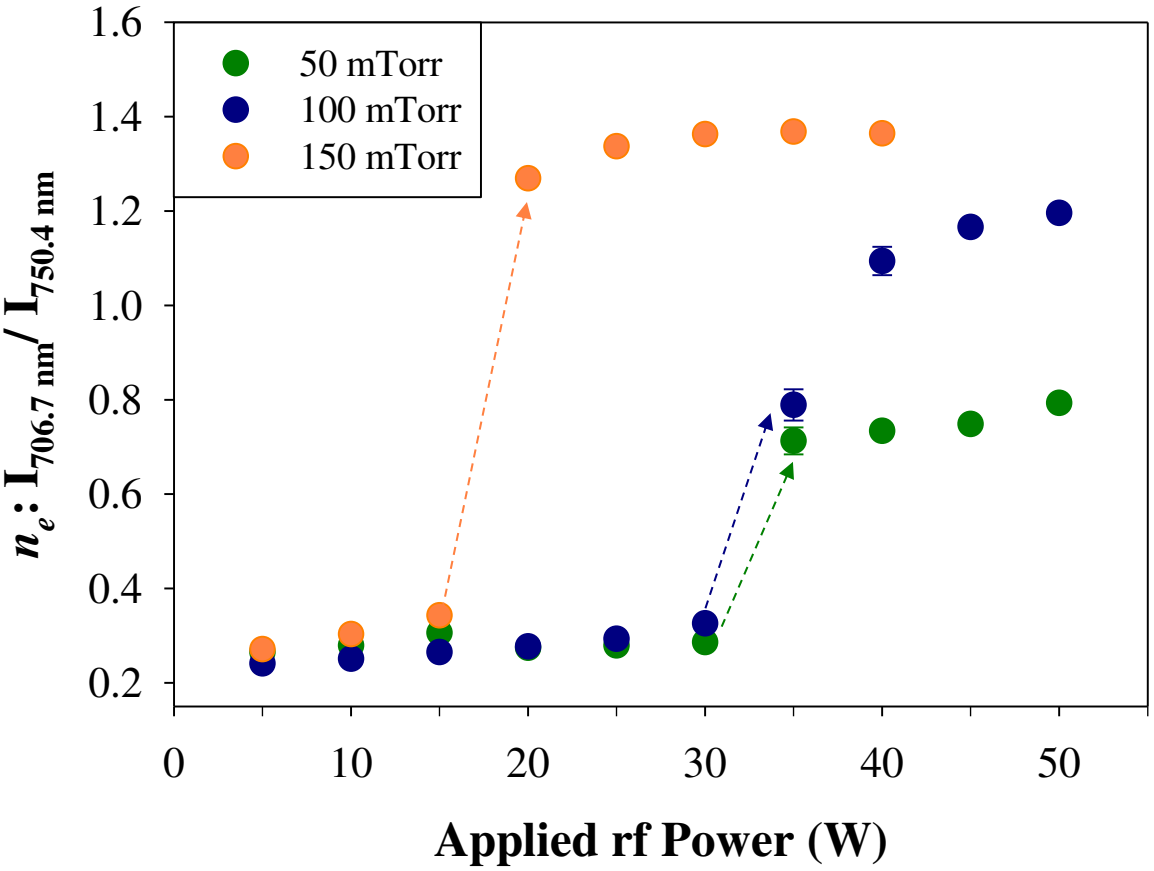

Figure 3.4. n_e sensitive line-ratio ($I_{706.7\ nm}/I_{750.4\ nm}$) determined in Ar plasmas as a function of p and P. Dashed lines represent a change from plasma operating from E-mode to H-mode.

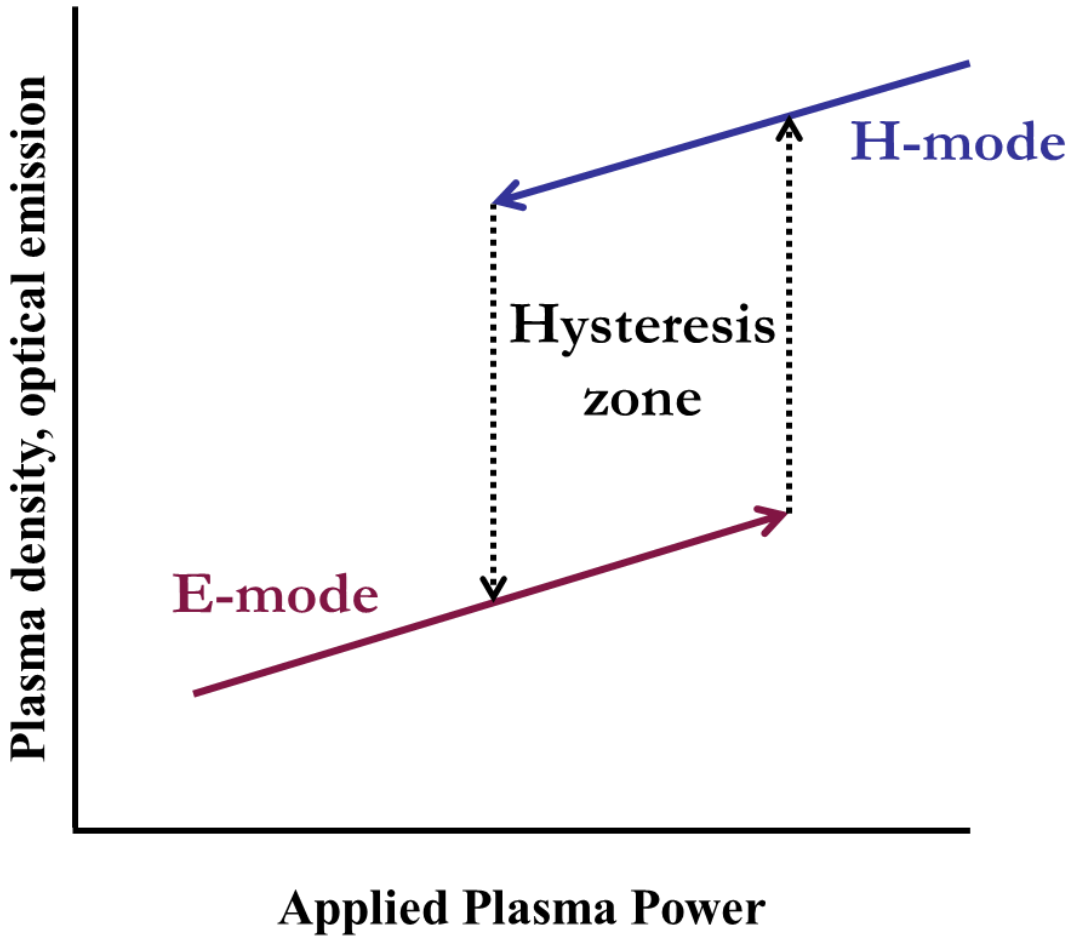

Figure 3.5. Pictorial representation of E-H mode change as a function of plasma density and power.

An additional n_e sensitive line-ratio, ($I_{696.5\ nm}/I_{750.4\ nm}$), was proposed by Crintea et al.;[82] within our rf ICP system, this ratio yielded similar results to those shown in Figure 3.4 for the ($I_{706.7\ nm}/I_{750.4\ nm}$) ratio. As shown in Figures 3.3 and 3.4, as rf power increases to a certain threshold, an E → H mode shift occurs. As power decreases, it has been theoretically and experimentally revealed the discharge mode will return to E mode, however hysteresis behavior can be present, pictorially represented in Figure 3.5. El-Fayoumi *et al.* argue this hysteresis is due to the nonlinearity of power absorption and dissipation within a discharge.[83]

As noted in the Section 3.2, these plasma properties are widely studied, yet can be system-dependent, therefore important to characterize for each discharge type and reactor set-up. Therefore, we sought to probe how incremental increases in power could influence fundamental plasma properties. In a previous Ar ICP study, a positive correlation with n_e and rf power was measured with a Langmuir probe, however this study was performed over a large power range (ΔP = 125 W).[80] Moreover, the density of ions increased from ~1 x 10^{10} to ~5 x 10^{10} cm^{-3} as power increased from 25 to 150 W. As power increases, that energy can be distributed to the formation of more Ar ions or higher energy metastable states.[80] Wang *et al*. compared effective electron temperature (T_{eff}) values measured via probe and OES analysis of a Ar ICP operating at 600 W, p = 1 – 25 mTorr, documenting as system pressure increases, T_{eff} decreases with a parallel increase in n_e.[30] The data shown in Figures 3.3 and 3.4 reflect these relationships between plasma properties and pressure. Recently, the study of the fundamental plasma properties (T_e, n_e, and T_g) was expanded by Durocher-Jean *et al.* with small admixtures of N_2, O_2, and H_2 into microwave Ar plasmas at atmospheric pressure.[84] Each of these admixtures are common plasma precursors with their own physical and chemical properties, therefore the authors sought to understand how the addition of these gases contribute to overall plasma

character. At the highest amount of admixture in the Ar plasma (1%), T_g generally increased with a concomitant decrease in n_e. As systems become more multifaceted, it is imperative to understand how fundamental properties evolve with increased complexity.

To further explore the relationship between electron dynamics and plasma conditions, TR-OES was employed to probe pulsed Ar plasmas, monitoring the 750.4 nm ($2p_1$) line and T_e line-ratio ($2p_1/2p_5$) as a function of time, shown in Figures 3.6a and 3.6b, respectively. Figure 3.6a contains TR-OES data for a pulsed Ar plasma (p = 100 mTorr), collected with a 50% d.c. at three different P_{eq}. Although there are clear intensity differences for the powers studied, the shape of the pulses is relatively independent of P_{eq} and plasma operating mode. Figure 3.5b depicts temporally-resolved T_e line-ratios for an Ar plasma (p = 100 mTorr) at three operating conditions, with P_{eq} = 5, 20, and 50 W. At P_{eq} = 5 W, T_e ratios increase sharply to ~2.0 at the start of the second and fourth pulses, with a subsequent decay to ~1.6. Boffard and coworkers monitored the 420.1 – 419.8 nm emission lines of Ar to elucidate temporally-resolved T_e, documenting enhanced T_e at the start of the pulse (time resolution 25 μs), followed by a decrease to a steady value within the cycle.[85] The tendency of T_e to overshoot steady-state values at the beginning of the active glow (plasma-on) and subsequent decrease to a steady-state value during the pulse cycle has been observed previously in both theoretical and experimental studies.[52,86,87] These initial "hot electrons" were not, however, detected at every cycle or P_{eq} in our pulsing-experiment; ; however, the TR-OES data shown in Figure 3.6 were collected with a 1.05 ms integration time, whereas the time-resolution in the Boffard study was 25 μs.[85] Therefore, the sharp increase or overshoot of T_e at the beginning of the active glow is likely occurring consistently, albeit sometimes on a time-scale experimentally unavailable with our current apparatus.

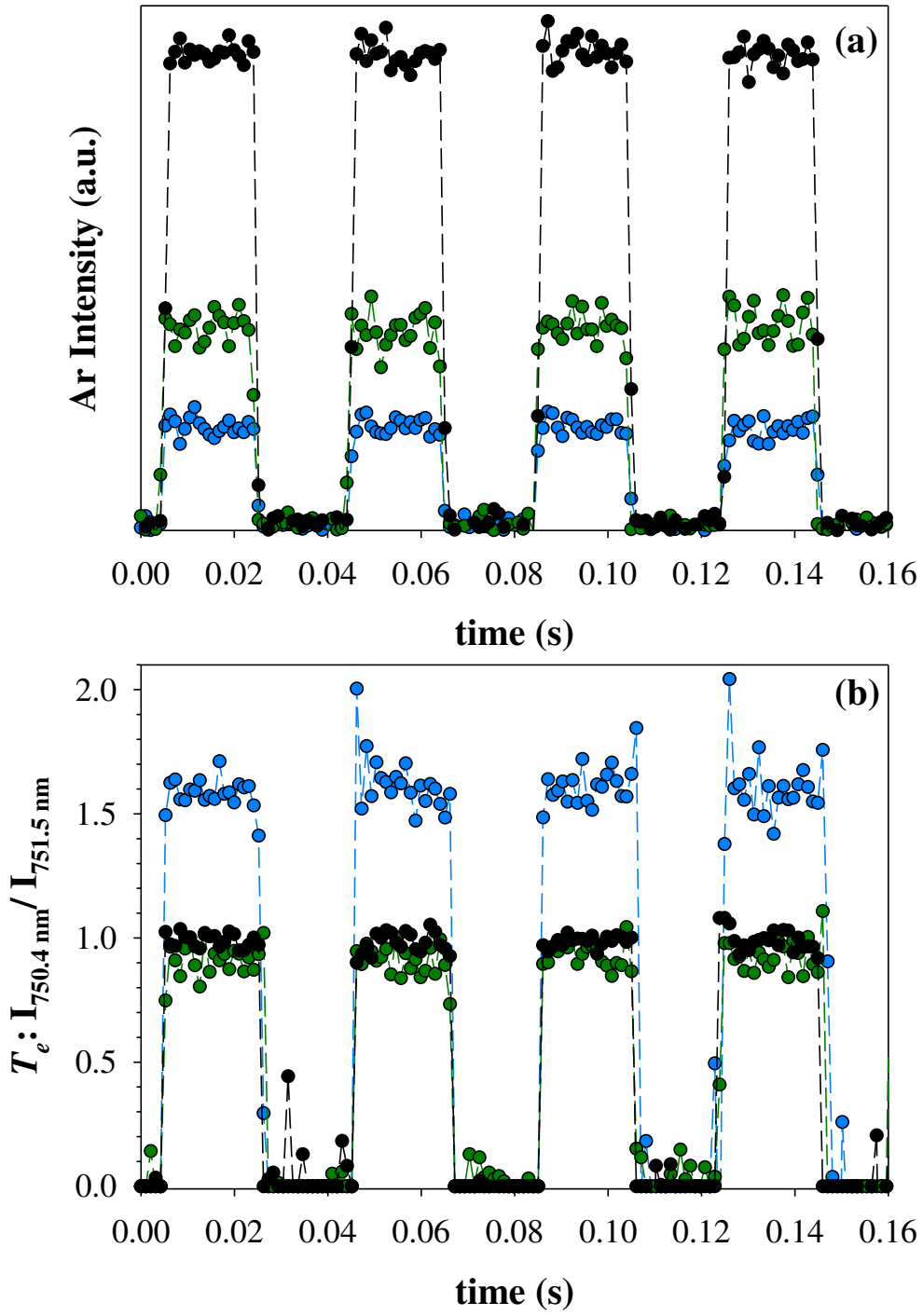

Figure 3.6. TR-OES of pulsed Ar plasma (p = 100 mTorr, 50 % d.c.) at (a) P_{eq} = 5 W (blue), 20 W (green), 50 W (black) and (b) corresponding T_e line ratios ($I_{750.4\ nm}/I_{751.5\ nm}$).

In the afterglow (plasma off), Boffard *et al.* noted significant electron cooling,[85] where T_e decreases rapidly due to inelastic collisions and fast electron escape to the wall, effectively approaching gas temperature due to diffusional cooling.[86] Specifically, Godyak measured T_e = 0.05 eV in the afterglow in an Ar ICP (4 MHZ) discharge at 3 mTorr.[86] Pulsing the discharge not only changes the applied power, but also modifies plasma parameters such as plasma sheath formation, potentials across the sheath, which in turn affects ion and electron energies.

Depicted in Figure 3.3c, within a CW Ar plasma (100 mTorr, 20 W), the plasma is operating in E-mode with a T_e line ratio value of 1.76. As power is increased to 40 W, the plasma shifts modes and the T_e line-ratio value decreased to 1.026. Studying the pulsed Ar system, (P_{eq} = 20 W, peak power = 40 W), the plasma was visually operating in H-mode. Shown in Figure 3.6b, the line-ratio technique yielded a T_e value of ~1 for both P_{eq} = 20 and 50 W, quantitively indicative of H-mode operation. Libermann and Ashida employed global models to study pulsed and continuous wave Ar discharges to describe the behavior of plasma density and electron temperature. Assuming a Maxwellian EEDF, they found the time-averaged plasma density can be considerably higher (up to 4 times greater) than that for CW discharges for the same time-averaged power.[88] Additionally, at P_{eq} = 5 W, a T_e value of ~1.6 was obtained, where the CW discharge resulted in T_e = 1.78. This discrepancy is unsurprising, as Logue and Kushner also report steady-state T_e values in the active glow of a pulsed plasma may differ from T_e within a CW discharge, even if ignited at the same P_{eq}.[89] By employing OES as a diagnostic tool, one can probe fundamental plasma properties as a function of time, effectively assessing the differences between CW and pulsed regimes of a discharge.

OES can also be used to characterize streamers generated by nanosecond pulsed discharges. Goekce *et al.* measured plasma dynamics with a spectrometer coupled with ICCD camera to

achieve time resolution of 2 ns, determining the average reduced electric field associated with surface streamers using transitions arising from atmospheric pressure air plasmas: Ar transitions ($2p_x - 1s_y$), as well as the first negative system of N_2^+ ($B^2\Sigma_u^+ - X^2\Sigma_g^+$), and the first positive ($B^3\Pi_g - A^3\Sigma_u^+$) and second positive system ($C^3\Pi_u - B^3\Pi_g$) of N_2.[47] For pulsed plasma systems, increased time resolution is critical if monitoring nanosecond pulse widths in comparison to the 10 ms pulse widths reported here. Clearly, however, the desired time resolution for a given experimental must be chosen carefully as it will depend heavily on the nature of the discharge, such as CW or pulsed, as well as the type of species to be monitored, whether molecular or atomic precursors or products of precursor decomposition, Figure 2.3. In the following chapters, we expand the examination of time-resolved studies of Ar pulsed plasmas to more complex systems, such as N_xO_y discharges.

3.4 Summary and Observations

Optical spectroscopy provides non-intrusive, *in situ* diagnostic tools (including OES, BAS, and LIF) to examine the complex chemistry in a range of plasma systems. Although OES has been frequently employed for plasma species identification and to elucidate species density with inert gas actinometry, the present work focused on recent literature and new results from the Fisher group that highlight specific ways to significantly enhance and expand these capabilities. The literature is rife with studies that characterized fundamental plasma properties, such as T_e and n_e, within a variety of discharge types and various operating conditions. We have also explored using a simple, OES line-ratio technique to explore how these parameters evolve over a range of pressure-power combinations. Using these line-ratios, we quantitatively determined applied power conditions where E to H mode shifts occur at different system pressures. Exploiting the temporal and spectral resolution of our spectrometer allows the collection of TR-

OES data, which provides additional insight on the kinetics of species formation within plasma systems. This is especially relevant when applied to the PAC platform that utilizes catalytic substrates, described in Chapters 7 and 8.

Perhaps even more powerful, the combination of optical spectroscopies can provide a more comprehensive view of the molecular-level plasma chemistry. Specifically, we used a combination of OES and BAS to document that vibrational energy distributions significantly differ between molecules and electronic states (both excited and ground state) within a given system, described further in Chapters 4 and 6. Knowledge of internal molecular temperatures and system kinetics for multiple species within a plasma system will significantly aid plasma modeling efforts. Likewise, combining OES with the LIF-based IRIS technique affords insight into the energetics and kinetics, including gas-substrate interactions (Chapter 4 and Appendix B).

Through optical spectroscopies, the influence of a substrate on the energetics and kinetics of the resulting gas-phase has been measured, where efforts to more efficiently tailor plasma processing techniques require a thorough knowledge of both the gas-phase and gas-surface interface. Aspects of work detailed here are universally relevant for plasma applications, thus furthering fundamental understanding of plasma systems required for improved or novel uses. We encourage the plasma community to incorporate optical diagnostic tools more deeply to enhance and enrich their characterization of complex plasma systems.

REFERENCES

1. Stillahn, J. M.; Trevino, K. J.; Fisher, E. R., Plasma Diagnostics for Unraveling Process Chemistry. *Annu. Rev. Anal. Chem.* **2008**, *1*, 261-291.
2. Grill, A., *Cold Plasma Materials Fabrications: From Fundamentals to Applications*. IEEE Press: Piscataway, NJ, 1994.
3. Park, H.; Choe, W., Parametric Study on Excitation Temperature and Electron Temperature in Low Pressure Plasmas. *Curr. Appl. Phys.* **2010**, *10*, 1456-1460.
4. Hanna, A. R.; Cuddy, M. F.; Fisher, E. R., Energy Partitioning and its Influence on Surface Scatter Coefficients within Fluorinated Inductively Coupled Plasmas. *J. Vac. Sci. Technol., A* **2017**, *35*, 05C308.
5. Mawardi, O. K., Use of Langmuir Probes for Low-Density Plasma Diagnostics. *Am. J. Phys.* **1966**, *34*, 112-120.
6. Konjević, N.; Jovićević, S.; Ivković, M., Optical Emission Spectroscopy for Simultaneous Measurement of Plasma Electron Density and Temperature in a Low-Pressure Microwave Induced Plasma. *Phys. Plasmas* **2009**, *16*, 103501.
7. Chai, K.-B.; Kwon, D.-H., Optical Emission Spectroscopy and Collisional-Radiative Modeling for Low Temperature Ar Plasmas. *J. Quant. Spectrosc. Radiat. Transfer* **2019**, *227*, 136-144.
8. Gizzatullin, A. R.; Zhelonkin, Y. O.; Voznesencky, E. F.; Gizzatullin, A. R., Application of Argon Collisional-Radiative Model for Inductive RF Discharge Research. *J. Phys.: Conf. Ser.* **2019**, *1328*, 012025.
9. Evdokimov, K. E.; Konishchev, M. E.; Pichugin, V. F.; Pustovalova, A. A.; Ivanova, N. M.; Sun', C., Determination of the Electron Density and Electron Temperature in a Magnetron Discharge Plasma Using Optical Spectroscopy and the Collisional-Radiative Model of Argon. *Russ. Phys. J.* **2017**, *60*, 765-775.
10. Navrátil, Z.; Dvořák, P.; Brzobohatý, O.; Trunec, D., Determination of Electron Density and Temperature in a Capacitively Coupled RF Discharge in Neon by OES Complemented with a CR Model. *J. Phys. D: Appl. Phys.* **2010**, *43*, 505203.
11. Yamashita, Y.; Yamazaki, F.; Nezu, A.; Akatsuka, H., Diagnostics of Low-Pressure Discharge Argon Plasma by Multi-Optical Emission Line Analysis Based on the Collisional-Radiative Model. *Jpn. J. Appl. Phys.* **2019**, *58*, 016004.
12. Bogaerts, A.; Gijbels, R.; Vlcek, J., Collisional-Radiative Model for an Argon Glow Discharge. *J. Appl. Phys.* **1998**, *84*, 121-136.
13. Lieberman, M. A.; Lichtenberg, A. J., *Principle of Plasma Discharges and Materials Processing*. Wiley: New York, 2005.
14. Iza, F.; Hopwood, J. A., Rotational, Vibrational, and Excitation Temperatures of a Microwave-Frequency Microplasma. *IEEE Trans. Plasma Sci.* **2004**, *32*, 498-504.
15. Drawin, H. W., Validity Conditions for Local Thermodynamic Equilibrium. *Z. Phys.* **1969**, *228*, 99-119.
16. Hey, J. D.; Chu, C. C.; Rash, J. P. S., Partial Local Thermal Equilibrium in a Low-Temperature Hydrogen Plasma. *J. Quant. Spectrosc. Radiat. Transfer* **1999**, *62*, 371-387.
17. Ivković, M.; Jovićević, S.; Konjević, N., Low Electron Density Diagnostics: Development of Optical Emission Spectroscopic Techniques and Some Applications to Microwave Induced Plasmas. *Spectrochim. Acta, Part B* **2004**, *59*, 591-605.

18. Sugai, H.; Ghanashev, I.; Hosokawa, M.; Mizuno, K.; Nakamura, K.; Toyoda, H.; Yamauchi, K., Electron Energy Distribution Functions and the Influence on Fluorocarbon Plasma Chemistry. *Plasma Sources Sci. Technol.* **2001**, *10*, 378-385.
19. Taccogna, F.; Dilecce, G., Non-Equilibrium in Low-Temperature Plasmas. *Eur. Phys. J. D* **2016**, *70*, 251.
20. Boffard, J. B.; Jung, R. O.; Lin, C. C.; Wendt, A. E., Optical Emission Measurements of Electron Energy Distributions in Low-Pressure Argon Inductively Coupled Plasmas. *Plasma Sources Sci. Technol.* **2010**, *19*, 065001.
21. Zhu, X.-M.; Pu, Y.-K.; Celik, Y.; Siepa, S.; Schüngel, E.; Luggenhölscher, D.; Czarnetzki, U., Possibilities of Determining Non-Maxwellian EEDFs from the OES Line-Ratios in Low-Pressure Capacitive and Inductive Plasmas Containing Argon and Krypton. *Plasma Sources Sci. Technol.* **2012**, *21*, 024003.
22. Scanlan, J. V.; Hopkins, M. B., Langmuir Probe Measurements of the Electron Energy Distribution Function in Radio-Frequency Plasmas. *J. Vac. Sci. Technol., A* **1992**, *10*, 1207-1211.
23. Franek, B. J.; Nogami, H. S.; Koepke, E. M.; Demidov, I. V.; Barnat, V. E., A Computationally Assisted Ar I Emission Line Ratio Technique to Infer Electron Energy Distribution and Determine Other Plasma Parameters in Pulsed Low-Temperature Plasma. *Plasma* **2019**, *2*.
24. Boffard, J. B.; Jung, R. O.; Lin, C. C.; Aneskavich, L. E.; Wendt, A. E., Argon 420.1–419.8 nm Emission Line Ratio for Measuring Plasma Effective Electron Temperatures. *J. Phys. D: Appl. Phys.* **2012**, *45*, 045201.
25. Siepa, S.; Danko, S.; Tsankov, T. V.; Mussenbrock, T.; Czarnetzki, U., On the OES Line-Ratio Technique in Argon and Argon-Containing Plasmas. *J. Phys. D: Appl. Phys.* **2014**, *47*, 445201.
26. Zhu, X.-M.; Pu, Y.-K., Optical Emission Spectroscopy in Low-Temperature Plasmas Containing Argon and Nitrogen: Determination of the Electron Temperature and Density by the Line-Ratio Method. *J. Phys. D: Appl. Phys.* **2010**, *43*, 403001.
27. Melnikov, A. D.; Usmanov, R. A.; Gavrikov, A. V.; Liziakin, G. D.; Smirnov, V. P.; Timirkhanov, R. A.; Vorona, N. A., Application of Line-Intensity-Ratio Method for Measurement of Electron Temperature of Radio-Frequency Plasma of Argon in Magnetic Field Inside the Plasma Separator. *J. Phys.: Conf. Ser.* **2019**, *1147*, 012131.
28. Abrar, M.; Qayyum, A.; Gilani, A. R.; Khan, A. W.; Saeed, A.; Naseer, S.; Zakaullah, M., Effect of Helium Mixing on Excitation Temperature and Nitrogen Dissociation in Inductively Coupled Plasma. *Curr. Appl. Phys.* **2013**, *13*, 969-974.
29. Wu, A. J.; Zhang, H.; Li, X. D.; Lu, S. Y.; Du, C. M.; Yan, J. H., Determination of Spectroscopic Temperatures and Electron Density in Rotating Gliding Arc Discharge. *IEEE Trans. Plasma Sci.* **2015**, *43*, 836-845.
30. Wang, S.; Wendt, A. E.; Boffard, J. B.; Lin, C. C.; Radovanov, S.; Persing, H., Noninvasive, Real-Time Measurements of Plasma Parameters Via Optical Emission Spectroscopy. *J. Vac. Sci. Technol., A* **2013**, *31*, 021303.
31. Belostotskiy, S. G.; Ouk, T.; Donnelly, V. M.; Economou, D. J.; Sadeghi, N., Gas Temperature and Electron Density Profiles in an Argon DC Microdischarge Measured by Optical Emission Spectroscopy. *J. Appl. Phys.* **2010**, *107*.

32. Lee, Y.-K.; Moon, S.-Y.; Oh, S.-J.; Chung, C.-W., Determination of Metastable Level Densities in a Low-Pressure Inductively Coupled Argon Plasma by the Line-Ratio Method of Optical Emission Spectroscopy. *J. Phys. D: Appl. Phys.* **2011**, *44*, 285203.
33. Evdokimov, K. E.; Konischev, M. E.; Pichugin, V. F.; Sun, Z., Study of Argon Ions Density and Electron Temperature and Density in Magnetron Plasma by Optical Emission Spectroscopy and Collisional-Radiative Model. *Resour.-Effic. Technol.* **2017**, *3*, 187-193.
34. Donnelly, V. M.; Malyshev, M. V.; Schabel, M.; Kornblit, A.; Tai, W.; Herman, I. P.; Fuller, N. C. M., Optical Plasma Emission Spectroscopy of Etching Plasmas Used in Si-based Semiconductor Processing. *Plasma Sources Sci. Technol.* **2002**, *11*, A26-A30.
35. Coburn, J. W.; Chen, M., Optical Emission Spectroscopy of Reactive Plasmas: A Method for Correlating Emission Intensities to Reactive Particle Density. *J. Appl. Phys.* **1980**, *51*, 3134-3136.
36. Gottscho, R. A.; Donnelly, V. M., Optical Emission Actinometry and Spectral Line Shapes in RF Glow Discharges. *J. Appl. Phys.* **1984**, *56*, 245-250.
37. Donnelly, V. M., Plasma Electron Temperatures and Electron Energy Distributions Measured by Trace Rare Gases Optical Emission Spectroscopy. *J. Phys. D: Appl. Phys.* **2004**, *37*, R217-R236.
38. Donnelly, V. M.; Kornblit, A., Plasma Etching: Yesterday, Today, and Tomorrow. *J. Vac. Sci. Technol., A* **2013**, *31*, 050825.
39. Fuller, N. C. M.; Herman, I. P.; Donnelly, V. M., Optical Actinometry of Cl_2, Cl, Cl^+, and Ar^+ Densities in Inductively Coupled Cl_2–Ar Plasmas. *J. Appl. Phys.* **2001**, *90*, 3182-3191.
40. Guha, J.; Donnelly, V. M.; Pu, Y.-K., Mass and Auger Electron Spectroscopy Studies of the Interactions of Atomic and Molecular Chlorine on a Plasma Reactor Wall. *J. Appl. Phys.* **2008**, *103*, 013306.
41. Alshaltami, K. A.; Daniels, S., Investigation of Etching Optimization in Capacitively Coupled SF_6–O_2 Plasma. *AIP Adv.* **2019**, *9*, 035047.
42. Kang, M.; Ko, Y.; Jang, I.-y.; Jung, J.; Hahn, J. W., Pseudo Actinometry for the Measurement of Reactive Species Density. *Opt. Lett.* **2017**, *42*, 1420-1423.
43. Cuddy, M. F.; Fisher, E. R., Investigation of the Roles of Gas Phase CF_2 and F During FC Processing of Si and ZrO_2 *J. Appl. Phys.* **2010**, *108*, 033303.
44. Stuckert, E. P.; Miller, C. J.; Fisher, E. R., Gas-phase Diagnostics During H_2 and H_2O Plasma Treatment of SnO_2 Nanomaterials: Implications for Surface Modification. *J. Vac. Sci. Technol., B* **2017**, *35*, 021802.
45. Hirao, S.; Hayashi, Y.; Makabe, T., Space-and Time-Resolved E–H Transition in an Inductively Coupled Plasma in Ar. *IEEE Trans. Plasma Sci.* **2008**, *36*, 1410-1411.
46. Gherardi, M.; Puač, N.; Marić, D.; Stancampiano, A.; Malović, G.; Colombo, V.; Petrović, Z. L., Practical and Theoretical Considerations on the Use of ICCD Imaging for the Characterization of Non-Equilibrium Plasmas. *Plasma Sources Sci. Technol.* **2015**, *24*, 064004.
47. Goekce, S.; Peschke, P.; Hollenstein, C.; Leyland, P.; Ott, P., OES Characterization of Streamers in a Nanosecond Pulsed SDBD Using N_2 and Ar Transitions. *Plasma Sources Sci. Technol.* **2016**, *25*, 045002.
48. van der Horst, R. M.; Verreycken, T.; van Veldhuizen, E. M.; Bruggeman, P. J., Time-Resolved Optical Emission Spectroscopy of Nanosecond Pulsed Discharges in Atmospheric-Pressure N_2 and N_2/H_2O mixtures. *J. Phys. D: Appl. Phys.* **2012**, *45*.
49. Maletić, D.; Puač, N.; Selaković, N.; Lazović, S.; Malović, G.; Đorđević, A.; Petrović, Z. L., Time-Resolved Optical Emission Imaging of an Atmospheric Plasma Jet for Different

Electrode Positions with a Constant Electrode Gap. *Plasma Sources Sci. Technol.* **2015**, *24*, 025006.
50. Jagannath, R. R.; Satija, A.; Lucht, R. P.; Bane, S. P. M., Characterization of Time-Resolved Emission of $N_2(C)$ in an Atmospheric Pressure Nanosecond Pulsed Air-Plasma Using Streak Spectroscopy. *Plasma Sources Sci. Technol.* **2019**, *28*, 01LT02.
51. Hofmann, S.; van Gils, K.; van der Linden, S.; Iseni, S.; Bruggeman, P., Time and Spatial Resolved Optical and Electrical Characteristics of Continuous and Time Modulated RF Plasmas in Contact with Conductive and Dielectric Substrates. *Eur. Phys. J. D* **2014**, *68*, 56.
52. Subramonium, P.; Kushner, M. J., Pulsed Plasmas as a Method to Improve Uniformity During Materials Processing. *J. Appl. Phys.* **2004**, *96*, 82-93.
53. Kang, N.; Britun, N.; Oh, S.-g.; Gaboriau, F.; Ricard, A., Experimental Study of Ar and $Ar–N_2$ Afterglow in a Pulse-Modulated ICP Discharge: Observation of Highly Excited Ar(6d) Afterpeak Emission. *J. Phys. D: Appl. Phys.* **2009**, *42*, 112001.
54. Bogaerts, A., The Afterglow Mystery of Pulsed Glow Discharges and the Role of Dissociative Electron–Ion Recombination. *J. Anal. At. Spectrom.* **2007**, *22*, 502-512.
55. Yan, X.; Lin, Y.; Huang, R.; Hang, W.; Harrison, W. W., A Spectroscopic Investigation of the Afterglow and Recombination Process in a Microsecond Pulsed Glow Discharge. *J. Anal. At. Spectrom.* **2010**, *25*, 534-543.
56. Jackson, G. P.; King, F. L., Bulk Plasma Properties in the Pulsed Glow Discharge. *Spectrochim. Acta, Part B* **2003**, *58*, 1417-1433.
57. Lopez, J.; Zhu, W.; Freilich, A.; Belkind, A.; Becker, K., Time-Resolved Optical Emission Spectroscopy of Pulsed DC Magnetron Sputtering Plasmas. *J. Phys. D: Appl. Phys.* **2005**, *38*, 1769-1780.
58. Belkind, A.; Zhu, W.; Lopez, J.; Becker, K., Time-Resolved Optical Emission Spectroscopy During Pulsed DC Magnetron Sputter Deposition of Ti and TiO_2 Thin Films. *Plasma Sources Sci. Technol.* **2006**, *15*, S17-S25.
59. Hioki, K.; Itazu, N.; Petrovic, Z. L.; Makabe, T., Optical Emission Spectroscopy of Pulsed Inductively Coupled Plasma in Ar. *Jpn. J. Appl. Phys.* **2001**, *40*, L1183-L1186.
60. Salmon, A.; Popov, N. A.; Stancu, G. D.; Laux, C. O., Quenching Rate of $N(^2P)$ Atoms in a Nitrogen Afterglow at Atmospheric Pressure. *J. Phys. D: Appl. Phys.* **2018**, *51*, 314001.
61. Bišćan, M.; Kregar, Z.; Krstulović, N.; Milošević, S., Time Resolved Spectroscopic Characterization of a-C:H Deposition by Methane and Removal by Oxygen Inductively Coupled RF Plasma. *Plasma Chem. Plasma Process.* **2010**, *30*, 401-412.
62. Cuddy, M. F.; Fisher, E. R., Contributions of CF and CF_2 Species to Fluorocarbon Film Composition and Properties for C_xF_y Plasma-Enhanced Chemical Vapor Deposition. *ACS Appl. Mater. Interfaces* **2012**, *4*, 1733-1741.
63. Bruggeman, P. J.; Sadeghi, N.; Schram, D. C.; Linss, V., Gas Temperature Determination from Rotational Lines in Non-Equilibrium Plasmas: A Review. *Plasma Sources Sci. Technol.* **2014**, *23*, 023001.
64. Chen, C.-J.; Li, S.-Z., Spectroscopic Measurement of Plasma Gas Temperature of the Atmospheric-Pressure Microwave Induced Nitrogen Plasma Torch. *Plasma Sources Sci. Technol.* **2015**, *24*.
65. Zhang, Q. Y.; Shi, D. Q.; Xu, W.; Miao, C. Y.; Ma, C. Y.; Ren, C. S.; Zhang, C.; Yi, Z., Determination of Vibrational and Rotational Temperatures in Highly Constricted Nitrogen Plasmas by Fitting the Second Positive System of N_2 Molecules. *AIP Adv.* **2015**, *5*.

66. Yang, F.; Mu, Z.; Zhang, J., Discharge Modes Suggested by Emission Spectra of Nitrogen Dielectric Barrier Discharge with Wire-Cylinder Electrodes. *Plasma Sci. Technol.* **2016**, *18*, 79-85.
67. Gangoli, S. P.; Gutsol, A. F.; Fridman, A. A., A Non-Equilibrium Plasma Source: Magnetically Stabilized Gliding Arc Discharge: I. Design and Diagnostics. *Plasma Sources Sci. Technol.* **2010**, *19*, 065003.
68. Raud, J.; Laan, M.; Jogi, I., Rotational Temperatures of N_2(C,0) and OH(A,0) as Gas Temperature Estimates in the Middle Pressure Ar/O_2 Discharge. *J. Phys. D: Appl. Phys.* **2011**, *44*.
69. Greig, A.; Charles, C.; Boswell, R. W., Neutral Gas Temperature Estimates and Metastable Resonance Energy Transfer for Argon-Nitrogen Discharges. *Phys. Plasmas* **2016**, *23*, 013508.
70. Ramos, R.; Cunge, G.; Touzeau, M.; Sadeghi, N., Absorption Spectroscopy in BCl_3 Inductively Coupled Plasmas: Determination of Density, Rotational, Translational and Vibrational Temperatures of BCl Molecule. *J. Phys. D: Appl. Phys.* **2008**, *41*, 115205.
71. Vinogradov, I. P.; Dinkelmann, A.; Lunk, A., Measurement of the Absolute CF_2 Concentration in a Dielectric Barrier Discharge Running in Argon/Fluorocarbon Mixtures. *J. Phys. D: Appl. Phys.* **2004**, *37*, 3000-3007.
72. Blechle, J. M.; Hanna, A. R.; Fisher, E. R., Determination of Internal Temperatures Within Nitric Oxide Inductively Coupled Plasmas. *Plasma Process. Polym.* **2017**, 1700041.
73. Hanna, A. R.; Blechle, J. M.; Fisher, E. R., Using Fundamental Spectroscopy to Elucidate Kinetic and Energetic Mechanisms within Environmentally Relevant Inductively Coupled Plasma Systems. *J. Phys. Chem. A* **2017**, *121*, 7627-7640.
74. Bruggeman, P.; Cunge, G.; Sadeghi, N., Absolute OH Density Measurements by Broadband UV Absorption in Diffuse Atmospheric-Pressure He–H_2O. *Plasma Sources Sci. Technol.* **2012**, *21*, 035019.
75. Wijaikhum, A.; Schröder, D.; Schröter, S.; Gibson, A. R.; Niemi, K.; Friderich, J.; Greb, A.; Schulz-von der Gathen, V.; O'Connell, D.; Gans, T., Absolute Ozone Densities in a Radio-Frequency Driven Atmospheric Pressure Plasma Using Two-Beam UV-LED Absorption Spectroscopy and Numerical Simulations. *Plasma Sources Sci. Technol.* **2017**, *26*, 115004.
76. Liu, W.-Y.; Xu, Y.; Liu, Y.-X.; Peng, F.; Gong, F.-P.; Li, X.-S.; Zhu, A.-M.; Wang, Y.-N., Absolute CF_2 Density and Gas Temperature Measurements by Absorption Spectroscopy in Dual-Frequency Capacitively Coupled CF_4/Ar Plasmas. *Phys. Plasmas* **2014**, *21*, 103501.
77. Reuter, S.; Sousa, J. S.; Stancu, G. D.; Hubertus van Helden, J.-P., Review on VUV to MIR Absorption Spectroscopy of Atmospheric Pressure Plasma Jets. *Plasma Sources Sci. Technol.* **2015**, *24*, 054001.
78. Lee, H.-C.; Seo, B. H.; Kwon, D.-C.; Kim, J. H.; Seong, D. J.; Oh, S. J.; Chung, C. W.; You, K. H.; Shin, C., Evolution of Electron Temperature in Inductively Coupled Plasma. *Appl. Phys. Lett.* **2017**, *110*, 014106.
79. Lee, H.-C.; Kim, D.-H.; Chung, C.-W., Discharge Mode Transition and Hysteresis in Inductively Coupled Plasma. *Appl. Phys. Lett.* **2013**, *102*, 234104.
80. Zhou, J.; Martin, I. T.; Ayers, R.; Adams, E.; Liu, D.; Fisher, E. R., Investigation of Inductively Coupled Ar and CH_4/Ar Plasmas and the Effect of Ion Energy on DLC Film Properties. *Plasma Sources Sci. Technol.* **2006**, *15*, 714-726.

81. Gudmundsson, J. T., On the Effect of the Electron Energy Distribution on the Plasma Parameters of an Argon Discharge: a Global (Volume-Averaged) Model Study. *Plasma Sources Sci. Technol.* **2001**, *10*, 76-81.
82. Crintea, D. L.; Czarnetzki, U.; Iordanova, S.; Koleva, I.; Luggenhölscher, D., Plasma Diagnostics by Optical Emission Spectroscopy on Argon and Comparison with Thomson Scattering. *J. Phys. D: Appl. Phys.* **2009**, *42*, 045208.
83. El-Fayoumi, I. M.; Jones, I. R.; Turner, M. M., Hysteresis in the E- to H-Mode Transition in a Planar Coil, Inductively Coupled RF Argon Discharge. *J. Phys. D: Appl. Phys.* **1998**, *31*, 3082-3094.
84. Durocher-Jean, A.; Delnour, N.; Stafford, L., Influence of N_2, O_2, and H_2 Admixtures on the Electron Power Balance and Neutral Gas Heating in Microwave Ar Plasmas at Atmospheric Pressure. *J. Phys. D: Appl. Phys.* **2019**, *52*, 475201.
85. Boffard, J. B.; Wang, S.; Lin, C. C.; Wendt, A. E., Detection of Fast Electrons in Pulsed Argon Inductively-Coupled Plasmas Using the 420.1–419.8 nm Emission Line Pair. *Plasma Sources Sci. Technol.* **2015**, *24*, 065005.
86. Godyak, V. A., Nonequilibrium EEDF in Gas Discharge Plasmas. *IEEE Trans. Plasma Sci.* **2006**, *34*, 755-766.
87. Gao, F.; Lv, X.-Y.; Zhang, Y.-R.; Wang, Y.-N., Complex Transients of Input Power and Electron Density in Pulsed Inductively Coupled Discharges. *J. Appl. Phys.* **2019**, *126*, 093302.
88. Lieberman, M. A.; Ashida, S., Global Models of Pulse-Power-Modulated High-Density, Low-Pressure Discharges. *Plasma Sources Sci. Technol.* **1996**, *5*, 145-158.
89. Logue, M. D.; Kushner, M. J., Electron Energy Distributions and Electron Impact Source Functions in Ar/N_2 Inductively Coupled Plasmas Using Pulsed Power. *J. Appl. Phys.* **2015**, *117*, 043301.

CHAPTER 4

ENERGY PARTITIONING AND ITS INFLUENCE ON SCATTER COEFFICIENTS WITHIN FLUORINATED INDUCTIVELY COUPLED PLASMAS[a]

This chapter examines energy partitioning for molecules (CF and CF_2) formed from fluorinated plasma systems, containing data and discussion from a full, invited manuscript to celebrate the life and work of plasma scientist Harold F. Winters. This manuscript was also selected as an Editor's Pick. The data reported for T_R(CF), T_V(CF), and T_R (CF_2) and species densities were collected and analyzed by Angela R. Hanna. These data have been combined with previously reported data for S(CF), S(CF_2), S(SiF), T_T(SiF), T_R(SIF), T_V(SiF). Dr. C.I Butoi, Ms. M.M. Morgan, Dr. K.L. Williams, Dr. J. Zhang, and Dr. M.F. Cuddy have greatly contributed to this work.

[a] Published in the *Journal of Vacuum Science and Technology A,* written by Angela R. Hanna, Michael F. Cuddy, and Ellen R. Fisher.

4.1 Introduction

An understanding of how energy is dispersed into rotational, vibrational, and translational modes of a gas-phase molecule by means of plasma-stimulated decomposition of a precursor lends critical insight into molecule formation mechanisms, decomposition pathways, and overall plasma chemistry. Knowledge of internal energies, including vibrational (T_V) and rotational (T_R) temperatures, is applicable to estimates of neutral gas temperatures and plasma modeling.[1] Moreover, information gleaned from internal temperatures can elucidate the processes that dictate the overall character of the plasma, as the values are dependent upon such attributes as species densities, electron temperature (T_e), formation reactions, and gas-phase and surface collisions of plasma species, among others.[2]

Non-thermal inductively coupled plasmas (ICPs) generally comprise molecules that follow a classical relationship wherein T_V is nominally greater than T_R and translational (T_T) temperatures, yet each temperature remains significantly less than the T_e of the plasma.[3,4] Notably, T_R values have long been employed as a measure of the neutral gas temperature of the plasma,[5-8] with the assumption that rotational and collective translational temperatures of the gas equilibrate within the plasma.[9] Although this estimate may be appropriate for analyses of the internal temperatures of actinometers, the Fisher Group has previously demonstrated that significant differences exist between T_R and T_T for species such as the silylidyne radical in silane plasmas.[10-12] Furthermore, different radicals in the same plasma system often exhibit distinct internal temperatures, as we have shown for SiF and SiF_2 molecules in tetrafluorosilane systems, using laser-induced fluorescence (LIF).[13] In addition, the same type of plasma species may be formed via different mechanisms, including direct gas-phase decomposition of a monomer gas or recombination

reactions in the plasma reactor. Thus, it is useful to explicitly examine the effect of formation pathways on internal temperatures and surface reactivity of plasma species.

Also of burgeoning interest is the correlation between internal energies and species behavior at surfaces. Our unique imaging of radicals interacting with surfaces (IRIS) technique affords the capability of monitoring *in situ* both the internal energies of selected plasma species and the propensity of such molecules to react at the surface of a specific substrate. In particular, we can calculate the surface scattering coefficient, S, for a given molecule, which is a measure of the likelihood of scattering to occur. Given that the full range of plasma species is incident on the substrate during our measurements, we have also sought to separate the effects arising from different types of species. For example, highly energetic plasma species, such as ions, can play an important role in determining S values for halogenated molecules such as CF_2 in fluorocarbon (FC) plasmas,[14] SiF_2 in SiF_4 systems,[15,16] and $SiCl_2$ in $SiCl_4$ plasmas.[17] We have previously illustrated the relationship between S and T_R for systems including the SiF molecule from LIF data.[16] Nonetheless, we have yet to offer a more comprehensive investigation into the interplay of molecular internal energies (T_R and T_V) with kinetic energy (as measured via T_T) and the impact of these on observed surface interactions (e.g. S values). Thus, we aim to understand the effect of energy dissipation among various degrees of freedom in a given molecule, probing the impact of different types of energy on a molecule's behavior when interacting with a surface. Ultimately, the goal would be to predict surface behavior of a molecule given the distribution of internal energies or the reverse.

In the arena of halocarbon plasma chemistry, Harold Winters and co-workers performed pioneering work by extensively exploring plasma-assisted etching of semiconductor materials using a range of halogenated systems.[18,19] Specifically, Coburn and Winters explored the role of

energetic ions in plasma-assisted etching in silicon-fluorine systems, studying the dynamic interplay between physical and chemical sputtering. The chemical sputtering of silicon and SiO_2 during argon-ion bombardment in the presence of a XeF_2 discharge was examined, wherein 75% of the silicon sputtered from the surface was emitted as SiF_4 gas.[20] Here, we investigated the internal energetics of SiF molecules formed within 100% SiF_4 discharges and their relation to species' behavior at surfaces. Winters and coworkers also studied the reflection and trapping of energetic particles, predominantly ions, within a plasma environment. A portion of this work examined the concentration of argon in sputtered nickel films as a function of film-growth temperatures, pressure, and bias voltage of argon ions. They found that particles with energy less than ~50 eV are not trapped within the film, whereas particles with kinetic energy >100 eV have a significant sticking probability.[20]

This fundamental work fueled the development of our IRIS technique, which examines the likelihood of molecules scattering (i.e., particles that are not trapped) from a specific substrate. Previous IRIS studies explored the interactions of CF_x molecules formed within C_xF_y ion-rich and ion-free plasma molecular beams,[21] as well as NO radicals on various surfaces,[22] wherein the knowledge of ion energies is essential to understanding and ultimately tailoring the chemistry occurring at the gas-surface interface. Winters and coworkers also developed a method for determining the total electron impact cross-sections for many fluoroalkanes and other gases relevant to materials processing in an energy range of 12.5 eV to 600 eV.[23,24] The interactions and collisions of electrons with molecules within the discharge governs the observed chemistry, partitioning between the pathways of excitation, dissociation, and ionization. Understanding these interactions and obtaining quantitative information describing these interrelated processes are critical to the accurate modelling and simulation of plasma systems. We have previously

explored the interdependence of radicals, ions, and surfaces in various plasma processes, concluding both ionic and neutral species must be considered in understanding the precise plasma-surface interactions that lead to specific processing outcomes.[25] Thus, we view our current work as a continuation of the foundational plasma studies completed by Winters, as we seek to develop a deeper understanding of both physical and chemical mechanisms within these plasma systems through our combination of gas-phase spectroscopy and gas-surface interface studies.

Several spectroscopic techniques have been used to measure internal temperatures of plasma species, including Langmuir probes,[26] Doppler broadening analysis of spectral lines,[27] optical emission spectroscopy (OES),[28] LIF spectroscopy,[29] and broadband absorption spectroscopy (BAS).[30-32] Of these, we exploit the latter three for their simplicity of use and the complementary information that can be obtained through excited and ground state species spectral analyses. We offer an approach toward understanding the energetic and surface interactions of plasma species that behave similarly with respect to the relationships between internal temperatures and surface reactivity using OES, LIF, and BAS. Specifically, we examine CF radicals and CF_2 produced from CF_4, C_2F_6, C_3F_8, C_3F_6, and hexafluoropropylene oxide (HFPO) plasmas and SiF from tetrafluorosilane ICPs. Each diatomic radical has the same ground- and first-excited state symmetry, and each demonstrates a comparable relationship between T_V and S. These radicals have been extensively studied by others[1,33-37] and in our laboratories,[11,13,15,16,38] yet a concise illustration of the effect of internal temperatures on surface scattering coefficients has been conspicuously absent. To understand the mechanisms that govern either the etching of or depositing onto a specified surface, we must gain quantitative information concerning the energetics of these systems. Thus, our current line of inquiry

represents a comprehensive investigation of the internal energies of plasma molecules exhibiting a strong relationship between surface scattering coefficients and vibrational energy; building upon the foundational work of Winters and co-workers to understand the physical and chemical mechanisms at play within these technologically-relevant plasma systems.

4.2 Results

Vibrational temperature data were acquired from OES data and simulated using LIFBASE[39] or pGopher.[40] A section of a typical experimental OES spectrum for a C_2F_6 plasma (p = 100 mTorr, P = 100 W) is shown in Figure 4.1 along with simulated data T_R = 315 K, T_V = 2340 K. A BAS spectrum and generated fit in pGopher for a C_3F_8 plasma (p = 50 mTorr, P = 50 W) is shown in Figure 4.2, yielding T_R = 400 K. Here, eight vibrational levels of the ground state were considered in the fit, with a single reported rotational temperature, whereas Lie *et. al*. determined an average temperature of only three bands (v'=4, 5, 6).[31] As depicted in Figure 4.2, the v'=8 band is slightly over-emphasized by the model, which could be negated if each band was fit individually. Rather, we sought for an efficient method to determine the distribution of rotational energies within an entire vibrational band, so a global rotational temperature is reported. These simulations represent the maximized peak correlation between the experimental data and simulated fit.[38] The quantum efficiency of the detector varies by only ~5% over the simulated wavelength range, and as such, these variations were not accounted for in the simulation. Similar procedures were used to determine T_R and T_V for all plasma parameters examined in this study (feed gas, applied power, and system pressure). Scatter coefficients and temperatures (T_T, T_V, and T_R) for SiF radicals are summarized in Table 4.1, where S(SiF) and internal temperatures increase with increasing power. Tables 4.2 and 4.3 contain data for CF radicals formed within a variety of C_xF_y systems at p = 50 and 100 mTorr, respectively.

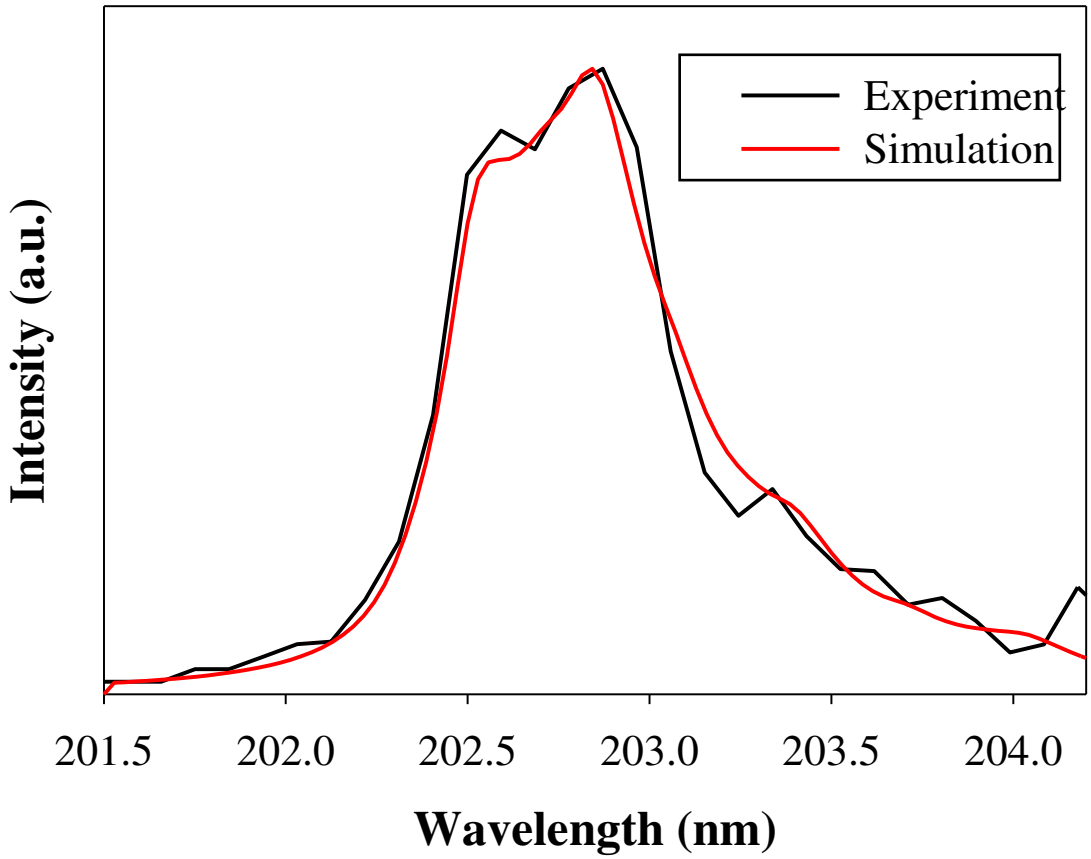

Figure 4.1. Raw OES data (solid black line) corresponding to the B→ X emission for CF in a C_2F_6 plasma (p = 100 mTorr, P = 100 W). The other represents a simulated fit to the data, with T_R = 315 K, T_V = 2340 K, created in LIFBASE 2.1.1.

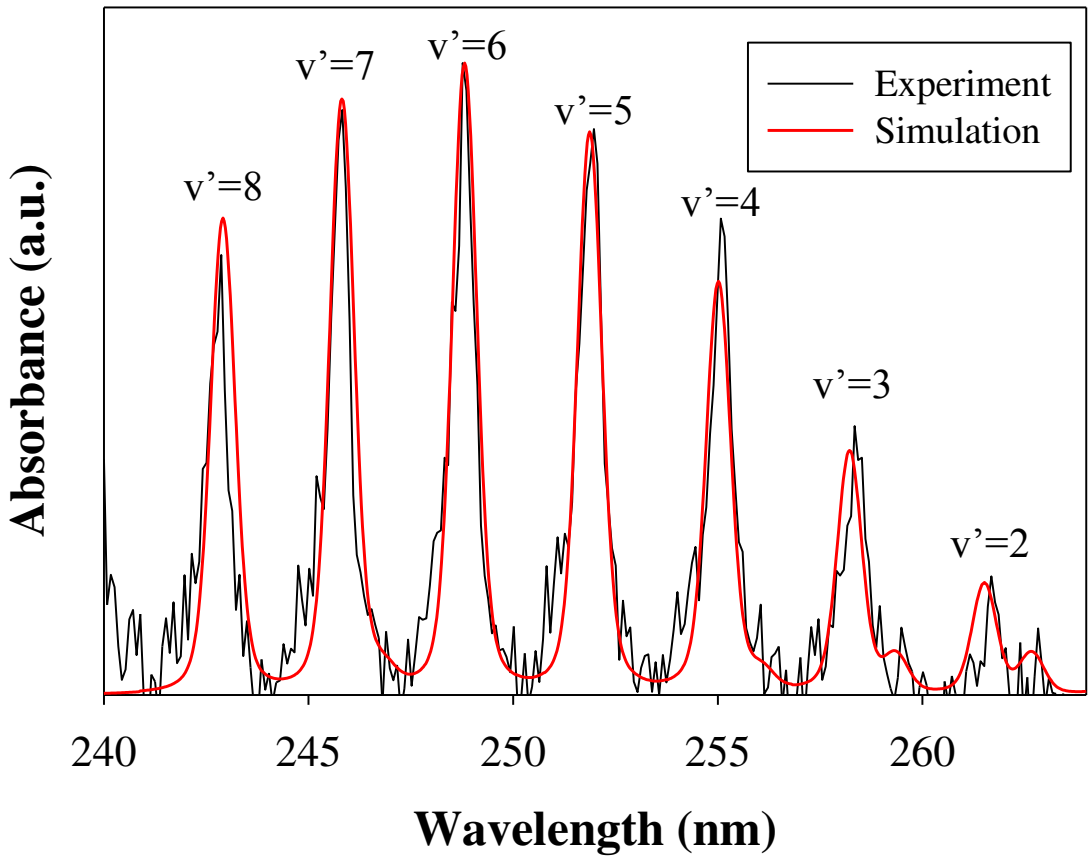

Figure 4.2. Absorbance spectrum corresponding to the A^1B_1 (0, v',0) $\rightarrow X^1A_1$ (0, 0 ,0) for CF_2 in a C_3F_8 plasma (p = 50 mTorr, P = 50 W), simulated in PGOPHER, T_R = 400 K.

Table 4.1. Scatter coefficients and T_T, T_V, and T_R for SiF in SiF_4 plasmas[a]

P (W)	S(SiF)	T_T(K)	T_V(K)	T_R(K)
20	0.21(0.14)			
40	0.43(0.14)			
80	0.79(0.13)	571(180)	1813(63)	735(78)
100		598(85)	1842(18)	818(46)
130		802(88)	1962(13)	870(28)
170	1.20(0.13)	831(120)	1947(10)	1032(3)
200		869(54)	2073(25)	1083(35)

[a]Values for T_V(SiF) and T_R(SiF) are reported here for the first time. S(SiF) and T_T(SiF) values were previously reported.[13,15]

Table 4.2. Scatter coefficients, T_V and T_R for CF ($B^2\Delta$) in FC plasmas[a,b]

Source	*P* (W)	*S*(CF)	T_V (K)	T_R (K)
CF_4 [b]	50	0.90(0.10)	3259(40)	313(14)
	100	1.52(0.09)	3373(51)	309(14)
	150	1.34(0.09)	3304(31)	317(7)
C_2F_6 [b]	50	0.98(0.09)	2935(23)	298(2)
	100	1.04(0.06)	2948(17)	298(2)
	150	1.17(0.10)	3029(16)	320(10)
C_3F_8 [b]	50	0.90(0.10)	2950(38)	298(6)
	100	1.02(0.06)	2940(23)	305(3)
	150	1.18(0.04)	3183(29)	315(10)
C_3F_6 [b]	50	0.74(0.06)	2842(19)	300(5)
	100	0.75(0.09)	2700(8)	308(3)
	150	0.64(0.09)	2732(10)	305(5)
HFPO	50	0.54(0.09)	2090(30)	298(3)
	100	0.85(0.09)	2160(20)	305(5)
	150	0.70(0.04)	2240(15)	305(5)

[a] p = 50 mTorr

[b] *S*(CF) data were previously reported.[41]

Table 4.3. T_V and T_R for CF ($B^2\Delta$) in fluorocarbon plasmas[a]

Source	P (W)	T_V (K)	T_R (K)
CF_4	50	2470(45)	306(3)
	100	2550(16)	310(5)
	150	2645(15)	303(4)
C_2F_6	50	2390(35)	303(3)
	100	2368(42)	311(3)
	150	2406(13)	308(5)
C_3F_8	50	-	-
	100	2315(40)	310(5)
	150	2500(15)	330(11)
C_3F_6	50	2360(25)	310(7)
	100	2495(20)	315(5)
	150	2385(20)	325(10)
HFPO	50	2050(25)	298(5)
	100	2118(40)	305(5)
	150	2215(5)	308(3)

[a]p = 100 mTorr.

Table 4.4. $S(CF_2)$ and T_R for CF_2 ($(\tilde{X}^1B_1)$ molecules in several fluorocarbon plasmas.[a]

Source	$S(CF_2)$	T_R (K) 50 mTorr	T_R (K) 100 mTorr
CF_4	1.50(0.10)	350(20)	
	1.50(0.20)	400(20)	
	1.90(0.20)	-	
C_2F_6	1.28(0.02)	410(35)	370(30)
	1.33(0.02)	405(25)	420(20)
	1.65(0.08)	450(-)	440(15)
C_3F_8	1.56(0.06)	375(25)	340(15)
	1.08(004)	430(20)	405(20)
	0.93(0.02)	450(25)	435(10)
C_3F_6	1.17(0.02)	430(35)	375(25)
	0.81(0.03)	510(15)	460(15)
	0.77(0.03)	550(20)	475(35)
HFPO	0.96(0.04)	400(20)	385(30)
	0.69(0.06)	480(30)	415(15)
	0.93(0.10)	475(15)	435(25)

[a] $S(CF_2)$ data were previously reported.[41]

Generally, T_R(CF) values are independent of P and plasma precursor, remaining approximately equal to room temperature regardless of system parameters. At p = 50 mTorr, T_V(CF) values ranged from ~2000 K – 3300 K, whereas at p = 100 mTorr, those values ranged from ~2000 – 2500 K. At both pressures, T_V(CF) values from HFPO plasmas demonstrate a direct dependence on P, whereas the remaining C_xF_y precursors exhibit little to no P dependence. $S(CF_2)$ and ground state $T_R(CF_2)$ at p = 50 and 100 mTorr are reported in Table 4.4. Notably, $S(CF_2)$ and $T_R(CF_2)$ values are generally higher than S(CF) and T_R(CF) under the same experimental conditions. $T_R(CF_2)$ for C_xF_y plasmas indicate a slight, direct relationship with P, whereas a decrease in T_R is noted as pressure is increased.

In addition to characterizing the energetics of rotational and vibrational degrees of freedom, we have determined T_e for fluorinated ICPs at p = 50 mTorr, P = 50 -175 W. Mean T_e values and standard deviations are listed in Table 4.5 for CF_4, C_2F_6, C_3F_8, C_3F_6, HFPO and SiF_4 plasmas. The values in Table 4.5 indicate that T_e neither differs appreciably among the C_xF_y plasma systems, nor appears to depend strongly on P over the range studied here. Notably, T_e values calculated from HFPO are elevated in comparison to the other plasma systems.

As noted in Section 4.1, we are fundamentally interested in the effects, if any, of internal energy on surface interactions of plasma radicals during surface modification. Thus, although some scatter coefficients have been reported previously for SiF, CF, and CF_2,[15,41] we have performed additional IRIS experiments on these species and provide these data here. LIF images and IRIS cross-sections are shown in Figure 4.3 for CF radicals in a C_2F_6 plasma molecular beam. An image containing only fluorescence from CF radicals in the molecular beam ("beam only", Figure 4.3b), is subtracted from the image in Figure. 4.3a, which corresponds to the fluorescence of CF in the beam and CF scattered from a Si substrate (beam + scatter).

Table 4.5. T_e (eV) calculated from Ar emission lines[a,b]

***P* (W)**	**CF_4**	**C_2F_6**	**C_3F_6**	**C_3F_8**	**HFPO**	**SiF_4**
50	1.82(0.02)	1.92(0.02)	1.96(0.03)	1.80(0.01)	2.32(0.03)	--
75	1.86(0.02)	1.82(0.02)	2.01(0.03)	1.87(0.02)	2.35(0.03)	1.91(0.02)
100	1.85(0.02)	1.87(0.02)	2.06(0.03)	1.98(0.02)	2.37(0.03)	1.82(0.02)
125	1.92(0.03)	1.92(0.02)	2.10(0.03)	2.02(0.02)	2.43(0.03)	1.93(0.02)
150	2.03(0.03)	1.96(0.02)	2.11(0.03)	2.00(0.02)	2.49(0.04)	1.89(0.02)
175	2.12(0.04)	2.10(0.03)	--	1.97(0.02)	2.51(0.04)	1.88(0.02)

[a]p = 50 mTorr.
[b]Values in parentheses represent standard error calculated from the mean of three trials.

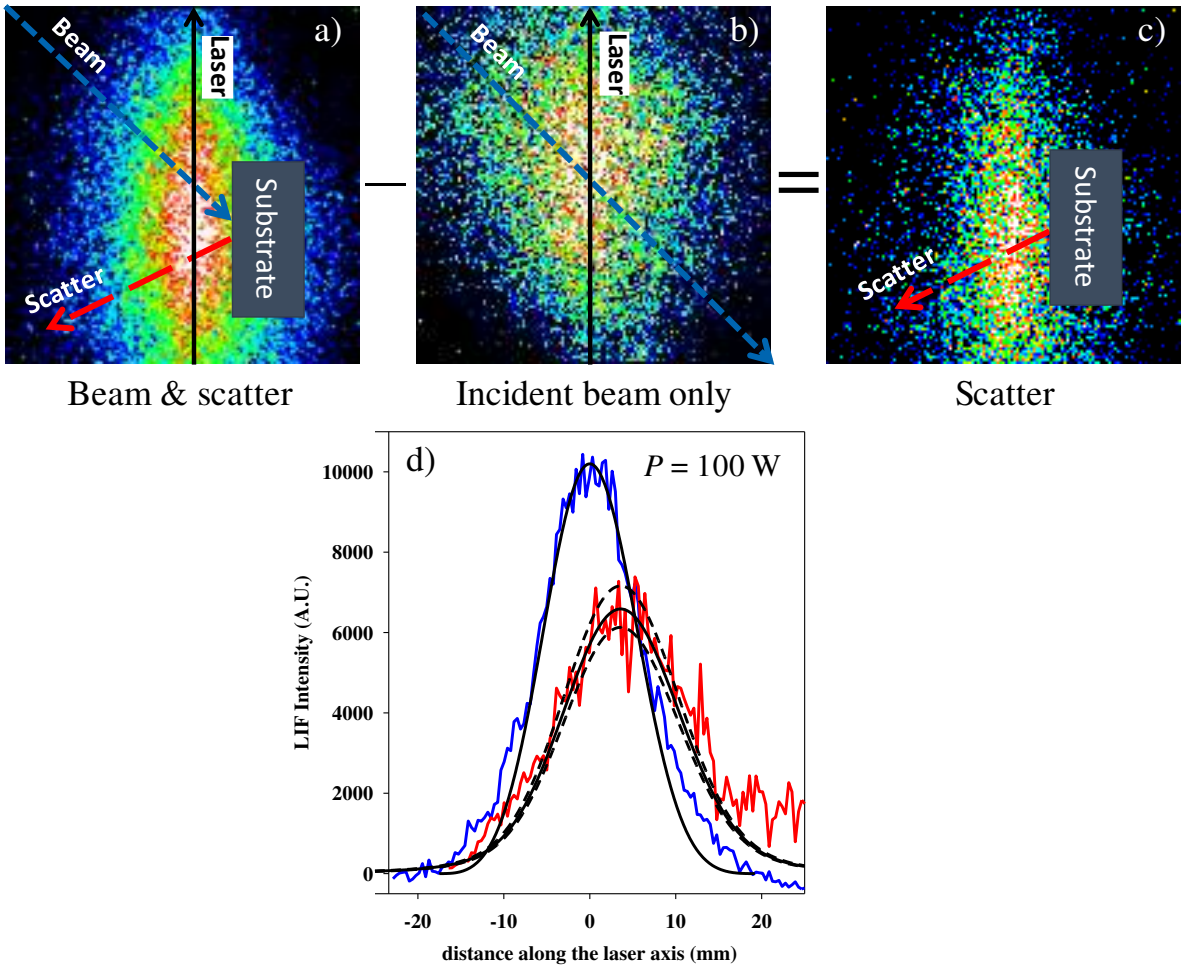

Figure 4.3. (a-c) IRIS images for CF species in a C_2F_6 plasma with P = 100 W. The solid white arrow indicates propagation of the plasma molecular beam, whereas the dashed arrow represents CF molecules scattering from the Si substrate. Image (a) corresponds to fluorescence signal collected from both CF in the plasma beam and CF scattered from the substrate (i.e. Si wafer) rotated into the path of the molecular beam. Image (b) represents CF signal arising only from the plasma molecular beam (i.e. no substrate), where laser propagation is denoted by the thin dotted arrow. Image subtraction yields (c) an image that contains only signal for scattered CF molecules. Cross-sections for CF LIF signals in the plasma molecular beam and CF scattered from a Si substrate are shown in (d) for P = 100 W. The simulated fits to the data correspond to S(CF) = 1.04. Data were collected by Dr. M.F. Cuddy.

This produces a spot corresponding to CF scatter only, Figure 4.3c. Cross-sections along the laser propagation axis are compared to simulated data to determine S values, where S(CF) = 1.04 for this specific data set (C_2F_6 plasma with p = 50 mTorr, P = 100 W). Similar data were collected, and calculations performed to determine S(CF), S(CF_2), and S(SiF). Although S(SiF) values within SiF_4 plasmas have been characterized previously, we have yet to determine vibrational and rotational temperatures of these radicals and relate system energetics to scatter properties. A comparison of SiF characteristic temperatures (T_T, T_R, and T_V) is provided in Figure 4.4a as a function of power. sVibrational temperatures are consistently approximately three times greater than the translational temperatures at all P, illustrated by nearly parallel linear fits to each data set where the slope m = 2.6 ± 0.6, 2.9 ± 0.2, and 2.0 ± 0.4 for T_T, T_R, and T_V respectively. Similar to the characteristic temperatures in Figure 4.4a, scatter coefficients for SiF, Figure 4.4b, increase with increasing power.

OES spectra with dilute additions of Ar were acquired for C_xF_y plasmas in which both CF* emission from the $B^2\Delta - X^2\Pi$ (201 – 204 nm) and CF_2* emission from the $A^1B_1 - X^1A_1$ transition (240 – 260 nm) are evident. The CF_2 emission line at 251.9 nm and CF emission line at 202.4 nm were used for actinometric analysis, as well as the $3s\ ^2P_2 - 3p\ ^2P_2$ line at 703.7 nm for F. Figure 4.5 shows actinometric excited state CF and CF_2 data as a function of P and precursor. In general, CF_4 plasmas produce the most CF at all P, whereas the highest concentrations of CF_2 are generated in the C_2F_6 plasmas. The amount of CF produced also generally decreases with the size of the FC precursor. In CF_4 plasmas, [CF_2] remain relatively constant with increasing P, whereas [CF] increases slightly from 50 W – 175 W.

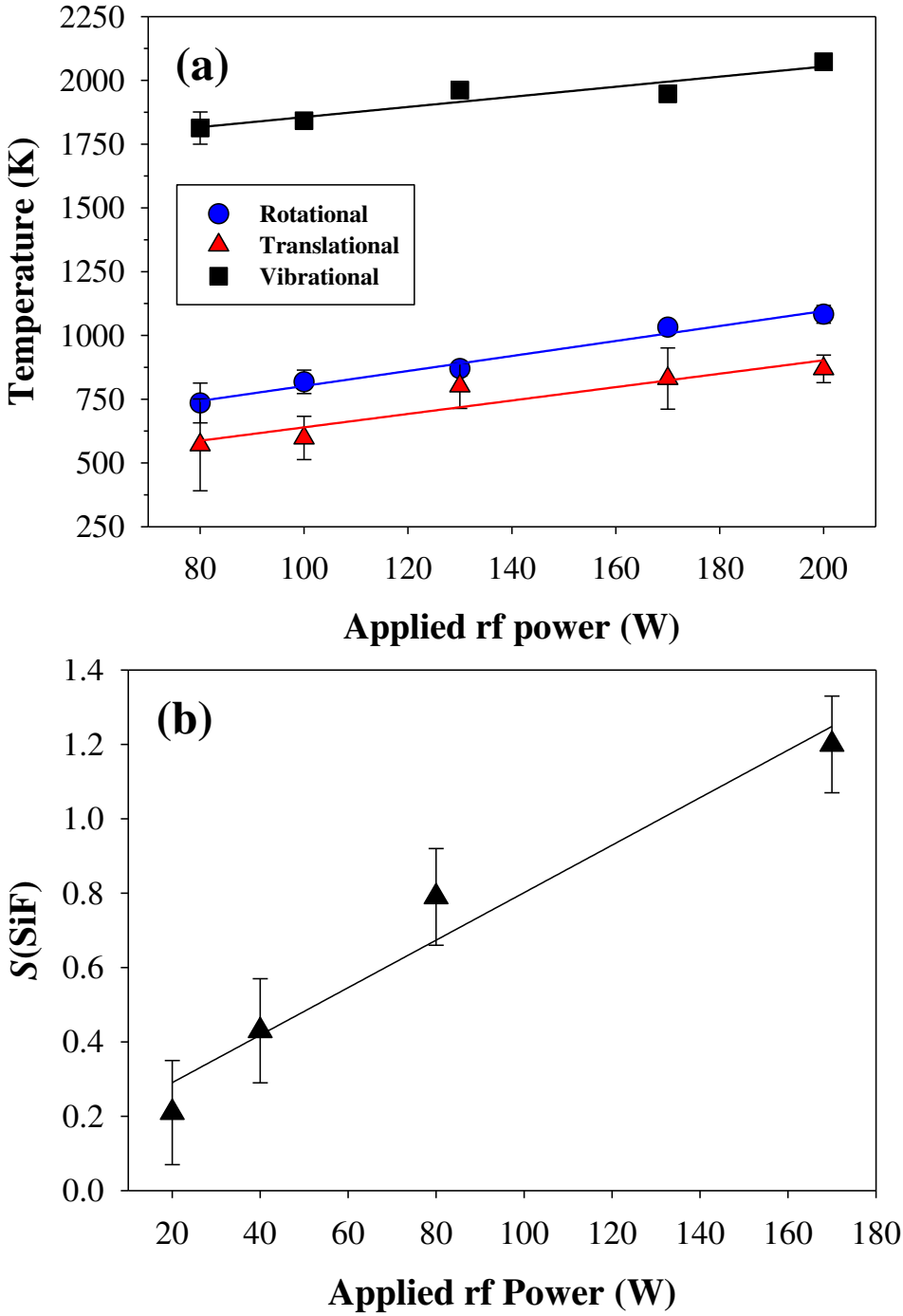

Figure 4.4. (a) T_T (red), T_R(blue), and T_V (black) are plotted as a function of P for SiF species in a 100% SiF_4 plasma at p = 100 mTorr. (b) Scatter coefficients for SiF interacting with Si substrates plotted as a function of P. The linear regression fit to these data yields a slope m = 0.0064 ± 0.0009 with R^2 = 0.96.

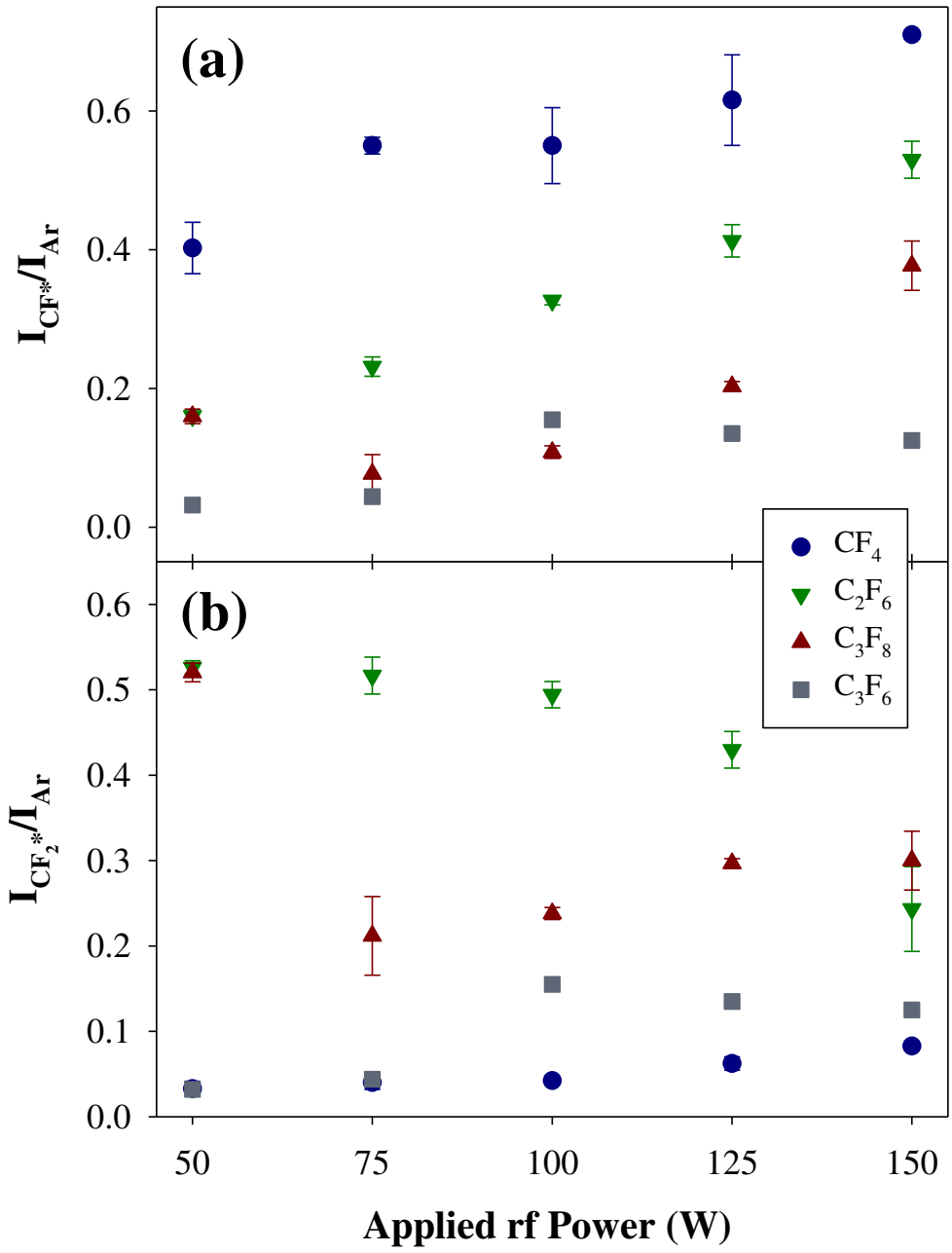

Figure 4.5. Actinometric OES for (a) CF* and (b) CF_2* in C_xF_y plasmas at p = 50 mTorr as a function of P.

In contrast, in the C_2F_6 plasma, relative concentrations of CF* increase with increasing *P*, and CF_2* concentrations monotonically decrease over the same *P* range. The CF* and CF_2* concentrations in the C_3F_8 plasma system exhibit similar trends with *P*, namely a high concentration at 50 W, a sharp decrease at 75 W, then a steady increase with increasing *P*. Within C_3F_6 plasmas, CF* and CF_2* concentrations show similar dependence on *P*, with slightly higher concentrations at higher *P*. Species' densities formed in HFPO plasmas as a function of *P*, Figure 4.6, reveals F* and O* densities remain relatively independent of *P*, whereas CF* increases dramatically with *P*. Notably, CF_2* concentrations increase from 50 W – 125 W, then decrease with increasing *P*.

Figure 4.7 depicts T_V for excited CF radicals in a variety of C_xF_y plasmas (*P* = 150 W, *p* = 50 and 100 mTorr). Regardless of plasma precursor, T_V decreases with an increase in *p* and is relatively independent of *P* at both pressures, although some variations are seen. The relationship between scatter coefficients and T_V(CF)is shown directly in Figure 4.8a, where *S*(CF) is plotted as a function of T_V(CF $B^2\Delta$) for radicals formed in five different FC plasmas. Each data point represents a discrete set of plasma conditions. The linear fit provided for the collective data in C_xF_y plasmas indicates that CF($^2\Pi$) scatter directly correlates to the vibrational temperature of excited state species. The relationship between T_V and *P* for C_xF_y and HFPO precursors is shown in Figure 4.8b; where a decrease in T_V occurs as the F/C ratio of the precursor decreases from 4 to 2.

As a final note, we acknowledge that an essential aspect to understanding the overall plasma chemistry of these systems is the role of neutral species. Using a deuterium-halogen light source, we sought to determine the energetics of ground state CF radicals via BAS.

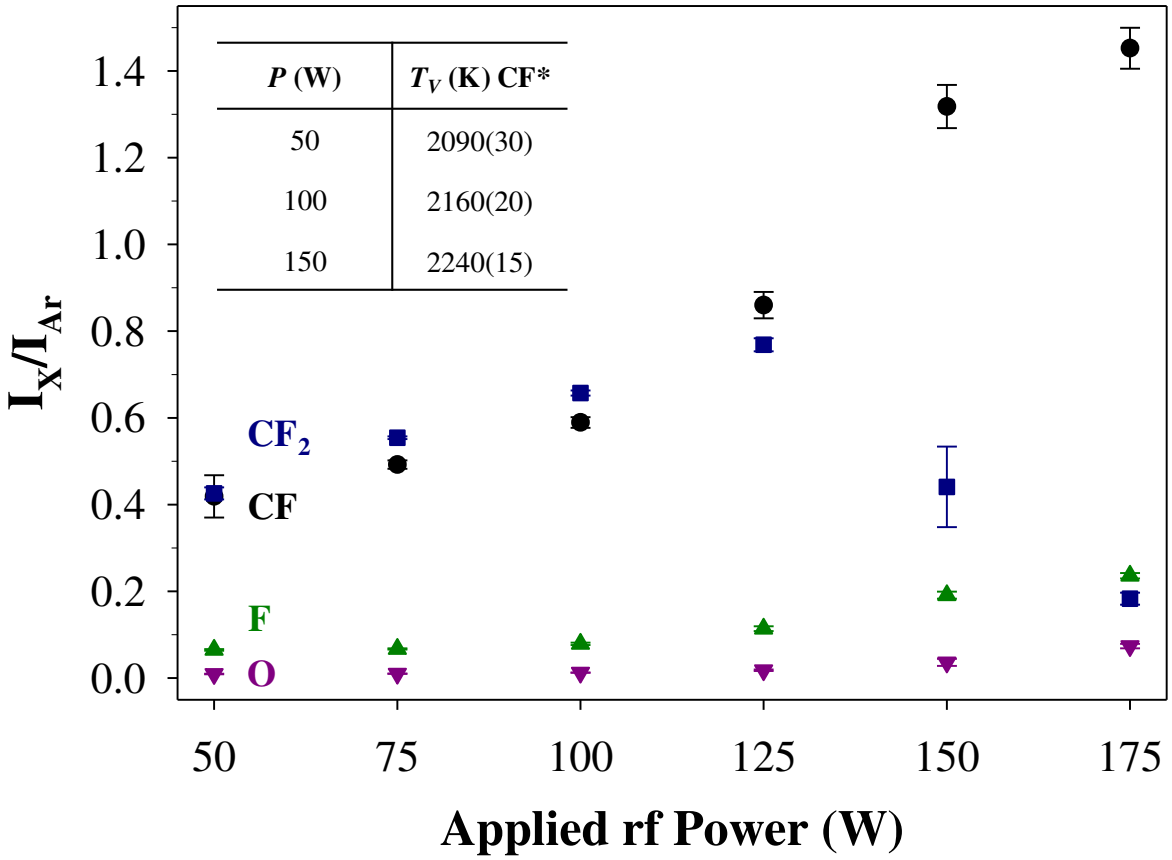

Figure 4.6. Actinometric OES for excited species formed in HFPO plasmas at p = 50 mTorr (with ~5% Ar dilution) as a function of P. The inset table shows the relationship between T_V(CF) and P in HFPO systems with no Ar added.

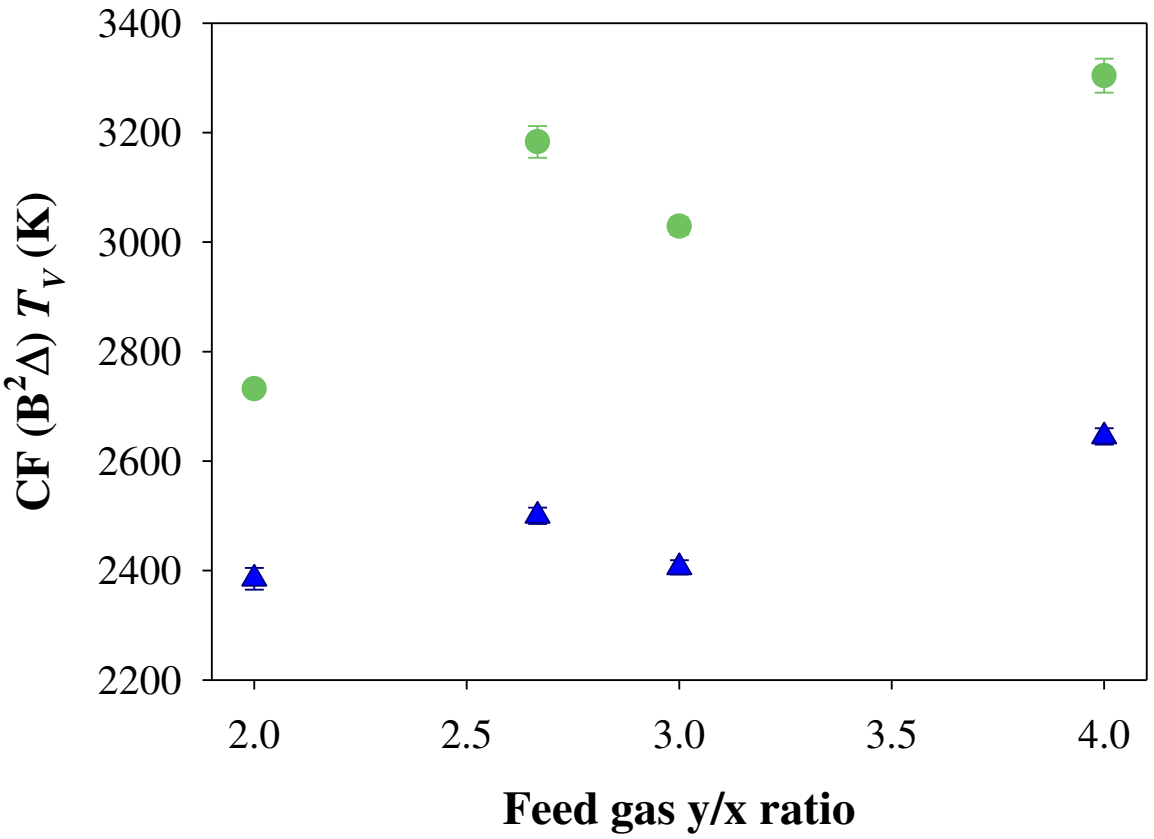

Figure 4.7. Vibrational temperature for CF in various C_xF_y plasmas, at P = 150 W, p = 50 mTorr (green circles) and p = 100 mTorr (blue triangles). Error bars represent ±1 standard deviation from the mean (n = 3).

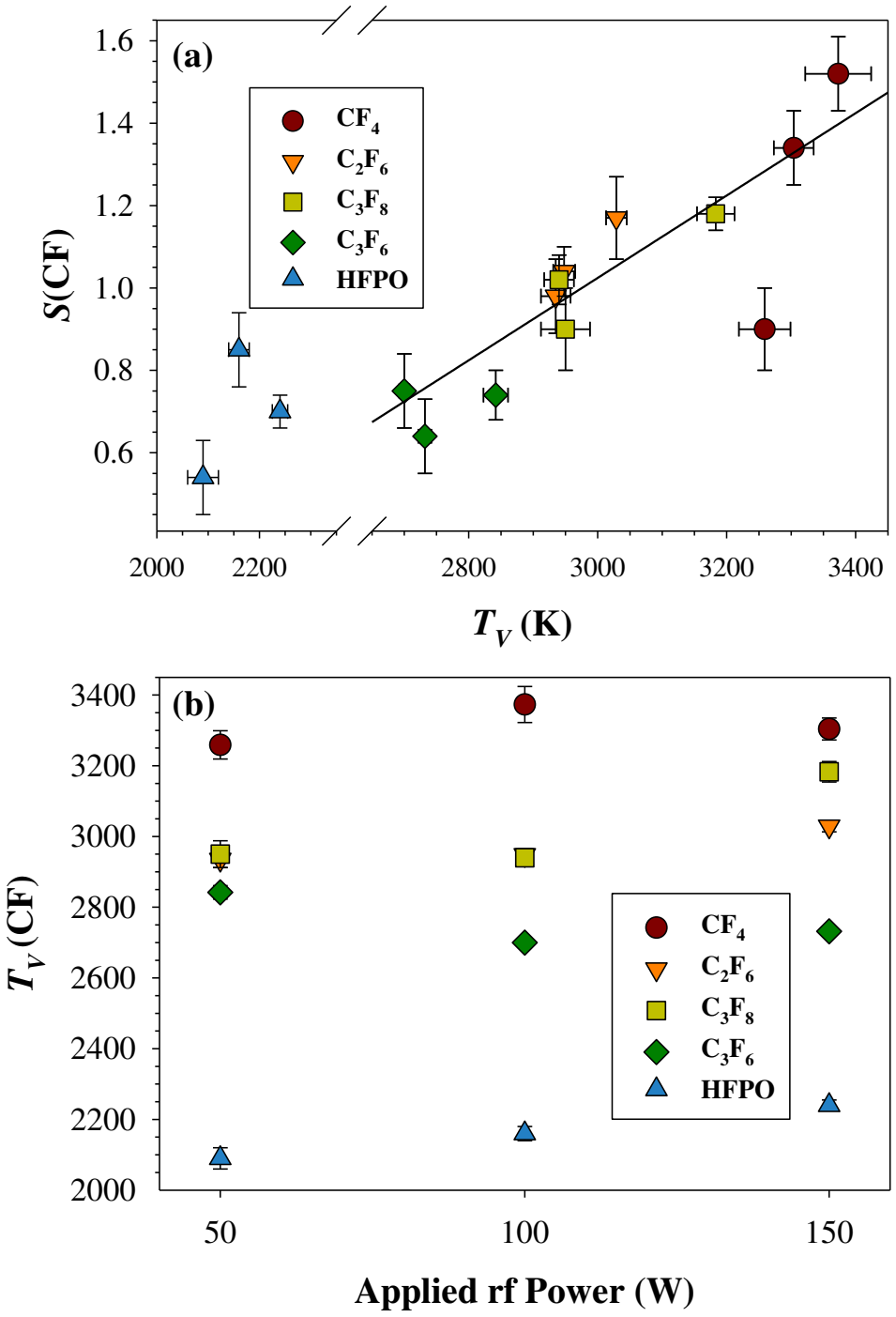

Figure 4.8. T_V (K) for CF species in CF_4, C_2F_6, C_3F_8, C_3F_6, and HFPO plasmas as a function of (a) S(CF) and (b) P. The linear regression fit to the data for the C_xF_y precursors (i.e. excluding HFPO) shown in (a) yields a slope $m = 0.0010 \pm 0.0002$ with $R^2 > 0.71$.

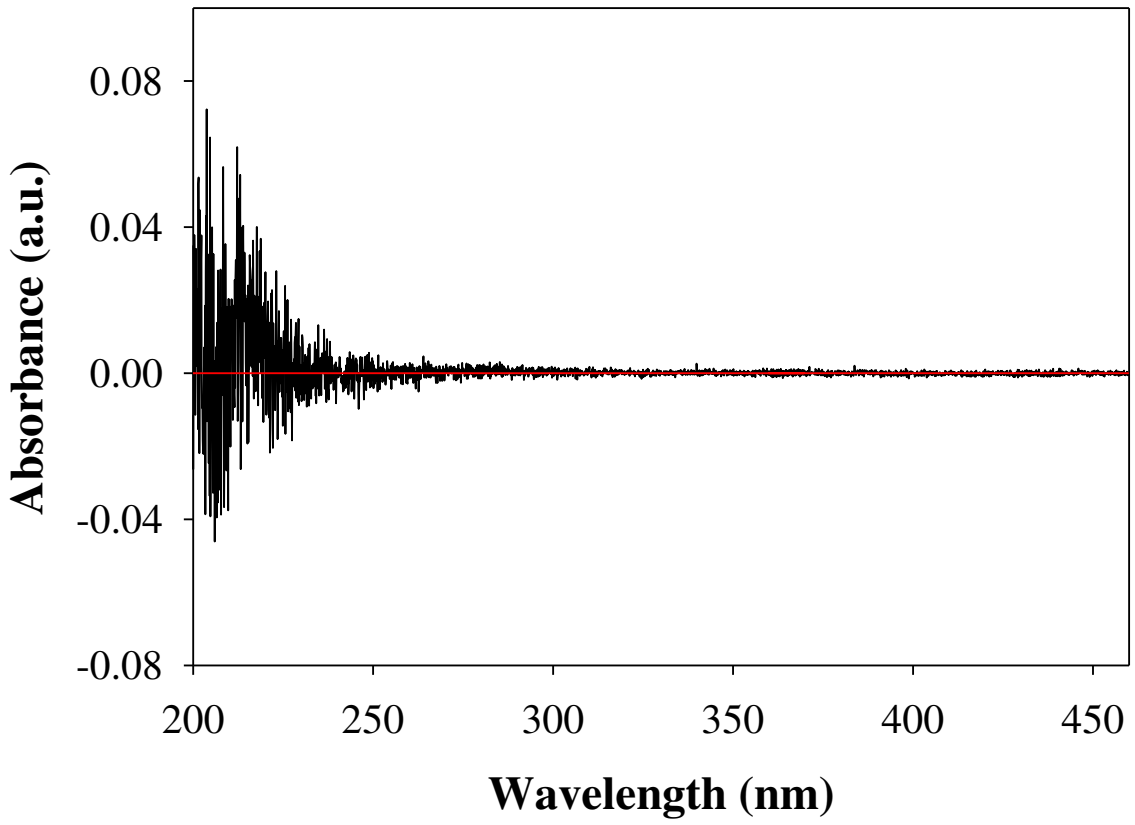

Figure 4.9. Experimental absorbance spectrum obtained of plasma reactor under vacuum (sans gas).

Figure 4.9 depicts the absorbance within the glass tubular plasma reactor under vacuum, with no gas present. A theoretical, perfect response is plotted in Figure 4.9 with a red trace; the experimental data, however, displays a significant increase in shot noise at wavelengths below 240 nm. Luque et. al. showed CF ($A^2\Sigma^+$ — $X^2\Pi$) absorbance measured at 204 – 235 nm, and CF ($B^2\Delta$ — $X^2\Pi$) absorbance peaks arising at ~198 nm and 202 – 204 nm.[34] As a result of the intensity of the measured shot noise between 200 – 235 nm, as well as the Avantes COL-UV/VIS-25 lenses only extending to 200 nm, we were unable to detect CF ($X^2\Pi$) radicals with our current experiment design. To probe transitions at lower wavelengths with minimized signal-to-noise ratios, alternative light sources (i.e. UV-enhanced Xe lamps) can be utilized for absorption experiments. In addition to using a different excitation source, plasma precursors that minimize the interference from CF_2 absorbance will be considered, such as combinations of argon and octofluorocyclobutane, as well as difluoromethane, to maximize CF signal.[34] In contrast, we have successfully determined the absorbance of NO ($X^2\Pi$) molecules through BAS using the same deuterium halogen light source (see Figure 4.11). This is likely because the relative intensity of NO is significantly higher than that of the CF radicals; thus, NO peaks (v'=0, v'=1) are observable above the signal-to-noise ratio.[42] Absorbance spectra for CF_2 ($\widetilde{A}^1B_1$ — $\widetilde{X}^1B_1$) were measured using our current BAS system (Figure 4.2). Figure 4.10 depicts $T_R(CF_2)$ values as a function of P and plasma precursor. Notably, $T_R(CF_2)$ values are approximately 100 – 200 K higher than T_R(CF). Also, T_R values at a given P are within error for precursors with larger y/x ratios. T_R increases linearly with P for all precursors, with the data for C_3F_6 and C_3F_8 plasmas exhibiting nearly perfect linearity, yielding R^2 values of 0.96 and 0.93, respectively, when a linear regression analyses were performed.

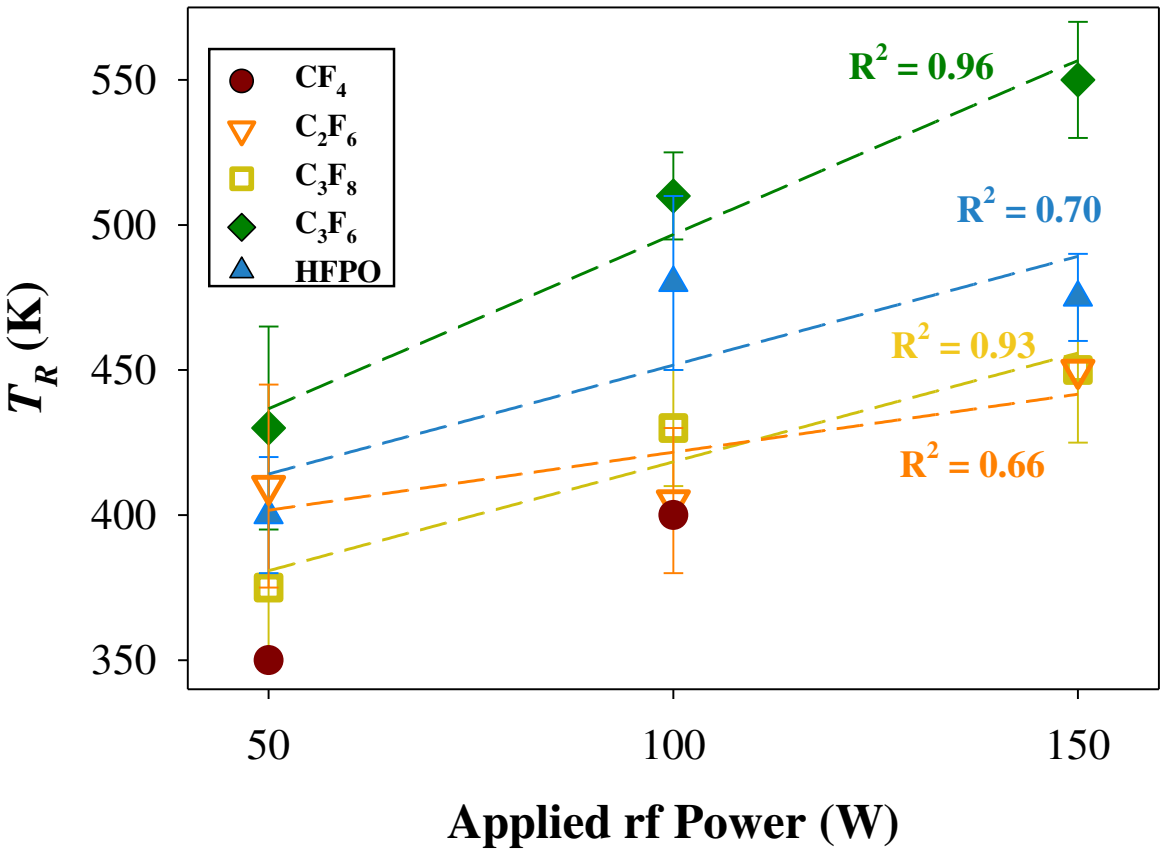

Figure 4.10. T_R for ground state CF_2 species in CF_4, C_2F_6, C_3F_8, C_3F_6, and HFPO plasmas at p = 50 mTorr as a function of P. R^2 values (all > 0.66) corresponding to linear regression fits for each precursor are reported.

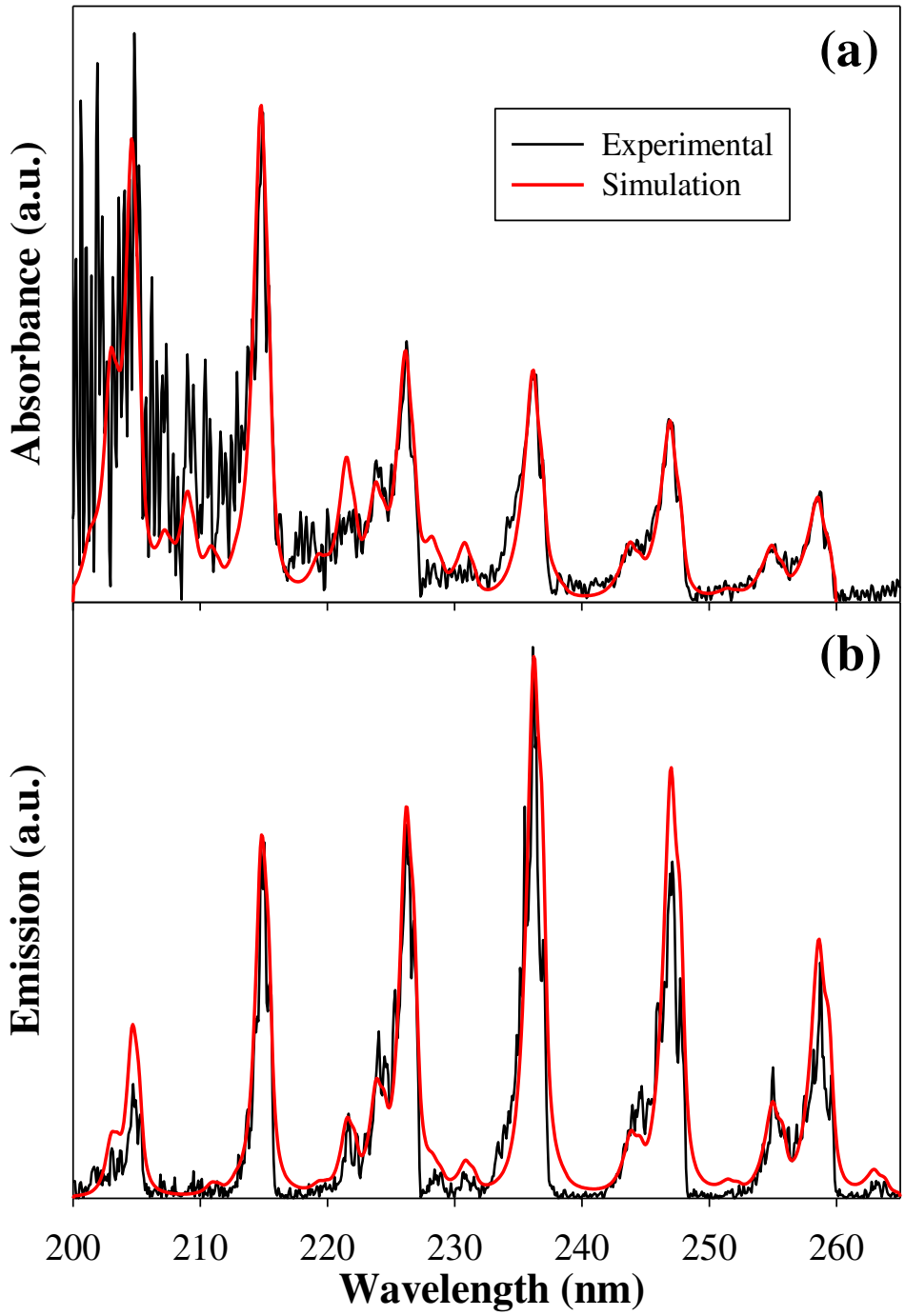

Figure 4.11. Experimental spectra and simulated fits of (a) NO absorbance and (b) emission from an NO plasma at p = 150 mTorr and P = 150 W. Peak correlations were >90%. As described above, noise from the deuterium-halogen lamp is present at lower wavelengths, however, the intensities of the ground (v=0) and first vibrational state (v=1) in the NO $X^2\Pi$ band is distinguishable above the noise.

4.3 Discussion

As noted in Section 4.1, the compilation of data on energy partitioning and surface interactions for plasma species is important to a molecular-level understanding of plasma chemistry. The goal with this work was to compare energy partitioning and surface scattering coefficients for two isoelectronic diatomic molecules, SiF and CF, as well as for the triatomic molecule CF_2 in a range of ICPs. Here, we report new data for T_V(SiF), T_R(SiF), T_V(CF), T_R(CF), T_R(CF_2), and surface scattering coefficients, S, for CF and CF_2 within HFPO plasmas. We have combined these new data with previously reported data for S(SiF) and T_T(SiF),[13,15,16] S(CF), and S(CF_2).[41] All of these data are provided in Tables 4.1 – 4.4.

Focusing first on the energy partitioning between T_T, T_V, and T_R for each diatomic gas-phase molecule, Tables 4.1 – 4.3, some interesting trends emerge. Notably, T_V values for all three molecules are significantly higher than T_R or T_T, regardless of experimental parameters. In general, T_R for CF radicals is approximately room temperature, independent of P and precursor. Rotational relaxation is a relatively fast process, typically requiring <10 collisions to reach equilibrium;[43] we estimate that a given diatomic molecule in our plasma reactor experiences >100 collisions per second. The T_R(SiF) values were ~400 K higher than room temperature and demonstrated a stronger dependence on P, indicating the plasma gas temperature is significantly higher for SiF_4 systems than in fluorocarbon systems studied herein.[42,44] Prior Fisher Group work used LIF spectra acquired in IRIS experiments to determine T_R for SiF and SiF_2. This work compared surface reactivities for different rotational transitions over a range of differing substrate temperatures, finding T_R(SiF) = ~450 ± 50 K in SiF_4 plasmas with p = 100 mTorr, P = 40, 80, and170 W (using the wavelength range 436.8 – 437.2 nm).[15] Our current approach, using OES, allows coaxial collection over the entire vibrational band of the SiF radical (427.5 – 465.0

nm), thereby offering, through our determined T_V and T_R values, a more representative image of the energetics of the SiF first excited state. Furthermore, examining the larger wavelength range enables us to probe higher level rotational states, potentially explaining the increased rotational temperatures reported herein.

Translational temperatures for plasma species are determined from velocity measurements obtained from incrementally increasing the gate delay on the IRIS ICCD camera as described previously.[12,13] These measurements necessitate a sufficiently long radiative lifetime (τ_r) for accurate determination of T_T. Of the three molecules studied here, SiF (τ_r = ~230 ns)[45] is the only one for which T_T can be determined accurately, although we have completed preliminary work in the determination of T_T for CF_2 molecules.[44] Translational, rotational, and vibrational temperatures for SiF molecules as a function of P are shown in Figure 4.4. Best-fit regression lines for each set of data are essentially parallel to each other, indicating each characteristic temperature has a similar dependence on P. Although these related rates of temperature rise with increasing P are notable, another clear observation is that the translational temperatures are in all cases less than half the measured T_V(SiF) values, whereas T_R and T_T differ by <125 K when considering error reported with each value. This likely indicates that the V-T energy transfer mechanism is the predominant pathway for vibrational relaxation of SiF^*, while rotationally excited SiF molecules are simultaneously present in this discharge. Specifically, the translational energies of SiF may be increased through collisions with SiF^*, transferring vibrational energy from the electronically excited molecule to the ground state radical. Alternatively, interactions of SiF^* with other gaseous species (M) may lead to loss of vibrational energy to M and electronic quenching of SiF^* as in Reaction 4.1. We hypothesize that a similar relaxation pathway exists for the diatomic oscillator CF.

$$SiF^* + M \rightarrow SiF + M^* \qquad (4.1)$$

The relationship between T_V and plasma parameters such as applied rf power and system pressure can also be explored further for each molecule. T_V(SiF) increases from 1813 K to 2073 K as P is increased from 80 - 200 W, Table 4.1. Likewise, T_V(CF) in HFPO plasmas generally increases with P, Tables 4.3 and 4.4, although the increase is not as pronounced as with SiF and for molecules in other systems examined by our laboratory.[42] Moreover, energy partitioning in SiF and CF appears to favor vibrational channels, as T_V values are much greater than T_T or T_R and they tend to increase with increased P. Interestingly, in the FC plasmas, T_V decreases with increasing p, Tables 4.2 and 4.3, but remain nearly an order of magnitude higher than T_R. At higher system pressures, the number of collisions between molecules in the discharge also increase, promoting further fragmentation of the parent gas and collisional quenching. As noted above, T_R(CF) is roughly around room temperature, indicating efficient collisional cooling of this degree of freedom. Clearly, the additional collisions CF molecules under go in higher p plasmas affords some measure of cooling of vibrational temperatures, but this is not a very efficient channel for energy transfer. Given this relationship between T_V and pressure, as well as the observed relationship between T_V and scatter, we can predict collisional cooling effects at increased p will also affect a molecule's ability to scatter at a surface.

One additional piece of information that helps characterize energy partitioning among vibrational modes in plasmas is the role of electrons. Electron temperatures were estimated for selected plasma systems from analyses of OES spectral lines, a process that has been widely used for a range of plasma systems.[26,46] This calculation assumes (1) all ionization and excitation events proceed via electron impact and (2) that there exists a Maxwellian distribution of electron energies. Assumption (1) is valid for dilute Ar in a low pressure plasma; however, assumption

(2) can be jeopardized because of the Druyvestyn distribution of electron energies common in plasma systems.[47] Nonetheless, for sufficiently low electron temperatures, the deviation of Druyvestyn distributions from Maxwell distributions is small and there is little discrepancy in the measured T_e. As discussed in the Results section, the values in Table 4.5 indicate that T_e does not differ appreciably among the plasma systems, nor does T_e appear to depend strongly on P over the range studied here. Indeed, comparison to the literature suggests that the values measured for the FC plasmas discussed herein are comparable to those measured using an *in situ* Langmuir probe in similar systems.[48] These observations suggest that T_e does not have a strong influence on T_V. One reason for this is that T_V values measured from OES data depend upon excited vibrational state densities, n_v, and the vibrational excitation rate constant k_v, via the following equation:[49]

$$n_v = n_e n_g k_v \qquad (4.2)$$

where n_e denotes the electron density in the plasma and n_g the ground vibrational state density. The rate constant k_v is, in turn, highly dependent upon T_e.[50] Because T_e does not change appreciably among systems or with changing P (ΔT_e <~10% for P = 50 - 150 W), the increases in T_V for a given molecule with increasing P are predominantly a consequence of increased electron density and not electron temperature. This notion is bolstered by the results of Kim *et al.*, who demonstrated that although n_e correlates directly with P in CF_4 inductively coupled plasmas, T_e remains independent of rf power.[51] Furthermore, Ono and Teii showed that N_2 vibrational temperatures increase with increasing n_e in $CO_2/N_2/He$ discharges.[52] We can thus infer that increases in T_V are proportional to increases in n_e in each case discussed here, thereby providing a metric for monitoring n_e *ex situ*, independent of a Langmuir probe.

Another aspect of this work measures surface scattering coefficients for radicals during plasma processing using the IRIS technique. As this technique is used to probe steady-state processes occurring at the plasma-surface interface, it measures the interface behavior of species interacting with a substrate or film deposited on a substrate. The plasmas chosen for this study each have different effects on surfaces. Specifically, SiF_4 plasmas tend to fluorinate Si surfaces whereas FC plasmas tend to deposit robust films. We have also examined oxidative systems, such as NO, which can create oxide layers on the surface of Si materials.[42] These net effects of plasma processing on surfaces have been verified through high-resolution XPS analyses.[16,41] Thus, the measured surface scatter coefficients must be interpreted in light of the overall impact of substrate processing in our ICPs. This multi-pronged approach of characterizing a variety of gas-surface interfaces enables us to consider more holistic elucidation of energy partitioning trends and how the gaseous plasma chemistry modifies the surface of a particular substrate (e.g. *p* type Si wafers).

SiF scatter coefficients measured in SiF_4/Si systems vary directly with P, having a linear fit of slope 0.0064 ± 0.0009, Figure 4.4b, and these changes in S(SiF) are commensurate with similar trends in both T_T(SiF) and T_V(SiF) values, Figure 4.4a. It should be noted, however, that other plasma species, such as ions, can contribute to increasing S values. In other ICP systems, energetic ions contribute significantly to surface production of radicals.[22,25,53] For example, surface production of both SiF_2 in SiF_4 and CF_2 in FC systems is enhanced by high ion densities in these plasmas.[14,15,54] The effect of ion contributions to the IRIS measured scatter coefficients was examined for SiF in SiF_4 plasmas at $P = 175$ W by employing a grounded mesh in the path of the plasma molecular beam.[15,16] In an essentially ion-free environment, the S(SiF) value decreased only slightly. This small change upon removal of ions relative to the strong

correlation between T_V(SiF) and S(SiF) indicates that ions do not play as significant a role in the surface production of SiF as does its vibrational temperature. Ion contributions to S(SiF) may be limited because of the tendency for the moiety to remain "buried" in the fluorinated silicon substrate. Oehrlein and coworkers showed through reactive ion etching experiments that SiF species dominate the deepest regions of a fluorosilane film, whereas the topmost layers of the film are SiF_3-rich.[55] Thus, if reactive ion penetration depth is smaller than the thickness of a given steady-state fluorosilane film at a substrate, SiF_x species (x = 2, 3) are more likely than SiF to desorb. Furthermore, formative work by Winters and Coburn reported F atom etch mechanisms, cleaving the Si-Si bond to form SiF_2 and SiF_4, which then desorb from the surface.[56] Ultimately then, the increasing scatter values measured here may have a strong dependence on the increasing translational energies of ground state SiF and/or the vibrational energy of electronically excited SiF^*. This relationship is further addressed below.

Scatter coefficients for CF radicals interacting with room temperature Si substrates have similar source gas and P dependences as T_V(CF), Tables 4.2 and 4.3. Specifically, S(CF) values decrease with decreasing F/C ratio for the precursor gas. We have previously reported on the relationship between choice of feed gas and the CF scatter coefficient,[41] and note that these measurements are heavily influenced by ion bombardment of the surface.[14,53] Nonetheless, vibrational temperatures for excited state CF radicals appear to correlate strongly with observed S(CF) values and F/C ratios. The most profound example of the apparent relationship between vibrational temperature on scatter coefficients for the three radicals studied here is provided in Figure 4.8a, where S(CF) values are plotted as a function of T_V(CF) for a range of FC precursors. As the vibrational temperature of excited state ($^2\Delta$) CF radicals increases, the observed scatter coefficient of the ground state species ($^2\Pi$) concomitantly grows, Figure 4.8a. Because S(CF)

values essentially measure a change in CF($^2\Pi$) density between scattered species and the gas-phase of the plasma molecular beam, this relationship implies that vibrationally hot CF in excited electronic states contribute significantly to the observed scatter of ground state species. We believe that this phenomenon can be rationalized in several ways. For example, the $^2\Delta$ CF radicals in the IRIS molecular beam (undetectable in the LIF scheme) may quench at the surface of the substrate and desorb as a ground state CF, yielding a high scatter value. Energy from this process may be dissipated into the surrounding FC film or passivation layer being deposited on the substrate. It is possible that enough excess energy may cause dislodging of additional $CF_{(s)}$ units by effectively heating the surface film, further enhancing the S(CF) value. Small increases in temperature also increase the diffusivity of F atoms through FC polymers,[57] rendering a significant portion of the exposed FC surface CF-rich. This CF experiences the full brunt of plasma species and as such is facilely removed, resulting in high observed scatter coefficients. In this way, highly vibrationally excited CF may act indirectly as an etchant to ablate FC material. Indeed, Tsai and coworkers[58] speculated on this phenomenon to explain resonant energy transfer of vibrationally hot molecules with growing surface Si-H bonds during silane depositions. This rationalization of the relationship between T_V(CF) and S(CF) may be extended to the other radicals as well. The F/C ratio in the precursor also has an impact on both the observed scatter and T_V(CF). As the F/C ratio decreases, concomitant decreases in T_V and S(CF) are also measured. Probing this for the CF radical, we expanded our line of inquiry to include scatter and temperature properties of CF_2 formed in these discharges.

As documented with CF, the choice of precursor also influences the propensity for CF_2 scatter: $S(CF_2)$ increases with increased feed gas y/x ratio. Scatter coefficients represent the probability for surface scatter of an individual species, therefor an increase in $S(CF_2)$ denotes a

decreased inclination for reactivity of a surface. Although the relationship between precursor and scatter between CF_x (x = 1 or 2) species is similar and has been previously published,[41] the relationship between gas-phase energetics of CF_2 molecules and the propensity for scatter needs elucidated. $T_R(CF_2)$ values suggest that CF_2 molecules produced in these discharges are only partially relaxed by collisions. An increase in P promotes the dissociation of the parent gas and these partially relaxed CF_2 molecules can participate in further fragmentation. Furthermore, the difficulty of determining absorbance of CF_2 at 150 W with high y/x feed gas ratios (i.e. 4 and 3), as well as at increased pressure (100 mTorr, CF_4) suggests CF_2 ground state molecules are additionally fragmented as more energetic collisions are occurring within the discharge. This non-thermalization of CF_2 rotational states can be used to hypothesize the increase in scatter for CF_2; as these molecules undergo energetic collisions and bombardment, they are more likely to scatter from a given substrate and continue to promote fragmentation and formation of CF within the discharge. Determination of $T_V(CF_2)$ values within the ground and excited state is necessary to elucidate the mechanisms occurring at the gas-surface interface, which will be the subject of a further publication.

In general, surface scatter coefficients for the radicals investigated here track with changes in their vibrational temperatures. We observe essentially no dependence of S(M), (M = CF and SiF) on T_R, leading us to infer that scatter coefficients are at least partially reliant upon the internal vibrational modes associated with the radical. In IRIS experiments, for a molecule formed in the plasma source to scatter from the substrate, it must have energy sufficient to overcome the potential barrier for desorption. Our data suggest that energy in vibrational modes preferentially provides a radical with the means to desorb over molecules with energy contributions from translational and rotational modes. For each molecule, we observe that the

greater the vibrational energy associated with the molecule, the higher the propensity for scatter from a surface. This suggests that vibrationally excited molecules interact with the substrate and rebound with some energy loss, as in Reaction 4.3 where M denotes CF or SiF,

$$M_{(g)}(v') \rightarrow M_{(ads)}(v') \rightarrow M_{(g)}(v^{"}) \qquad (4.3)$$

Reaction 4.3 also implies that contributions from quenching of higher excited states not probed in the IRIS experiment could affect increases in scatter coefficients. Kim and coworkers showed that increases in n_e (and, as such, increased T_V as discussed above) result in greater number densities of excited electronic populations.[59] Thus, molecule M in a given IRIS experiment, existing in an excited electronic state with correspondingly high T_V in the plasma molecular beam, could quench upon contact with the substrate and subsequently desorb in a ground electronic state. This scenario would result in molecule M being LIF-transparent in the molecular beam of the plasma, but producing LIF signal as a scattered molecule, resulting in an apparently higher S(M) value, as discussed in the case of CF radicals above. Note that preliminary results for CF interactions with ZrO_2 substrate are similar to the S(CF) values reported here for interactions with Si substrates.[44] Ultimately, then, the relationship between internal temperatures and scatter coefficients for these molecules could provide the capability to predict surface reactivity of plasma species. It should be noted, however, that although the contribution of vibrationally hot molecules to surface reactivity is significant, it certainly does not represent a complete embodiment of surface reactions. Other processes, including ion bombardment and/or neutralization, vibrational relaxation, particle flux, recombination reactions, and photodetachment all occur simultaneously at surfaces in these systems. Nonetheless, a clear relationship emerges linking vibrational energies to surface scatter coefficients for three distinct

systems. Thus, even if internal energy contributions to surface reactivity are not exclusively causative, they are most certainly correlated to plasma-surface interactions.

A remaining question focuses on the generality of the relationship between vibrational temperature and scatter observed here for CF and SiF. We have previously speculated that the multiplicity (2S + 1 for angular spin momentum S) of a molecule influences its surface interactions, citing data which imply that molecules with singlet electronic configurations tend to have the greatest propensity for surface scatter (i.e. are least reactive).[60,61] Scatter coefficients for singlet molecules, including C_3, CHF, and CF_2, tend to be high under all plasma conditions.[61] The molecules studied here have a doublet multiplicity, and their scatter coefficients also tend to be relatively high and change with changing applied power. Conversely, not all doublet species adhere to this overall trend in surface reactivity. For example, CH molecules exhibit low scatter coefficients (i.e. are primarily reactive at surfaces), regardless of plasma and substrate conditions and gas-phase formation mechanism. Note that the transition monitored for the CH molecule is $A^2\Delta$—$X^2\Pi$, whereas the transition used to calculate scatter coefficients in our LIF-based IRIS experiments is $A^2\Sigma^+$—$X^2\Pi$ for CF and SiF. This difference in symmetry in the electronic configuration of the excited state molecule may contribute to the differences in observed scatter coefficients. Future work will further explore this with additional plasma species, including main group hydrides OH, NH, CH and SiH, along with species having different electronic ground states. It is also informative to consider the kinetics and energetics of ground state molecules, with various symmetries, within plasma discharges. Ground state species can be monitored *ex situ* using BAS, gaining for both temporally and spatially resolved information. This holistic approach, coupling multiple spectroscopic techniques together to probe electronic states, is necessary to understanding the complex phenomena within plasma processing.

4.4 Summary

Following in the footsteps of the seminal work performed by Winters and coworkers in the arena of halogenated plasma processing, the present work has extended our understanding of energy partitioning and molecule-surface interactions within a range of fluorinated ICPs. Using a complement of gas-phase diagnostics, we have measured internal and kinetic temperatures of three molecules, SiF, CF, and CF_2, along with T_e in SiF_4 and a host of FC plasmas. In all cases, we found the vibrational temperatures measured were significantly higher than the rotational temperatures, often by an order of magnitude or more, suggesting collisional relaxation is most effective for rotational degrees of freedom. In contrast, the electron temperatures derived from our OES spectra reveal only small differences, regardless of plasma precursor or other parameters. This may be attributable to the highly electronegative nature of the gases studied.

Perhaps the most notable result from these studies is the observed relationship between vibrational temperature and surface scatter coefficients for the isoelectronic diatomic radicals CF and SiF formed within fluorinated ICPs. The preferential partitioning of energy into vibrational modes correlates with an increased propensity for scatter when a molecule interacts with a substrate. Thus, these data suggest that radical surface scatter coefficients are at least partially reliant upon the vibrational energy of the radical. We propose that electronically excited, vibrationally hot radicals are significant contributors to observed S values. Ultimately, the intimate relationship between internal energies of gas-phase constituents, electronic configuration, and the overall reactivity of plasma species must be considered when developing new plasma applications as well as comprehensive models of plasma chemistry.

REFERENCES

1. Cruden, B. A.; Rao, M.; Sharma, S. P.; Meyyappan, M., Neutral Gas Temperature Estimates in an Inductively Coupled CF_4 Plasma by Fitting Diatomic Emission Spectra. *J. Appl. Phys.* **2002**, *91*, 8955-8964.
2. Nagai, M.; Hori, M., Temperature and Density of CF Radicals in 60 MHz CCP FC Gas Plasma. *Jpn. J. Appl. Phys., Part 1* **2007**, *46*, 1176-1180.
3. Britun, N.; Gaillard, M.; Ricard, A.; Kim, Y. M.; Kim, K. S.; Han, J. G., Determination of the Vibrational, Rotational and Electron Temperatures in N_2 and Ar–N_2 rf Discharge. *J. Phys. D: Appl. Phys.* **2007**, *40*, 1022.
4. Fridman, A., *Plasma Chemistry*. Cambridge University Press: New York, 2008.
5. Golubovskii, Y. B.; Telezhko, V. M., Measurement of Gas Temperature from the Unresolved Rotational Structure of the First Positive Band System of Nitrogen. *J. Appl. Spectrosc.* **1983**, *39*, 999-1003.
6. Porter, R. A.; Harshbarger, W. R., Gas Rotational Temperature in an RF Plasma. *J. Electrochem. Soc.* **1979**, *126*, 460-464.
7. Davis, G. P.; Gottscho, R. A., Measurement of Spatially Resolved Gas-Phase Plasma Temperatures by Optical Emission and Laser-Induced Fluorescence Spectroscopy. *J. Appl. Phys.* **1983**, *54*, 3080-3086.
8. Schabel, M. J.; Donnelly, V. M.; Kornblit, A.; Tai, W. W., Determination of Electron Temperature, Atomic Fluorine Concentration, and Gas Temperature in Inductively Coupled Fluorocarbon/Rare Gas Plasmas Using Optical Emission Spectroscopy. *J. Vac. Sci. Technol., A* **2002**, *20*, 555-563.
9. Shimada, M.; Tynan, G. R.; Cattolica, R., Rotational and Translational Temperature Equilibrium in an Inductively Coupled Plasma. *J. Vac. Sci. Technol., A* **2006**, *24*, 1878-1883.
10. Bogart, K. H. A.; Cushing, J. P.; Fisher, E. R., Effects of Plasma Processing Parameters on the Surface Reactivity of $OH(X^2\Pi)$ in Tetraethoxysilane/O_2 Plasmas during Deposition of SiO_2. *J. Phys. Chem. B* **1997**, *101*, 10016.
11. Kessels, W. M. M.; McCurdy, P. R.; Williams, K. L.; Barker, G. R.; Venturo, V. A.; Fisher, E. R., Surface Reactivity and Plasma Energetics of SiH Radicals during Plasma Deposition of Silicon-Based Materials. *J. Phys. Chem. B* **2002**, *106*, 2680.
12. McCurdy, P. R.; Venturo, V. A.; Fisher, E. R., Velocity Distributions of NH_2 Radicals in an NH_3 Plasma Molecular Beam. *Chem. Phys. Lett.* **1997**, *274*, 120.
13. Zhang, J.; Williams, K. L.; Fisher, E. R., Velocity Distributions of SiF and SiF_2 in an SiF_4 Plasma Molecular Beam. *J. Phys. Chem. A* **2003**, *107*, 593-597.
14. Martin, I. T.; Fisher, E. R., Ion Effects on CF_2 Surface Interactions During C_3F_8 and C_4F_8 Plasma Processing of Si. *J. Vac. Sci. Technol., A* **2004**, *22*, 2168-2176.
15. Williams, K. L.; Butoi, C. I.; Fisher, E. R., Mechanisms for Deposition and Etching in Fluorosilane Plasma Processing of Silicon. *J. Vac. Sci. Technol., A* **2003**, *21*, 1688-1701.
16. Williams, K. L.; Fisher, E. R., Substrate Temperature Effects on Surface Reactivity of SiF_x (x = 1, 2) Radicals in Fluorosilane Plasmas. *J. Vac. Sci. Technol., A* **2003**, *21*, 1024-1032.
17. Liu, D.; Martin, I. T.; Zhou, J.; Fisher, E. R., Radical-Surface Interactions During Film Deposition: A Sticky Situation? *Pure Appl. Chem.* **2006**, *78*, 1187-1202.
18. Coburn, J. W.; Winters, H. F., Ion - and Electron -Assisted Gas - Surface Chemistry—An Important Effect in Plasma Etching. *J. Appl. Phys.* **1979**, *50*, 3189-3196.

19. Coburn, J. W.; Winters, H. F., Plasma-Assisted Etching: Ion-Assisted Surface Chemistry. *Appl. Surf. Sci.* **1985**, *22*, 63-71.
20. Coburn, J. W.; Winters, H. F., The Role of Energetic Ion Bombardment in Silicon-Fluorine Chemistry. *Nucl. Instrum. Methods Phys. Res., Sect. B* **1987**, *27*, 243-248.
21. Winters, H. F.; Kay, E., Gas Incorporation into Sputtered Films. *J. Appl. Phys.* **1967**, *38*, 3928-3934.
22. Blechle, J. M.; Cuddy, M. F.; Fisher, E. R., Effect of Ion Energies on the Surface Interactions of NO Formed in Nitrogen Oxide Plasma Systems. *J. Phys. Chem. A* **2013**, *117*, 1204-1215.
23. Winters, H. F.; Inokuti, M., Total Dissociation Cross Section of CF_4 and Other Fluoroalkanes for Electron Impact. *Phys. Rev. A* **1982**, *25*, 1420-1430.
24. Baio, J. E.; Yu, H.; Flaherty, D. W.; Winters, H. F.; Graves, D. B., Electron-Impact Dissociation Cross Sections for CHF_3 and C_3F_8. *J. Phys. D: Appl. Phys.* **2007**, *40*, 6969.
25. Fisher, E. R., On the Interplay Between Plasma Ions, Radicals and Surfaces: Who Dominates the Interaction? *Plasma Sources Sci. Technol.* **2002**, *11*, A105.
26. Abdel-Fattah, E.; Bazavan, M.; Sugai, H., Langmuir Probe Diagnostics of Electron Energy Distributions with Optical Emission Spectroscopy in Capacitively Coupled rf Discharge in Nitrogen. *J. Appl. Phys.* **2011**, *110*, 113303.
27. Hollmann, E. M.; Pigarov, A. Y.; Taylor, K., Measurement and Modeling of H_2 Vibrational and Rotational Temperatures in Weakly Ionized Hydrogen Discharges. *J. Nucl. Mater.* **2005**, *337*, 451-455.
28. Staack, D.; Farouk, B.; Gutsol, A. F.; Fridman, A., Spectroscopic Studies and Rotational and Vibrational Temperature Measurements of Atmospheric Pressure Normal Glow Plasma Discharges in Air. *Plasma Sources Sci. Technol.* **2006**, *15*, 818.
29. Lalo, C.; Deson, J.; Cerveau, C.; Ben-Aim, R. I., Air Microwave-Induced Plasma: Detection of NO in Post-Discharge Using an ArF Laser. *Plasma Chem. Plasma Process.* **1993**, *13*, 351.
30. Foucher, M.; Marinov, D.; Carbone, E.; Chabert, P.; Booth, J.-P., Highly Vibrationally Excited O_2 Molecules in Low-Pressure Inductively-Coupled Plasmas Detected by High Sensitivity Ultra-Broad-Band Optical Absorption Spectroscopy. *Plasma Sources Sci. Technol.* **2015**, *24*.
31. Liu, W.-Y.; Xu, Y.; Liu, Y.-X.; Peng, F.; Gong, F.-P.; Li, X.-S.; Zhu, A.-M.; Wang, Y.-N., Absolute CF_2 Density and Gas Temperature Measurements by Absorption Spectroscopy in Dual-Frequency Capacitively Coupled CF_4/Ar Plasmas. *Phys. Plasmas* **2014**, *21*, 103501.
32. Cruden, B. A.; Gleason, K. K.; Sawin, H. H., Relationship of CF_2 Concentration to Deposition Rates in the Pyrolytic Chemical Vapor Deposition Process. *J. Vac. Sci. Technol., B* **2002**, *20*, 690-695.
33. Studer, D.; Boubert, P.; Vervisch, P., Demonstration of NO Production in Air Plasma-Metallic Surface Interaction by Broadband Laser-Induced Fluorescence. *J. Phys. D: Appl. Phys.* **2010**, *43*, 315202.
34. Luque, J.; Hudson, E. A.; Booth, J. P., CF $A^2\Sigma^+$–$X^2\Pi$ and $B^2\Delta$–$X^2\Pi$ Study by Broadband Absorption Spectroscopy in a Plasma Etch Reactor: Determination of Transition Probabilities, CF $X^2\Pi$ Concentrations, and Gas Temperatures. *J. Chem. Phys.* **2003**, *118*, 622-632.

35. Booth, J.-P.; Hancock, G.; Toogood, M. J.; McKendrick, K. G., Quantitative Laser-Induced Fluorescence Spectroscopy of the CF $A^2\Sigma^+$--$X^2\Pi$ Transition: Electronic Transition Dipole Moment Function and Predissociation. *J. Phys. Chem.* **1996**, *100*, 47-53.
36. Hebner, G. A., Spatially Resolved CF, CF_2, SiF and SiF_2 Densities in Fluorocarbon Containing Inductively Driven Discharges. *Appl. Surf. Sci.* **2002**, *192*, 161-175.
37. Ohta, T.; Hara, K.; Ishida, T.; Hori, M.; Goto, T.; Ito, M.; Kawakami, S.; Ishii, N., Measurement of Si, SiF, and SiF_2 Radicals and SiF_4 Molecule Using Very High Frequency Capacitively Coupled Plasma Employing SiF_4. *J. Appl. Phys.* **2003**, *94*, 1428-1435.
38. Morgan, M. M.; Cuddy, M. F.; Fisher, E. R., Gas-Phase Chemistry in Inductively Coupled Plasmas for NO Removal from Mixed Gas Systems. *J. Phys. Chem. A* **2010**, *114*, 1722-1733.
39. Crosley, J. L. D. R. *LIFBASE: Database and Spectral Simulation Program (Version 1.5)*; 1999.
40. Western, C. M., PGOPHER: A Program for Simulating Rotational, Vibrational and Electronic Spectra. *J. Quant. Spectrosc. Radiat. Transfer* **2017**, *186*, 221-242.
41. Cuddy, M. F.; Fisher, E. R., Contributions of CF and CF_2 Species to Fluorocarbon Film Composition and Properties for C_xF_y Plasma-Enhanced Chemical Vapor Deposition. *ACS Appl. Mater. Interfaces* **2012**, *4*, 1733-1741.
42. Blechle, J. M.; Hanna, A. R.; Fisher, E. R., Determination of Internal Temperatures Within Nitric Oxide Inductively Coupled Plasmas. *Plasma Process. Polym.*, 1700041.
43. Parker, J. G., Rotational and Vibrational Relaxation in Diatomic Gases. *Phys. Fluids A* **1959**, *2*, 449-462.
44. Cuddy, M. F. Contributions of Gas-Phase Plasma Chemisry to Surface Modifications and Gas-Surface Interations: Investigations of Fluorocarbon rf Plasmas. Colorado State University, ProQuest Dissertations Publishing, 2012.
45. Davis, S. J.; Hadley, S. G., Measurement of the Radiative Lifetime of the $A^2\Sigma(v'=0)$ State of SiF. *Phys. Rev. A: At. Mol. Opt. Phys.* **1976**, *14*, 1146-1150.
46. Boogaard, A.; Kovalgin, A. Y.; Aarnink, A. A. I.; Wolters, R. A. M.; Holleman, J.; Brunets, I.; Schmitz, J. In *Measurement of Electron Temperatures of Argon Plasmas in a High-Density Inductively-Coupled Remote Plasma System by Langmuir Probe and Optical-Emission Spectroscopy*, Proceedings of the 9th annual workshop on Semiconductor Advances for Future Electronics and Sensors 2006, Utrecht, The Netherlands, 2006/11/23/; Technology Foundation STW: Utrecht, The Netherlands, pp 412-418.
47. Grill, A., *Cold Plasma Materials Fabrications: From Fundamentals to Applications*. IEEE Press: Piscataway, NJ, 1994.
48. Sugai, H.; Ghanashev, I.; Hosokawa, M.; Mizuno, K.; Nakamura, K.; Toyoda, H.; Yamauchi, K., Electron Energy Distribution Functions and the Influence on Fluorocarbon Plasma Chemistry. *Plasma Sources Sci. Technol.* **2001**, *10*, 378.
49. Huang, X.-J.; Xin, Y.; Yang, L.; Yuan, Q.-H.; Ning, Z.-Y., Spectroscopic Study on Rotational and Vibrational Temperature of N_2 and N_2^+ in Dual-Frequency Capacitively Coupled Plasma. *Phys. Plasmas* **2008**, *15*, 113504-113506.
50. Rehman, N. U.; Khan, F. U.; Khattak, N. A. D.; Zakaullah, M., Effect of Neon Mixing on Vibrational Temperature of Molecular Nitrogen Plasma Generated at 13.56 MHz. *Phys. Lett. A* **2008**, *372*, 1462-1468.

51. Kim, J.-H.; Shin, Y.-H.; Chung, K.-H.; Yoo, Y.-S., Relation Between the CF_2 Radical and Plasma Density Measured Using LIF and Cutoff Probe in a CF_4 Inductively Coupled Plasma. *Appl. Phys. Lett.* **2004**, *85*, 1922-1924.
52. Ono, S.; Teii, S., Vibrational Temperature in a Weakly Ionised CO_2-N_2-He Discharge. *J. Phys. D: Appl. Phys.* **1985**, *18*, 441.
53. Cuddy, M. F.; Blechle, J. M.; Fisher, E. R., Ion Contributions to Gas–Surface Interactions in Inductively-Coupled Fluorocarbon Plasmas. *Int. J. Mass Spectrom.* **2012**, *330–332*, 46-57.
54. Cuddy, M. F.; Fisher, E. R., Investigation of the Roles of Gas Phase CF_2 and F During FC Processing of Si and ZrO_2 *J. Appl. Phys.* **2010**, *108*, 033303.
55. Oehrlein, G. S., Effects of Ion Bombardment in Plasma Etching on the Fluorinated Silicon Surface Layer: Real-Time and Postplasma Surface Studies. *J. Vac. Sci. Technol., A* **1993**, *11*, 34-46.
56. Winters, H. F.; Coburn, J. W., Surface Science Aspects of Etching Reactions. *Surf. Sci. Rep.* **1992**, *14*, 162-269.
57. Standaert, T. E. F. M.; Schaepkens, M.; Rueger, N. R.; Sebel, P. G. M.; Oehrlein, G. S.; Cook, J. M., High Density Fluorocarbon Etching of Silicon in an Inductively Coupled Plasma: Mechanism of Etching Through a Thick Steady State Fluorocarbon Layer. *J. Vac. Sci. Technol., A* **1998**, *16*, 239-249.
58. Tsai, C. C.; Knights, J. C.; Chang, G.; Wacker, B., Film Formation Mechanisms in the Plasma Deposition of Hydrogenated Amorphous Silicon. *J. Appl. Phys.* **1986**, *59*, 2998-3001.
59. Kim, J. H.; Choi, Y. H.; Hwang, Y. S., Electron Density and Temperature Measurement Method by Using Emission Spectroscopy in Atmospheric Pressure Nonequilibrium Nitrogen Plasmas. *Phys. Plasmas* **2006**, *13*, 093501.
60. Stillahn, J. M.; Fisher, E. R., Gas Phase Energetics of CN Radicals in Radio Frequency Discharges: Influence on Surface Reaction Probability During Deposition of Carbon Nitride Films. *J. Phys. Chem. A* **2010**, *114*, 5287-5294.
61. Liu, D.; Cuddy, M. F.; Fisher, E. R., Comparison of CH, C_3, CHF, and CF_2 Surface Reactivities During Plasma-Enhanced Chemical Vapor Deposition of Fluorocarbon Films. *ACS Appl. Mater. Interfaces* **2009**, *1*, 934-943.

CHAPTER 5

TAILORING THE SURFACE PROPERTIES OF POROUS ZEOLIE CONSTRUCTS USING PLASMA PROCESSING[a]

Zeolites have been widely used for adsorption, catalysis, and gas separation processes. Despite their extensive use, the ability to control the surface properties of zeolites remains unoptimized. Plasma modification presents an ideal modification methodology with a wide parameter range and the potential to create tailored surface properties and functionalities. Here, zeolite constructs were modified with C_xF_y and $H_2O_{(v)}$ discharges to tune the material wettability. This work was supported by the National Science Foundation (NSF CBET – 1803067) and the American Chemical Society Petroleum Research Fund (ACS PRF 59776 – ND6). I would like to thank Carina Ammerlahn for her work on zeolite (8-12 mesh, 4 Å pore size) modification studies.[1] Specific acknowledgments for this chapter include Dr. Patrick McCurdy (assistance with SEM and XPS analyses); and Dr. Brian Newell (PXRD expertise); as well as Dr. Morgan J. Hawker and Dr. Michelle M. Mann (assistance with WCA).

[a] This chapter is reproduced from an article submitted to *Microporous and Mesoporous Materials* by Angela R. Hanna and Ellen R. Fisher.

5.1 Introduction

Zeolites are a broad class of crystalline aluminosilicates consisting of a three–dimensional (3D) framework, with pores ranging from nanometers to microns. Their high specific surface area, stability, and shape selectivity have made zeolites a frequent choice for utilization in a range of applications including catalysis, adsorption, and separation technologies.[2-4] Despite their extensive use, the ability to control the surface properties of zeolites remains unoptimized. Currently, zeolites are often modified via wet chemical methods to obtain desired surface properties. Although there are numerous successful reports using aqueous solutions as a modification strategy, these methods are undesirable because they can produce excess waste and introduce possible structural damage. Briefly, Ramos-Martinez *et al.* modified zeolite 13x with gamma-aminobutyric acid through ion exchange to improve removal efficiency of creatine and urea.[5] Liu *et al.* sought to improve the performance of natural zeolites in the removal of nitrite from aqueous sources.[6] The authors investigated a wide range of zeolite modification strategies, including acid (H_2SO_4), base (NaOH), salt (NaCl), and organic surfactant (cetyl trimethyl ammonium bromide) treatments.[6] Acid modified zeolites increased nitrite adsorption by ~7 fold, the other modification techniques (i.e., base, salt, organic surfactant) did not improve the zeolite adsorption capacity.[6] Shi *et al.* reviewed modification techniques and their impact on wastewater treatments, reporting acid modification as a straightforward means to improve adsorption capacity.[7] Using natural zeolites, Zhang *et al.* reported the removal rate of Sb^{3+} increased from 63.1% to 82.7% as HNO_3 concentration increased from 0.2 M to 0.8 M; however, as the acid concentration increased to 1 M, the adsorption rate decreased to 62.8 %.[8] This reduction can be attributed to lowered cation exchange capacity or structural damage to the Si-tetrahedra, inherent disadvantages of acid modification.[7]

Overall, the potential for zeolites to function as adsorbents in the removal of heavy metals improved via acid surface modification. Acid reactions are also commonly used to alter the SiO_2/Al_2O_3 ratio, ultimately impacting zeolite performance.[9,10] The hydrophilic–hydrophobic properties of a zeolite nominally arise from the SiO_2/Al_2O_3 ratio within the material.[11] Zeolites with lower SiO_2/Al_2O_3 ratios tend to be more hydrophilic, and are therefore often employed to remove ammonium and heavy metals from wastewater.[12] Munoz *et al.* investigated zeolite-A (low SiO_2/Al_2O_3 ratio) coatings on stainless steel substrates and found they increased hydrophilicity and decreased evaporation time, compared to the stainless steel subtrates.[13] In addition to zeolite coatings, zeolite/polymer composite blends have gained recent attention for biological applications, especially wound-healing, tissue engineering, and drug delivery.[14] Surface properties of these composites often need to be tailored for enhanced biocompatibility, such as increasing the wettability or modifying chemical functionality.

Zeolites with higher SiO_2/Al_2O_3 ratios tend to be more hydrophobic and are utilized to remove hydrophobic contaminates in water.[11] Highly hydrophobic materials, especially those with high surface areas are useful for oil/water separation and organic-pollutant enrichment. Numerous materials and methodologies have been designed to alleviate the detrimental impact of oil released/leaked into the environment.[15] These spills contain a complex mixture of low and high molecular weight hydrocarbons, the latter of which persist in the environment because of low volatility and solubility. In recent years, the role of wettability in oil/water separations has garnered increasing attention; specifically, materials that show different wetting properties for oil and water for efficient separation are of great interest.[16] Hydrophobic zeolites are, however, more difficult to fabricate than their hydrophilic counterparts.[17]

Plasma modification presents an ideal modification methodology with the potential to create tailored surface properties (i.e., specific wettability) and functionalities (i.e. surface chemistries). Described in Chapter 1, non-thermal plasmas can etch, deposit conformal films, or functionalize porous substrates with low temperature, solution free processing. Furukawa *et al.* used a radio frequency (rf) capacitively-coupled plasma discharges to modify zeolite H-Y with CF_4. The authors argue –OH functionality was replaced with $–CF_3$ and –F groups, evidenced by energy dispersive spectroscopy and infrared (IR) adsorption techniques. Zeolite crystallinity was assessed after plasma processing, where the authors note the crystal structure of the zeolite was damaged via XRD.[18] CF_4 plasmas are known etchants for a range of materials, including silicon-containing substrates,[19] which likely contributed to the reported decrease in crystallinity in the Furukawa study.[18] Here, four C_xF_y precursors were employed to modify the surface properties of zeolites. We deployed a range of characterization tools to assess materials before and after plasma treatment. X-ray photoelectron spectroscopy (XPS), scanning electron microscopy, and powder X-ray diffraction were utilized to investigate surface chemistry, substrate morphology, and bulk characteristics of the material, respectively, before and after plasma exposure. Optical spectroscopies examined the gas-phase of the plasma, both with and without zeolites, to evaluate the impact of the material on the plasma gas-phase. Through the use of complementary techniques, the interconnected relationships between plasma chemistry and resulting material modification can be probed.

5.2 Results and Discussion

Noted in Section 5.1, the inherent versatility of zeolite materials arises from their chemical properties and porous structure. A large portion of this work therefore sought to study how the surface chemistry and morphology of these materials are impacted by plasma modification. As

all plasma treatments were performed under vacuum conditions, treating free powder substrates can be problematic. Therefore, native zeolite powder was secured to glass slides with C tape and a simple straightforward pellet fabrication technique was also used with ground zeolite powder (Figure 2.8a).

Figure 5.1 depicts SEM images of two of the three types of untreated substrates, the as-received native materials (Figure 5.1a and 5.1b) and the pressed zeolite powder pellets (Figure 5.1c and 5.1d). At low magnification (25x), Figure 5.1a highlights the size distribution of the individual zeolite particles, whereas the pellet surface appears much smoother, with visible pores (Figure 5.1). Utilizing a higher magnification (4500x) emphasizes the interconnected network of pores within the zeolite substrate (Figure 5.1b and 5.2d). Moreover, the overall size of the major features remains approximately the same. High-resolution XPS spectra were collected to determine compositional data for both morphologies of untreated zeolites. The Si/Al ratio, determined from XPS analyses, was 3.3 ± 0.2 and 3.63 ± 0.2 for native and pellet constructs, respectively, indicating our materials are Si-rich zeolites. High-resolution Si_{2p} spectra, Figure 5.2a and 5.2b, display primarily $Si(–O)_x$ binding environments, corresponding to an inorganic SiO_2 silicon network. Oxygen (~58 %) within the material is largely bound to Si and to the small amount of Al in the zeolite network, shown in the high-resolution O_{1s} spectra (Figure 5.2c and 5.2d). Due to the porous nature of these substrates, adsorption of adventitious carbon is expected and clearly documented by the XPS results.

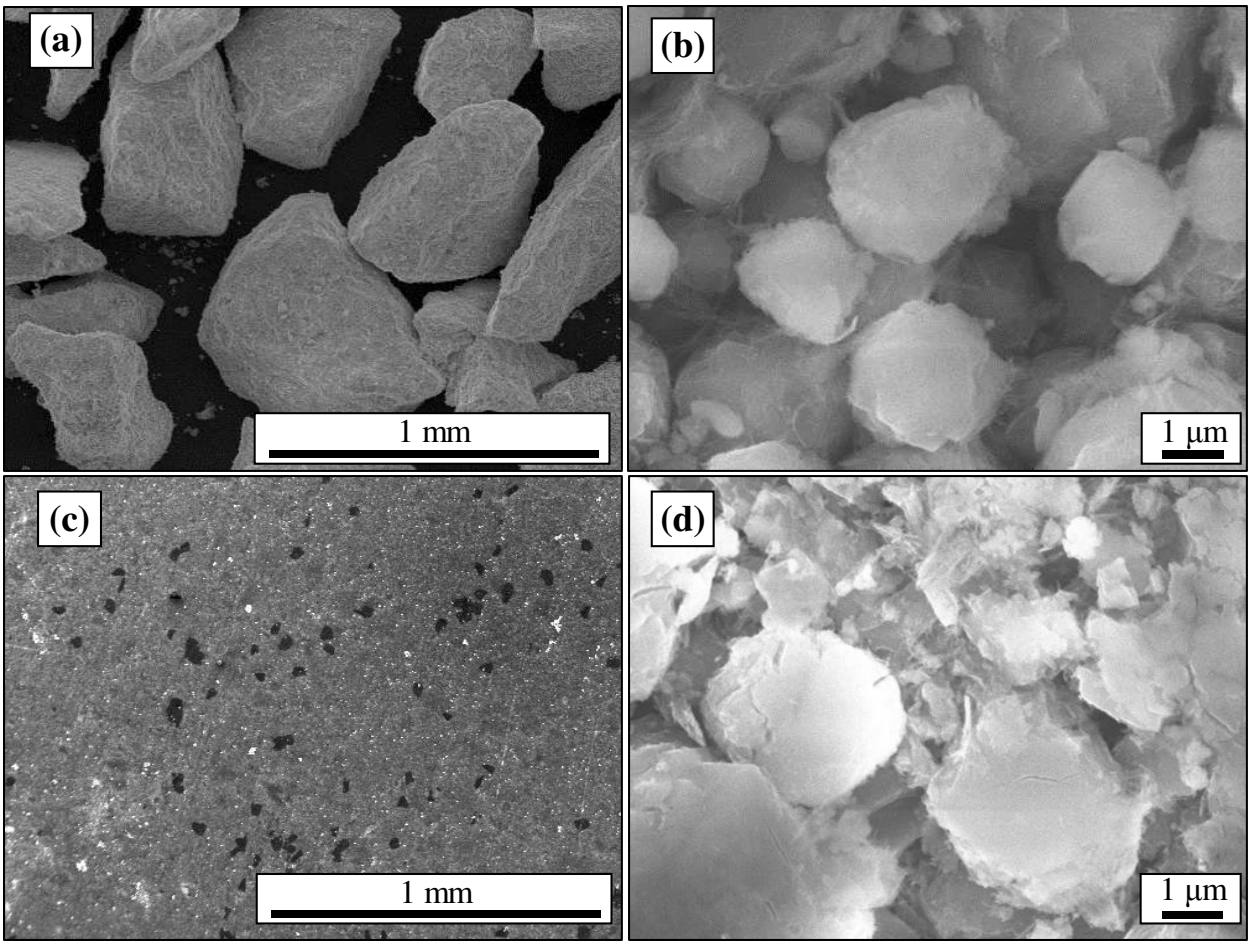

Figure 5.1. SEM images of untreated native zeolite (a,b) and pellets (c,d) at magnifications (a,c) 25x and (b,d) 4500x.

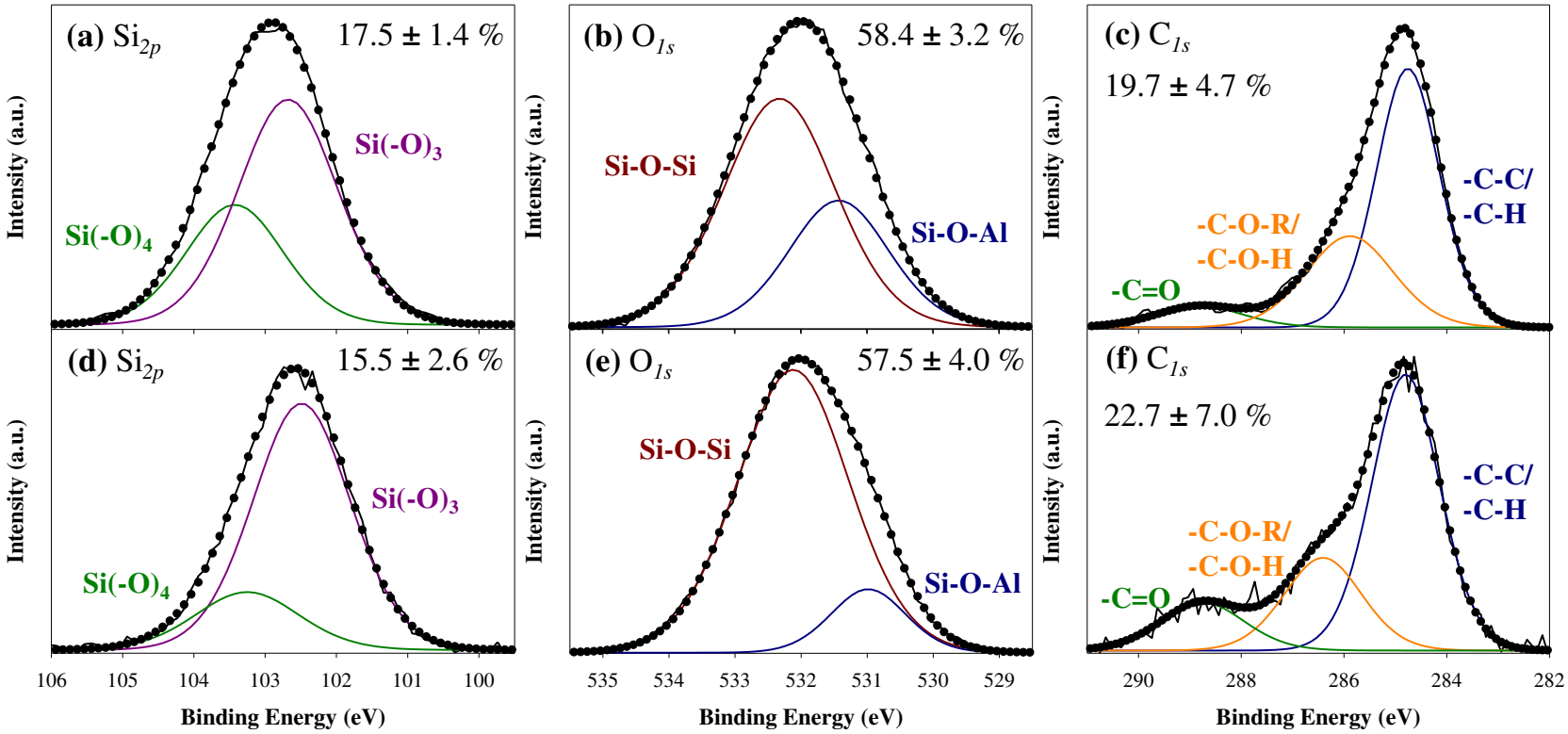

Figure 5.2. XPS high resolution Si_{2p} (a, b), O_{1s} (c, d), and C_{1s} (e, f) spectra for untreated native zeolite (top) and pressed pellets (bottom). The percent atomic composition with error (in parentheses) is listed in each panel. Both the native and pellet zeolites also contained 4.4 ± 0.6 % Al (not shown).

High-resolution C_{1s} XPS spectra for untreated zeolite constructs (Figure 5.2e and 5.2f) suggest the surface consists of carbon environments corresponding to C–C/C–H, C–O–H/C–O–C, and C=O at binding energies 284.8, 286.4, and 288.8 eV, respectively. In a previous study, zeolite pellets were oven calcinated (150 °C, 3 hours) to remove adsorbed H_2O and carbon contaminants, decreasing the carbon content to 8.9 ± 0.8.[20] The current study used the as-received native and pressed zeolite pellets without introducing additional fabrication procedures. As evidenced by the C_{1s} spectra, some oxygen is clearly bound to carbon in these materials. The binding energy for O – C functionality within the O_{1s} envelope, however, is difficult to deconvolute from the Si–O–Si and Si–O–Al bridges. As such, we have not specifically assigned peaks or portions of peaks within the O_{1s} binding environment to O – C. Ultimately, these data demonstrate fabrication of the pellet construct does not largely impact the morphology or surface chemistry of the zeolites based on SEM and XPS analyses.

Recently, fabricating zeolites into a fibrous form has attracted scientific inquiry for new applications in adsorption, optics, chemical sensors, and petroleum refining.[21-24] Zeolite fibers can be synthesized via hydrothermal methods, electrophoretic deposition, and electrospinning (Figure 2.8b). Electrospinning is commonly used to fabricate polymer fibers;[25] however, recent efforts have focused on fabricating composite,[26] metal oxide,[27] and micro- and nano-sized zeolite fibers.[24,28] Several factors affect fiber morphology, including electrospinning distance, applied voltage, solution flow rate, choice of polymer, and overall solution composition. Here, the distance between the needle tip and conductive disk was optimized to 15 cm by electrospinning 100 % PVP fibers, Figure 5.3a. Ground NaX zeolites and PVP were combined as described above, and electrospun at 16 kV for one hour to create zeolite-PVP composite fibers, Figure 5.3b.

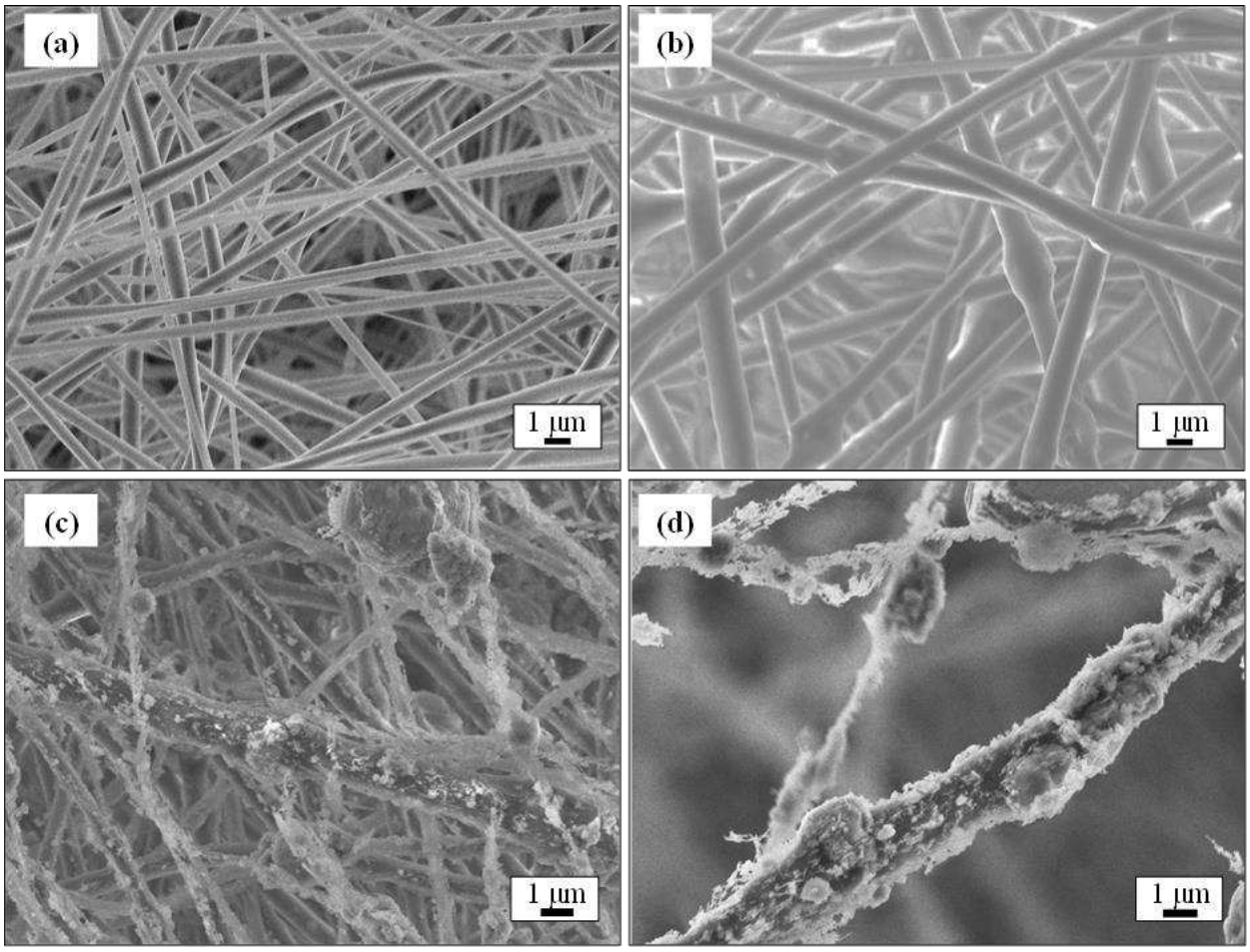

Figure 5.3. SEM images (a-c: 5000x, d: 7000x) of electrospun (a) 100% PVP, (b) zeolite: PVP (1:2, 15 cm, 16 kV) (c) O_2 and (d) Ar plasma calcinated zeolite fibers.

Anis and Hashaikeh fabricated zeolite –Y fibers via oven calcination at 550 °C for 2 hours to remove the polymer used in the fabrication process.[29] The fabrication of zeolite-Y fibers was verified with SEM, EDS, XRD, and BET analyses.[29] Oven calcination of NaX zeolite:PVP fibers is discussed in Appendix A. To avoid high temperature exposure, we chose to employ O_2 and Ar plasmas (100 mTorr, 100 W, 15 min) to remove the polymeric phase, the results of which can be seen in Figure 5.3c and 5.3d, respectively. EDS compositional maps were collected in conjunction with SEM images to probe morphology and to evaluate removal of the polymeric phase via compositional distributions, discussed in Appendix A. Although these SEM data suggest the successful fabrication of zeolite NaX fibers via plasma calcination, the evaluation of surface chemistry is also important.

Figure 5.4a depicts a representative XPS survey scan of the as-spun zeolite- PVP fibers. The chemical structure of PVP is included in Figure 5.4a, demonstrating the anticipated O_{1s}, N_{1s}, and C_{1s} binding environments. Following O_2 and Ar plasma treatments (Figure 5.4b and 5.4c), new binding environments corresponding to zeolites were measured (i.e., Na_{1s} and Si peaks) with significant reduction of the N_{1s} and C_{1s} environments. Thus, plasma calcination offers a facile, relatively fast strategy to remove the PVP from composite fibers. Moreover, upon removal of the polymer phase, the zeolite particles appear largely adhered together to maintain a random network of fibers, Figure 5.3c and 5.3d. Although there are significant areas for calcination improvement to engineer coherent and continuous zeolite fibers, these results clearly demonstrate the efficacy for relatively short (i.e., 15 min) plasma exposure to yield fibrous zeolites. Additionally, these results support employing a complement of analytical techniques to study these materials, addressing both bulk and surface properties.

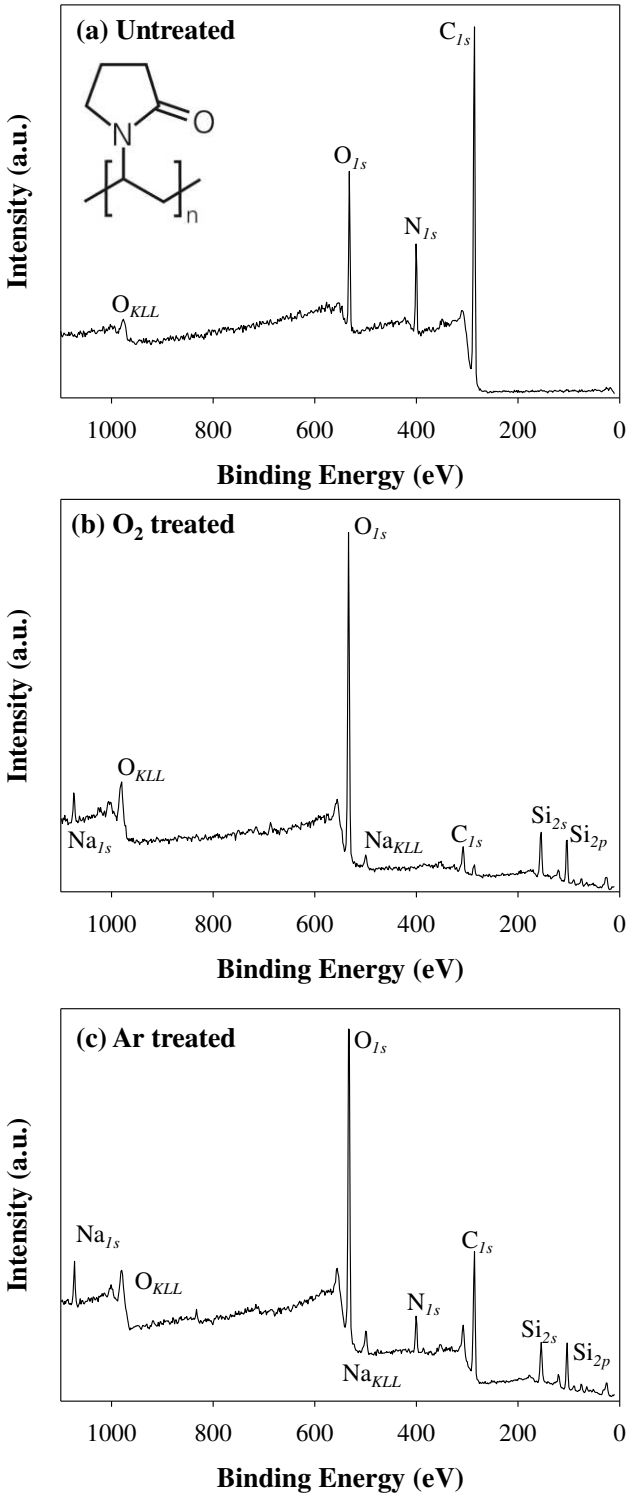

Figure 5.4. Representative XPS survey scans of (a) as-spun zeolite: PVP fibers (1:2 ratio, 15 cm, 16 kv), as well as (b) O_2 and (c) Ar plasma calcinated fibers *(p* = 100 mTorr, *P* = 100 W, *t* = 15 min).

As described in the Introduction, a significant motivation for this work was to develop the ability to tune the wettability of zeolites via plasma surface modification. Figure 5.5 depicts time-resolved photographs of a 2 μL water drop interacting with untreated and plasma treated materials at three different time points (1, 3, and 10 s). The untreated zeolite is relatively hydrophilic and as such, the water droplet is almost entirely adsorbed into the material at t = 10 s. After $H_2O_{(v)}$ and C_2F_6 plasma treatments (100 mTorr, 50 W, 5 min), surface wettability increased, as indicated by the observation that the 2 μL water droplet is almost adsorbed after 3 s. The C_3F_8 treatment at the same experimental conditions yielded a highly hydrophobic coating, where the water droplet sits on the substrate with a high profile and is largely unchanged as a function of time. These data highlight the ability to monitor wettability qualitatively, however, we sought to also quantify contact angle as a function of drop age on the surface. Hawker *et al.* provided an intensive literature study, reviewing the application of static and dynamic WCA measurements for plasma-modified porous constructs, nominally supplying the community with guidelines and best practices for how to represent and report WCA results.[30] They argue evaluating the wettability of 3D materials via dynamic techniques (e.g., measuring WCA as a function of time in conjunction with absorption rate analysis) has a numerous advantages and is a robust approach to evaluating wettability. Therefore, dynamic WCA and absorption rates are reported for all wettable materials fabricated herein.

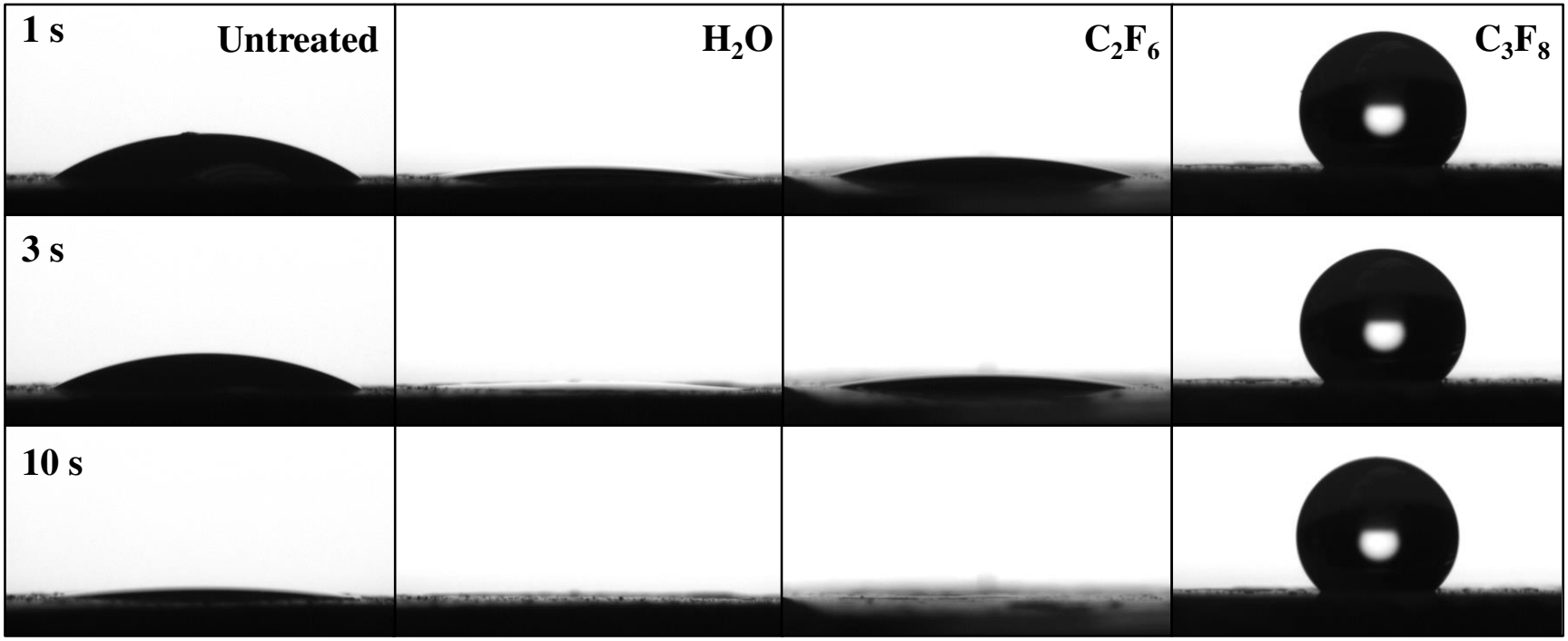

Figure 5.5. Time-resolved photographs of 2 μL water drops interacting with untreated and plasma treated zeolite pellets (100 mTorr, 50 W, 5 min), showing the relative contact angles of the zeolite pellet substrates. Rows correspond to drop time on zeolite: top (1 s), middle (3 s), and bottom (10 s).

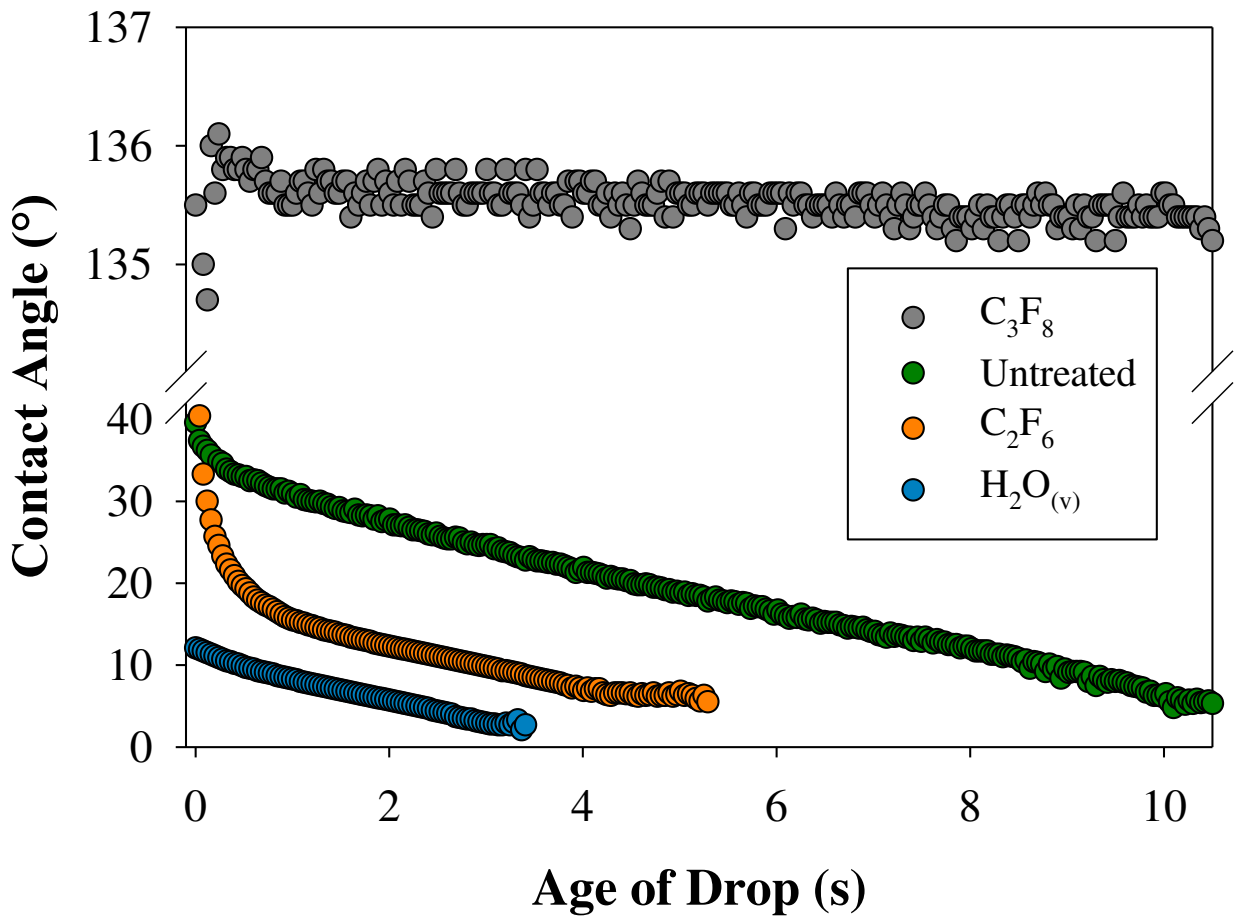

Figure 5.6. WCA as a function of drop age for untreated, $H_2O_{(v)}$, and C_xF_y treated zeolite pellets. All treatments were performed at 100 mTorr, 50 W for 5 min.

Figure 5.6 depicts WCA as a function of drop age for untreated and plasma-modified substrates. As evidenced in Figures 5.5 and 5.6, C_3F_8 plasma exposure yielded a superhydrophobic surface, with a 135.5 ± 2.2 ° contact angle (CA). A second fluorocarbon (FC) precursor, C_2F_6, was employed and surprisingly rendered the zeolite more hydrophilic than the untreated construct (Figure 5.6). Specifically, complete absorption occurred with a 0.53 ± 0.17 μLs^{-1} rate for the C_2F_6 modified zeolite, whereas a a 0.19 ± 0.022 μLs^{-1} rate was measured for the untreated material. The Figure 5.6 data suggest that following an $H_2O_{(v)}$ treatment at the same experimental conditions (100 mTorr, 50 W, 5 min), the wettability of the zeolite was further improved. The calculated absorption rate for H_2O modified zeolites, however, is 0.53 ± 0.10 μLs^{-1}, which is within experimental error of the C_2F_6 modified zeolite. Static and dynamic WCA on porous constructs are often more difficult to interpret as both surface chemistry and roughness can impact these measurements, ultimately leading to higher experimental errors relative to flat surfaces (i.e., glass slides and wafers).[30] These data exemplify the need to analyze numerous samples, accounting for variation between samples and plasma treatments. To further assess the zeolite – plasma interactions with C_xF_y and $H_2O_{(v)}$ systems, TR-OES was employed to study the evolution of gas-phase species during plasma processing.

The study of FC discharges to create new materials or modify surfaces has grown in past decades due to dualistic nature of these systems as they are known to both etch a variety of materials (i.e., microelectronics) and to deposit conformal FC coatings.[31] In particular, FC plasmas provide a prime example of multiple, competitive processes occurring simultaneously as they can both deposit FC films and etch a wide variety of materials. Through altering discharge operating conditions, precursor, or feed gas additives, it is possible to tailor the etching or depositing capacity of the plasma.[31] Nevertheless, few studies have sought to investigate substrate-dependent

processes in these systems.[32] Cuddy and Fisher previously explored the roles of neutral and gas-phase species, as well as ions, during FC plasma (CF_4 and C_2F_6) processing of Si and ZrO_2 wafers.[32] They documented that addition of a substrate can dramatically influence relative species densities as measured by OES, where Si and ZrO_2 wafers impacted the gas-phase chemistry differently. The relative density of atomic F within C_2F_6/Si and C_2F_6/ZrO_2 systems was not substantially impacted by applied power.[32] CF_2 densities, however, were significantly lower at all powers (50 –150 W) within the C_2F_6/ZrO_2 system.[32] Here, we also employed TR-OES to monitor gas-phase species within FC plasmas and introduced additional complexity to the plasma-substrate system by using a 3D, microporous material.

Figure 5.7 depicts relative species density as a function of time throughout a 5 min FC plasma treatment with and without a zeolite pellet. When no substrate is present, [CF_2] is greater than the other species in both the C_2F_6 and C_3F_8 systems. Moreover, little to no emission from atomic F or CO is observed in the substrate-free discharges. This is logical as the only source of oxygen in the plasma would arise from etching of the glass reactor walls, which has not previously been observed for these systems under the conditions used here.

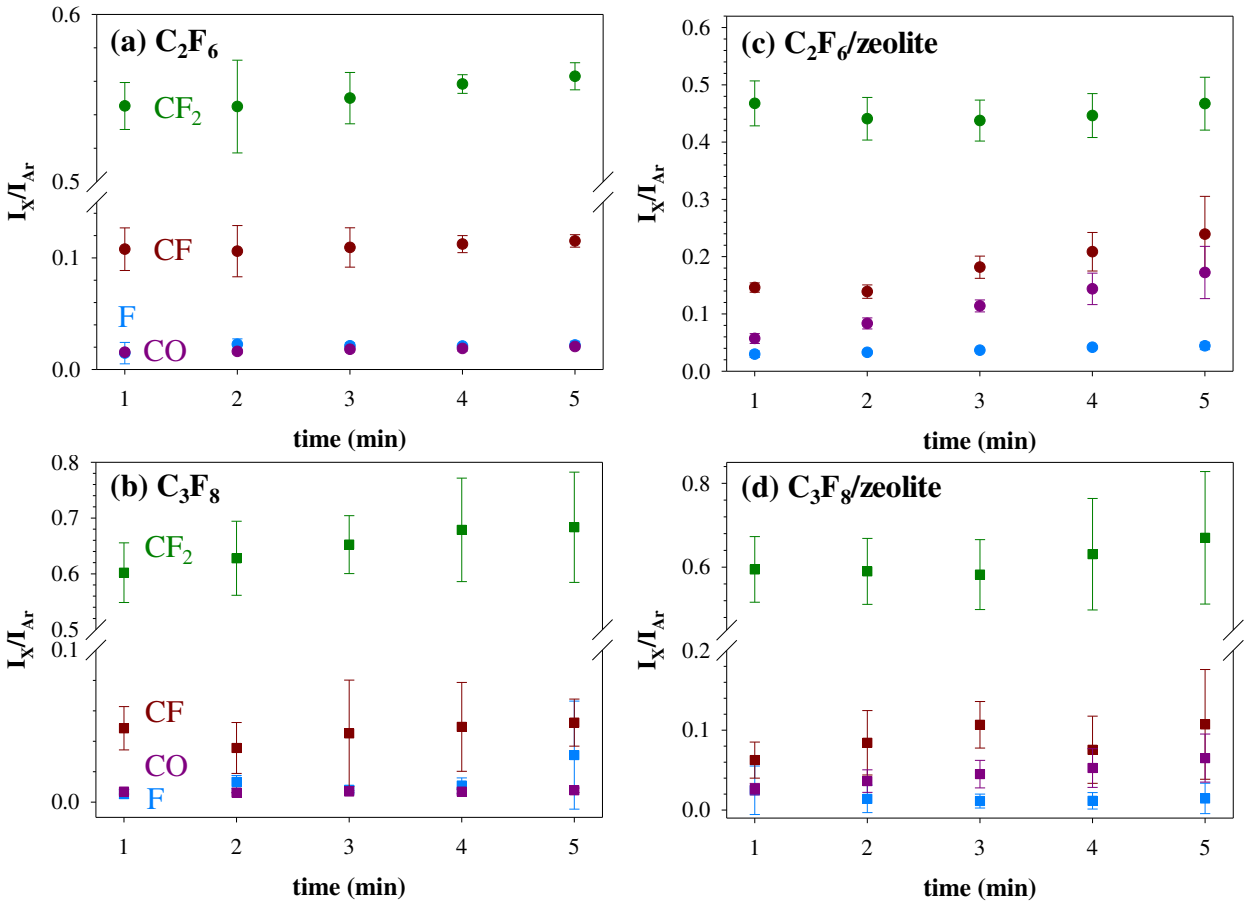

Figure 5.7. Relative species densities within C_2F_6 (a,b) and C_3F_8 (c,d) discharges without (a,c) and with (b,d) a zeolite pellet in the coil region (p = 100 mTorr, P = 50 W).

The low level of atomic F is also expected as the relatively low applied rf power does not fully fragment the feed gases. Cuddy and Fisher also measured small amounts of F* within 50 mTorr C_2F_6 plasms at a range of powers (50 – 150 W).[32] Upon addition of a zeolite pellet, the production of CF_2 appears largely unaffected, Figure 5.7c and 5.7d, as nominally these data are within experimental error of and comparable to the substrate-free system, regardless of precursor. There are, however, slightly elevated amounts of F in the C_2F_6/zeolite discharge (t = 5 min, 0.044 ± 0.0065) compared to C_3F_8/zeolite system (t = 5 min, 0.015 ± 0.0090). Additionally, [F] marginally increased from 0.030 ± 0.0056 to 0.044 ± 0.0065 throughout the 5 min C_2F_6 zeolite treatment, indicating this plasma condition may lean towards an etching regime. Within CF_4 discharges, a prototypical etchant system, Cuddy and Fisher measured more atomic F than CF_2 during plasma processing of Si ($P \geq 75$ W) and ZrO_2 wafers ($P \geq 50$ W).[32] These results suggest atomic F has an important role in the resulting etching or deposition capacity of the plasma, however, it is important to note that only excited state species are probed via OES. Ground state neutrals and ions (e.g., CF_3^+)[33] can also impact plasma behavior and the resulting material modification.

Within C_2F_6 discharges, [CO] significantly increases in the presence of a zeolite pellet and appears to increase linearly as a function of time. This suggests either oxygen is being removed from the surface and undergoing subsequent reactions in the gas phase (Figure 5.7c) to form CO or that intact CO is being removed (etched) from the surface. In addition, we see a steady rise in the amount of CF in the gas phase over time, whereas without a substrate [CF] remains relatively constant as a function of time. This could indicate that some FC material is being deposited on the pellet and subsequently removed from the surface as it evolves. Regardless of the exact mechanism, these gas-phase data bolster the hypothesis that a C_2F_6 plasma at p = 100 mTorr,

P = 50 W operates in an etching regime, which may help explain the observed increase in surface wettability measured via WCA (Figure 5.6). Within the C_3F_8/zeolite system, there is an increase in signal arising from CO upon the addition of a zeolite pellet, Figure 5.7d, but we do not observe significant increases over time. This further supports the idea that significant competition between etching and deposition occurs within all FC discharges; however, ultimately a hydrophobic coating is deposited in the C_3F_8 plasma. As a final observation regarding the etch-deposition competition, representative SEM images of untreated and FC plasma treated zeolites are illustrated in Figure 5.8. After C_2F_6 plasma exposure (100 mTorr 50 W, 5 min), there is evidence of potential surface etching (Figure 5.8b, denoted with red box), compared to SEM images of untreated (Figure S1a) and C_3F_8 plasma treated pellets (Figure 5.8c). Additionally, the individual features in the C_2F_6 treated sample appear to have rougher edges compared to the smoother, more rounded features observed in the C_3F_8 treated material. By using complementary techniques to evaluate surface wettability and morphology, as well as the relative densities of plasma species, a more comprehensive understanding of plasma –zeolite interactions can be obtained. Specifically, the increased absorption rate (verified via WCA); evidence of etched trenches and jagged features in the material (SEM); and elevated formation of $CO_{(g)}$ species combine to support the hypothesis that surface etching is occurring during C_2F_6 plasma processing of zeolite pellets. Here, WCA was employed to provide further indicators of film deposition (or etching) in FC systems.

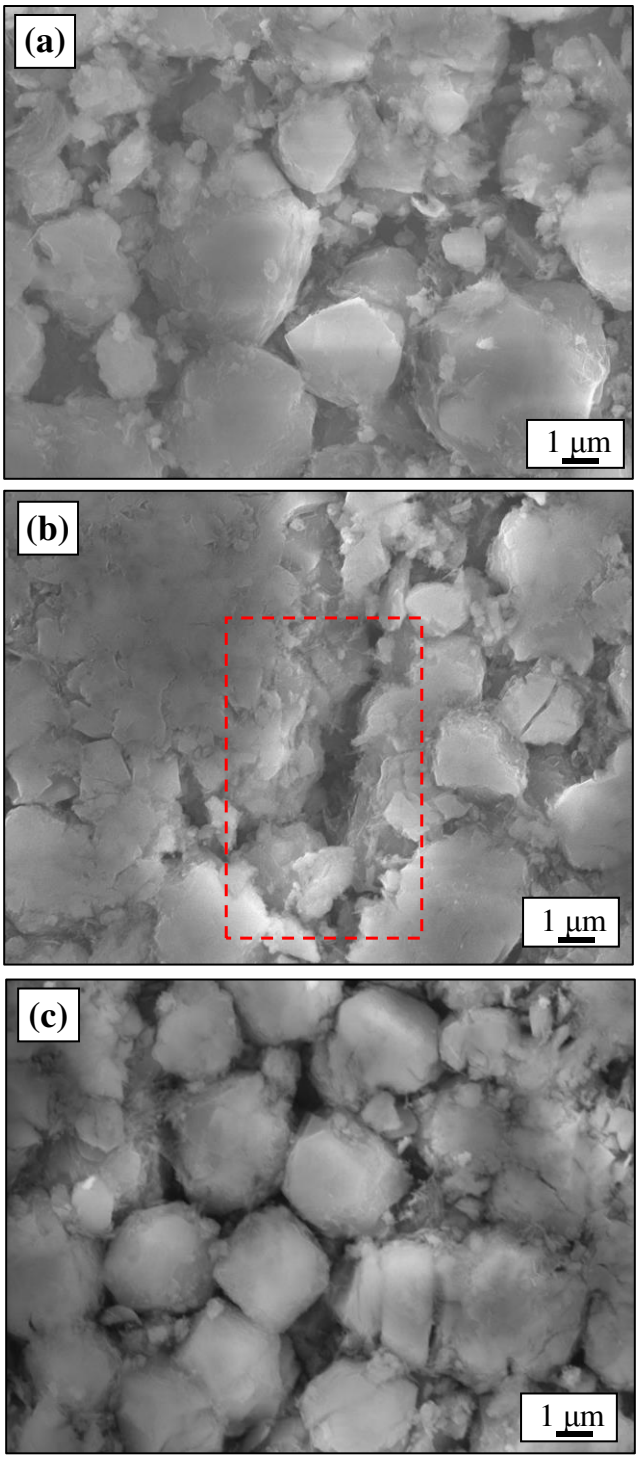

Figure 5.8. Representative SEM images (7000x) of (a) untreated, (b) C_2F_6, and (c) C_3F_8 plasma treated (p = 100 mTorr, 50 W, t = 5 min) zeolite pellets.

Table 5.1 lists static WCA values obtained for C_3F_8 plasma-modified zeolites as a function of applied power and system pressure, where all treatments were 5 min with the pellet in the coil region (Figure 2.1a). At P = 50 W, contact angles increased from 123.9 ± 4.3 ° to 135.5 ± 2.2 ° with increasing system pressure. All other plasma conditions yielded static WCA values that were within experimental error of each other, however under all treatment conditions a hydrophobic surface was observed. Substrate positioning in the discharge can also impact the resulting surface properties, therefore changing the placement within the discharge may allow for additional surface property optimization. Additionally, Hawker *et. al* determined a linear relationship between FC film thickness and C_3F_8 deposition time (p =50 mTorr, P = 50 W, t = 5 – 90 min) on Si wafers, therefore longer treatment times could render thicker FC film formation,[34] potentially resulting in blanket-type coatings of the zeolite features, as opposed to the relatively conformal coatings observed here.

Noted in the Introduction, system pressure, applied rf power, and treatment time are operating conditions that can heavily influence the plasma modification processes, specifically the balance between etching and deposition within FC systems. To understand the extent of these influences, plasma operating parameters were varied to determine conditions that ultimately resulted in some FC deposition after exposure to a C_2F_6 discharge, verified via WCA. A static CA of 19.4 ± 4.5 ° was obtained at p = 50 mTorr, P = 25 W, t = 5 min, the lowest power and pressure studied herein.

Table 5.1. Static WCA values C_3F_8 plasma-modified zeolite pellets[a]

***P* (W)**	***p* (mTorr)**	**WCA (°)**
25	50	138.2 (4.4)
	100	134.5 (2.6)
50	50	123.9 (4.3)
	100	135.5 (2.2)
100	50	130.1 (2.2)
	100	132.3 (8.0)

[a]All analyses were performed for an n = 9; the mean standard deviation are reported

[b]Treatments were performed in the coil region for 5 min.

Cuddy and Fisher measured the propensity of CF and CF_2 molecules to scatter from Si and ZrO_2 substrates using the Imaging of Radicals Interacting with Substrates (IRIS) technique, reporting scatter coefficients (*S*) as a function of C_xF_y precursor and operating parameters.[32,35] At 50 mTorr, $S(CF_2)$ from a Si wafer increased from 1.28 ± 0.02 to 1.65 ± 0.08 as power increased from 50 to 150 W. Scatter values greater than unity indicate surface production of CF_2. Additionally, CF_2 species and oligomeric units are hypothesized to contribute to surface passivation and fluorocarbon film formation.[35] Therefore, at p = 50 mTorr and low powers (i.e., 25 W), it is likely less CF_2 scatter occurs, suggesting these parameters promote CF_2 reactivity at a surface and subsequent film deposition. Although this material is not hydrophobic, a stable droplet remained on the surface compared to the complete absorption documented for the untreated pellets. At the same experimental conditions, a 138.2 ± 4.4 ° static WCA was measured after C_3F_8 plasma exposure (Table 5.1). Illustrated in Figure 5.9, the inset photographs highlight the difference in resulting material wettability after the two different plasma treatments. XPS was also used to study the resulting surface chemistry after plasma exposure.

Figure 5.9 depicts high-resolution XPS spectra for C_3F_8 and C_2F_6 treated zeolite pellets (p = 50 mTorr, P = 25 W, t = 5 min), revealing several CF_x surface moieties present after C_3F_8 treatment (Figure 5.9a). Additionally, the majority of the F is bound to C species, with a much smaller amount bound to Si in the underlying zeolite, Figure 5.9b. Figure 5.9c and 5.9d show the C_{1s} and F_{1s} binding environments for C_2F_6 treated pellets. Notably, a similar array of CF_x binding environments is observed; however, the majority of the carbon (54.3 ± 3.7 %) resides in an aliphatic C-C/C-H environment (284.8 eV), suggesting low levels of CF_x species from a deposited FC film. Furthermore, in the corresponding F_{1s} spectrum, the fluorine is almost equally split between F-C and F-Si binding environments, Figure 5.9d.

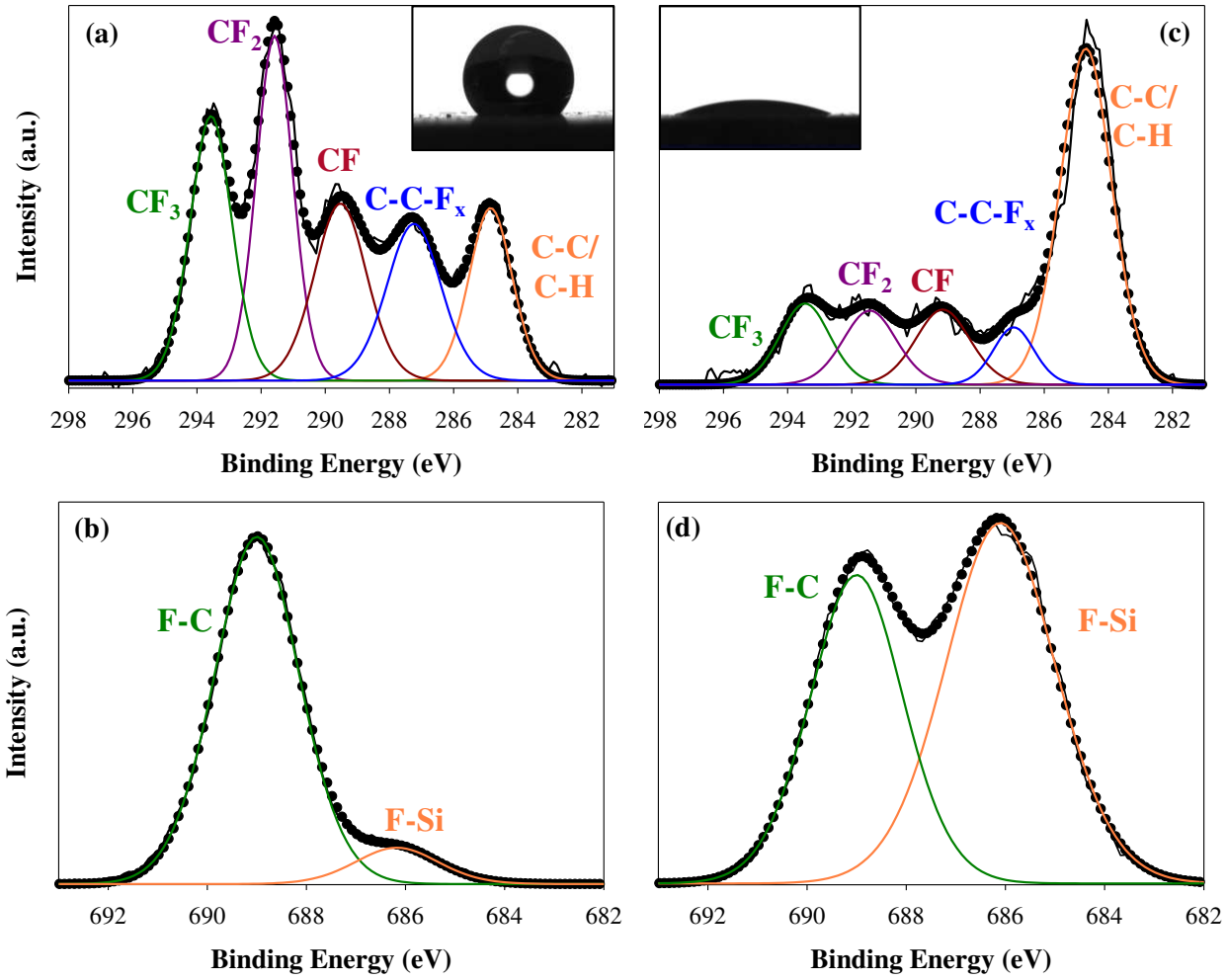

Figure 5.9. High-resolution XPS spectra for C_3F_8 (a, b) and C_2F_6 (c,d) plasma treated zeolite pellets (p = 50 mTorr; P = 25 W; t = 5 min) are shown for C_{1s} (a,c) and F_{1s} (b,d) binding environments. Inset are photographs of water drops with 138.2 ± 4.4 ° and 19.4 ± 4.5 ° static WCAs measured on (a) C_3F_8 and (b) C_2F_6 plasma treated zeolites.

Cuddy and Fisher previously measured deposition rates of 1.0 ± 0.1 and 3.4 ± 0.4 nm/min for C_2F_6 and C_3F_8 rf ICPs, respectively (p = 50 mTorr).[35] The increased deposition rate for the C_3F_8 precursor corroborates the increased hydrophobicity of the zeolite pellet compared to the C_2F_6 modified materials. Although the aforementioned deposition rates were determined on Si wafers and not explicitly on the zeolite materials studied herein, we believe the same trends would hold and note that it is difficult to accurately measure film thickness on a 3D, porous substrates.[34]

C_2F_6 treatments at other applied powers and system pressures increased the water absorption rate, compared to the untreated pellet, Table 5.2. At P = 100 W, absorption rates increased from 0.35 ± 0.1 uLs^{-1} to 0.89 ± 0.2 uLs^{-1} as pressure was increased from 50 to 100 mTorr. Interestingly, the opposite trend was documented at P = 50 W, where an increase in pressure corresponded to a decrease in absorption rate. Although a clear relationship between power, pressure, and resulting material wettability was not determined, these data highlight the ability to modify the surface properties via C_xF_y plasma exposure. FC film growth is hypothesized to be more efficient as the y/x ratio of C_xF_y precursors is decreased,[31] a notion that is supported by the data provided in Tables 5.1 and 5.2. Additives to FC plasmas can be employed to increase the deposition or etching efficiency of the plasma system; H_2 additions have been shown to promote deposition whereas O_2 additives tend to favor etching regimes.[31] Utilizing WCA as a tool to measure outcomes, we sought to quantify wettability behavior of zeolite pellets after exposure to a range of C_xF_y precursors, as well as adding dilute amounts of H_2 and O_2 to the gas feed.

Figure 5.10 shows WCA (°) as a function of the F/C ratio within a C_xF_y precursor, where dilute amounts of O_2 or H_2 (e.g., ~10 %) were added to promote surface etching or polymerization, respectively. As the F/C increases to 4 (CF_4), the discharges nominally primarily etch the materials, where a wettable surface is indicated by a WCA < 10°.

Table 5.2. Average absorption rate for plasma-modified zeolite pellets[a]

Precursor	*P* (W)	*p* (mTorr)	Rate (µL/ s)
Untreated	-	-	0.19 (0.022)
C_2F_6	25	50	--[b]
		100	0.39 (0.15)
	50	50	0.53 (0.17)
		100	0.26 (0.078)
	100	50	0.35 (0.10)
		100	0.89 (0.20)

[a]All analyses were performed for an n = 6 – 9

[b]Static WCA of 19.4 (4.5)°

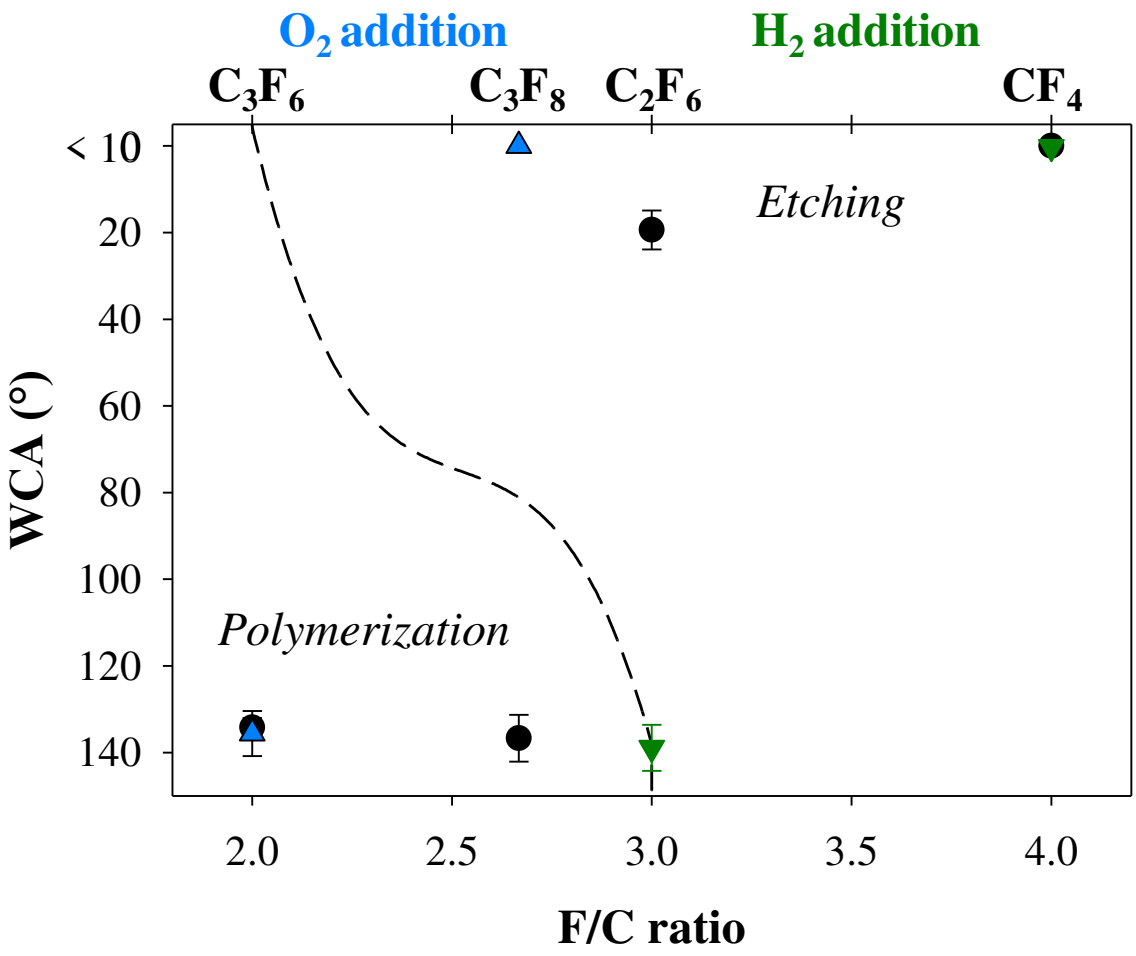

Figure 5.10. WCA as a function of F/C ratio, where WCA <10 ° describes a hydrophilic surface, where the water droplet was completely absorbed by the material. All treatments were performed at p = 50 mTorr; P = 25 W; t = 5 min. 10% H_2 (green triangles) or O_2 (blue triangles) were added to feed gas. The dashed line is intended to guide the reader's eye to separate polymerization and etching regimes.

When H_2 was added to C_2F_6, the overall process shifts to deposition, with a hydrophobic coating being deposited, as evidenced by high WCA values, (Figure 5.10). Note that the dashed line in Figure 10 is intended to guide the reader's eye and was fashioned after a similar illustration developed by d'Agostino and coworkers who demonstrated hydrogen addition to C_2F_6 discharges increases the distribution of CF_x groups within the deposited material.[31] Specifically, "Teflon-like" films were created from a C_2F_6 /H_2 (80/20) discharge, where the film is nominally composed of only CF_2 groups. These CF_2 thin films were obtained after seconds of plasma exposure. At longer discharge durations (e.g., the 5 min exposure used here), a large CF_2 binding environment is present in the XPS C_{1s} spectrum after C_2F_6 /H_2 (90/10) plasma treatment; however, additional carbon moieties are also observed, Figure 5.11. Additionally, only a F-C binding environment (689.0 eV) was measured in the corresponding F_{1s} spectrum, Figure 5.11b. The underling $(SiO)_x$ network was not detected, suggesting the film was at least as thick as the 10 nm XPS sampling depth.[36]

Table 5.3 details XPS atomic composition of zeolites after FC plasma treatments. Upon H_2 addition to a C_2F_6 discharge, the amount of C on the surface increased from 23.5 ± 1.9 to 41.3 ± 0.7 % and the amount of F embedded increased from 40.3 ± 7.3 to 57.9 ± 1.1 Addition of hydrogen to discharges is hypothesized to deplete the amount of $F_{(g)}$ in the system, and thereby decrease etching capabilities.[31] Cuddy proposed excited state $H_{(g)}$ reacts with CF_2 to form gaseous CF and HF species, although this phenomena was only observed for H_2 dilutions ≥ 50 %.[37] The inset SEM image in Figure 5.11b also suggests the formation of a film on the microporous material.

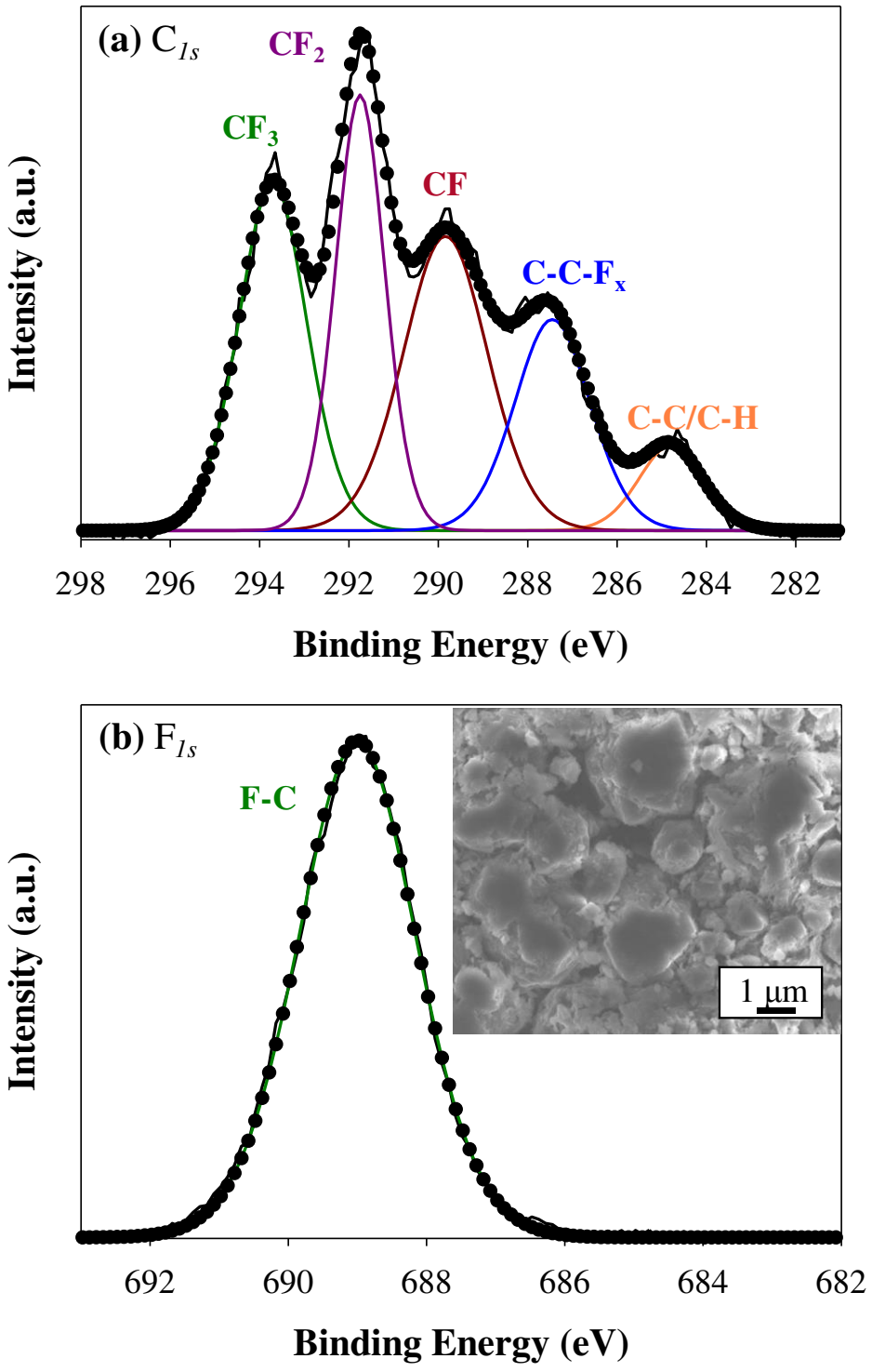

Figure 5.11. High-resolution (a) C_{1s} and (b) F_{1s} XPS spectra for C_2F_6:H_2 treated zeolite pellets (p = 50 mTorr; P = 25 W; t = 5 minutes). Inset corresponds to representative SEM image after the same plasma conditions (7000x).

Table 5.3. XPS atomic composition of FC plasma treated zeolites[a,b,c]

	C (%)	O (%)	Si (%)	Al (%)	F (%)
UT native	19.7 (4.8)	58.4 (3.2)	17.5 (1.4)	4.4 (0.6)	--
UT pellet[b]	22.7 (7.0)	57.5 (4.0)	15.5 (2.6)	4.4 (0.6)	--
C_3F_8	34.5 (1.5)	9.3 (2.4)	3.7 (0.8)	--	52.5 (4.0)
C_2F_6	23.5 (1.9)	22.6 (6.6)	8.5 (2.2)	5.1 (0.4)	40.3 (7.3)
C_2F_6/H_2[c]	41.3 (0.7)	< 1.0	--	--	57.9 (1.1)

[a]All analyses were performed for an n = 6 – 9; standard deviation from mean are reported
[b] Previsouly reported[38]
[c]~10% H_2 dilution

Although C_2F_6/H_2 processing resulted in a hydrophobic coating, the materials were still wettable after a CF_4/H_2 plasma treatment, suggesting etching still predominates in this system. Interestingly, the C_3F_8/O_2 system also resulted in a hydrophilic surface, whereas the addition of O_2 to C_3F_6 did not impact the overall wettability. These data exemplify the tunability of plasma processing as a robust avenue for surface modification.

Non-thermal O_2 plasmas are commonly used to etch materials, as well as increase the amount of oxygen functional groups on the material surface. These include numerous studies of O_2 plasma treatments of nanomaterials, carbonaceous materials, and polymers. For example, Stuckert and Fisher used Ar/O_2 plasmas to etch the surface of SnO_2 nanomaterial gas sensors to create surface oxygen vacancies, ultimately to fabricate an improved gas sensors.[39,40] Nevertheless, modification of zeolites via O_2 plasma processing has not been widely documented, with few studies reporting extensive materials characterization before and after plasma exposure. De Velasco-Maldonado *et al*. used an rf at 13.56 MHz O_2 plasma [p = 1 mbar (~750 mTorr), P = 75 W, t = 9 min] to modify natural clinoptilolite, systematically analyzing potential changes in morphology, chemical functionality, and performance before and after plasma treatments.[41] Ultimately, these authors argue the plasma conditions they studied had little to no effect on chemical or structural properties of the clinoptilolite, using FT-IR with an attenuated total reflectance, XRD, and SEM.[41] Plasma processing is nominally a surface-sensitive modification, therefore XPS and WCA goniometry can provide information regarding changes to the first ten nanometers of the material, compared to bulk properties.[42] These characterization techniques were employed by Ammerlahn and Fisher after plasma modifying zeolite pellets (8-12 mesh, 4 Å pore size.[1] An increase in surface oxygen after O_2 rf ICP plasma treatments [at 100 mTorr, 200 W,

8 min] was observed,[1] including a substantial increase in $Si(-O)_4$ binding environments in the high-resolution Si_{2p} XPS spectrum. Dynamic water contact angle was performed with drop sizes of 5 μL, where H_2O and O_2 plasma treatments increased surface wettability.[1] Gao *et al.* report the successful modification of mesoporous silica SBA-15 pore channels with an O_2 dielectric barrier discharge (DBD).[43] Fahmy *et al*. modified zeolite-A materials using rf O_2 plasmas to increase cadmium ion adsorption capabilities.[44] The authors argue -OH functionality is necessary to increase Cd adsorption capacity, where O_2 plasma ignition generates a variety of energetic oxygen species, which subsequently interact with adsorbed H_2O within pores to generate OH radicals.[44] As $H_2O_{(v)}$ discharges also generate gas-phase OH radicals and O-containing species, we used OES to examine an $H_2O_{(v)}$/Ar (90/10) plasma without and with a zeolite pellet, Figure 5.12. Emission from OH, H_2, atomic H, O, and Ar are observed. Moreover, the Fisher Group has previously documented the efficacy of $H_2O_{(v)}$ treatments to improve the wettability of numerous polymeric constructs, including filtration membranes, scaffolds, and fibers.[45,46] Therefore, we further explored using this system to achieve hydrophilic modification of zeolite materials.

As shown in Figure 5.6, $H_2O_{(v)}$ treatment [100 mTorr, 50 W, 5 min] increased the absorption rate to 0.56 ± 0.10 μLs^{-1}. As detailed in Table 5.4, increasing the power from 50 to 100 W significantly impacted the absorption rate, as a 1.64 ± 0.085 μLs^{-1} rate was measured following a 100 W, 100 mTorr, 15 min treatment. In contrast, increasing treatment time from 5 to 15 min had no noticeable effect on the absorption rate at either power studied here. Material morphology was also maintained for native and zeolite pellets after 5 and 15 min treatments, illustrated in Figure 5.13. In addition, the relative densities of H_α, OH, and atomic O were measured as a function of time with no substrate and with a zeolite pellet in the coil, Figure 5.14a and 5.14b, respectively.

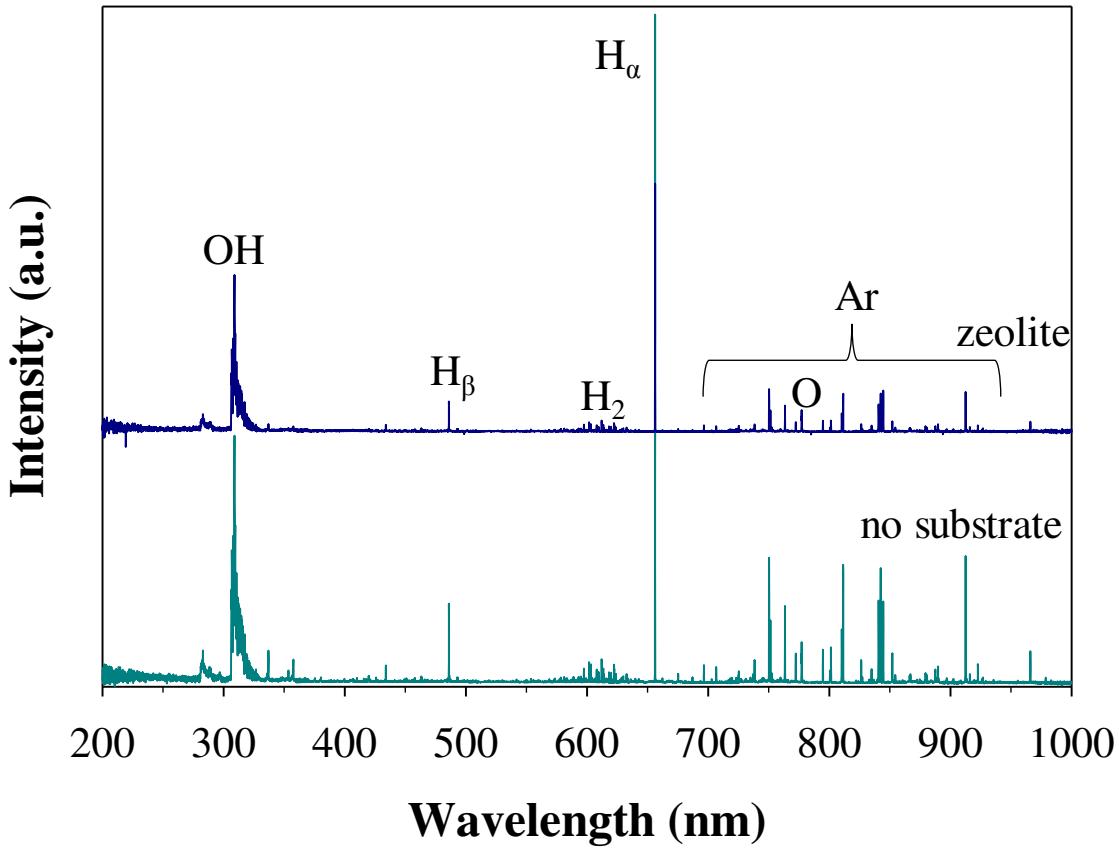

Figure 5.12. Representative OES spectrum without (bottom) and with zeolite pellet (top) in an rf ICP (100 mTorr, P = 100 W, t = 15 min).

Table 5.4. Average absorption rate for plasma-modified zeolite pellets[a,b]

Precursor	time (min)	*P* (W)	Rate (µL/ s)
Untreated	-	-	0.19 (0.022)
H_2O	5	50	0.56 (0.10)
		100	1.29 (0.34)
	15	50	0.55 (0.22)
		100	1.64 (0.085)

[a]All analyses were performed for an n = 3 – 9; the mean standard deviation are reported
[b]p = 100 mTorr

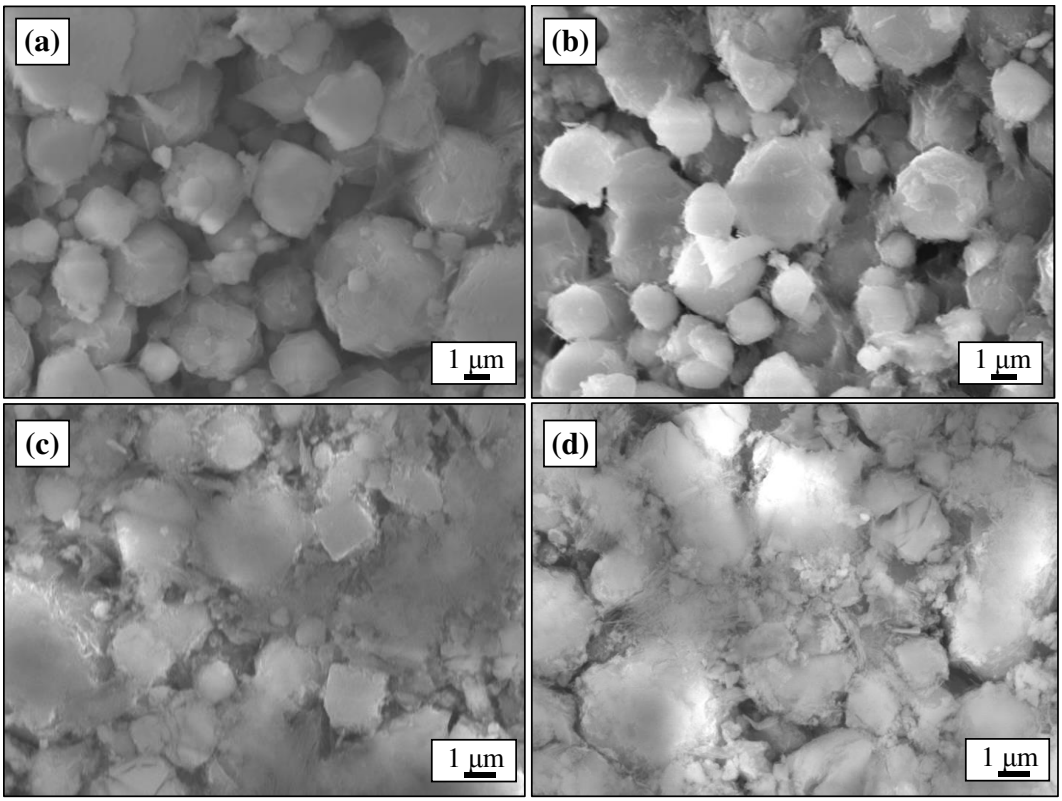

Figure 5.13. SEM images of H_2O treated (a,b) native zeolite and (c,d) zeolite pellet at magnifications 4,500x and 5,000x, respectively. Treatment conditions were p = 100 mTorr, 100 W (a,c) t = 5 min, (b,d) t = 15 min.

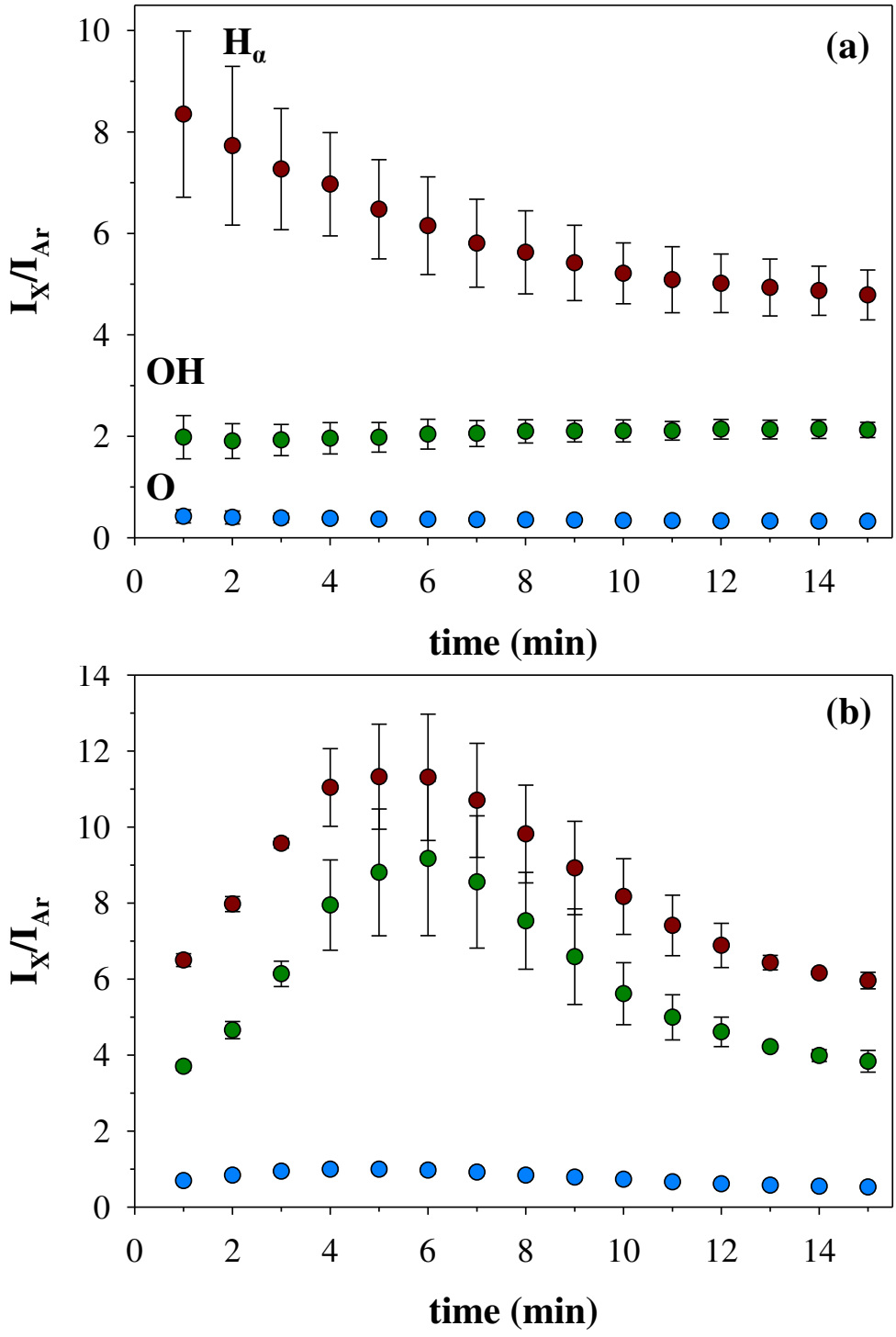

Figure 5.14. Relative density of species within a H_2O (100 mTorr, 100 W) plasma system (a) with no substrate and (b) a zeolite pellet in the coil region. Error bars represent one standard deviation from the mean (n = 3).

In the substrate-free H_2O plasma, the relative densities of atomic O and OH do not change over time, however, a slight exponential decay of H_α is measured, Figure 5.14a. The addition of a zeolite pellet directly impacted the density of gas-phase species, as the amount of OH in the discharge increases until ~4 – 6 min and a subsequent decrease is documented as time increases to 15 min, Figure 5.14b. A similar temporal behavior was also measured for H_α emission, Figure 5.14b. These data suggest the addition of a microporous zeolite impacts the resulting gas-phase chemistry, potentially also altering surface functionality after $H_2O_{(v)}$ plasma exposure.

XPS atomic compositions for $H_2O_{(v)}$ treated native and zeolite pellets are listed in Table 5.5, as well as computed O/Si and O/C ratios. The resulting O/C ratios for native (5 min) and pellet (5 and 15 min) zeolites increased from ~2.5 – 2.8 (untreated) to ~4 – 4.7 after plasma treatment. Interestingly, as time increases from 5 to 15 min for the native substrates, the O/C ratio increases from 2.6 ± 0.5 to 4.6 ± 0.9, where the O/C ratios are within experimental error for the 5 and 15 min treated pellets. Often, uniquely shaped materials (e.g., nanoparticles, nanowires) are suspended in a solution (e.g., methanol or ethanol) and then applied to glass or Si substrates prior to plasma treatment.[39,47,48] Native zeolite powder was secured to glass slides with C tape for SEM analysis, where isolated zeolites are visible at 25x magnification (Figure 5.1a), compared to the smoother surface of the zeolite pellet at the same magnification (Figure 5.1b). These morphological differences may explain the need for a longer treatment time (15 min) to oxidize the 3D native zeolites. Additionally, these materials may benefit from utilizing a rotating reactor system, wherein the free, unsupported particles are rotated throughout plasma processing.[49] A rotating drum rf reactor that can be interfaced to the plasma reactor shown in Figure 1c, was previously employed to functionalize Fe_2O_3 nanoparticles via allyl alcohol discharges.[50]

Table 5.5 XPS atomic compositions for untreated and H_2O (v) treated zeolite constructs[a,b]

precursor	construct	*t* (min)	C (%)	O (%)	Si (%)	Al (%)	Si/Al	O/Si	O/C
untreated	native	--	19.9 (4.8)	58.4 (3.2)	17.5 (1.4)	4.4 (0.6)	3.8 (0.6)	3.5 (0.3)	2.5 (0.4)
	pellet	--	22.7 (7.0)	57.5 (4.0)	15.5 (2.6)	4.4 (0.6)	3.5 (0.2)	3.8 (0.5)	2.8 (0.8)
H_2O	native	5	22.3 (3.4)	55.9 (2.1)	17.1 (1.2)	4.8 (0.5)	3.5 (0.4)	3.3 (0.1)	2.6 (0.5)
		15	14.0 (2.4)	62.5 (1.3)	20.6 (0.7)	2.8 (2.3)	3.2 (2.6)	3.0 (0.1)	4.6 (0.9)
	pellet	5	13.6 (1.2)	63.7 (1.4)	17.5 (0.3)	5.2 (0.3)	3.4 (0.2)	3.6 (0.1)	4.7 (0.4)
		15	15.2 (1.4)	60.4 (0.8)	19.3 (0.7)	5.2 (0.2)	3.7 (0.3)	3.1 (0.08)	4.0 (0.4)

[a]All analyses were performed for an n = 9; the mean standard deviation are reported

[b]Treatments were performed at p = 100 mTorr, P = 100 W in the coil region

These preliminary results reporting $H_2O_{(v)}$ treatments of the native zeolites were included here to highlight the wide tunability of plasma processing, where operating conditions (e.g., power, pressure, time), discharge configuration (e.g., static, rotating, pulsed), and precursors (O_2, H_2O, allyl alcohol) can be varied to optimize performance for a given application.

The placement of a substrate within the plasma reactor can impact the resulting surface functionalization. For example, previous work in the Fisher group showed that positioning polymeric ultrafiltration membranes downstream within an $H_2O_{(v)}$ plasma increased hydrophilicity while avoiding damage to the polymeric material.[45,46] Polymers are particularly suspectable to morphological damage at increased pressures and powers; therefore $H_2O_{(v)}$ treatments of these materials are usually at $P \leq 50$W or positioned downstream from the energetic coil region.[45,46,51] The zeolites, however, were exposed to an $H_2O_{(v)}$ plasma (100 mTorr, 100 W) for 15 min without substantial morphological changes, Figure 5.13. Nevertheless, a substrate position study was performed, where wettability was measured for pellets treated 15, 20, and 35 cm downstream from the upstream side of the coil (Figure 2.1b). Detailed in Table 5.6, absorptions rates were within experimental error following a p = 100 mTorr, P = 100 W, t = 5 min treatment, regardless of position in the reactor. Under these conditions, the plasma visually appears homogenous throughout the entire length of the reactor, therefore it is likely energetic plasma species (e.g., O, OH, H) are still interacting with downstream substrates. To further assess this hypothesis, a distance study was performed at p = 100 mTorr, P = 25 W, t = 5 minutes, Table 5.6. Preliminary data reveal a 20 cm downstream placement yields an enhanced absorption rate for materials treated at P = 25 W. As the zeolite is placed farther downstream (35 cm), the absorption rate decreases to 0.63 ± 0.10 μLs^{-1}, likely due to fewer energetic species-surface interactions.

Table 5.6. Average absorption rate for plasma-modified zeolite pellets[a,b]

Precursor	distance (cm)	*P* (W)	Rate (µL/ s)
Untreated	--	--	0.19 (0.022)
H_2O	coil	25	0.45 (0.052)
		100	1.29 (0.34)
	15	25	0.77 (0.048)
		100	0.90 (0.09)
	20	25	0.97 (0.033)
		100	1.01 (0.28)
	35	25	0.63 (0.10)
		100	0.96 (0.26)

[a]All analyses were performed for an $n \geq 3$; the mean and standard deviation are reported

[b]p = 100 mTorr, t = 5 minutes

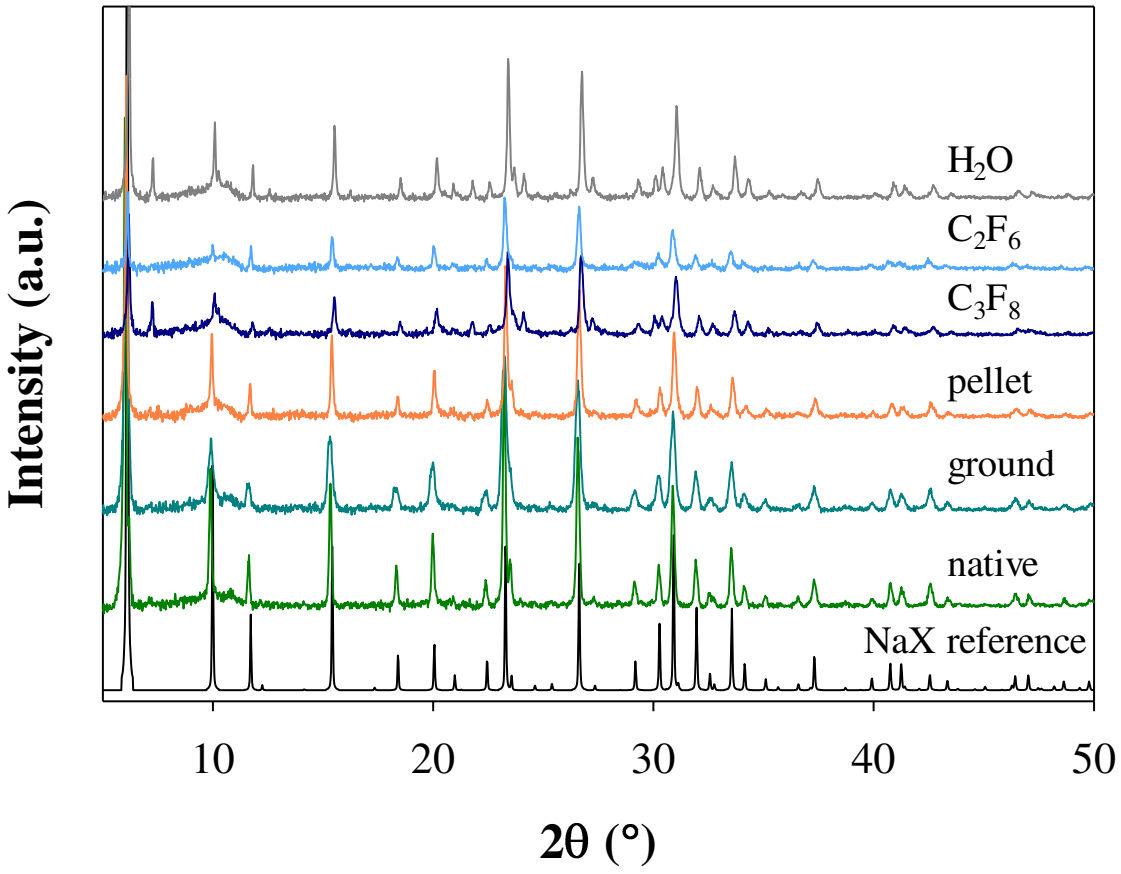

Figure 5.15. PXRD patterns for NaX reference zeolite; untreated native (as-received), ground, and pressed zeolite pellets; as well as C_3F_8, C_2F_6, and H_2O treated zeolite pellets. All treatments were performed at 100 mTorr, 100 W, 5 minutes.

These data show the ability to increase the hydrophilicity of zeolite pellets with an $H_2O_{(v)}$ plasmas, without generating excess waste (i.e., acid modification).

Described in Section 5.1, acid and CF_4 plasmas have previously introduced structural damage to the zeolite framework. Plasma modification, however, is often described as a powerful strategy to modify surfaces while maintaining bulk properties. Therefore, PXRD data were collected through each step of the pellet fabrication process, as well as after FC and H_2O plasma treatments, Figure 5.15, to assess any changes in material crystallinity. The black trace corresponds to a reference NaX diffraction pattern obtained from the International Zeolite Association database.[52] The diffraction patterns depicted in Figure 5.15 nominally demonstrate the bulk crystallinity of the material is unaffected by the formation of pellets or by plasma processing.

5.3 Summary

Zeolites are microporous, aluminosilicate materials that, despite their extensive use in a variety of applications, the ability to control the surface properties of zeolites remains unoptimized. Here, plasma modification strategies were employed over a range of fluorocarbon precursors, as well as $H_2O_{(v)}$ to tune the wettability of zeolite substrates. XPS analysis revealed surface fluorination and/or formation of hydrophobic coating on the material under conditions when the F/C ratio of the feed gas is lowered. Under certain experimental conditions, C_2F_6 plasma treatments created a more hydrophilic surface, suggesting competitive etching and depositing regimes within fluorocarbon plasmas that are heavily influenced by operating conditions and precursor. $H_2O_{(v)}$ plasmas were also employed to create a more hydrophilic zeolite surface, while maintaining a porous, interconnected network. Regardless of surface treatment, the bulk crystallinity of the zeolite constructs was unchanged, verified by X-ray diffraction.

By also studying the gas-phase, we can glean how the material changes the plasma environment. Time-resolved emission spectroscopy was employed to *in situ* probe relative densities of key gas-phase species. The increased density of etch products (i.e., CO) in the gas-phase further corroborate the competing surface modification processes within fluorinated plasma systems. Moreover, our approach to understand the fundamental plasma chemistry allows us to provide significant insight into mechanisms that will ultimately provide a more thorough evaluation of plasma processing for zeolite surface modification. In addition to the surface modification of zeolite pellets, brief coverage of a zeolite-fiber fabrication scheme with plasma calcination is provided. After electrospinning zeolite-PVP fibers, O_2 and Ar plasmas were used to remove the polymeric phase, ultimately revealing zeolite fibers. Consequently, plasma technology has an enormous potential to modify and fabricate new zeolite constructs, increasing the potential utility and performance of these microporous materials. Ultimately, the study herein revealed important connections between gas-phase species, the gas-surface interface, and the resulting plasma modified surface properties for zeolite materials.

REFERENCES

1. Ammerlahn, C.; Fisher, E. R. Plasma Surface Modification of Zeolite Materials. Universitat Duisburg-Essen 2015.
2. Davis, M. E., Ordered Porous Materials for Emerging Applications. *Nature* **2002**, *417*, 813-821.
3. Cundy, C. S.; Cox, P. A., The Hydrothermal Synthesis of Zeolites: History and Development from the Earliest Days to the Present Time. *Chem. Rev.* **2003**, *103*, 663-702.
4. Misaelides, P., Application of Natural Zeolites in Environmental Remediation: A Short Review. *Microporous Mesoporous Mater.* **2011**, *144*, 15-18.
5. Ramos-Martinez, V. H.; Ramirez-Vargas, E.; Medellin-Rodriguez, F. J.; Ávila-Orta, C. A.; Gallardo-Vega, C. A.; Jasso-Salcedo, A. B.; Andrade-Guel, M. L., Zeolite 13X Modification with Gamma-aminobutyric Acid (GABA). *Microporous Mesoporous Mater.* **2020**, *295*, 109941.
6. Liu, J.; Cheng, X.; Zhang, Y.; Wang, X.; Zou, Q.; Fu, L., Zeolite Modification for Adsorptive Removal of Nitrite From Aqueous Solutions. *Microporous Mesoporous Mater.* **2017**, *252*, 179-187.
7. Shi, J.; Yang, Z.; Dai, H.; Lu, X.; Peng, L.; Tan, X.; Shi, L.; Fahim, R., Preparation and Application of Modified Zeolites as Adsobents in Wastewater Treatment. *Water Sci. Technol.* **2018**, *2017*, 621-635.
8. Zhang, P.; Ding, W.; Zhang, Y.; Liu, W., Heavy Metal Ions Removal From Water Using Modified Zeolite. *J. Chem. Pharm. Res.* **2014**, *6*, 507-514.
9. Caballero, I.; Colina, F. G.; Costa, J., Synthesis of X-type Zeolite from Dealuminated Kaolin by Reaction with Sulfuric Acid at High Temperature. *Ind. Eng. Chem. Res.* **2007**, *46*, 1029-1038.
10. Al-Harahsheh, M.; Shawabkeh, R.; Al-Harahsheh, A.; Tarawneh, K.; Batiha, M. M., Surface Modification and Characterization of Jordanian Kaolinite: Application for Lead Removal from Aqueous Solutions. *Appl. Surf. Sci.* **2009**, *255*, 8098-8103.
11. Wang, C.; Leng, S.; Guo, H.; Cao, L.; Huang, J., Acid and Alkali Treatments for Regulation of Hydrophilicity/Hydrophobicity of Natural Zeolite. *Appl. Surf. Sci.* **2019**, *478*, 319-326.
12. Malekian, R.; Abedi-Koupai, J.; Eslamian, S. S.; Mousavi, S. F.; Abbaspour, K. C.; Afyuni, M., Ion-Exchange Process for Ammonium Removal and Release Using Natural Iranian Zeolite. *Appl. Clay Sci.* **2011**, *51*, 323-329.
13. Munoz, R. A.; Beving, D.; Yan, Hydrophilic Zeolite Coatings for Improved Heat Transfer. *Ind. Eng. Chem. Res.* **2005**, *44*, 4310-4315.
14. Lopes, A. C.; Martins, P.; Lanceros-Mendez, S., Aluminosilicate and Aluminosilicate Based Polymer Composites: Present Status, Applications and Future Trends. *Prog. Surf. Sci.* **2014**, *89*, 239-277.
15. Nikolopoulou, M.; Pasadakis, N.; Kalogerakis, N., Evaluation of Autochthonous Bioaugmentation and Biostimulation During Microcosm-simulated Oil Spills. *Mar. Pollut. Bull.* **2013**, *72*, 165-173.
16. Xue, Z.; Cao, Y.; Liu, N.; Feng, L.; Jiang, L., Special Wettable Materials for Oil/Water Separation. *J. Mater. Chem. A* **2014**, *2*, 2445-2460.
17. He, C.-T.; Jiang, L.; Ye, Z.-M.; Krishna, R.; Zhong, Z.-S.; Liao, P.-Q.; Xu, J.; Ouyang, G.; Zhang, J.-P.; Chen, X.-M., Exceptional Hydrophobicity of a Large-Pore Metal–Organic Zeolite. *J. Am. Chem. Soc.* **2015**, *137*, 7217-7223.

18. Furukawa, K.; Tian, S. R.; Yamauchi, H.; Yamazaki, S.; Ijiri, H.; Ariga, K.; Muraoka, K., Characterization of H–Y Zeolite Modified by a Radio-Frequency CF_4 Plasma. *Chem. Phys. Lett.* **2000**, *318*, 22-26.
19. Flamm, D. L.; Donnelly, V. M.; Ibbotson, D. E., Basic Chemistry and Mechanisms of Plasma Etching. *J. Vac. Sci. Technol., B* **1983**, *1*, 23-30.
20. Hanna, A. R.; Fisher, E. R., Efforts Towards Unraveling Plasma Assisted Catalysis: Determination of Kinetics and Molecular Temperatures within N_2O Discharges. *ACS Catal.* **2020**, *manuscript in revision*.
21. Goergen, S.; Saada, M. A.; Soulard, M.; Rouleau, L.; Patarin, J., Dry Gel Conversion Synthesis of Shape Controlled MFI Type Zeolite Materials. *J. Porous Mater.* **2010**, *17*, 635-641.
22. Zhang, J.; Luo, M.; Xiao, H.; Dong, J., Interferometric Study on the Adsorption-Dependent Refractive Index of Silicalite Thin Films Grown on Optical Fibers. *Chem. Mater.* **2006**, *18*, 4-6.
23. Wang, Z.; Ge, Q.; Shao, J.; Yan, Y., High Performance Zeolite LTA Pervaporation Membranes on Ceramic Hollow Fibers by Dipcoating−Wiping Seed Deposition. *J. Am. Chem. Soc.* **2009**, *131*, 6910-6911.
24. Anis, S. F.; Khalil, A.; Saepurahman; Singaravel, G.; Hashaikeh, R., A Review on the Fabrication of Zeolite and Mesoporous Inorganic Nanofibers Formation for Catalytic Applications. *Microporous Mesoporous Mater.* **2016**, *236*, 176-192.
25. Huang, Z.-M.; Zhang, Y. Z.; Kotaki, M.; Ramakrishna, S., A Review on Polymer Nanofibers by Electrospinning and Their Applications in Nanocomposites. *Compos. Sci. Technol.* **2003**, *63*, 2223-2253.
26. Zhang, G.; Song, A.; Duan, Y.; Zheng, S., Enhanced Photocatalytic Activity of TiO_2/Zeolite Composite for Abatement of Pollutants. *Microporous Mesoporous Mater.* **2018**, *255*, 61-68.
27. Macías, M.; Chacko, A.; Ferraris, J. P.; Balkus, K. J., Electrospun Mesoporous Metal Oxide Fibers. *Microporous Mesoporous Mater.* **2005**, *86*, 1-13.
28. Di, J.; Zhao, Y.; Yu, J., Fabrication of Molecular Sieve Fibers by Electrospinning. *J. Mater. Chem.* **2011**, *21*, 8511-8520.
29. Anis, S. F.; Hashaikeh, R., Electrospun Zeolite-Y fibers: Fabrication and Morphology Analysis. *Microporous Mesoporous Mater.* **2016**, *233*, 78-86.
30. Hawker, M. J.; Pegalajar-Jurado, A.; Fisher, E. R., Innovative Applications of Surface Wettability Measurements for Plasma-Modified Three-Dimensional Porous Polymeric Materials: A Review. *Plasma Process. Polym.* **2015**, *12*, 846-863.
31. d'Agostino, R.; Cramarossa, F.; Fracassi, F.; Illuzzi, F., 2 - Plasma Polymerization of Fluorocarbons. In *Plasma Deposition, Treatment, and Etching of Polymers*, d'Agostino, R., Ed. Academic Press: San Diego, 1990; pp 95-162.
32. Cuddy, M. F.; Fisher, E. R., Investigation of the Roles of Gas Phase CF_2 and F During FC Processing of Si and ZrO_2 *J. Appl. Phys.* **2010**, *108*, 033303.
33. Cuddy, M.; Blechle, J.; Fisher, E., Ion Contributions to Gas-Surface Interactions in Inductively-Coupled Fluorocarbon Plasmas. *Int. J. Mass Spectrom.* **2012**, *330-332*.
34. Hawker, M. J.; Pegalajar-Jurado, A.; Fisher, E. R., Conformal Encapsulation of Three-Dimensional, Bioresorbable Polymeric Scaffolds Using Plasma-Enhanced Chemical Vapor Deposition. *Langmuir* **2014**, *30*, 12328-12336.

35. Cuddy, M. F.; Fisher, E. R., Contributions of CF and CF_2 Species to Fluorocarbon Film Composition and Properties for C_xF_y Plasma-Enhanced Chemical Vapor Deposition. *ACS Appl. Mater. Interfaces* **2012**, *4*, 1733-1741.
36. Welker, R. W., Chapter 4 - Size Analysis and Identification of Particles. In *Developments in Surface Contamination and Cleaning*, Kohli, R.; Mittal, K. L., Eds. William Andrew Publishing: Oxford, 2012; pp 179-213.
37. Cuddy, M. F. Contributions of Gas-Phase Plasma Chemisry to Surface Modifications and Gas-Surface Interations: Investigations of Fluorocarbon rf Plasmas. Colorado State University, ProQuest Dissertations Publishing, 2012.
38. Hanna, A. R.; Van Surksum, T. L.; Fisher, E. R., Investigating the Impact of Catalysts on N_2 Rotational and Vibrational Temperatures in Low Pressure Plasmas. *J. Phys. D: Appl. Phys.* **2019**, *52*, 345202.
39. Stuckert, E. P.; Fisher, E. R., Ar/O_2 and H_2O Plasma Surface Modification of SnO_2 Nanomaterials to Increase Surface Oxidation *Sens. Actuators B* **2015**, *208*, 379-388.
40. Stuckert, E. P.; Miller, C. J.; Fisher, E. R., The Effect of Ar/O_2 and H_2O Plasma Treatment of SnO_2 Nanoparticles and Nanowires on Carbon Monoxide and Benzene Detection. *ACS Appl. Mater. Interfaces* **2017**, *9*, 15733-15743.
41. De Velasco-Maldonado, P. S.; Hernández-Montoya, V.; Montes-Morán, M. A.; Vázquez, N. A.-R.; Pérez-Cruz, M. A., Surface Modification of a Natural Zeolite by Treatment with Cold Oxygen Plasma: Characterization and Application in Water Treatment. *Appl. Surf. Sci.* **2018**, *434*, 1193-1199.
42. Grill, A., *Cold Plasma Materials Fabrications: From Fundamentals to Applications*. IEEE Press: Piscataway, NJ, 1994.
43. Gao, J.; Zhu, X.; Bian, Z.; Jin, T.; Hu, J.; Liu, H., Paving the Way for Surface Modification in One-Dimensional Channels of Mesoporous Materials Via Plasma Treatment. *Microporous Mesoporous Mater.* **2015**, *202*, 16-21.
44. Fahmy, A.; Elzaref, A.; Youssef, H.; Shehata, H.; Wassel, M.; Friedrich, J.; Poncin, F.; Debarnot, D., Plasma O_2 Modifies the Structure of Synthetic Zeolite-A to Improve the Removal of Cadmium Ions From Aqueous Solutions. *Turk. J. Chem.* **2019**, *43*, 172-184.
45. Tompkins, B. D.; Dennison, J. M.; Fisher, E. R., H_2O Plasma Modification of Track-Etched Polymer Membranes for Increased Wettability and Improved Performance. *J. Membr. Sci.* **2013**, *428*, 576-588.
46. Pegalajar-Jurado, A.; Mann, M. N.; Maynard, M. R.; Fisher, E. R., Hydrophilic Modification of Polysulfone Ultrafiltration Membranes by Low Temperature Water Vapor Plasma Treatment to Enhance Performance. *Plasma Process. Polym.* **2016**, *13*, 598-610.
47. Shearer, J.; Fisher, E., Enhancing Surface Functionality of Supported Fe_2O_3 Nanoparticles Using Pulsed Plasma Deposition of Allyl Alcohol. *Nanosci. Nanotechnol. Lett.* **2013**, *4*, 358-363.
48. Shearer, J. C.; Fisher, M. J.; Hoogeland, D.; Fisher, E. R., Composite SiO_2/TiO_2 and Amine Polymer/TiO_2 Nanoparticles Produced Using Plasma-Enhanced Chemical Vapor Deposition. *Appl. Surf. Sci.* **2010**, *256*, 2081-2091.
49. Trevino, K. Understanding the Molecular-Level Chemistry of Water Plasmas and the Effects of Surface Modification and Deposition on a Selection of Oxide Substrates. Colorado State University, ProQuest Dissertations Publishing, 2011.
50. Shearer, J. C.; Fisher, E. R., Design and Operation of a Rotating Drum Radio Frequency Plasma Reactor for the Modification of Free Nanoparticles. *Rev. Sci. Instrum.* **2013**, *84*, 063904.

51. Steen, M. L.; Jordan, A. C.; Fisher, E. R., Hydrophilic Modification of Polymeric Membranes by Low Temperature H_2O Plasma Treatment. *J. Membr. Sci.* **2002**, *204*, 341-357.
52. Olson, D. H., Zeolites. Structure Commission of the International Zeolite Association 1995; pp 439-443.

CHAPTER 6

USING FUNDAMENTAL SPECTROSCOPY TO ELUCIDATE KINETIC AND ENERGETIC MECHANIMS WITHIN ENVIRONMENTALLY RELEVANT INDUCTIVELY COUPLED PLASMA SYSTEMS[a]

This chapter focuses on energy partitioning for NO and N_2 molecules formed from several nitrogen- and oxygen-containing plasma systems. The work presented here examines plasma gas-phase phenomena, with a focus on the determination of electron, vibrational, and rotational temperatures for both nitric oxide and molecular nitrogen as a function of plasma parameters. These energetic data have been combined with kinetic rate constants, determined previously by Dr. J. M. Blechle,[1] to provide a more holistic approach to understanding gas-phase plasma phenomena.

[a] Reproduced with permission from an invited article published in *Journal of Physical Chemistry A* virtual special issue "Veronica Vaida Fetschrift" by Angela R. Hanna, Joshua M. Blechle, and Ellen R. Fisher.

6.1 Introduction

Nitrogen oxides (N_xO_y) have long been the focus of numerous research investigations, from fundamental characterization to technologically relevant advancements.[2-4] A seemingly simple heteronuclear diatom, NO is the object of significant inquiry, as it participates in many biological processes including blood pressure regulation, coagulation, antimicrobial action, and controlled drug release.[5-8] NO_X have also been studied because of their environmental impact, where reactions between nitric oxide and related byproducts can be detrimental to the atmosphere.[9] The need to understand reactions involving N_xO_y species arises from a distinct concern with increasing water and air pollution, where anthropogenic sources such as industrial and vehicular combustion are major pollution contributors. The byproducts of N_xO_y reactions, closely monitored by the Environmental Protection Agency, include contaminates that contain primarily N_xO_y species, carbon monoxide, lead, particulate matter, and volatile organic compounds (VOCs).[10,11] Both N_xO_y species and VOCs can react with sunlight to produce photochemical smog,[9] where secondary organic aerosols (SOA) can be produced in the atmosphere through the oxidation of VOCs. These aerosols are a major component of fine particle pollution and have been linked to heart and lung disease.[12,13]

In the arena of fundamental atmospheric science, Vaida and co-workers have investigated the molecular mechanisms and dynamics of sunlight-initiated atmospheric reactions, where the nature of photochemistry is both molecule and environment-specific.[14] Utilizing fundamental, gas-phase spectroscopy, Vaida and co-authors identified and characterized vibrational overtone transitions of the OH-stretch within pyruvic acid, a key species in SOA formation.[15]

Understanding foundational spectroscopic principles is essential to understanding the role of these compounds within the atmosphere, a holistic approach that is directly parallel to the work

presented herein. Furthermore, spectroscopic analysis is a key methodology employed to examine the dynamics of unimolecular reactions, where knowledge of mechanisms and kinetic formation for multiple electronic states can be obtained.[14,16] It is of fundamental and practical importance to elucidate the physical and chemical properties that are determining factors in the lifetime and atmospheric impact of environmentally-relevant species, such as SOA, VOCs, and N_xO_y.

One technique to abate atmospheric pollutants (e.g., N_xO_y derivatives) from vehicular exhaust is via three-way catalytic converters (TWCs).[17] Since the implementation of TWCs in vehicles in 1981, nitrate levels in various water sources throughout the United States have decreased.[18] Using catalytic processes, several approaches have been explored to improve NO decomposition and nitrogen oxide species removal. These efforts include the investigation of a range of catalytic materials, photocatalytic decomposition, and plasma-assisted catalysis (PAC).[19-21] PAC has been recently investigated because of the non-thermal nature of the plasmas employed (allowing access to thermally unfavorable processes), as well as the enormous potential to increase feed gas conversion.[22] The state of knowledge regarding PAC systems remains largely phenomenological;[23] ultimately for PAC to become a viable method for pollution control, the fundamental chemistry of precursor gases must be fully elucidated, before and after substrates are introduced to the discharge.[24]

Optical plasma diagnostics provide a non-intrusive platform to obtain molecular-level information; from measuring energy partitioning in gas-phase species (electrons, neutral and excited species) and the kinetics of species formation and destruction.[25] For example, understanding how energy is dispersed into rotational and vibrational modes of a particular gas-phase molecule during N_xO_y plasma processing can provide insight into molecule formation

mechanisms, decomposition pathways, and overall plasma chemistry.[26,27] Several spectroscopic techniques have been used to measure rotational (T_R) and vibrational temperatures (T_V) of plasma species, including Doppler broadening analysis of spectral lines,[28] laser-induced fluorescence,[29] optical emission spectroscopy (OES),[30] and broadband absorption spectroscopy (BAS).[31-33] All have inherent advantages (e.g., non-intrusive, molecule-specific) and disadvantages (e.g., limited to molecules with optically-active transitions; limited to either excited or ground state molecules); therefore, we have employed a combination of spectroscopic techniques (OES and BAS) to achieve a more complete examination of plasma phenomena.

Non-thermal, low temperature plasmas comprise a variety of high energetic electrons, ions, atoms, and molecules; plasma molecules typically follow a relationship wherein T_V is greater than T_R or translational temperatures, and each of these characteristic temperatures is significantly lower than electron (T_e) and ion temperatures.[34,35] Although N_2 energetic studies have been performed for various plasma sources,[36-38] there is a lack of foundational data for energy partitioning within plasma systems relevant to PAC. We have also employed time-resolved OES (TR-OES) to probe changes in plasma species density over time, yielding insight into the possible mechanisms of species formation and decay within N_xO_y plasma systems. The use of TR-OES to examine the temporal evolution of plasma species has been limited,[39-41] especially regarding the formation of molecular species within continuous-wave systems. Therefore, this work seeks to demonstrate the utility of TR-OES in elucidating formation kinetics and relevant mechanistic information for continuous-wave, non-thermal plasma systems.[42,43]

For this study, we performed two different sets of experiments to determine some of the fundamental plasma chemistry: (1) examining energy partitioning within steady-state, continuous wave plasmas and (2) measuring rate constants with TR-OES. The BAS and OES data presented

herein focuses on exploiting absorption and emission transitions, respectively for N_2 ($B^3\Pi_g \leftrightarrow C^3\Pi_u$) and NO ($X^2\Pi \leftrightarrow A^2\Sigma^+$) to determine energy distributions within N_2, N_2O, and mixed N_2/O_2 plasmas. In addition, we use TR-OES data to determine formation and destruction rate constants. These results are also compared to previously reported results from 100% NO plasmas.[31] By using multiple techniques, with a focus on *in situ* probing of plasma chemistry, a more complete understanding of plasma chemistry phenomena can be gained, regardless of end applications.

6.2 Results

The data presented herein focus on the gas-phase energy distributions between multiple degrees of freedom within N_xO_y plasma systems and the corresponding kinetic relationships. A multitude of ground and excited state species are generated in these systems, paramount of these are NO and N_2, as they are the primary pollutant and the desired by-product in remediation systems, respectively. Thus, we have examined the energetics (T_e, T_V, and T_R) and kinetics (k_f and k_d) of NO and N_2 as a function of plasma parameters (power, pressure, and precursor).

Plasma Energetics. Energy partitioning within a plasma can be difficult to measure as a plethora of species are simultaneously created and destroyed. Moreover, these species and their concentrations are known to vary significantly with a range of plasma parameters. In general, determining the characteristic temperatures (electron, vibrational, rotational, etc.) can provide a more complete picture of the energetics within the plasma system. Therefore, T_e values were determined from OES spectral lines, as described in detail previously,[32] to characterize the role of electrons. Table 6.1 lists T_e values for N_2, N_2O, and NO plasmas at p = 50 mTorr, P = 25 – 175 W.

Table 6.1. T_e for selected plasma systems, p = 50 mTorr[a]

***P* (W)**	**N_2 (eV)**	**N_2O (eV)**	**NO (eV)**
25	1.63 (0.03)	1.53 (0.02)	1.61 (0.02)
50	1.62 (0.03)	1.59 (0.02)	1.66 (0.03)
75	1.61 (0.02)	1.59 (0.02)	1.63 (0.03)
100	1.60 (0.02)	1.60 (0.03)	1.62 (0.03)
125	1.61 (0.03)	1.62 (0.03)	1.63 (0.03)
150	1.64 (0.03)	1.64 (0.03)	1.64 (0.03)
175	1.64 (0.03)	1.65 (0.03)	1.65 (0.03)

[a]Calculated from Ar emission lines. Values in parentheses represent standard deviation calculated from the mean of three trials

From these values, T_e clearly does not change between the three plasma systems, nor does it depend strongly on P over the range studied here. However, there appears to be a steady, albeit small, increase in T_e with P in the N_2O system (ΔT_e = 0.12 eV between 25 and 175 W).

A representative emission spectrum, acquired with OES, of the second positive system ($B^3\Pi_g \leftarrow C^3\Pi_u$) in an N_2 plasma (p = 100 mTorr, P = 150 W) is shown in Figure 6.1a, along with Specair simulated fits to the data, where T_R = 340 K, T_V = 4700 K. Figure 6.1b displays a representative absorbance spectrum ($B^3\Pi_g \rightarrow C^3\Pi_u$), acquired with BAS, obtained under the same experimental conditions, yielding T_R = 315 K, T_V = 3500 K. Important to note, these temperature values were determined for a single trial, therefore error is not reported. The fits generated in both Speciar (and LIFBASE) have a minimum 90 % peak correlation. The error associated with the reported internal temperatures in this work is the standard deviation from the mean of a minimum of three trials.

To more adequately investigate the energy partitioning between rotational and vibrational modes within N_2 plasmas, a range of pressures and plasma powers were explored. Figure 6.2a and 6.2b display P and p dependence for both T_R and T_V in the upper electronic state of N_2 ($C^3\Pi_u$). Average T_R and T_V values were also determined for the absorbing, lower electronic state N_2 species ($B^3\Pi_g$), shown as functions of both P and p in Figure 6.2c and 6.2d, respectively. Linear regression analyses for each pressure regime reveals plasma temperatures have a positive, linear dependence on P (e.g., $R^2 \geq 0.84$). Notably, for both N_2 electronic states studied here, regardless of experimental conditions, T_V values are significantly higher than T_R values, a phenomenon that is well-documented within non-thermal discharges.[35-38] Upon further examination of the OES data (Figure 6.2a and 6.2b), we see a clear, direct dependence on P for both T_R and T_V, where both temperatures decrease with increasing system p.

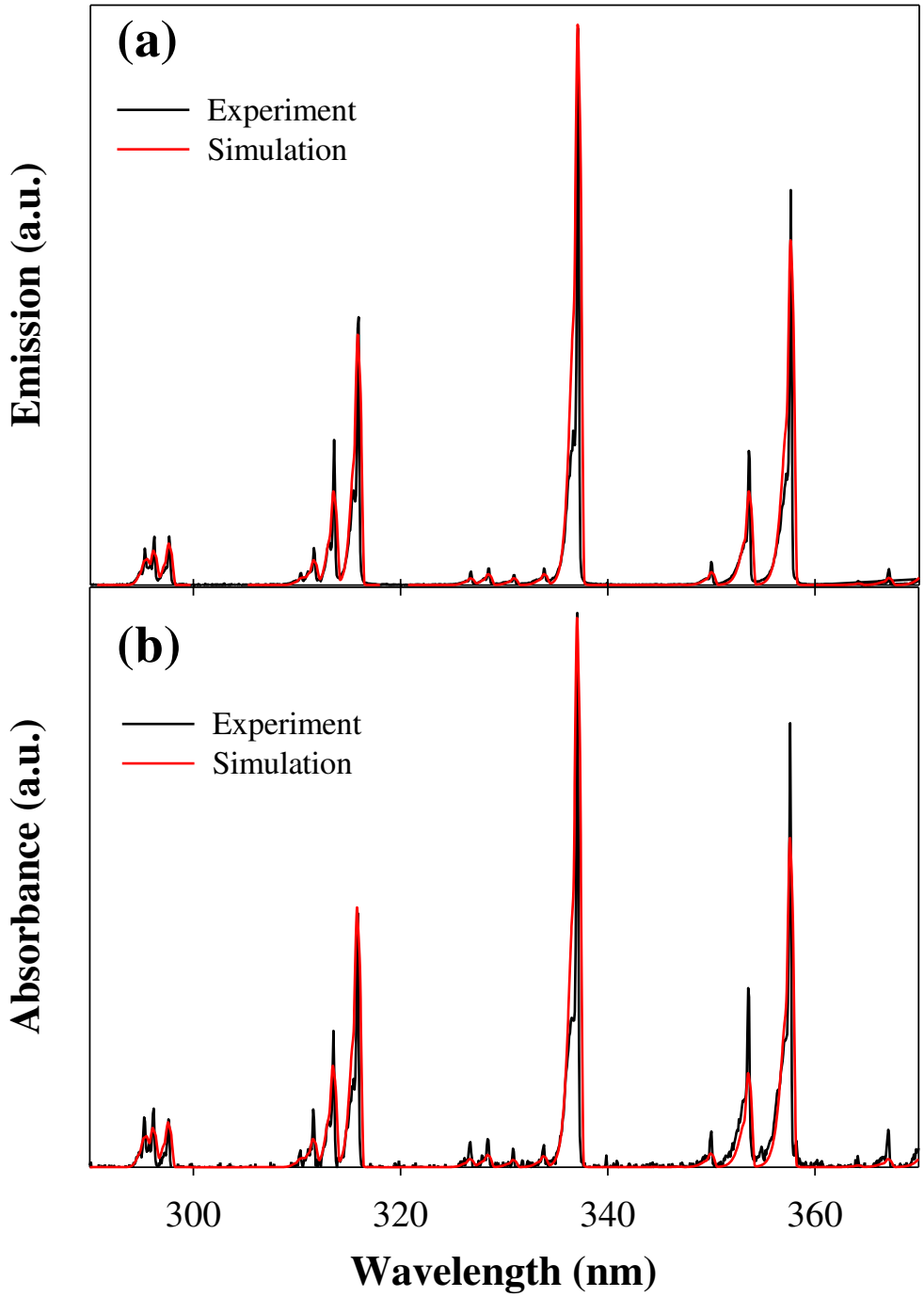

Figure 6.1. A representative (a) emission spectrum and (b) absorbance spectrum for an N_2 plasma system at p = 100 mTorr, P = 150 W. The simulations to these individual experimental spectra were acquired with (a) T_R = 340 K, T_V = 4700 K and (b) T_R = 315 K, T_V = 3500 K.

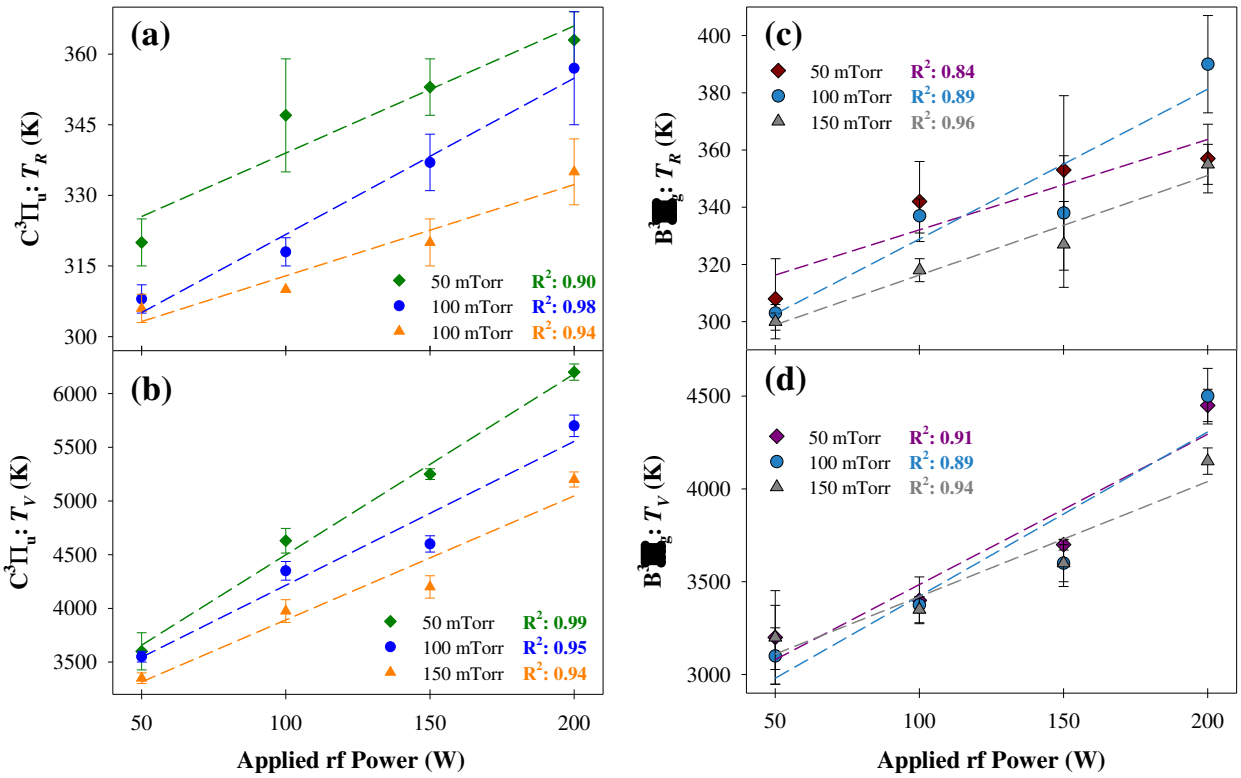

Figure 6.2. Average T_R (a,c) and T_V (b,d) values for N_2 determined from the emission (a-b) and absorbance (c-d) within N_2 plasmas are plotted as a function both of p and P. Error bars represent ±1 standard deviation from the mean ($n \geq 3$). R^2 values are reported from a linear fit.

occurring in N_xO_y systems. We therefore expanded our energy partitioning portfolio by choosing a more complex plasma precursor (e.g. N_2O) that still leads to formation of both N_2 and NO. Figure 6.3 provides representative emission and absorbance spectra for a p = 100 mTorr, P = 150 W N_2O plasma. The emission spectrum, Figure 6.3a, contains radiative bands from both NO and N_2 molecules, but the excited state N_2 molecules dominate the spectral character. In contrast, there is a clear shift in peak intensity within the N_2O absorbance spectrum, Figure 6.3b, as the NO peaks dominate. As discussed elsewhere,[44,45] directly comparing peak intensities with OES spectra can be problematic due to inconsistencies in excitation and de-excitation pathways of different plasma species. Therefore, OES and BAS were used to determine T_R and T_V values for NO and N_2 molecules formed within N_2O plasmas, summarized in Table 6.2. The relationship between T_V and P is shown in Figure 6.4 for emitting and absorbing NO and N_2 species at p = 100 mTorr. A linear regression analysis is provided for each molecule (N_2 and NO) and each electronic transition, indicating vibrational temperatures are directly correlated with P in these N_2O plasma systems ($R^2 \geq 0.90$).

In a separate set of experiments, we used mixtures of N_2 and O_2 to form our plasma. In this mixed gas system, we varied the % N_2 and O_2 in the feed gas by means of partial pressure, keeping a total system pressure of 100 mTorr. Figure 6.5 displays excited state T_V values for NO and N_2 at different P, as a function of % N_2 in the feed gas. In these systems, T_V depends strongly on P, but displays little to no dependence on % N_2. Also, T_V values for emitting N_2 molecules are elevated compared to those for emitting NO species. Tabulated data (including T_R and T_V for both NO and N_2) are provided in Table 6.3 (emission data) and Table 6.4 (absorbance

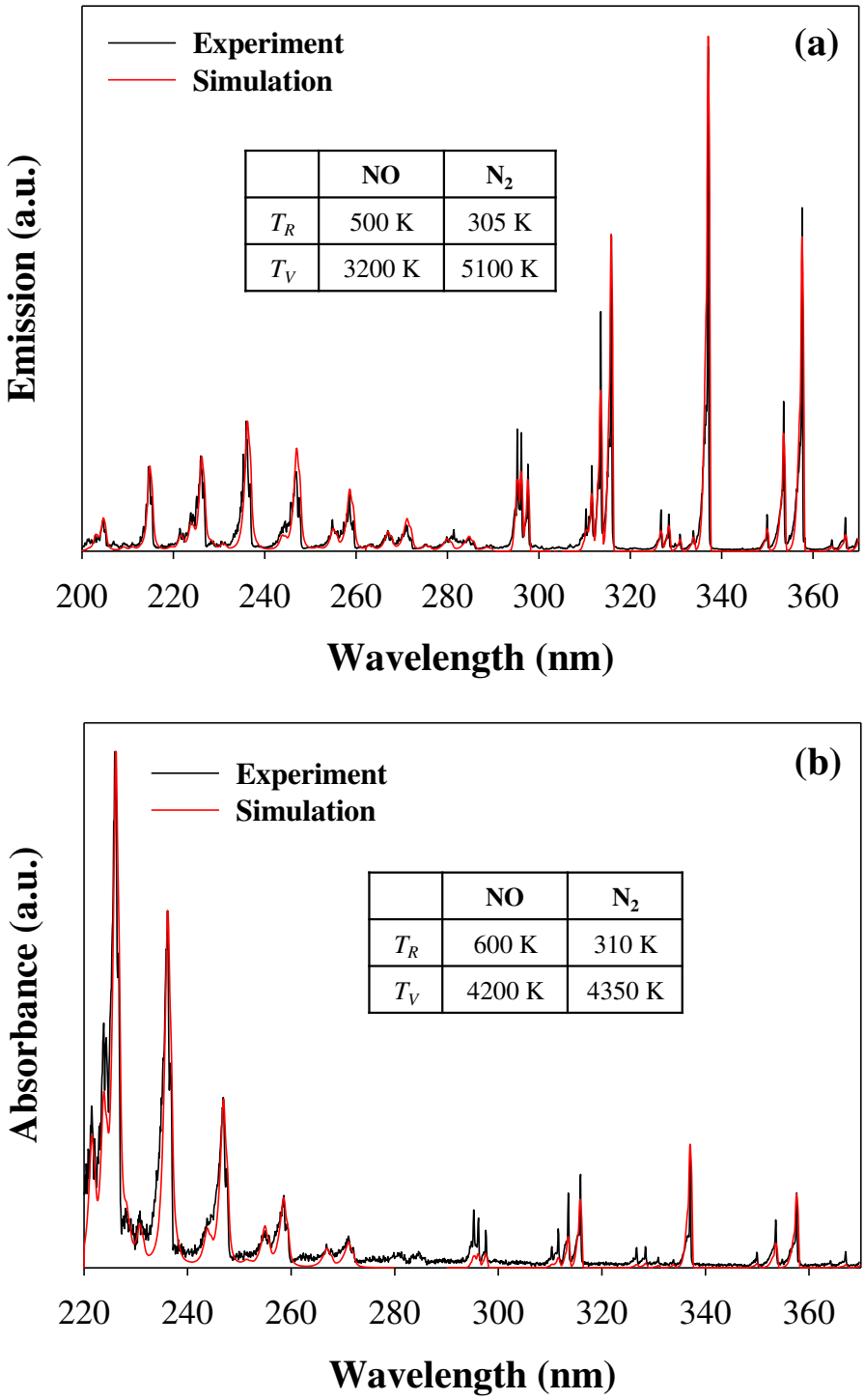

Figure 6.3. Representative (a) emission and (b) absorbance spectra for an N_2O plasma, with both NO ($X^2\Pi \leftrightarrow A^2\Sigma^+$) and N_2 ($B^3\Pi_g \leftrightarrow C^3\Pi_u$) bands fit. Internal temperatures are reported within inset tables.

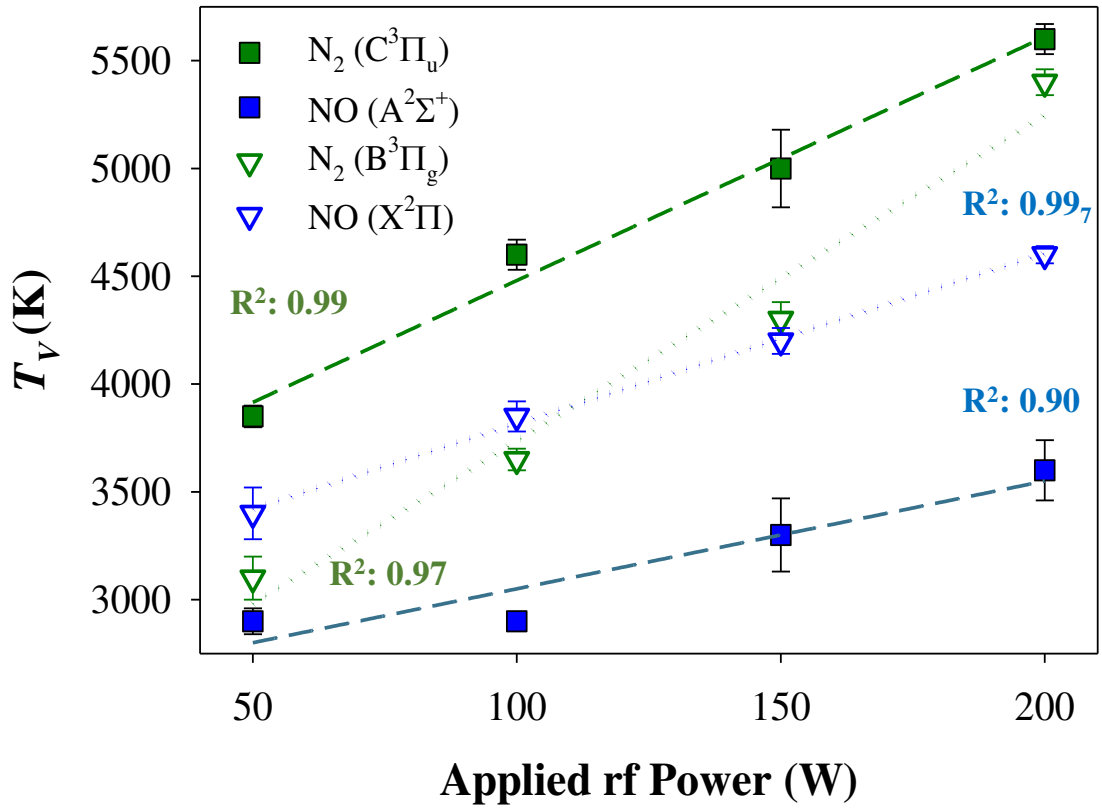

Figure 6.4. T_V values for specific states of N_2 and NO are plotted as a function of P for both emission and absorbance data from a p = 100 mTorr N_2O plasma system. Values for the lower states (N_2: $B^3\Pi_g$, NO: $X^2\Pi$) were derived from absorbance data, values for upper states (N_2: $C^3\Pi_u$, NO: $A^2\Sigma^+$) were determined from emission data. Error bars represent ±1 standard deviation from the mean ($n \geq 3$).

Table 6.2. T_R and T_V values for NO and N_2, determined from emission and absorbance of N_2O plasmas[a]

p **(mTorr)**	***P*** **(W)**	T_R **(K)**				T_V **(K)**			
		NO (X)	**NO (A)**	**N_2 (B)**	**N_2 (C)**	**NO (X)**	**NO (A)**	**N_2 (B)**	**N_2 (C)**
50	50	535 (15)	550 (15)	310 (15)	310 (10)	3200 (320)	2500 (20)	3300 (180)	3300 (50)
	100	550 (5)	575 (25)	350 (10)	320 (10)	2200 (140)	2800 (200)	3950 (70)	4000 (60)
	150	620 (20)	630 (10)	350 (25)	330 (5)	3600 (115)	2900 (15)	4500 (50)	4300 (75)
	200	740 (30)	670 (20)	500 (25)	350 (10)	4300 (200)	3400 (100)	5700 (15)	5500 (100)
100	50	460 (10)	535 (10)	310 (5)	305 (10)	3400 (120)	2900 (60)	3100 (100)	3850 (50)
	100	520 (10)	530 (5)	315 (5)	310 (5)	3850 (70)	2900 (10)	3650 (50)	4600 (70)
	150	600 (20)	520 (20)	320 (10)	310 (10)	4200 (60)	3300 (170)	4300 (80)	5000 (180)
	200	720 (20)	500 (20)	430 (5)	320 (5)	4600 (40)	3600 (140)	5400 (60)	5600 (70)
150	100	600 (10)	520 (5)	310 (5)	315 (5)	5200 (70)	2900 (30)	3400 (115)	4700 (80)
	150	640 (10)	585 (5)	325 (5)	310 (5)	5500 (140)	3000 (15)	4000 (80)	5200 (25)
	200	700 (15)	640 (10)	400 (15)	320 (5)	6300 (70)	3500 (40)	5000 (100)	5700 (50)

[a]For the NO ground state $X^2\Pi$ (denoted here by X) and the lower, $B^3\Pi_g$, N_2 state (denoted here by B) was determined from BAS measurements. The NO upper state, $A^2\Sigma^+$ (denoted by A) and the upper $C^3\Pi_u$, N_2 state (denoted here by C) was determined via OES measurements.

Table 6.3. T_R and T_V values for NO and N_2, determined from emission of N_2/O_2 plasma mixtures

N_2/O_2 p (mTorr)	P (W)	T_R (K)		T_V (K)	
		N_2	NO	N_2	NO
25: 75	50	--	--	--	--
	100	320 (10)	530 (10)	3900 (80)	3600 (40)
	150	350 (20)	560 (15)	4300 (70)	3800 (40)
	200	440 (20)	620(15)	5200 (50)	4200 (90)
50: 50	50	310 (5)	550 (20)	3300 (50)	3150 (30)
	100	320 (5)	575 (20)	4000 (60)	3500 (40)
	150	330 (5)	630 (10)	4300 (80)	3700 (20)
	200	350 (10)	670 (20)	5500 (100)	4300 (120)
75: 25	100	350 (10)	600 (5)	4150 (50)	3750 (60)
	150	380 (5)	670 (15)	4800 (80)	4000 (80)
	200	420 (20)	715 (15)	5650 (100)	4400 (80)

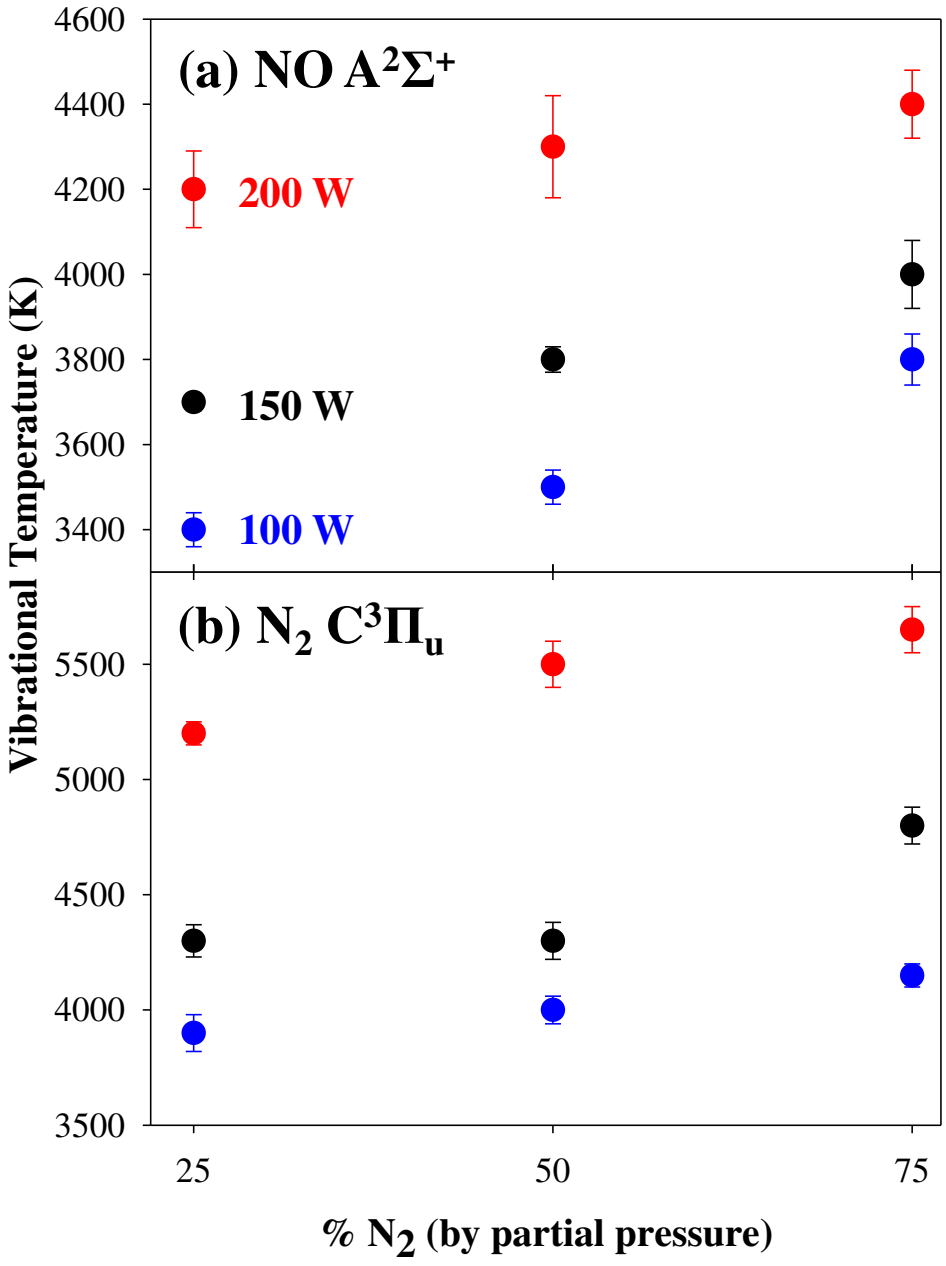

Figure 6.5. T_V values as a function of P and % N_2 in the feed gas for excited state (a) NO and (b) N_2, determined via OES.

Table 6.4. T_R and T_V values for NO and N_2, determined from absorbance of N_2/O_2 plasmas

N_2/O_2 p (mTorr)	P (W)	T_R (K)		T_V (K)	
		N_2	NO	N_2	NO
25: 75	100	330 (5)	600 (20)	3250 (70)	4700 (150)
	150	350 (10)	760 (20)	3500 (50)	4900 (60)
	200	440 (10)	860 (10)	4300 (80)	5300 (80)
50: 50	100	320 (10)	725 (20)	3300 (40)	4600 (200)
	150	370 (20)	780 (10)	3600 (80)	5300 (130)
	200	460(20)	855 (10)	4500 (70)	5400 (50)
75: 25	100	340 (5)	640 (10)	3400 (120)	4400 (170)
	150	360 (10)	670 (15)	3700 (30)	5200 (100)
	200	410 (15)	790 (10)	4600 (60)	5200 (200)

data). The analysis of steady-state plasma conditions enables us to illuminate the energy distributions occurring within these continuous wave discharges.

Plasma Kinetics. Although plasma energetics and species interactions are related to one another, temporally-resolved data are necessary to accurately probe the intricate dynamics within non-equilibrium environments. For example, species formation can result from precursor decomposition, bimolecular (or multiple) collisions, or plasma-wall reactions, all of which occur on very different time scales.[34] Here, a small subset of the reaction dynamics in N_xO_y plasmas were evaluated with TR-OES. Representative raw OES spectra are depicted in Figure 6.6 for emission collected from an NO plasma (p = 100 mTorr, P = 200 W) at various time points after plasma ignition. The spectra show an increase in N_2 emission intensity from the $B^3\Pi_u \leftarrow C^3\Pi_g$ transition (290 – 370 nm), corresponding to the time dependence of the species production. The NO emission lines from the $X^2\Pi \leftarrow A^2\Sigma^+$ transition around 200 – 280 nm also increase in intensity as t increases to 0.42 s, although it appears NO decomposes over time, nominally recombining to form N_2. These data qualitatively demonstrate there is strong time-dependent component of species production and decomposition within these plasma discharges. As described in the Chapter 2, we sought to quantify these interactions through the determination of k_f and k_d to obtain a more accurate description of molecular interactions in N_xO_y plasma systems.

Comparing the destruction of NO* (Figure 6.7a) and the formation of N_2* (Figure 6.7b) within an NO plasma system as a function of p and P allows us to elucidate kinetic trends within this parameter space. Noticeably, at p = 150 and 200 mTorr, k_d(NO*) increases slightly as P increases (Figure 6.7a). At p = 100 mTorr, k_d(NO*) values increase between 50 – 100 W and are significantly higher compared to the other pressures studied, whereas higher powers (200 W) show little to no p dependence. Shown in Figure 6.7b, k_f(N_2*) values at p = 100 mTorr are also

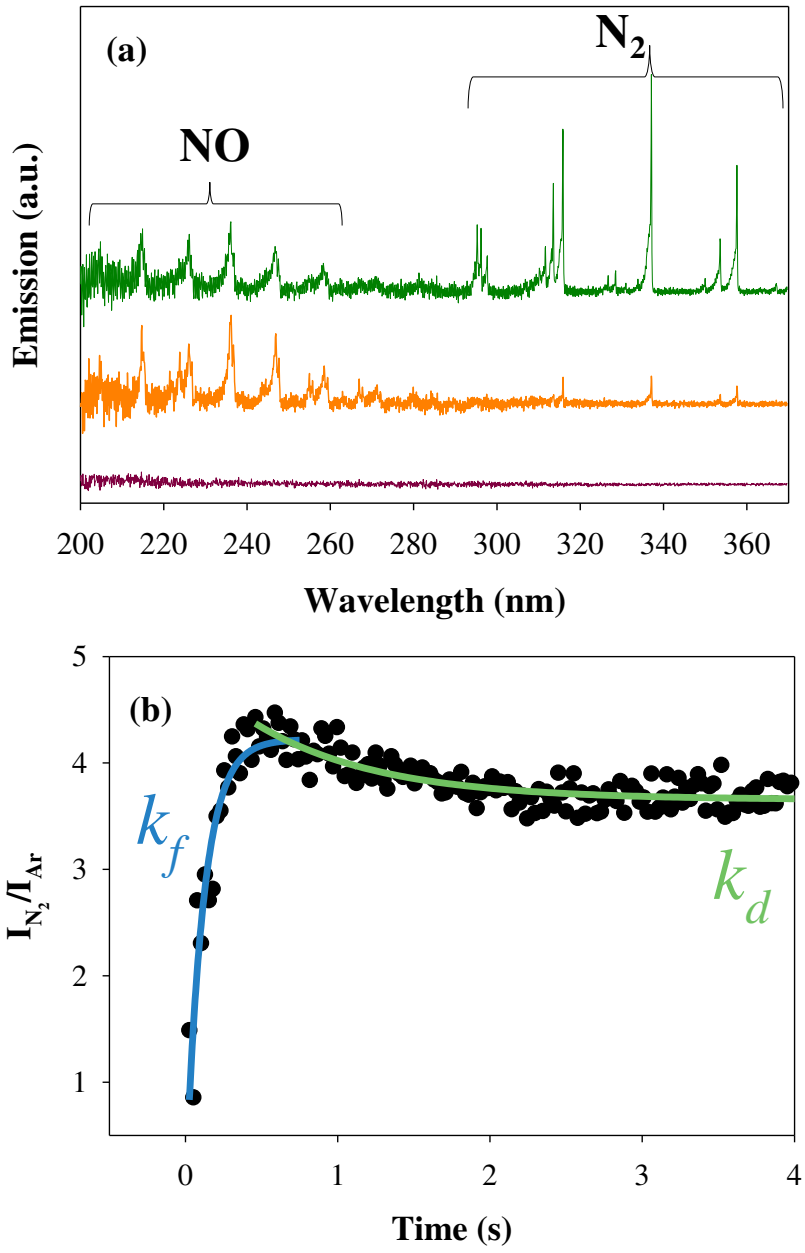

Figure 6.6. (a) Raw OES spectra collected at t = 0, 0.42, and 1.63 s after NO (p = 100 mTorr, P = 200 W) plasma ignition. (b) TR-OES profile, monitoring the relative intensity of N_2 with an Ar actinometer in a NO (p = 100 mTorr, P = 100 W) plasma. The rise and decay are fit with exponentials to determine first order rate constants of k_f and k_d, reported to be 16 ± 2 s^{-1} and 1.2 ± 0.2 s^{-1} respectively.

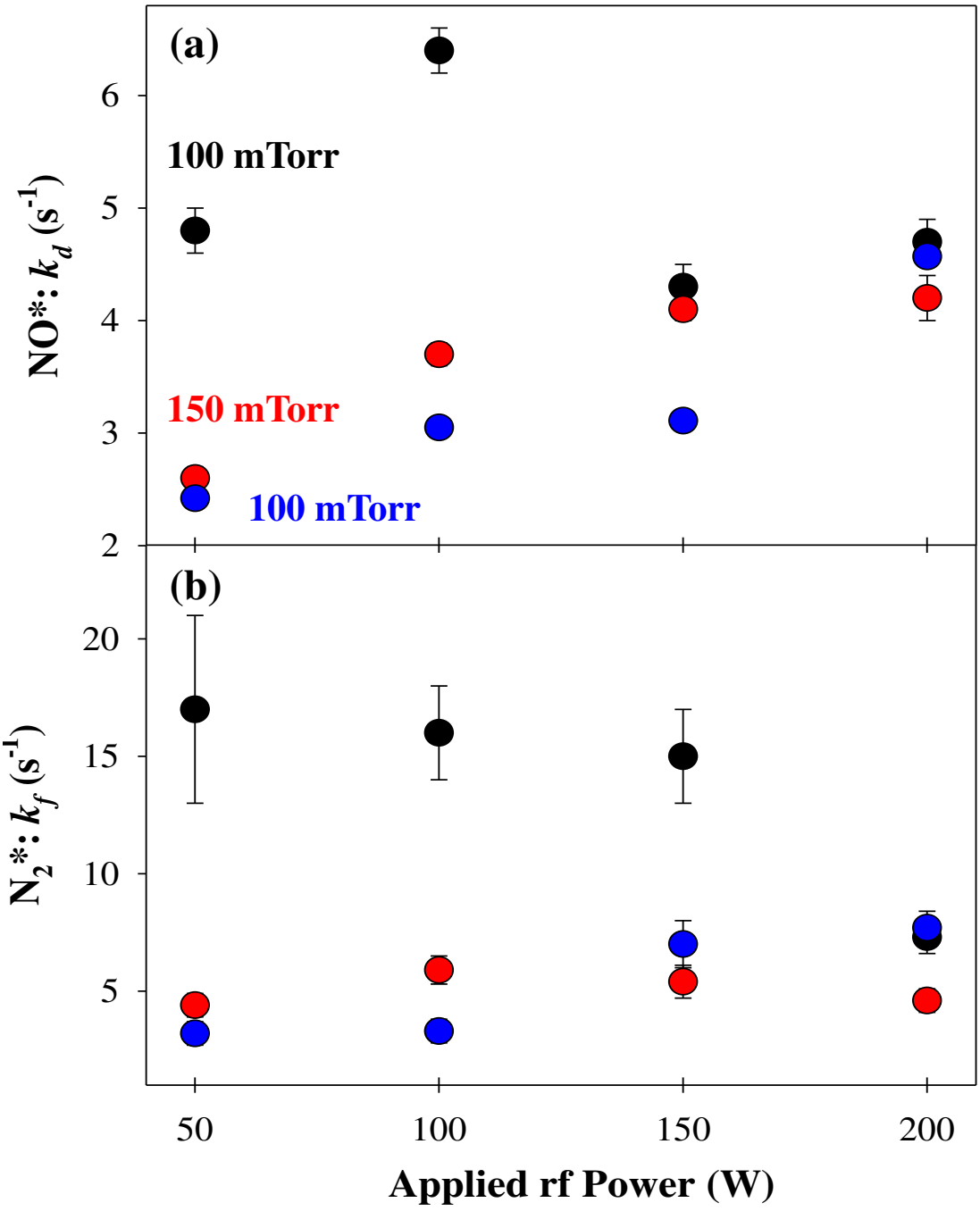

Figure 6.7. Destruction rate constants for (a) NO* and formation rate constants for (b) N_2* species formed in NO plasmas as a function of P and p.

Table 6.5. Calculated values for k_f and k_d for N_2 and NO[a]

Source	p (mTorr)	P (W)	k_f (s^{-1})		k_d (s^{-1})	
			N_2	NO	N_2	NO
NO	100	50	17 (4)	--	1.3 (0.5)	4.8 (0.2)
		100	16 (2)	--	1.2 (0.2)	6.4 (0.2)
		150	15 (2)	--	0.67 (0.02)	4.3 (0.2)
		200	7.3 (0.7)	--	0.68 (0.08)	4.7 (0.2)
	150	50	4.4 (0.5)	--	<0.1	2. 6 (0.1)
		100	5.9 (0.6)	--	0.9 (0.2)	3.7 (0.1)
		150	5.4 (0.7)	--	1.2 (0.02)	4.1 (0.1)
		200	4.6 (0.5)	--	1.0 (0.1)	4.2 (0.2)
	200	50	3.2 (0.5)	--	6 (1)	2.4 (0.05)
		100	3.3 (0.5)	--	1.1 (0.3)	3.1 (0.04)
		150	7 (1)	--	1.3 (0.2)	3.1 (0.06)
		200	7.7 (0.6)	--	1.1 (0.1)	4.6 (0.08)
N_2O	100	50	--	--	1.6 (0.5)	2.9 (0.2)
		100	5 (2)	--	2.0 (0.3)	4.3 (0.3)
		150	15 (5)	--	2.2 (0.2)	3.3 (0.2)
		200	20 (4)	--	2.0 (0.2)	4.8 (0.2)
	150	50	--	--	4.0 (0.6)	3.4 (0.2)
		100	9 (4)	--	2.3 (0.3)	5.0 (0.3)
		150	10 (8)	--	1.6 (0.1)	7.0 (0.3)
		200	6 (1)	11 (8)	1.8 (0.1)	6.9 (0.4)
	200	50	--	--	4 (2)	5 (2)
		100	--	--	3.7 (0.5)	3.3 (0.1)
		150	11 (8)	--	2.9 (0.5)	3.5 (0.1)
		200	10 (3)	--	3.3 (0.4)	2.7 (0.2)
N_2/O_2	100	50	--	NA	2.5 (0.9)	NA
		100	--	NA	1.4 (0.1)	NA
		150	--	3 (2)	1.7 (0.2)	--
		200	--	1.7 (0.5)	1.8 (0.03)	--
	150	50	--	NA	1.3 (0.5)	NA
		100	--	1.6 (0.8)	1.4 (0.2)	--
		150	--	3 (2)	2.1 (0.1)	--
		200	--	15 (8)	1.9 (0.2)	8 (3)
	200	50	--	NA		NA
		100	--	12 (4)	1.4 (0.7)	--
		150	--	11 (3)	1.3 (0.3)	--
		200	--	26 (8)	1.3 (0.1)	--

[a]"--" represents conditions where non-zero concentrations are seen, but rate constants cannot be determined. "NA" represent conditions where formation of NO cannot be observed above experimental noise.

6.3 Discussion

As described in the Introduction, plasma assisted catalysis can be a viable tool in pollution abatement, however there is a vast data gap in fundamental, gas-phase information. It is necessary to probe the distributions of energy within these non-equilibrium discharges, as they have a significant impact on the chemistry occurring in these systems. As described in Chapter 2, continuous wave discharges were ignited via rf power, where energy from the rf source can be transferred to electrons, internal and translational energy of atoms, molecules, and ions. We first examined the energetics of electrons due to their crucial role in governing the overall plasma chemistry; electrons in the plasma gain energy from the external electromagnetic field and transfer that energy to excite and sustain the plasma.[34] As shown in Table 6.1, T_e does not appear to depend on P or plasma precursor. In the N_2O system, there appears to be a slight dependence in looking exclusively at data obtained from the highest and lowest P systems (a difference of 0.12 eV). This admittedly slight dependence on P in the N_2O system, where none exists in either N_2 or NO plasmas, may arise because N_2O is slightly more polarizable than N_2 and NO, which have virtually identical polarizability.[46] Similar results were observed previously in a variety of fluorocarbon plasma systems, although somewhat higher T_e values (~ 1.8 – 2.51 eV) were determined, Table 4.5;[32] again these higher values are reflective of the significantly higher polarizability of the fluorocarbon molecules.[46] Overall, however, this suggests that when more energy is being provided to the system (by increasing rf power), it is not distributed into heating the electrons, rather is appears to be directed at increasing the internal energy of neutrals or ions.

These hypotheses were examined in a previously study of mean ion energies ($\langle E_i \rangle_{total}$) formed within N_xO_y plasmas[47] and by evaluating T_R and T_V values within ground and electronically-

excited plasma molecules in the current study. Both electrons and ions play a substantial role in the chemical reactions occurring in the plasma. Electron impact with neutral gas-phase molecules leads to the production of excited state atoms and molecules,[34] which is largely governed by T_e. However, T_e is effectively independent of plasma precursor and power, therefore reactions between heavy species (i.e. ions, radicals, molecules) play a substantial role. A goal of this work is to elucidate how the internal energies and kinetics of neutral species influence plasma chemistry.

Within nitrogen plasmas, under the conditions shown in Figure 6.1 (p = 100 mTorr, P = 150 W), T_R and T_V are higher for the upper N_2 state ($C^3\Pi_u$); however, for both N_2 electronic states, T_R is significantly lower than T_V. This suggests the pathways for rotational cooling are more efficient in comparison to vibrational channels, which was documented across all pressures and powers studied herein (Figures 6.2a– d). However, at P = 50 W, T_V shows little p dependence, a mere ~100 K difference when p triples from 50 to 150 mTorr. In contrast, at P = 200 W, a pronounced difference in T_V (~1000 K) emerges when pressure is increased from 50 mTorr to 150 mTorr. Generally, as p increases, fragmentation of the precursor increases through increased number of collisions, causing a relaxation of the vibrationally and rotationally excited N_2 molecules.[48] Clearly, the additional collisions upper state N_2 molecules ($C^3\Pi_u$) undergo at higher pressures affords some measure of T_V cooling. This is not, however, an efficient channel for energy transfer compared to rotational relaxation pathways, as T_R values are only slightly above room temperature. Using OES, T_R values for N_2 molecules have been documented within this range (~300 – 400 K) for a variety of nitrogen plasma systems, including atmospheric pressure plasma jets afterflow[49,50] and 50 MHZ ICP nitrogen plasmas.[51]

Considering the absorbing N_2 species, Figure 6.2c and 6.2d, T_R and T_V values exhibit a strong, linear dependence on P, with little to no dependence on p. Examining the two N_2 electronic states of the second positive system, there is little difference between T_R values determined within the lower $B^3\Pi_g$ state (~300 – 390 K) compared to the upper $C^3\Pi_u$ state (~300 – 365 K). This further bolsters the idea that rotational relaxation and thermalization occurs within N_2 rf discharges. In contrast, T_V values of the $B^3\Pi_g$ state are lower than the $C^3\Pi_u$ state and there is a smaller temperature range (~3100 – 4500 K) compared to (~3300 – 6200 K). The energy difference between the electronics states is ~3.67 eV,[52,53] therefore we hypothesize species populating the higher vibrational levels within the lower $B^3\Pi_g$ state have sufficient energy to be promoted to the $C^3\Pi_u$ state as a result of electron-impact collisions. Furthermore, theoretical models suggest the main population pathways for N_2 molecules in $B^3\Pi_g$ state originate from the $X^1\Sigma^+_g$ and $A^3\Sigma^+_u$ states through electron impact excitations.[53-55] In addition to this pathway, the excited $B^3\Pi_g$ and $C^3\Pi_u$ states can be partially populated by the pooling reactions of the metastable N_2 $A^3\Sigma^+_u$ state.[50] Within N_2 discharges, there are clearly complex and intertwined energetic relationships. Through the examination of these data, we can begin to elucidate energy distribution profiles for rotational and vibrational degrees of freedom for a diatomic system. Previously reported, internal molecular temperatures (T_V and T_R) within NO plasma discharges have been determined, a tabulated comparison of NO T_V values for ground and excited state NO is provided in Table 6.6 as a function of applied rf power and pressure.[31]

Table 6.6. T_V values for NO formed in N_2O and NO plasma systems[a]

***p* (mTorr)**	***P* (W)**	**NO ($X^2\Pi$) T_V (K)**		**NO ($A^2\Sigma^+$) T_V (K)**	
		NO	**N_2O**	**NO**	**N_2O**
50	50	--	3200 (320)	--	2500 (20)
	100	5800 (300)	2200 (140)	4500 (70)	2800 (200)
	150	6100 (200)	3600 (115)	4900 (80)	2900 (15)
	200	6300 (200)	4300 (200)	5100 (70)	3400 (100)
100	50	--	3400 (120)	--	2900 (60)
	100	5200 (100)	3850 (70)	3700 (10)	2900 (10)
	150	6000 (200)	4200 (60)	4100 (50)	3300 (170)
	200	6500 (40)	4600 (40)	4400 (50)	3600 (140)
150	100	5150 (150)	5200 (70)	3400 (180)	2900 (30)
	150	5850 (150)	5500 (140)	3900 (20)	3000 (15)
	200	6800 (150)	6300 (70)	4050 (110)	3500 (40)

[a] T_V values for 100 % NO systems are previously reported[31]

As noted above, the investigation of diatomic N_2 and NO plasma systems establishes a foundation that can be built upon through the investigation of more complex N_xO_y precursors, such as N_2O. As depicted in Figure 6.4, where T_V is plotted as a function of P for emitting and absorbing N_2 and NO molecules, a few interesting trends can be noted. First, the NO ($A^2\Sigma^+$) state has the lowest vibrational temperatures of all four species measured; ground state NO T_V values are consistently higher than those of the first excited state. The energy difference between the $X^2\Pi$ and $A^2\Sigma^+$ electronic states of NO is ~5.4 eV;[56] therefore higher vibrational levels ($v' \geq 3$) within the ground state are populated without being promoted to the first excited state. Second, the N_2 ($C^3\Pi_u$) excited state records the highest T_v values of all four molecules, regardless of P. Interestingly, at P = 100 and 150 W, T_V for NO ($X^2\Pi$) and N_2 ($B^3\Pi_g$) are approximately the same, whereas at P = 50 W, NO ($X^2\Pi$) has a T_V value ~100 K greater than N_2 ($B^3\Pi_g$), and at P = 200 W, not only is T_V for N_2 ($B^3\Pi_g$) higher than that for NO ($X^2\Pi$), the delta is nearly 1000 K. This alone demonstrates the interplay of energetics between species formed through decomposition within an environmentally-relevant plasma system. If the goal is to design a method for NO conversion into ambient species, such as N_2, determination of these energetic differences can provide unparalleled insight.

Similar to the 100 % N_2 plasma systems, as P increases within N_2O discharges, an increase in T_V is noted for both emitting and absorbing N_2 species, regardless of system pressure. Examining the emission of N_2 species in the discharge, we see that as p is increased, a slight increase of T_V (~800 K) is observed. At higher P (e.g., 200 W), however, there is no T_V dependence on p. Upon studying the absorbing N_2 species in the plasma, we observe a decrease in T_V with increasing p, as described above. Rotational temperatures for N_2 molecules in both electronic states show little p dependence and are approximately equivalent to room temperature

at lower powers (50 – 150 W). This does not hold true at P = 200 W for N_2 ($B^3\Pi_g$), where T_R values decrease from 500 – 400 K as p increases from 50 to 150 mTorr. Notably, plasma species can be produced via a variety of mechanisms (decomposition, recombination, etc.), all of which could contribute to the differences observed in T_V and T_R values. These mechanisms also include effects of other species in the system, such as nitrogen and oxygen atoms and nitric oxide species; thus, examination of energetic information for NO molecules formed in the system is also warranted.

For excited state NO formed in N_2O plasmas, T_R values exhibit a slight, positive dependence on P (apart from p = 100 mTorr data where no P dependence is observed), and little to no pressure dependence. Excited state NO molecules are rotationally hotter (by ~ 200 K) than N_2 molecules in either electronic state studied herein, and their vibrational temperatures increase with increasing P, displaying little p dependence. The opposite trend is true for ground state molecules. As pressure is increased, a significant increase in T_V (~2000 K) is observed, regardless of P. To characterize the energetic relationships within the N_2O plasma system, we have compared the plasma temperatures obtained from 100% N_2O, N_2 (above) and NO systems[31] to those obtained in the more complex precursor. Within NO plasmas, as shown in Table 6.6, T_V values ranged from ~3500 – 5000 K and ~5000 – 7000 K for the NO ($A^2\Sigma^+$) and NO ($X^2\Pi$) species, respectively.[31] T_V values for both ground and excited state NO formed through decomposition (of N_2O, for example) are significantly lower (across all P and p), compared to the 100 % NO system.[31] One proposed pathway is shown in Reaction 6.1, where the excited NO molecules formed from N_2O decomposition can further relax to NO ($X^2\Pi$) via multiple pathways (not shown here). Within the N_2O emission spectrum, little to no atomic nitrogen peaks are

present where the spectral character is dominated by the N_2 molecular transitions, suggesting atomic N formed via Reaction 6.1 participates in further chemical processes within the plasma.

$$N_2O + e^- \rightarrow NO^* + N + e^- \qquad (6.1)$$

Comparing the energetics of N_2 within a 100 % N_2 plasma to those for N_2 formed in an N_2O plasma, we find molecules in both the $B^3\Pi_g$ and $C^3\Pi_u$ states are vibrationally hotter in the N_2O plasma system, except for molecules in the $C^3\Pi_u$ state at the lowest pressures (p = 50 mTorr). Interestingly, upon examination of the $B^3\Pi_g$ state, the differences in energetics between the 100 % N_2 and N_2O plasma systems becomes increasingly larger as P increases, such that at P = 50 W (all p), T_V values are approximately equivalent and at P = 200 W, T_V values differ by 700 – 1,100 K. Multiple potential pathways exist through which excited molecular nitrogen can form, one of which is proposed in Reaction 6.2. Furthermore, with N_2O plasma discharges, strong atomic O peaks are present at 777 nm ($3p^5P - 3s^5S^0$) and 844 nm ($3p^3P - 3s^3S^0$).

$$N_2O + 2e^- \rightarrow N_2 + O + 2e^- \rightarrow N_2^* + O + 2e^- \qquad (6.2)$$

Within plasma systems, ionization, dissociation, and excitation processes can occur simultaneously; therefore, there is a multitude of excited and metastable nitrogen states that can be populated through electron collisions.[57] Through examination of different molecules in multiple electronic states, we can begin to untangle and interpret complex species interaction and the interdependence of energy partitioning. Moreover, the energetics associated with N_2 and NO molecules produced primarily through formation mechanisms will provide additional insights into plasma processing phenomena.

Examining the Figure 6.5 data for mixtures of N_2 and O_2 at a total pressure of 100 mTorr, reveals that T_V (N_2) generally has very little to no dependence on the amount of N_2 in the feed gas. Both emitting and absorbing NO and N_2 molecules show a strong, positive correlation to P

(Tables 6.3 and 6.4). This relationship in N_2/O_2 mixed plasma systems has been previously documented with atmospheric pressure plasma jets at similar powers.[50] Under all experimental conditions, T_R values for both ground and excited state NO molecules are elevated in comparison to N_2, suggesting the rotational excitation and relaxation processes are slower for NO species, a phenomena that has been documented within 2.45 GHZ microwave discharges.[58] As documented within 100 % N_2 plasmas, T_R vales for N_2 molecules in $B^3\Pi_g$ and $C^3\Pi_u$ states show a positive dependence on P, however do not exceed 460 K, demonstrating the effectiveness of the rotational cooling pathways. A time-dependent kinetic model, studying the energy transfer to gas heating in N_2/O_2 plasmas, demonstrated the energy transferred to the translational mode (gas heating) increased with increasing O_2 concentration.[59] Assuming T_R and gas temperature have equilibrated within the discharge,[60] a similar trend emerges: as oxygen concentration increases within the feed gas, there is in an increase in T_R for N_2 $B^3\Pi_g$ molecules (Table 6.4).

T_V values for NO molecules in both electronic states are significantly lower in the mixed gas systems, compared to the 100 % NO plasmas, where NO ($X^2\Pi$) T_V values are again elevated compared to the exited state. These data indicate that production of NO from formation mechanisms, such as the Zel'dovich chain (Reactions 6.3 and 6.4), generates ground state NO and does not preferentially transfer vibrational energy to the molecule.

$$O_{(g)} + N_{2(g)} \rightarrow NO_{(g)}(X^2\Pi) + N_{(g)} \quad (6.3)$$

$$N_{(g)} + O_{2(g)} \rightarrow NO_{(g)}(X^2\Pi) + O_{(g)} \quad (6.4)$$

$$NO^* + M \rightarrow NO_{(g)}(X^2\Pi) + M^* \quad (6.5)$$

Vibrationally hot N_2 is requisite for propagation of the Zel'dovich chain in non-thermal plasmas.[35] We correspondingly observe vibrationally excited N_2 (approximately equivalent to 100% N_2 plasmas) in the afterglow of N_2/O_2 systems, suggesting N_2 molecules with significantly

high T_V are not consumed in the reactions forming NO. Given the relatively high T_V measured for N_2 in our systems, Reaction 6.5 is suggested as the primary route for relaxation of vibrationally excited NO molecules, where interactions of NO* with other species (M) may lead to a transfer of vibrational energy to species M and electronic quenching of NO*. Hence, we see larger vibrational temperatures for ground state NO and excited state N_2 in mixed gas plasma systems. Thus, NO energetics appear to be dependent on the source of the NO molecule, where the partitioning of energy favors vibrational channels, with little to no dependence on electron temperatures. Clearly, N_xO_y plasmas exhibit a complex chemistry; with a dynamic interplay between the electrons, and the molecular vibrational, and rotational degrees of freedom. Another crucial aspect to consider is the chemical kinetic processes occurring, therefore we have employed time-resolved spectroscopy to further probe these non-equilibrium discharges. Note, the kinetic information presented in this chapter was collected with an AvaSpec-2048L-USB2-RM multichannel spectrometer with a 25.5 ms integration time (described in Chapter 2).

We specifically chose to investigate formation and destruction of key excited state species to provide foundational and mechanistic insight that could be correlated with the system energetics data discussed above. It is important to understand what the rate constant values shown in Figures 6.7 and 6.8 and Table 6.5 tell us about the processes occurring in our plasmas. Assuming both excitation and de-excitation are direct processes, the formation and relaxation of these species is first order with respect to the molecule (NO is included as an example in Reactions 6.6 and 6.7). Thus, simulation of the intensity profiles is performed with both exponential rise and decay of the form e^{-kt}, corresponding to a first-order process.

$$NO + e^- \rightarrow NO^* + e^- \quad (6.6)$$

$$NO^* \rightarrow NO + h\nu \quad (6.7)$$

Deviations from the profile presented in Figure 6.6b can provide further insight into the chemistry within nitrogen oxide plasma systems. For example, excited state species must be formed within the plasma, as they are not present natively in the gas-phase precursor; therefore, a formation profile must exist in some capacity. An inability to discern changes in emission intensity after plasma ignition thus indicates the formation process is faster than the time resolution of our experiment. With NO as the system precursor, formation profiles are observed for N_2*, but not NO*, suggesting direct electron-impact (Reaction 6.6) is the primary route for nitric oxide excitation. The density of electrons within these dischargers are several orders of magnitude higher compared to other species in the system,[34] therefore NO-electron collisions are more likely to occur compared to NO-NO collisions. In contrast, molecular nitrogen must be formed in the discharge through decomposition and recombination reactions before excitation can occur. Thus, formation of N_2* was examined with TR-OES to further explore this phenomenon in these systems.

As described above, the formation of N_2* in nitric oxide plasma systems can proceed via several different pathways; one such pathway is described by Reaction 6.8.

$$e^- + 2NO \rightarrow 2N + 2O + e^- \rightarrow N_2^* + O_2 + e^- \quad (6.8)$$

Additionally, NO could react with some other species (M) that has been formed previously within the plasma to form NOM. This reaction could generate a larger intermediate that subsequently decomposes into N_2, Reaction 6.9.

$$2NO + 2R + e^- \rightarrow 2NOM \rightarrow MONNOM + e^- \rightarrow N_2^* + 2OM + e^- \quad (6.9)$$

Importantly, our data do not necessarily provide exclusive evidence for a single formation or destruction mechanism, as there are limitations to our ability to discern competing processes. In our TR-OES studies, however, N_2* specifically refers to the $C^3\Pi_u$ state, which is shown to be

formed directly in Reactions 6.8 and 6.9. Once molecular nitrogen is formed, however, excitation can occur by separate steps from a multitude of electronic states, including from ground state N_2 or the reaction of singlet metastable states of N_2.[30] Regardless of the excitation step, it is likely that the NOM mechanism (Reaction 6.9) would take considerably longer than the more direct process shown in Reaction 6.8, because the formation of the NOM species would also be a time-consuming and less energetically favorable process. As such, this possible mechanism would likely be lost within the steady-state concentration of the plasma, essentially concealed by the more prevalent competing pathways. Thus, our data support a multi-step formation mechanism for N_2*, as opposed to a direct formation mechanism, but do not necessarily provide information about the exact process occurring.

Interestingly, the N_2O precursor behaves essentially the same way as the NO precursor, in that NO* formation is not observed, Table 6.5. This suggests that the excited state is formed directly upon electron impact (Reaction 6.1) or at the very least, that it is the predominant mechanism. When compared to the observed trends in the NO system (Table 6.5), N_2* formation in N_2O suggests this process is indirect and involves some decomposition and reaction prior to excitation, Reaction 6.2. Indeed, this interpretation is further validated by observations made within the N_2/O_2 precursor system. Here, the onset of N_2* formation is not detected, whereas NO* formation can easily be determined (i.e., opposite behavior to NO and N_2O systems). This suggests that N_2 as a parent molecule in the feed gas undergoes a direct excitation that cannot be detected within the time resolution of our apparatus, whereas NO* formation is evidence of further decomposition reactions necessary for generating NO in this system. The intensity profile indicates, however, that the rate-limiting step is still first order, as the data still follow the same e^{-kt} behavior. Additionally, we can make a few assumptions about conditions

under which destruction constants cannot be determined (whereas formation rate constants can). First, under such conditions, it is likely that quenching of the excited state is occurring at the same rate as steady-state production of the excited state. Second, under these conditions there are likely no alternative pathways for the quenching of the excited state. Notably, this behavior is only observed for NO* in the N_2/O_2 precursor.

As a final piece of information, we provide some context for the kinetic data obtained in these studies. As the actinometric intensity ratio is simply proportional to concentration, so too are reported values for both k_f and k_d. The comparison of these values across the varied parameter space chosen in these studies provides insight into probable reaction mechanisms within the first few seconds of plasma ignition. Because precursor gas flow is continuous, the system achieves a steady-state concentration of these various species. This results in constant [N_2*] and [NO*] throughout the life of the plasma, as equilibrium with respect to k_f and k_d is achieved. The first moments after ignition, however, are shown to be dynamic with respect to the reactivity of these molecules. Indeed, Meddeb and coworkers saw a very similar trend with respect to SiH* intensity as a function of time.[42] They report comparable rise/decay trends over the first few seconds after plasma ignition, with varying profiles, before ultimately arriving at steady-state concentrations. Additionally, by relating these profiles to cross-sectional transmission electron microscopy images, they are able to hypothesize mechanisms for silane film production.

Another work of interest by Burnette *et al.* investigated the kinetics of N_xO_y species in the afterglow region of a plasma filament discharge.[61] The authors suggest that downstream and post-discharge chemistry is highly dependent on neutral species reactivity and that little evidence exists to suggest an excited state influence, meaning that these areas are likely dominated by the

Zel'dovich mechanisms. Such observations highlight the importance of coordinated efforts to explore the role of excited state species within the bulk discharge region, as highlighted here.

Beyond these studies, however, direct comparison of values and trends reported herein is difficult. As noted in the Introduction, many TR-OES efforts have focused on modular plasmas generated from a variety of high-energy sources. Even so, context for broader TR-OES efforts can be achieved by way of comparison. Sridhar et al. for example, monitored various Si* and Cl* emissions with the help of an Ar* actinometer, similar to the approach used here.[62] With these data, the authors were able to highlight potential etching mechanisms and the impact of system parameters on species losses. Alternatively, Liang and coworkers utilized TR-OES methods to study N_2-plasma ablation of graphite and determined the impact of plasma parameters on the formation of C_2 radicals within the system.[63] The formation of CN radicals through gas-phase reactions of N_2 and C_2 were also examined, concluding ionized and excited N_2 promote the formation of CN radicals, ultimately outlining potential formation mechanisms through time-resolved spectroscopy. The work presented herein also to demonstrate the utility of TR-OES within plasma diagnostics, both in terms of temporal insight and mechanism elucidation.

Within this work, we examined energy partitioning within steady-state plasmas as well as determining rate constants with time-resolved optical emission spectroscopy. Internal (i.e., vibrational and rotational) temperatures strongly depend on plasma parameters (i.e., power and pressure). Rate constants of excited state species also depend on rf power and precursor, where evidence supports direct excitation of NO in both NO and N_2O plasma. These energetic and kinetic observations are essential to furthering the utility of these complex discharges for plasma assisted catalysis processes.

6.4 Summary

Plasma species can be produced via a variety of mechanisms (direct-impact excitation, decomposition, recombination, etc.); therefore, information regarding the formation and destruction mechanisms, as well as the distribution of energy, is crucial to understanding fundamental plasma chemistry. Optical emission and broadband absorption spectroscopy techniques were employed to examine energy partitioning within inductively coupled plasmas (ICPs), focusing on NO ($X^2\Pi \leftrightarrow A^2\Sigma^+$) and N_2 ($B^3\Pi_g \leftrightarrow C^3\Pi_u$) radiative transitions formed within a variety of different plasma precursors. This work also highlights the utility of TR-OES in elucidating components of the complex kinetic parameters that exist within N_xO_y plasma systems. T_V and T_R of ground and excited state species, as well as the rate constants of excited state species, appear to depend on both applied rf power and system pressure. There is also evidence to support direct excitation of NO in both NO and N_2O plasma systems, whereas direct excitation of N_2 is likely only observed in the N_2/O_2 system. Such observations are key to furthering the utility of these systems for plasma-assisted catalysis processes. Using complementary spectroscopic techniques is beneficial to elucidating the multifaceted nature of plasma kinetics, in the first few seconds of the plasma ignition and steady-state conditions.

REFERENCES

1. Blechle, J. M. Investigations of Nitrogen Oxide Plasmas: Fundamental Chemistry and Surface Reactivity and Monitoring Student Perceptions in a General Chemistry Recitation. Ph.D., Colorado State University, Fort Collins, CO, 2016.
2. Änggård, E., Nitric Oxide: Mediator, Murderer, and Medicine. *The Lancet* **1994**, *343*, 1199-1206.
3. Cech, T. R.; Bennett, D.; Jasny, B.; Kelner, K. L.; Miller, L. J.; Szuromi, P. D.; Voss, D. F.; Kiberstis, P. A.; Parks, S.; Ray, L. B., The Molecule of the Year. *Science* **1992**, *258*, 1861.
4. Domingos, P.; Prado, A. M.; Wong, A.; Gehring, C.; Feijo, J. A., Nitric Oxide: A Multitasked Signaling Gas in Plants. *Molecular Plant* **2015**, *8*, 506-520.
5. Carpenter, A. W.; Schoenfisch, M. H., Nitric Oxide Release: Part II. Therapeutic Applications. *Chem. Soc. Rev.* **2012**, *41*, 3742-3752.
6. Fang, F. C., Perspectives Series: Host/Pathogen Interactions. Mechanisms of Nitric Oxide-Related Antimicrobial Activity. *J. Clin. Invest.* **1997**, *99*, 2818 - 2825.
7. Radomski, M. W.; Moncada, S., The Biological and Pharmacological Role of Nitric Oxide in Platelet Function. In *Mechanisms of Platelet Activation and Control*, Springer: 1993; pp 251-264.
8. Mann, M. N.; Neufeld, B. H.; Hawker, M. J.; Pegalajar-Jurado, A.; Paricio, L. N.; Reynolds, M. M.; Fisher, E. R., Plasma-modified Nitric Oxide-Releasing Polymer Films Exhibit Time-Delayed 8-log Reduction in Growth of Bacteria. *Biointerphases* **2016**, *11*, 031005.
9. Devahasdin, S.; Fan Jr, C.; Li, K.; Chen, D. H., TiO_2 Photocatalytic Oxidation of Nitric Oxide: Transient Behavior and Reaction Kinetics. *J. Photochem. Photobiol., A* **2003**, *156*, 161-170.
10. Lucena, P.; Vadillo, J. M.; Laserna, J. J., Compositional Mapping of Poisoning Elements in Automobile Three-Way Catalytic Converters by Using Laser-Induced Breakdown Spectrometry. *Appl. Spectrosc.* **2001**, *55*, 267-272.
11. NOx, How Nitrogen Oxides Affect the Way We Live and Breathe the Regional Transport of Ozone : New EPA Rulemaking on Nitrogen Oxide Emissions. U.S. Environmental Protection Agency, Office of Air Quality Planning and Standards: Research Triangle Park, NC :, 1998.
12. Lohmann, U.; Feichter, J., Global Indirect Aerosol Effects: A Review. *Atmos. Chem. Phys.* **2005**, *5*, 715-737.
13. Newman, S. P.; Pavia, D.; Morén, F.; Sheahan, N.; Clarke, S. W., Deposition of Pressurised Aerosols in the Human Respiratory Tract. *Thorax* **1981**, *36*, 52-55.
14. Vaida, V., Spectroscopy of Photoreactive Systems: Implications for Atmospheric Chemistry. *J. Phys. Chem. A* **2009**, *113*, 5-18.
15. Plath, K. L.; Takahashi, K.; Skodje, R. T.; Vaida, V., Fundamental and Overtone Vibrational Spectra of Gas-Phase Pyruvic Acid. *J. Phys. Chem. A* **2009**, *113*, 7294-7303.
16. Reed Harris, A. E.; Doussin, J.-F.; Carpenter, B. K.; Vaida, V., Gas-Phase Photolysis of Pyruvic Acid: The Effect of Pressure on Reaction Rates and Products. *J. Phys. Chem. A* **2016**, *120*, 10123-10133.
17. Shelef, M.; McCabe, R. W., Twenty-five Years after Introduction of Automotive Catalysts: What Next? *Catal. Today* **2000**, *62*, 35-50.
18. Our Nation's Air - Status and Trends Through 2010. Agency, U. S. E. P., Ed. Office of Air Quality Planning and Standards: Research Triangle Park, North Carolina, 2012.

19. Sun, Y.; Zwolińska, E.; Chmielewski, A. G., Abatement Technologies for High Concentrations of NO_x and SO_2 Removal from Exhaust Gases: A Review. *Crit. Rev. Environ. Sci. Technol.* **2016**, *46*, 119-142.
20. Whitehead, J. C., Plasma-Catalysis: The Known Knowns, the Known Unknowns, and the Unknown Unknowns. *J. Phys. D: Appl. Phys.* **2016**, *49*, 243001 (243024pp).
21. Neyts, E. C.; Bogaerts, A., Understanding Plasma Catalysis Through Modelling and Simulations - A Review *J. Phys. D: Appl. Phys.* **2014**, *47*, 224010.
22. Thevenet, F.; Sivachandiran, L.; Guaitella, O.; Barakat, C.; Rousseau, A., Plasma-Catalyst Coupling for Volatile Organic Compound Removal and Indoor Air Treatment: A Review. *J. Phys. D: Appl. Phys.* **2014**, *47*, 224011 (224014 pp).
23. Kim, H.-H.; Teramoto, Y.; Negishi, N.; Ogata, A., A Multidisciplinary Approach to Understand the Interactions of Nonthermal Plasma and Catalyst: A Review. *Catal. Today* **2015**, *256*, 13-22.
24. Penetrante, B.; Brusasco, R.; Merritt, B.; Vogtlin, G., Environmental Applications of Low-Temperature Plasmas. *Pure Appl. Chem.* **1999**, *71*, 1829-1835.
25. Stillahn, J. A.; Trevino, K. J.; Fisher, E. R., Plasma Diagnostics for Unraveling Process Chemistry. *Annu. Rev. Anal. Chem.* **2008**, *1*, 261-291.
26. Shimada, M.; Tynan, G. R.; Cattolica, R., Rotational and Translational Temperature Equilibrium in an Inductively Coupled Plasma. *J. Vac. Sci. Technol. A* **2006**, *24*, 1878-1883.
27. Staack, D.; Farouk, B.; Gutsol, A. F.; Fridman, A., Spatially Resolved Temperature Measurements of Atmospheric-Pressure Normal Glow Microplasmas in Ar. *IEEE Trans. Plasma Sci.* **2007**, *35*, 1448-1455.
28. Hollmann, E. M.; Pigarov, A. Y.; Taylor, K., Measurement and Modeling of H_2 Vibrational and Rotational Temperatures in Weakly Ionized Hydrogen Discharges. *J. Nucl. Mater.* **2005**, *337*, 451-455.
29. Lalo, C.; Deson, J.; Cerveau, C.; Ben-Aim, R. I., Air Microwave-Induced Plasma: Detection of NO in Post-Discharge Using an ArF Laser. *Plasma Chem. Plasma Process.* **1993**, *13*, 351.
30. Morgan, M. M.; Cuddy, M. F.; Fisher, E. R., Gas-Phase Chemistry in Inductively Coupled Plasmas for NO Removal From Mixed Gas Systems. *J. Phys. Chem. A* **2010**, *114*, 1722-1733.
31. Blechle, J. M.; Hanna, A. R.; Fisher, E. R., Determination of Internal Temperatures Within Nitric Oxide Inductively Coupled Plasmas. *Plasma Process. Polym.*, 1700041-n/a.
32. Hanna, A. R.; Cuddy, M. F.; Fisher, E. R., Energy Partitioning and its Influence on Surface Scatter Coefficients within Fluorinated Inductively Coupled Plasmas. *J. Vac. Sci. Technol., A* **2017**, *35*, 05C308.
33. Bruggeman, P.; Cunge, G.; Sadeghi, N., Absolute OH Density Measurements by Broadband UV Absorption in Diffuse Atmospheric Pressure He-H_2O RF Glow Discharges. *Plasma Sources Sci. Technol.* **2012**, *21*, 035019.
34. Grill, A., *Cold Plasma Materials Fabrications: From Fundamentals to Applications*. IEEE Press: Piscataway, NJ, 1994.
35. Fridman, A., *Plasma Chemistry*. Cambridge University Press: 2008.
36. Ambrico, P. F.; Bektursunova, R.; Dilecce, G.; De Benedictis, S., Nitrogen Vibrational Excitation in a N_2/He Pulsed Planar-ICP RF Discharge. *Plasma Sources Sci. Technol.* **2005**, *14*, 676-685.

37. Shakhatov, V. A.; Mavlyudov, N. B.; Lebedev, Y. A., Studies of the Distribution Functions of Molecular Nitrogen and Its Ion over the Vibrational and Rotational Levels in the DC Glow Discharge and the Microwave Discharge in a Nitrogen-Hydrogen Mixture by the Emission Spectroscopy Technique. *High Temp.* **2013**, *51*, 551-565.
38. Britun, N.; Gaillard, M.; Ricard, A.; Kim, Y. M.; Kim, K. S.; Han, J. G., Determination of the Vibrational, Rotational and Electron Temperatures in N_2 and Ar–N_2 rf Discharge. *J. Phys. D: Appl. Phys.* **2007**, *40*, 1022.
39. Van der Horst, R.; Verreycken, T.; Van Veldhuizen, E.; Bruggeman, P., Time-Resolved Optical Emission Spectroscopy of Nanosecond Pulsed Discharges in Atmospheric-Pressure N_2 and N_2/H_2O Mixtures. *J. Phys. D: Appl. Phys.* **2012**, *45*, 345201.
40. Hui, L.; Xinbing, W.; Duluo, Z., Time-Resolved Optical Emission Spectroscopy Diagnosis of CO_2 Laser-Produced SnO_2 Plasma. *Plasma Sci. Technol.* **2016**, *18*, 902.
41. Garofano, V. R.; Stafford, L.; Despax, B.; Clergereaux, R.; Makasheva, K. In *Time-resolved Optical Emission Spectroscopy of Dusty Low-pressure RF Plasmas with Pulsed Injection of Hexamethyldisiloxane*, 22nd International Symposium on Plasma Chemistry, Antwerp, Belgium, Antwerp, Belgium, 2015.
42. Meddeb, H.; Bearda, T.; Abdulraheem, Y.; Dimassi, W.; Ezzaouia, H.; Gordon, I.; Szlufcik, J.; Poortmans, J., In-situ Optical emission Spectroscopy Diagnostic of Plasma Ignition Impact on Crystalline Silicon Passivation by a-Si: H Films. *Superlattices Microstruct.* **2016**, *96*, 253-258.
43. Mackus, A.; Heil, S.; Langereis, E.; Knoops, H.; Van de Sanden, M.; Kessels, W., Optical Emission Spectroscopy as a Tool for Studying, Optimizing, and Monitoring Plasma-Assisted Atomic Layer Deposition Processes. *J. Vac. Sci. Technol., A* **2010**, *28*, 77-87.
44. Gottscho, R. A.; Donnelly, V. M., Optical Emission Actinometry and Spectral Line Shapes in rf Glow Discharges. *J. Appl. Phys.* **1984**, *56*, 245-250.
45. Malyshev, M. V.; Donnelly, V. M., Determination of Electron Temperatures in Plasmas by Multiple Rare Gas Optical Emission, and Implications for Advanced Actinometry. *J. Vac. Sci. Technol., A* **1997**, *15*, 550-558.
46. Hohm, U., Experimental Static Dipole–dipole Polarizabilities of Molecules. *J. Mol. Struct.* **2013**, *1054–1055*, 282-292.
47. Blechle, J. M.; Cuddy, M. F.; Fisher, E. R., Effect of Ion Energies on the Surface Interactions of NO Formed in Nitrogen Oxide Plasma Systems. *J. Phys. Chem. A* **2013**, *117*, 1204-1215.
48. Abdel-Fattah, E.; Bazavan, M.; Sugai, H., Langmuir Probe Diagnostics of Electron Energy Distributions with Optical Emission Spectroscopy in Capacitively Coupled rf Discharge in Nitrogen. *J. Appl. Phys.* **2011**, *110*, 113303.
49. Zhang, Q. Y.; Shi, D. Q.; Xu, W.; Miao, C. Y.; Ma, C. Y.; Ren, C. S.; Zhang, C.; Yi, Z., Determination of Vibrational and Rotational Temperatures in Highly Constricted Nitrogen Plasmas by Fitting the Second Positive System of N_2 Molecules. *AIP Adv.* **2015**, *5*, 057158.
50. Xiao, D.; Cheng, C.; Shen, J.; Lan, Y.; Xie, H.; Shu, X.; Meng, Y.; Li, J.; Chu, P. K., Characteristics of Atmospheric-Pressure Non-Thermal N_2 and N_2/O_2 Gas Mixture Plasma Jet. *J. Appl. Phys.* **2014**, *115*, 033303.
51. Takeshi, K.; Toshiki, N.; Seiji, S.; Toshiaki, M., Diagnostics of N_2 Dissociation in RF Plasmas by Vacuum Ultraviolet Emission and Absorption Spectroscopy. *Plasma Sources Sci. Technol.* **2008**, *17*, 024018.

52. Dieke, G. H.; Heath, D. *The First and Second Positive Bands of N_2*; JOHNS HOPKINS UNIV BALTIMORE MD: 1959.
53. Mavadat, M.; Ricard, A.; Sarra-Bournet, C.; Laroche, G., Determination of Ro-vibrational Excitations of N_2 (*B,v'*) and N_2 (*C,v'*) states in N_2 Microwave Discharges Using Visible and IR Spectroscopy. *J. Phys. D: Appl. Phys.* **2011**, *44*, 155207.
54. Benedictis, S. D.; Dilecce, G.; Simek, M., Excitation and Decay of $N_2(B^3\Pi_g,v)$ States in a Pulsed Discharge: Kinetics of Electrons and Long-lived Species. *J. Chem. Phys.* **1999**, *110*, 2947-2962.
55. Supiot, P.; Blois, D.; Benedictis, S. D.; Dilecce, G.; Barj, M.; Chapput, A.; Dessaux, O.; Goudmand, P., Excitation of N_2 ($B^3\Pi_g$) in the Nitrogen Short-Lived Afterglow. *J. Phys. D: Appl. Phys.* **1999**, *32*, 1887-1893.
56. Gilmore, F. R., Potential Energy Curves for N_2, NO, O_2 and Corresponding Ions. *J. Quant. Spectrosc. Radiat. Transfer* **1965**, *5*, 369-IN363.
57. Levaton, J.; Amorim, J.; Souza, A. R.; Franco, D.; Ricard, A., Kinetics of Atoms, Metastable, Radiative and Ionic Species in the Nitrogen Pink Afterglow. *J. Phys. D: Appl. Phys.* **2002**, *35*, 689.
58. Hao, T.; Atsushi, N.; Haruaki, M.; Hiroshi, A., Spectroscopic Determination of Vibrational and Rotational Temperatures of NO Molecules in N_2 –O_2 Mixture Microwave Discharge. *Jpn. J. Appl. Phys.* **2015**, *54*, 01AB06.
59. Pintassilgo, C. D.; Guerra, V., Power Transfer to Gas Heating in Pure N_2 and in N_2–O_2 Plasmas. *J. Phys. Chem. C* **2016**, *120*, 21184-21201.
60. Bruggeman, P.; Sadeghi, N.; Schram, D. C.; Linss, V., Gas Temperature Determination from Rotational Lines in Non-Equilibrium Plasmas: A Review. *Plasma Sources Sci. Technol.* **2014**, *23*, 023001.
61. Burnette, D.; Montello, A.; Adamovich, I.; Lempert, W., Nitric Oxide Kinetics in the Afterglow of a Diffuse Plasma Filament. *Plasma Sources Sci. Technol.* **2014**, *23*, 045007.
62. Sridhar, S.; Liu, L.; Hirsch, E. W.; Donnelly, V. M.; Economou, D. J., Insights into the Mechanism of In-Plasma Photo-Assisted Etching Using Optical Emission Spectroscopy. *J. Vac. Sci. Technol., A* **2016**, *34*, 061303.
63. Liang, P.; Li, Y.; You, Q.; Cai, H.; Yang, X.; Sun, J.; Xu, N.; Wu, J., Formation of Diatomic Molecular Radicals in Reactive Nitrogen-Carbon Plasma Generated by Electron Cyclotron Resonance Discharge and Pulsed Laser Ablation. *Phys. Plasmas* **2014**, *21*, 043512.

CHAPTER 7

INVESTIGATING THE IMPACT OF CATALYSTS ON N_2 ROTATIONAL AND VIBRATIONAL TEMERPATURE IN LOW PRESSURE PLASMAS[a]

This chapter examines energy partitioning and kinetic distributions for excited state N_2(g) molecules within a N_2 plasma discharge with the presence of catalysts, as well as resulting materials characterization post plasma processing. The Fisher Group protocol for utilizing the Boltzmann plot method for T_V (N_2) determination, as well as all data herein pertaining to N_2 plasma without substrates and zeolite materials were established, collected and analyzed by Angela R. Hanna. The entirety of the work with TiO_2 nanomaterials was performed by Tara L. Van Surksum and will be included in her dissertation. Collectively, work included in this chapter was supported by the National Science Foundation (CBET-1803067). Specific acknowledgments for this Chapter include contributions provide by Dr. Joseph A. DiVerdi (assistance with the determination of surface area); Dr. Patrick McCurdy (assistance with SEM and XPS analyses); and Dr. Brian Newell (PXRD expertise).

[a] This chapter is reproduced with permission from an article published in *Journal of Physics D: Applied Physics* by Angela R. Hanna, Tara L. Van Surksum, and Ellen R. Fisher, as well as some results published in an invited review article in *Journal of Vacuum Science and Technology A* by Angela R. Hanna and Ellen Fisher (most of which is reproduced in Chapter 3).

7.1 Introduction

Plasma-assisted catalysis (PAC) generally describes the combining of a plasma system with a catalytic material for enhanced decomposition of a waste stream. PAC has recently received much attention within the plasma community because the non-thermal nature of the plasmas employed allows access to processes energetically unavailable under thermal conditions and because of the enormous potential to increase feed gas conversion.[2-5] PAC can be widely applied across a wide range of disciplines and applications, including treatment of waste gases;[6,7] CO_2 capture and conversion to high-value materials;[8,9] methane reforming;[10,11] ammonia synthesis;[12] and fabrication of carbon nanostructures and supported nanocatalysts via non-thermal plasma methods.[13,14] Regardless of end application, the fundamental scientific questions and challenges that must be addressed before implementation of PAC as a viable technology are remarkably similar, such as optimized reactor and catalyst design. Indeed, paramount to the future of PAC development are a number of essential pieces, such as understanding of plasma generation and general operating conditions; the selection of catalysts, where both chemical and physical properties need to considered; and the elucidation of interactions between plasma and material.[15,16]

In single-stage PAC systems, the catalyst is placed directly in the discharge, allowing all plasma species to interact with the surface of the catalyst. The resulting range of dissociation products can lead to a complex and entangled chemistry within the plasma system. Although it is generally understood that catalyst particle size can influence the overall rate and efficiency of PAC processes,[3,4] little is understood about how low-temperature plasmas (LTPs) interact with micro- and nano-structured materials. Furthermore, most studies to date have primarily explored optimizing PAC systems from the standpoint of how well the plasma removes a pollutant[4,17] or

how the plasma affects the material,[2,18-20] with fewer focusing on how the material affects the gas-phase chemistry, energy partitioning within the plasma, or interactions between the plasma and the surface. Energy distributions within non-thermal plasmas typically follow the relationship wherein vibrational temperatures are greater than rotational or gas temperatures, and higher energy electrons and ions play a crucial role in the overall plasma character.

As the precursor gas becomes more complex, these interactions between gas-phase species and catalysts will undoubtedly also become more convoluted and potential synergisms may be difficult to deconstruct. Hence, in this study we examined nitrogen plasmas, a relatively inert, homonuclear, diatomic system that somewhat diminishes the complexity by at least limiting the number and type of gas-phase species that can be formed. Moreover, as evidenced by the selected works listed in Table 7.1, N_2 plasmas have been extensively studied in the literature over decades. Table 7.1 demonstrates the wide range of N_2 plasma operating conditions, including source ignition, pressure regimes, and power (or charge), and consequently a wide range of rotational and vibrational (T_R and T_V, respectively) have been documented. Although not an exhaustive list, the Table 7.1 studies all examined gas-phase characteristics of N_2 plasmas, without the complexity of adding a catalyst.

Table 7.1. Summary of T_V & T_R measurements in N_2 glow discharges.

Source	***p* (Torr)**	***P* (W)**	T_R **(K)**	T_V **(K)**	**Ref**
rf	1	1000	600	--	Porter(1979)[21]
DC	0.1-2	*n/a* (I = 50 mA)	--	2500-3000, 7200	Cernogora(1984)[22]
DBD	0.15	*n/a* (U = 800 V)	480	--	Zhang(2002)[23]
C-DBD	200–600	25-60	360	2270-3030	Masoud(2005)[24]
IPC-rf	--	--	370/470	5000-12000	Britun (2007)[25]
RGA	--	--	2200-2500	3200-3700	Gangoli (2010)[26]
RGA	atm.	*n/a* (U = 7-10 kV)	1160-1508	4874-5105	Wu (2015)[27]
DBD	atm.	140	350-575	2200-2500	Yang (2016)[28]
ICP-rf	0.05-0.2	50-200	300-500	2000-7000	Hanna (2017)[1]
GAP	atm.	*n/a* (I = 230 mA)	5500	--	Groger (2019)[29]

Two additional studies that examined internal temperatures of N_2 plasma species in model PAC systems measured T_V and T_R of N_2 utilizing TiO_2 in a packed bed atmospheric dielectric barrier discharge (DBD) system [system pressure (p) of ~101 Pa][30] and Co-ZSM-5 in a radio frequency (rf) plasma, operated near atmospheric pressure (p = 90 Pa).[31] Tu *et al.* found that $T_V(N_2)$ increased dramatically from ~2300 – 2800 K to ~3200 – 4100 K when TiO_2 pellets were placed in the plasma and attributed this to an increase in electron temperature (T_e) as a result of the catalyst.[30] Interestingly, the TiO_2 catalyst had no effect on $T_R(N_2)$ at the lowest applied discharge power (P) of 40 W and removed all the positive linear dependence of $T_R(N_2)$ on P observed without TiO_2 (P = 40 – 70 W). Although Tu *et al.* noted some of these changes may indicate heating of the substrate, although the true origin of these effects remains unclear. Niu *et al.* observed differences in T_V and T_R when employing Co-ZSM-5 as a catalyst.[31] Here, however, $T_V(N_2)$ was ~3100 – 3400 K *with* the catalyst, more than 1000 K lower than that measured without the Co-ZSM-5 (~4300 – 5000 K). Although a slight decrease was observed as a function of rf power with the catalyst, the opposite trend was observed without the catalyst. In addition, $T_R(N_2)$ ranged from ~375 K at the lowest P to ~500 K at the highest P, with very little difference between values measured with and without the catalyst. Notably, all of the measurements made in this study were made at P = 5– 25 W, discharge powers considerably lower than the lowest used by Tu *et al.*.[30] Although no explanation was provided for the differences between these internal temperature values and those measured by Tu *et al.*, variations in P and the catalyst type could account for the observed dissimilarities.

When nanostructured or porous materials are placed in plasma discharges, spatial inhomogeneity can be created (i.e., microplasmas within pores, localized electric fields) which alters the electrical characteristics of the plasma.[32] Described in Chapter 1, significant

experimental and theoretical efforts have explored the formation of microdischarges in different catalytic pores in recent years. Zhang *et al.* simulated micro-and nanosized catalyst pores with a two-dimensional particle-in-cell/Monte Carlo collisional model, demonstrating the formation of microdischarges in both μm- and nm-sized pores; electron density and electron impact ionization rate drastically increase when the plasma stream permeates in the micrometer pore.[33] Likewise, Gu *et al.* computationally demonstrated that the discharge is more enhanced on the surface of porous catalysts compared to inside the pores.[34] Clearly, plasma-material synergisms arise from the introduction of a catalysts in a discharge, where the chemical identity and pore size, position in reactor, and amount of catalyst in the discharge are important variables to consider and study. Tu and Whitehead demonstrated different packing methods with Ni/γ-Al_2O_3 catalysts in DBD reactor systems impact the dry reforming of CH_4.[10] In a fully packed-bed reactor, the authors found a decrease in conversions of CH_4 and CO_2 compared to the system with no catalyst present. When the Ni/γ-Al_2O_3 catalyst particles are partially packed in the discharge, the conversion rate of CH_4 increased to 38% compared to the 30% conversion of the no catalyst system. The authors concluded that the manner of catalyst packing in a discharge plays an important role in single-stage PAC systems.[10]

Here, we further explore all these phenomena by examining the effects of adding catalysts to an N_2 inductively coupled plasma (ICP) operated at relatively low pressure (~50 – 150 mTorr or ~7– 20 Pa). TiO_2 nanoparticles were studied here for direct comparison to the results of Tu *et al.*; PAC studies within N_2 plasmas were expanded to probe the impact of micro-structured NaX zeolite (Si/Al ratio of 3.5 ± 0.2) on resulting plasma energetics and kinetics. Specifically, $T_V(N_2)$ and $T_R(N_2)$ were measured as a function of power and pressure via OES. We have also examined the morphology and chemical composition of the catalysts using scanning electron

microscopy (SEM) and X-ray photoelectron spectroscopy (XPS) both before and after plasma exposure to determine the impact of the plasma on the materials. To further probe the impact of catalyst packing on the synergisms between the plasma and catalysts, we have studied single-substrate systems, where a single catalyst pellet or substrate was placed in the coil region of our rf ICP reactor and a multi-substrate configuration, where the glass tubular reactor was aligned with zeolite pellets (Figure 2.2b). Our holistic approach to plasma diagnostics (i.e., determination of T_R and T_V as well as species densities and kinetic information) and comprehensive materials characterization enables us to more thoroughly investigate potential synergisms arising from the coupling of low temperature plasma and catalytic materials.

7.2 Results and Discussion

As the Table 7.1 data suggest, one of the key characteristics of N_2 plasmas is the internal temperatures of excited state N_2 in the plasma. As such, we first characterized our N_2 plasma without any substrates using optical emission spectroscopy.[1] Figure 7.1 shows a typical N_2 emission spectrum acquired with no substrate present (p = 50 mTorr, P = 25 W). $T_R(N_2)$ for the $C^3\Pi_u \rightarrow B^3\Pi_g$ transition was determined from simulated fits of experimental spectral data using Specair.[35] As described by Tu *et al.*,[30] a Boltzmann plot of ln ($I\lambda/A$) as a function of vibrational energy (E_V) was used to calculate $T_V(N_2)$, described in Chapter 2. The inset in Figure 7.1 shows a representative Boltzmann plot for a 100% N_2 plasma (sans substrate) created from the corresponding spectrum and the Table 2.5 data.

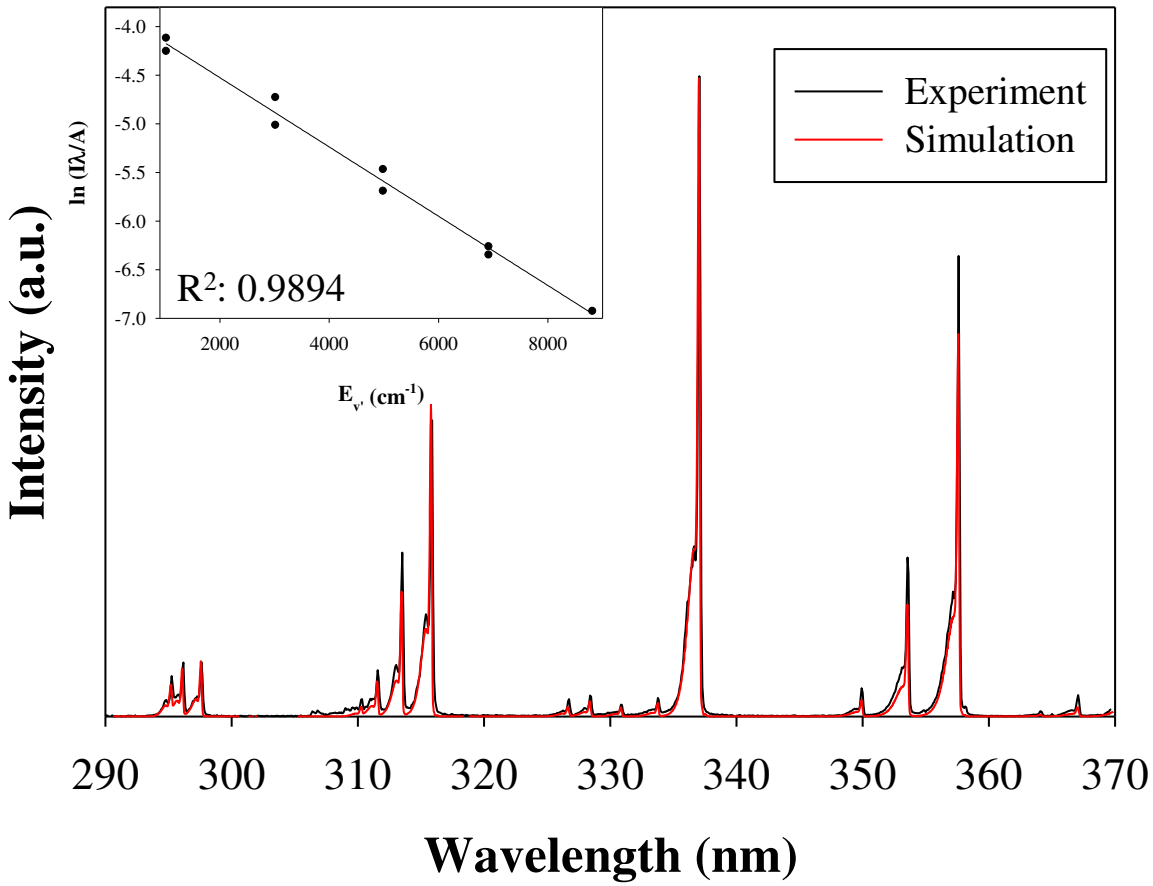

Figure 7.1. Representative emission spectrum at p = 50 mTorr, P = 25 W for N_2 ($C^3\Pi_u \rightarrow B^3\Pi_g$) in a N_2 plasma with no substrate. Simulation of the spectrum using Specair yields T_R = 310 K. Inset shows a Boltzmann plot of N_2 vibrational distribution in a 100% N_2 plasma under the same conditions, calculated using the Table 2.5 values.

The slope of the linear regression is inversely proportional to T_V, which ultimately yields T_V = 2910 ± 90 K for the particular set of conditions shown in Figure 7.1. A minimum of three trials were collected and fit for each condition reported, described in Chapter 2. We previously reported $T_V(N_2)$ values in N_2 plasmas;[1] however, these values were calculated using the "Temperature Loop" function within Specair.[35] The simulation process within the Specair program uses Boltzmann distributions to determine vibrational temperatures, but does so while simultaneously considering electronic, rotational, and translational temperatures to achieve a best "fit" to an experimental spectrum. It is not possible to simulate a spectrum with just vibrational temperature. Furthermore, the presence of zeolite substrates changes the corresponding emission spectrum, where there is clear overlap with the OH ($A^2\Sigma^+ \rightarrow X^2\Pi$) transition, Figure 7.2. Therefore, fitting the entirety of the N_2 ($C^3\Pi_u \rightarrow B^3\Pi_g$) emission spectrum using Specair was challenging, whereas the Table 2.5 spectral transitions utilized in the Boltzmann plot are independent of potential species (OH and NO) overlap. Thus, we believe the Boltzmann plot provides a more straightforward method to calculate T_V. In some cases, the previously reported values are within combined experimental error of those reported here. In those instances where the values differ appreciably, the methodology used herein results in higher T_V values than those acquired via the Specair simulation.

Noted in Section 7.1, N_2 T_R and T_V values within an N_2 discharge with and without a TiO_2 substrate have been measured as a function of operating conditions, reported in Tables 7.2 and 7.3. The $T_R(N_2)$ data in the 100% N_2 plasma (no substrate), reported previously,[1] show a small, but fairly linear increase with increasing applied power, with values near room temperature (~310 –340 K). The addition of a TiO_2 substrate does not appreciably change the overall T_R values, but the P dependence has largely disappeared, within experimental error.

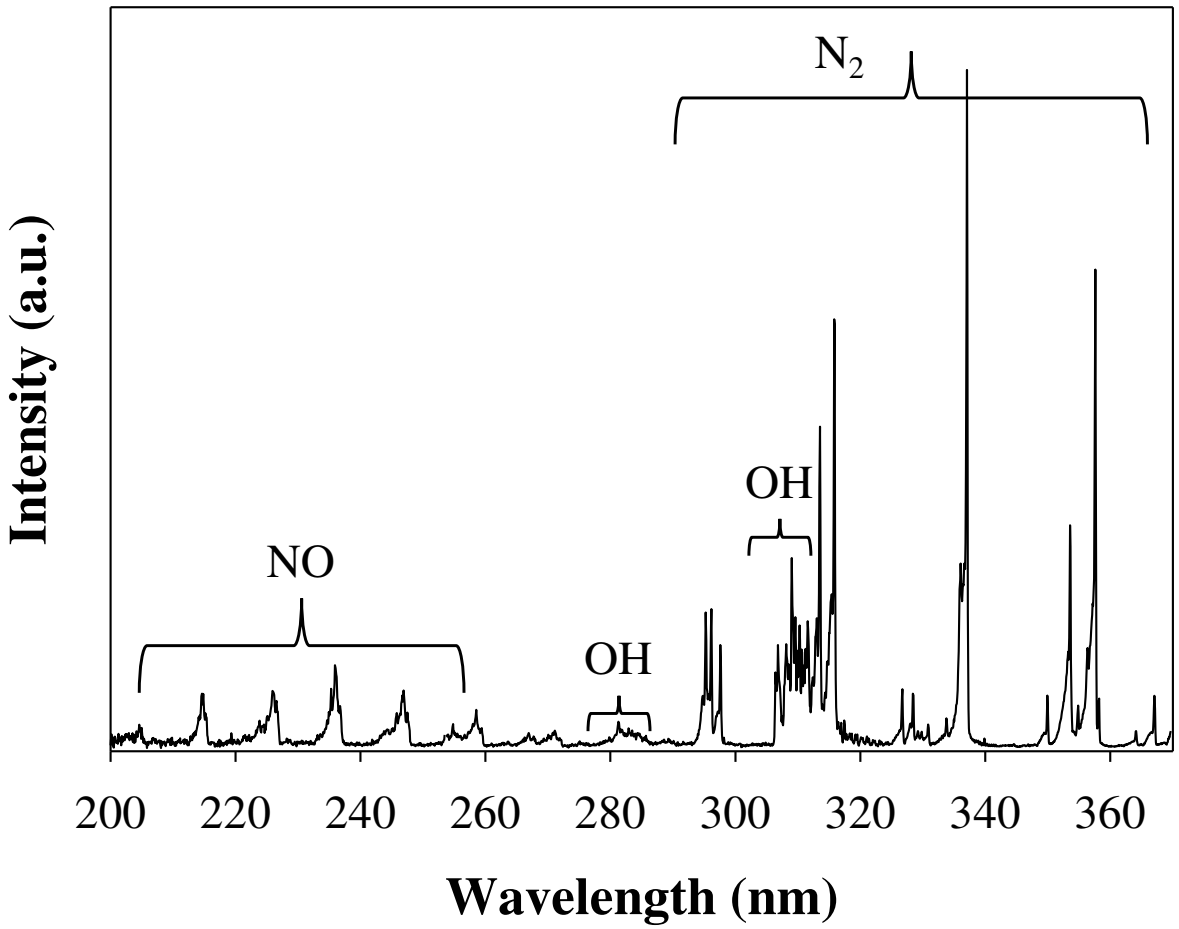

Figure 7.2. Representative emission spectrum at p = 150 mTorr, P = 100 W for N_2 ($C^3\Pi_u \rightarrow B^3\Pi_g$) in a N_2 plasma with zeolite pellet where spectral transitions corresponding to NO ($A^2\Sigma^+ \rightarrow X^2\Pi$) and OH ($A^2\Sigma^+ \rightarrow X^2\Pi$) transitions are observed.

In contrast, the T_V values listed in Table 7.3 show a strong linear dependence on applied power, both with and without the TiO_2 catalyst in the plasma. Interestingly, with the catalyst, the measured temperatures decrease by ~400 –1000 K and the dependence on power decreases by approximately a factor of 2. This decrease in $T_V(N_2)$ was documented at all pressures studied herein (50 – 150 mTorr), Table 7.3. Notably, $T_V(N_2)$ reaches values nearly an order of magnitude higher than $T_R(N_2)$, suggesting that rotational relaxation is more efficient than vibrational relaxation. Within N_2 plasmas containing a TiO_2 substrate, as p increases from 50 mTorr (6.7 Pa) to 150 mTorr (20 Pa), some interesting trends emerge. At lower P (25 – 75 W), $T_V(N_2)$ at 100 and 150 mTorr are within experimental error but are elevated compared to the 50 mTorr data. At higher P, as pressure is increased to 150 mTorr, there is significant quenching of the vibrational excited states, resulting in a decrease in T_V as a function of pressure.

These results clearly demonstrate the presence of a TiO_2 catalyst within the plasma can dramatically impact T_V and agree to a certain extent with the results reported by Tu *et al.* for a TiO_2 packed DBD system.[30] Overall, the actual values measured are similar to the literature work, with $T_R(N_2)$ slightly higher than room temperature (~300 – 600 K) and $T_V(N_2)$ significantly higher at ~2500 – 4500 K in both systems. In the DBD configuration, however, the dependence of $T_V(N_2)$ on discharge power and catalyst display the opposite behavior to that observed here: namely $T_V(N_2)$ decreases with applied power and significantly increases in the presence of the packed TiO_2. Notably, this power dependence previously observed was attributed to greater vibrational-translational relaxation at higher rf powers, and the increase with the catalyst was attributed to an enhancement of the average electron energy in the plasma.[30]

Possible explanations for these different trends lie primarily with the differences in the two plasma systems. Generally, emission intensity within a plasma is influenced by a number of

factors, including electron energy distribution function (EEDF), direct or dissociative excitation, cascade processes, radiation transport, as well as elastic and inelastic collisions.[36] First, the DBD system operates at atmospheric pressure, whereas our systems operate at much lower pressures, thereby increasing the mean free path in the system. At atmospheric pressure, electronic quenching (the process by which a collision with species *M* removes energy from excited state species towards any other final product[37]) determines the lifetime of the excited electronic state, occurring on a longer timescale compared to radiative decay. As such, fewer collisions are likely to occur in our systems than in the DBD. Upon the addition of a substrate, there is greater likelihood of productive plasma-surface collisions, effectively quenching the N_2 excited states. Furthermore, plasma processing time is an important consideration, as the DBD system studied by Tu *et al.* operated on the μs time scale,[30] whereas our temperature studies investigate steady-state emissions from N_2 molecules on the timescale of minutes. Arguably, there can be vast differences in long-lived and short-lived species within plasma discharges,[38] therefore future studies probing plasma internal temperatures as a function of time may be useful to understanding species' evolution during plasma processing.

Table 7.2. N_2 T_R (K) values in N_2 plasma systems[a]

p (mTorr)	P (W)	no substrate	TiO_2[b]	Zeolite
50	25	305 (5)	300 (10)	310 (10)
	50	320 (5)	300 (10)	310 (5)
	75	320 (1)	310 (10)	320 (10)
	100	350 (10)	320 (10)	335 (5)
	125	360 (10)	320 (10)	340 (5)
	150	355 (5)	370 (10)	355 (5)
100	25	310 (5)	320 (10)	310 (10)
	50	310 (3)	320 (10)	340 (20)
	75	315 (5)	320 (10)	360 (5)
	100	320 (3)	330 (10)	350 (10)
	125	330 (5)	330 (10)	330 (10)
	150	340 (10)	320 (10)	360 (10)
150	25	300 (5)	300 (10)	305 (5)
	50	305 (5)	300 (10)	320 (10)
	75	--	330 (10)	320 (5)
	100	310 (5)	330 (10)	340 (14)
	125	--	330 (10)	350 (20)
	150	320 (5)	340 (10)	350 (10)

[a]Values in parentheses represent standard deviation calculated from the mean of $n \geq 3$ trials.

[b] TiO_2 data collected and analyzed by Tara L. Van Surksum

Table 7.3. $T_V(N_2)$ values in N_2 plasma systems[a]

p (mTorr)	P (W)	no substrate	TiO_2[b]	Zeolite
50	25	2910 (90)	2310 (20)	2670 (100)
	50	4080 (70)	2560 (10)	3050 (90)
	75	3780 (50)	2780 (10)	3270 (100)
	100	4750 80)	3120 (120)	3800 (190)
	125	5560 (20)	3700 (270)	4230 (130)
	150	7000 (70)	4620 (70)	5070 (200)
100	25	2750 (200)	2550 (10)	2690 (185)
	50	3220 (30)	2780 (10)	3300 (40)
	75	3900 (70)	2970 (20)	3550 (50)
	100	4300 (180)	3140 (20)	3640 (120)
	125	4700 (15)	3350 (10)	3860 (200)
	150	4600 (90)	3560 (20)	3760 (200)
150	25	3320 (160)	2520 (20)	2990 (180)
	50	4470 (70)	2770 (10)	3530 (20)
	75	--	3010 (10)	3870 (30)
	100	5230 (140)	3150 (10)	4250 (40)
	125	--	3310 (20)	4500 (100)
	150	6020 (20)	3480 (10)	4980 (40)

[a]Values in parentheses represent standard deviation calculated from the mean of $n \geq 3$ trials.

[b] TiO_2 data collected and analyzed by Tara L. Van Surksum

Second, the catalyst in our system occupies only a small fraction of the total plasma volume, whereas Tu *et al.*'s reactor is completely packed with TiO_2 nanoparticles. Thus, the surface area of catalyst available for interaction with the plasma is much larger in the Tu system. Moreover, the packed reactor reduces the plasma volume and gives rise to changes in the discharge mode which could promote decomposition or non-uniform electric fields in the system.[3] If the hypothesis that the catalyst enhances the average electron energy in the plasma is true, then this enhancement could be dependent on the amount of catalyst present. We have used the OES spectra acquired in our system to measure the T_e in our plasmas. We previously reported T_e for a 100% N_2 plasma (no substrate) and found T_e ~1.6 eV, regardless of power.[1] Here, we found T_e ~1.8 eV for the same system with a TiO_2 substrate, also independent of applied power at p = 50 and 100 mTorr. The lack of significant dependence on P suggests increasing the overall energy of the system preferentially results in increasing the internal energy of neutrals or positive ions, rather than heating the electrons. Nevertheless, T_e appears to be slightly elevated in the presence of the TiO_2 catalytic material, indicating this catalyst does indeed slightly enhance the average T_e in our systems.

Exploring the impact of TiO_2 photocatalysts on the energy partitioning of N_2 plasmas allowed for a direct comparison to the work by Tu *et al.*[30] To further explore this work, we have also examined the impact of a different catalytic material on the gas-phase chemistry of an N_2 plasma. Figure 7.3 shows $T_R(N_2)$ and $T_V(N_2)$ as a function of P with and without a zeolite pellet in a 100% N_2 plasma. Although not nearly as dramatic as with TiO_2, a single zeolite pellet also decreases $T_V(N_2)$, especially at the highest applied power, Figure 7.3b. The behavior for $T_R(N_2)$ is much more complex. At the lower P (i.e., 50 – 100 W), $T_R(N_2)$ with the zeolite pellet is higher than that measured in the system without the catalyst, Figure 7.3a.

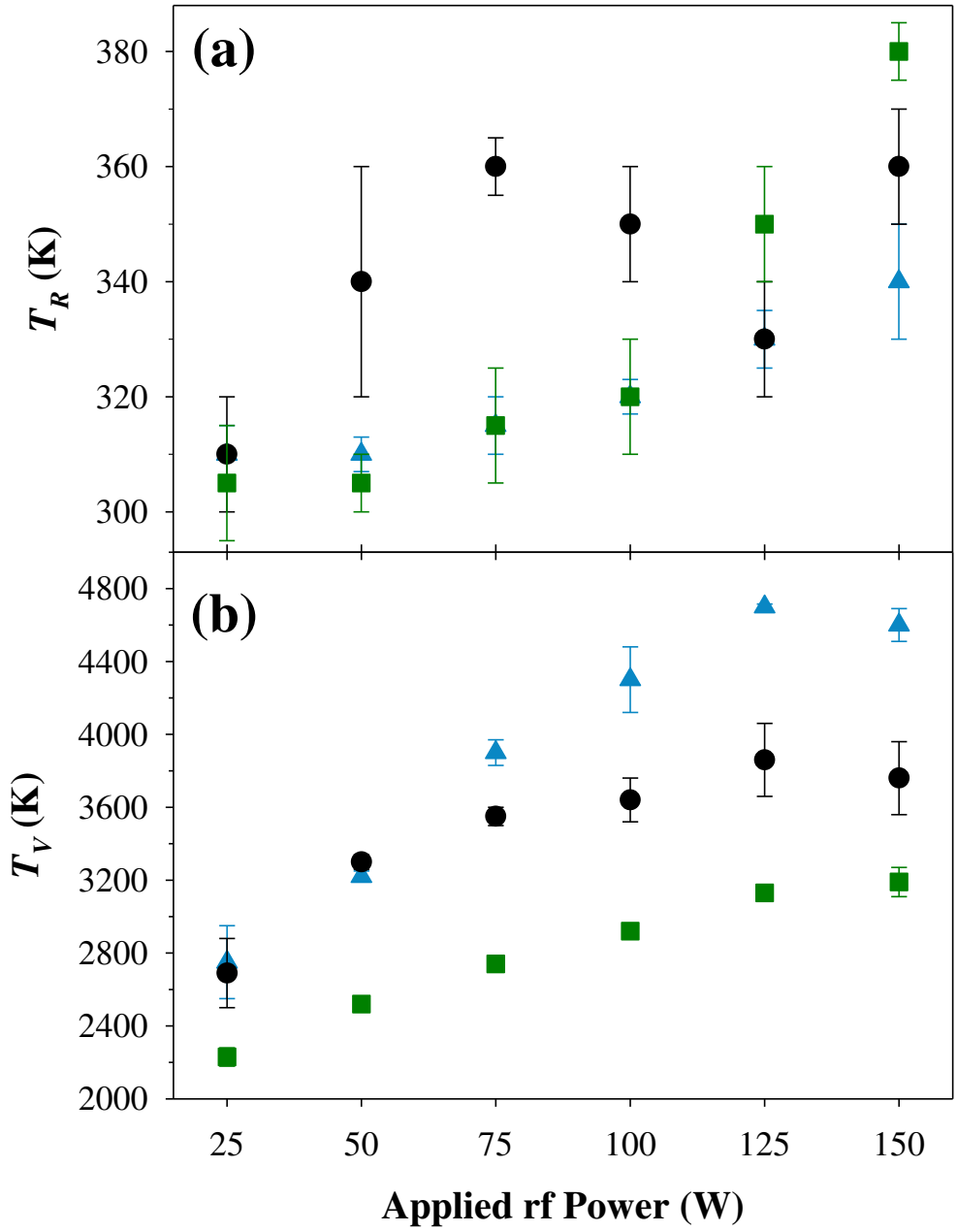

Figure 7.3. (a) $T_R(N_2)$ and (b) $T_V(N_2)$ from a N_2 plasma system at p = 100 mTorr with (black circles) and without (blue triangles) a zeolite substrate. Values for T_R without a substrate were previously reported.[1]

At $P \geq 125$ W, however, the values are the same within experimental error. Note, however, that $T_R(N_2)$ values lie between 310 and 380 K, regardless of plasma conditions. Thus, these subtle fluctuations in values suggest T_R is relatively independent of applied P, where rotational relaxation processes are less prominent in the presence of either catalyst. As noted above, a single catalyst in the coil region of the ICP reactor makes up a small fraction of the plasma volume; thus, a multiple zeolite substrate system (Figure 2.2a) was also examined. As shown in Figure 7.3a, at $P \leq 125$ W, the addition of more zeolite catalysts to the N_2 discharge does not appreciably affect rotational cooling pathways. At $P = 150$ W, $T_R(N_2)$ in the multiple substrate system is somewhat elevated compared to the other systems. The plasma discharge switches between operating in E and H mode between 125 and 150 W, such that at 150 W the plasma is operating in H mode. Consequently, the change in T_R is likely a result of this mode shift. Catalyst packing can change the plasma operating mode, which has been studied experimentally and theoretically in DBD systems.[39,40] Tu *et al.* reported packing their entire reactor altered the discharge mode.[10] Thus, we hypothesize that as our ICP reactor became more "packed" with zeolite catalysts, the accompanying mode shift may impact rotational energy distributions. Depicted in Figure 7.3b, the decrease in vibrational temperature observed with one pellet becomes more pronounced in the presence of multiple zeolite substrates. Vibrationally excited N_2 molecules clearly interact with the zeolite catalyst surface and can scatter with some energy loss; hence a decrease in vibrational energy is observed when a single zeolite pellet is present, and a larger decrease is documented in the multiple substrate system. These interactions can be explained through Reaction 7.1,

$$N_{2\,(g)}(v') \rightarrow N_{2(ads)}(v') \rightarrow N_{2\,(g)}(v'') \qquad (7.1)$$

where v' and v'' indicate two different vibrational states, with v'' having a lower vibrational energy.

As shown in Figure 7.4, inert gas actinometry was used to determine relative species' density as a function of *P* without and with a zeolite substrate in the coil region, wherein molecular emissions from N_2 (337.0 nm), NO (235.9 nm), OH (309.0 nm) and atomic emission from O (777.2 nm) were monitored. Without a substrate, the amount of N_2 in the discharge decreases with increasing *P*, where there is little to no observable emissions from NO, OH, or O. N_2 emission displays a similar *P* dependence with a zeolite pellet in the plasma; however, the amount of NO, OH, and O all increase with increasing *P* in the catalyst loaded system. The increase in the oxygen-containing gas-phase species likely arise from the plasma interacting with SiO_2-rich zeolite, resulting in removal of surface oxygen. This decrease in T_V (K) in the presence of either catalyst suggest that within these low pressure discharges, vibrationally excited molecules interact with the substrates and rebound with some energy loss, hence a lower T_V (K) is measured.[41] Evaluating steady-state emission spectroscopy provides valuable information regarding energy distributions and relative species densities, however, it is essential to utilize temporally resolved data to probe the entangled dynamics in PAC relevant systems.[42]

Depicted in Figure 7.5, intensity arising from N_2 emission at 337.0 nm was monitored as a function of time, where rate constants of formation (k_f) and destruction (k_d) were determined by fitting the intensity curve with a first order exponential (e^{-kt}). As evidenced in Figure 7.5a, the system with no substrate reached a steady state with no subsequent decay, hence a k_d is not reported. The addition of a zeolite catalysts significantly impacts the gas-phase chemistry, where a clear N_2 decay is documented.

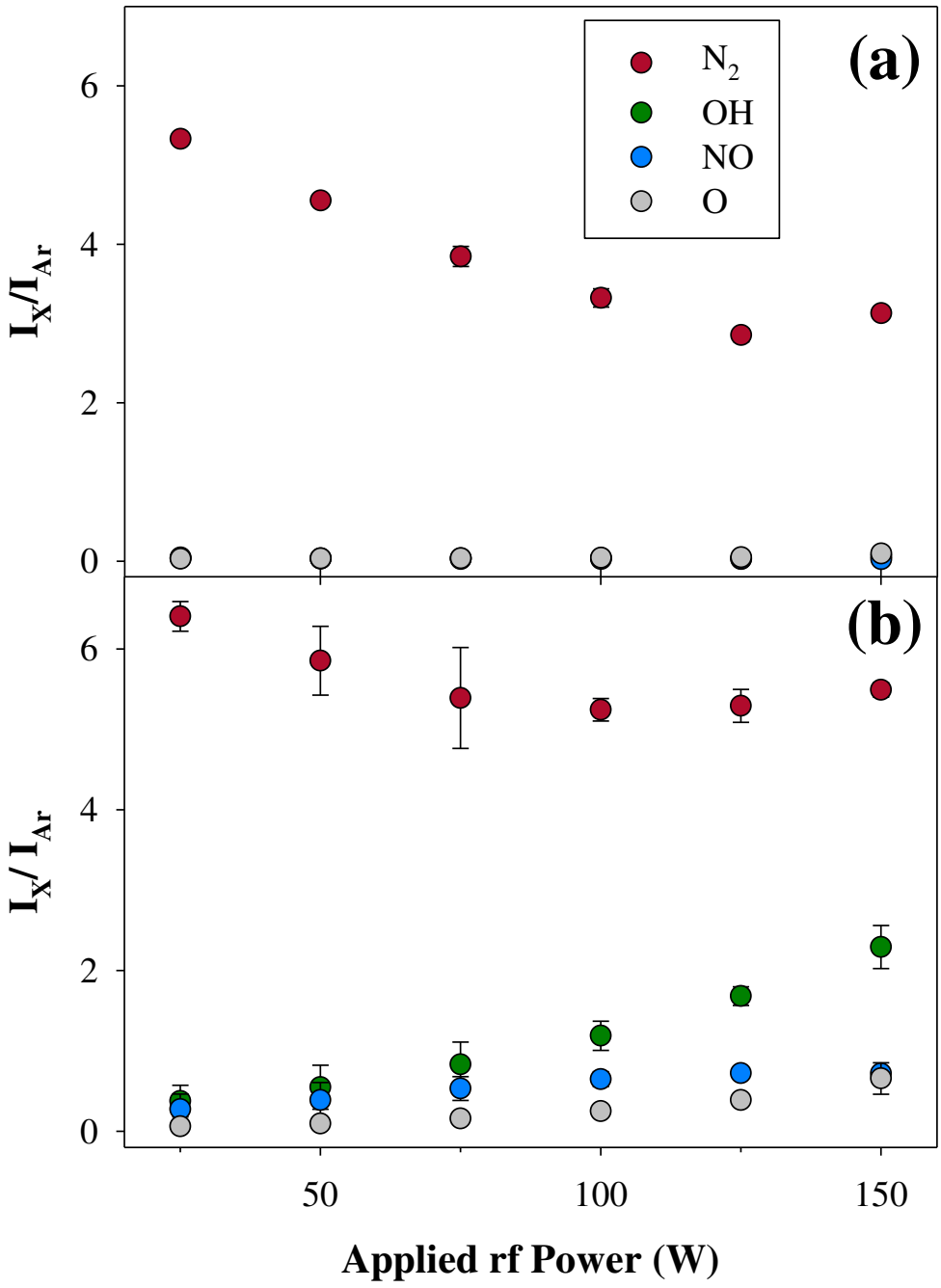

Figure 7.4. Steady-state relative species density as a function of applied rf power in a 100 mTorr N_2 plasma system without (a) and with (b) zeolite substrate.

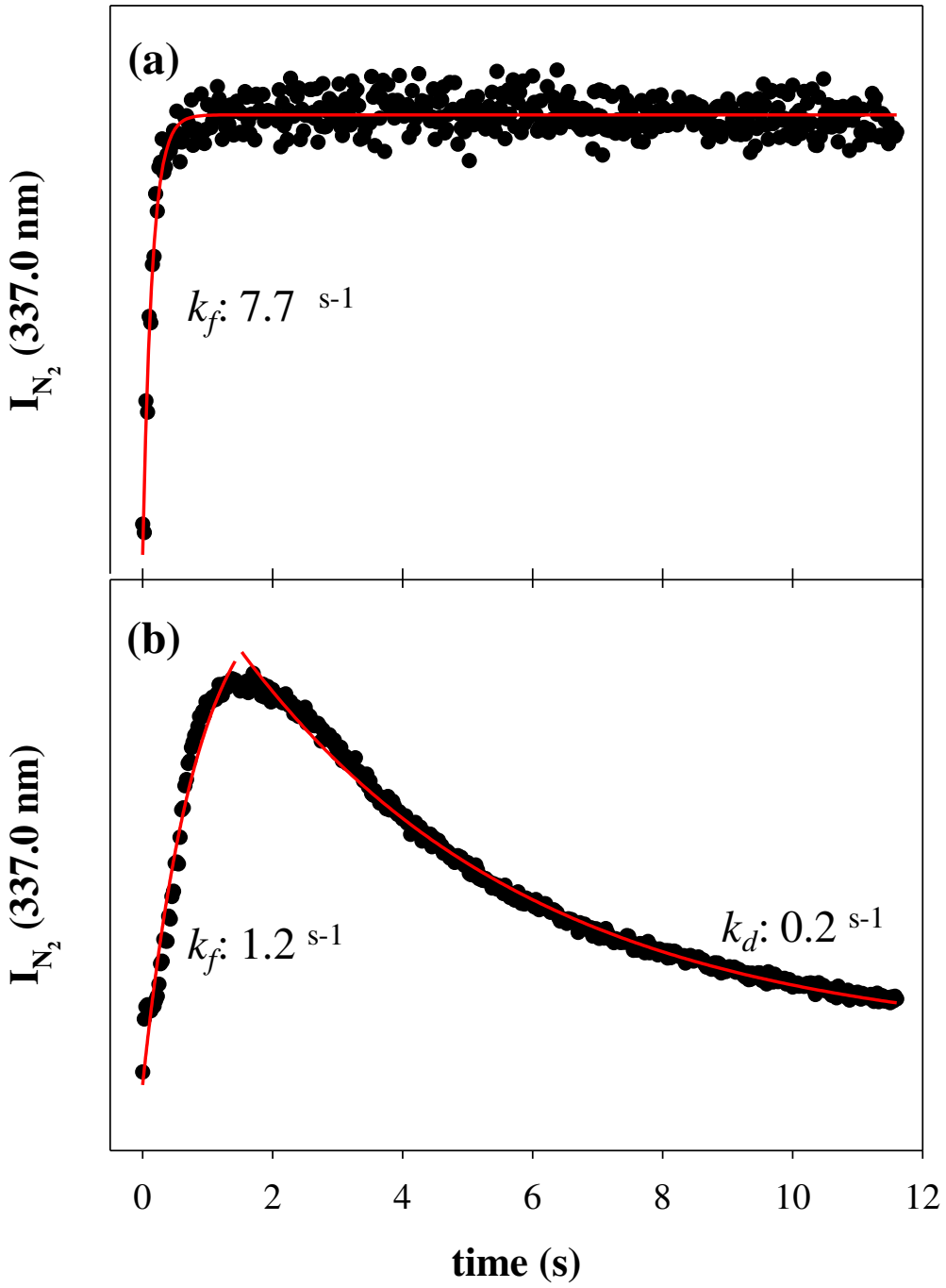

Figure 7.5. Intensity of N_2 emission plotted as a function of time at (a) p = 100 mTorr, P = 50 W with no substrate present; (b) p = 100 mTorr, P = 150 W with a single zeolite pellet. Rate constants of formation and destruction were determined by fitting a first order exponential to each curve.

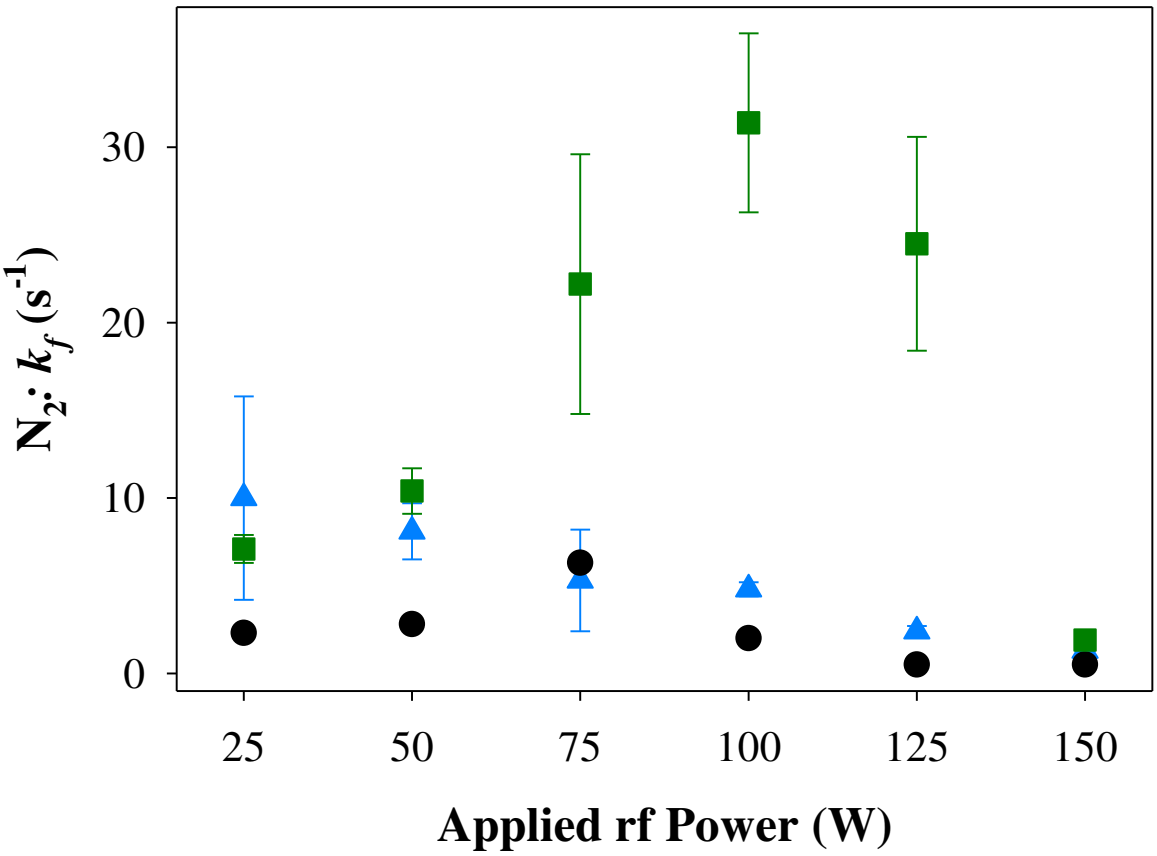

Figure 7.6. N_2 k_f (s^{-1}) from a N_2 plasma system at p = 100 mTorr without a catalyst (blue triangles); with a single zeolite pellet (black circles); and with multiple substrates (green squares).

To further assess the dynamics within these systems, time-resolved spectroscopy was collected as a function of power, in the presence of single and multiple zeolite substrates (Figure 7.6; Tables 7.4 and 7.5).

Without a catalyst present, $k_f(N_2)$ values decreases as a function of power, upon addition of catalysts to the system interesting trends emerge. In the single zeolite system, rate constants increase from $P = 25 - 75$ W, then a corresponding decrease occurs as P is increased to 150 W. Although the rate constants for the multi-substrate reactor are significantly higher at $P = 50 - 125$ W, all systems are within experimental error at 150 W. Aforementioned, the discharge is operating at H (electromagnetic) mode at this condition, suggesting the catalysts have a greater impact on reaction kinetics when the plasma is operating in E (electrostatic) mode. Table 7.4 documents k_f for N_2, OH, and NO molecules in an N_2 plasma. There is little to no emission arising from NO or OH species in the system without a catalyst (Figure 7.4), hence no kinetic information is available. At lower P in the single zeolite system (i.e., 25 – 75 W), there are emission peaks from NO (235.9 nm) and OH (309.0 nm), however, rate constants were not able to be quantified due to poor signal-to-noise ratios. Upon addition of more catalysts in the reactor, rate constants were determined at lower powers, suggesting that the interactions occurring at the surface of a single catalyst are further enhanced upon additional of more substrates. The determined rate constants largely unaffected by the amount of catalyst in the system. Table 7.5 details rate constants of destruction in the N_2 plasma with catalysts. Notably, a decay to steady-state emission is nominally only documented at higher P. Mehta *et al*. argue the gas-phase is heavily influenced by active nitrogen species (i.e., N, N_2^+, and vibrationally excited N_2) and increased reaction rates in the presence of catalysts arise from N_2 molecules in low vibrational states on the surface.[39]

Table 7.4. k_f (s^{-1}) values in N_2 plasma systems with and without zeolite substrates[a,b]

k_f (s^{-1})	P (W)	no substrate	single substrate	multi-substrate
N_2	25	10.0 (5.8)	6.6 (2.3)	7.1 (0.8)
	50	8.1 (1.6)	11.1 (2.8)	10.4 (1.3)
	75	5.3 (2.9)	22.6 (6.3)	22.2 (7.4)
	100	4.8 (0.4)	15.3 (2.0	31.4 (5.1)
	125	2.4 (0.3)	3.6 (0.5)	24.5 (6.1)
	150	1.3 (0.06)	1.6 (0.5)	1.9 (0.5)
OH	25	NA	--	9.3 (2.5)
	50		--	11.0 (5.4)
	75		--	9.6 (1.9)
	100		4.4 (0.4)	3.6 (0.8)
	125		3.4 (0.5)	3.7 (0.6)
	150		1.1 (0.2)	2.1 (0.3)
NO	25	NA	--	--
	50		--	10.0 (1.9)
	75		--	8.7 (4.0)
	100		9.2 (1.4)	9.6 (5.1)
	125		3.9 (0.5)	5.6 (0.3)
	150		1.7 (0.5)	2.8 (0.5)

[a]Values in parentheses represent standard deviation calculated from the mean of $n \geq 3$ trials.

[b]"--" represents emission peaks were present, but could not be quantified

Table 7.5. k_d (s^{-1}) values in N_2 plasma systems with zeolite substrates[a]

k_f (s^{-1})	P (W)	single substrate	multi-substrate
N_2	75	--	0.0092 (0.00014)
	100	--	0.013 (0.0051)
	125	0.055 (0.028)	0.019 (0.0088)
	150	0.16 (0.085)	0.054 (0.013)
OH	125	--	0.028 (0.00085)
	150	0.053 (0.027)	0.038 (0.0012)

[a]Values in parentheses represent standard deviation calculated from the mean of $n \geq 3$ trials.

For the data provided in Figures 7.3 and 7.6, at $P = 75 - 125$ there is a clear enhancement in formation of excited N_2 molecules, while concomitantly a lower T_V (K) (i.e., less vibrationally active) is documented for the multi-substrate system. These data were collected at intervals of 25 ms, it would be beneficial to obtain μs temporally resolved spectra to gain additional insight into reaction kinetics, described in Chapter 8. Clearly, the gas-phase and surface chemistry of the catalyst has a measurable impact on plasma-catalysis kinetics.

As noted in the Introduction, we sought to examine how the presence of a catalyst impacts the energetics within the discharge using both micro- and nano-structured materials. When comparing $T_V(N_2)$ in the systems with a catalyst, the vibrational temperatures documented with a zeolite pellet present are elevated relative to those in the TiO_2 system under all experimental conditions, Table 7.3. Factors to consider when comparing the two substrates include size and geometry of pores, as well as chemical properties. With a two-dimensional fluid model, Zhang *et al*. demonstrated that the shape of a catalyst pore has significant impact on the electric field within a plasma, thus substantial impact on the resulting plasma properties.[43] Their results indicated that the electric field enhancement was largest for conical pores, and that those with small openings experienced a large increase in ionization rate relative to those with larger openings. In our systems, the pores in the TiO_2 substrates have significantly smaller openings than those in the zeolite pellets, suggesting plasma generation near and in the pores of the TiO_2 may be heightened, ultimately leading to more vibrational quenching interactions with the catalyst surface. As TiO_2 is also a known photocatalyst, the UV light generated from the plasma may further active these materials and contribute to additional vibrational quenching of the N_2 ($C^3\Pi_u$) state. Nasonova and Kim coated zeolite materials with TiO_2 particles to observe possible synergisms upon coupling a catalyst with a photocatalyst for NO and SO_2 removal.[44] The

authors demonstrated these hybrid materials increased both NO and SO_2 removal efficiencies;[44] however, they did not characterize plasma internal temperatures. As TiO_2 nanoparticles supported on glass substrates have a large impact on $T_V(N_2)$ within our low-temperature rf discharges, a logical step forward would be to assess the impact on TiO_2 particles supported on materials with larger surface areas. Regardless of the pore size or surface area of a specific catalyst, clearly addition of a catalyst alters the gas-phase plasma chemistry. Consequently, we also examined how the catalysts were changed through gas-surface interactions in the plasma.

Specifically, N_2 plasmas have been used to create metal nitrides and other materials and nitrogen is known to readily replace oxygen in metal oxide lattices.[45,46] We therefore performed extensive materials characterization before and after plasma exposure to ascertain potential N-doping or modification of the catalysts via SEM and XPS. The commercially purchased TiO_2 material agglomerates into nanoparticle clusters with a porous structure when pasted onto the glass substrate; morphology does not change appreciably upon exposure to the N_2 plasma (p = 100 mTorr, P = 150 W, t = 10 min).[47] Likewise, the morphology of the zeolite pellet does not change appreciably upon plasma treatment, depicted in Figure 7.7. As described in Section 7.1, a goal of this work was to investigate the impact of materials (both nano- and micro-structured) on gas-phase composition and energetics, as well as assess material properties post plasma exposure.

Compositional data from high-resolution XPS spectra, Table 7.6, reveal untreated zeolite pellets are nominally composed of Si, O, and Al, with ~23 % C bound in environments corresponding to -C-C/-C-H, -C-O-R/-C-O-H, and -C=O (Figure 7.8). As shown in SEM images, Figure 7.7, zeolites are porous materials with a high surface area, therefore the adsorption of large amounts of atmospheric (adventitious) carbon is expected on the surface.

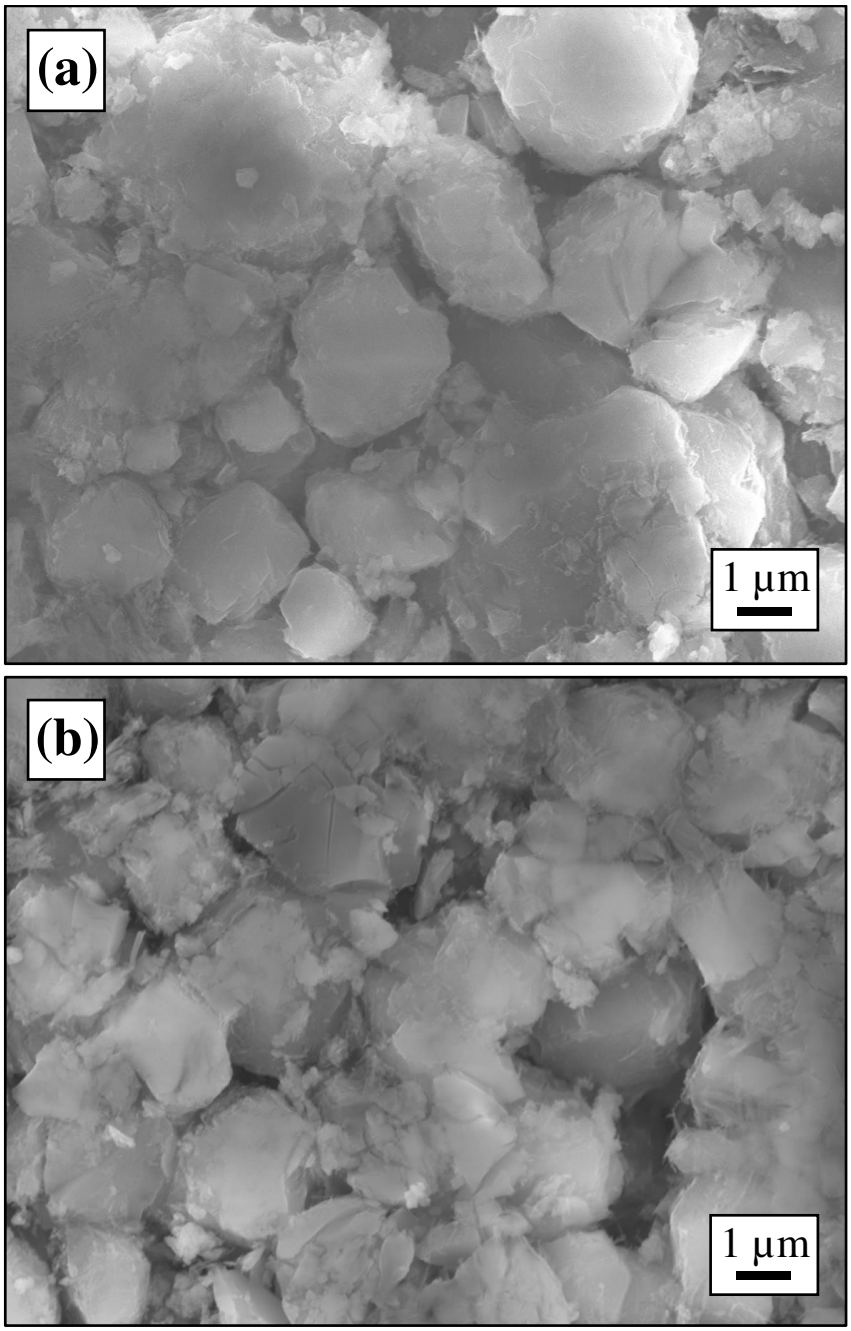

Figure 7.7. Representative SEM images (x7000) of (a) untreated zeolites and (b) post N_2 plasma exposure (P = 150 W; p = 100 mTorr; t = 10 min).

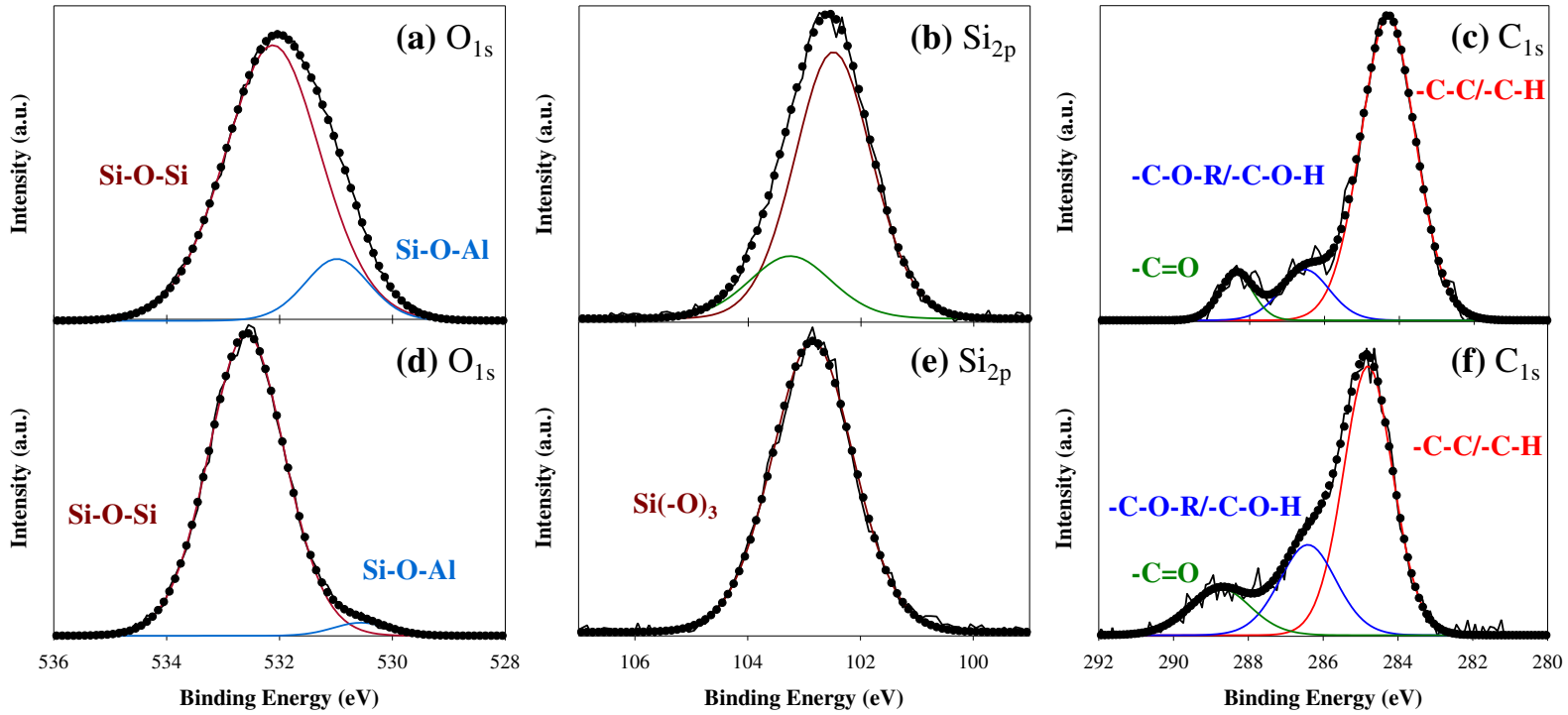

Figure 7.8. XPS high resolution O_{1s} (a, d), Si_{2p} (b, e), and C_{1s} (a, b) data for zeolite pellets prior to plasma exposure (top) and after N_2 plasma (p = 100 mTorr, P = 150 W, t = 10 min) exposure (bottom).

High-resolution O_{1s} and Si_{2p} spectra, Figure 7.8, further corroborate this evidence, as the primary oxygen binding environments include the Si-O-Si band at 531.7 eV and the Si-O-Al band at 530.8 eV.[48,49] Oxygen adsorbed to the material or bound to adventitious carbon can be present at binding energies 532.6 – 532.1 eV, which is difficult to deconvolute from the Si-O-Si band. High-resolution Si_{2p} data, Figure 7.8b and 7.8e, primarily show two Si binding environments, Si(-O_4) at 103.4 eV and Si(-O_3) at 102.8 eV[50], corresponding to an inorganic SiO_2 network, which nominally changes to a single binding environment at 102.8 eV post N_2 plasma treatment, Figure 7.8e. For PAC to be a viable and usable technology, these catalysts must be robust and able to withstand intense plasma exposure. Table 7.6 documents elemental composition of zeolite pellets post N_2 plasma exposure at a range of *P*. At 125 and 150 W, there are little to no changes in elemental composition, within error, except for the Al. At both *P*, the percent of Al slightly increases from the untreated, suggesting removal of adventitious carbon and oxygen from the surface. This is further substantiated by the gas-phase chemistry and SEM, where an increase in NO, OH, and O is documented (Figure 7.4). In Figure 7.7b, there appears to be areas that have been etched (or pitted), likely disrupting the zeolite Si-O-Si and Si-O-Al bonding bridges. At *P*=175 W, the most intense plasma conditions studied herein, the XPS data show significant nitrogen incorporation into the surface of the material. Furthermore, the O_{1s} and Si_{2p} binding environments are largely unchanged compared to the untreated material (Figure 7.8) as well as the morphology (Figure 7.7) and overall bulk crystallinity of the material (Figure 7.9), suggesting these materials still retain the properties that make them desirable catalysts.

Table 7.6. XPS atomic composition data for zeolite pellets[a,b]

	Untreated	**125 W**	**150 W**	**175 W**
Si (%)	15.5 (2.6)	23.1 (2.9)	18.7 (5.2)	21.0 (0.5)
O (%)	57.5 (4.0)	59.7 (3.5)	56.4 (5.3)	53.1 (0.5)
Al (%)	4.4 (0.6)	6.8 (0.7)	13.1 (7.7)	4.3 (0.3)
C (%)	22.7 (7.0)	10.5 (6.0)	11.8 (3.0)	14.1 (1.0)
N (%)	--	--	--	7.4 (0.3)

[a]Values in parentheses represent one standard deviation for the measurement
[b]Treatment conditions: p = 100 mTorr, t = 10 min

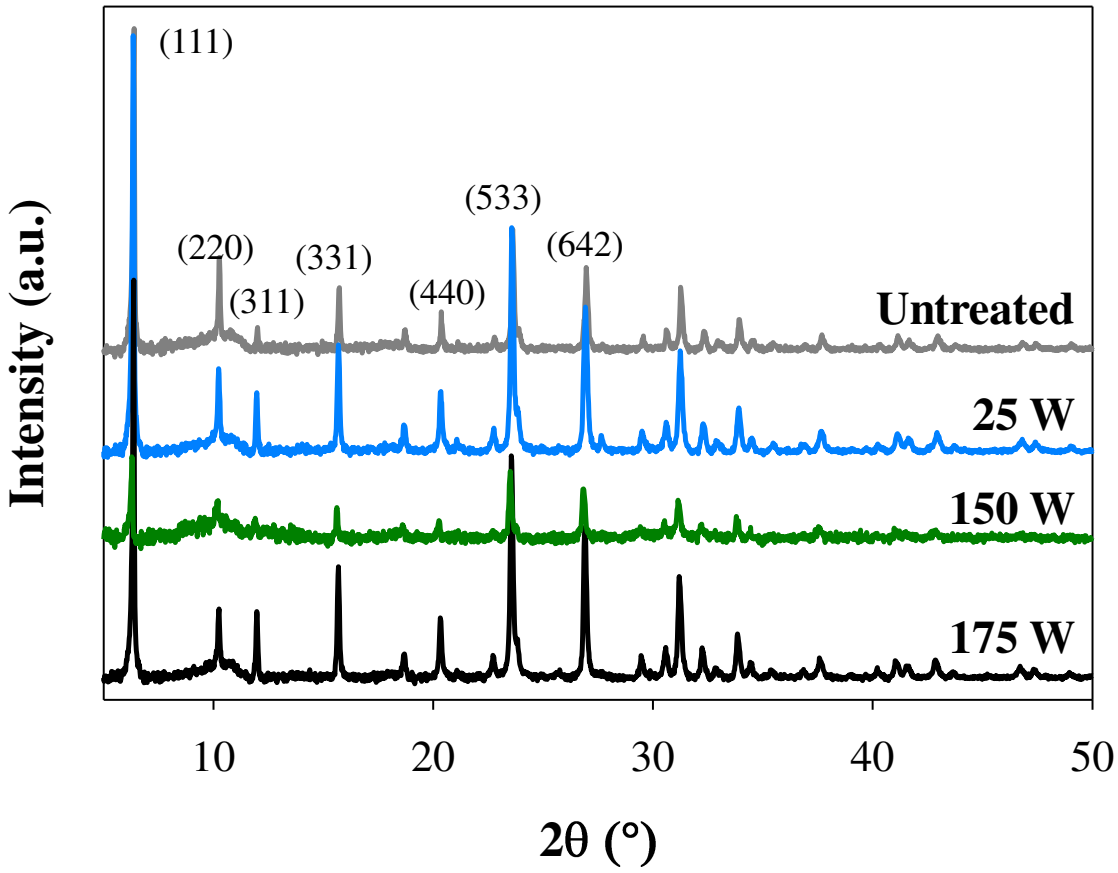

Figure 7.9. Diffraction patterns for untreated and treated (p = 100 mTorr, t = 10 min) zeolite pellets.

Large bandgap nitride materials have become increasingly important in catalytic and semiconductor processes. Nitrogen doping via plasma modification can enhance chemical and electrical properties of a wide variety of materials, ranging from metal oxides to carbon nanostructures.[51,52] In this study, we documented the implantation of N into both TiO_2 and zeolite substrates with a CW N_2 rf plasma.[53] This study was expanded to employ TR-OES to characterize pulsed N_2 plasmas (P_{eq} = 175 W, 50% d.c.), with and without a porous zeolite substrate in the coil region.[54] For the N_2 system without a substrate, Figure 7.10a, shows the intensity of N_2 emission (337.0 nm) slightly decreased through the duration of the 10 ms pulse widths, and little to no signal arising from NO (235.9 nm) was observed. Upon addition of a zeolite, signal from NO appears, Figure 7.10b, suggesting its formation in the system arises from the removal of surface oxygen. In comparison to our data, Mackus *et al.* used TR-OES to study pulsed-plasmas used in atomic layer deposition (ALD), providing a mechanism for monitoring thin-film growth in real time.[55] By monitoring emission intensities during plasma processing, the authors determined failures in plasma ignition during ALD cycles and could pinpoint the time at which gas flow failed.[55] The ability to use TR-OES as an *in-situ*, non-intrusive method to monitor and detect a range of advanced materials manufacturing techniques could substantially impact the adoption of industrial ALD processing. For process optimization, regardless of specific application, the plasma-material interface must be considered.

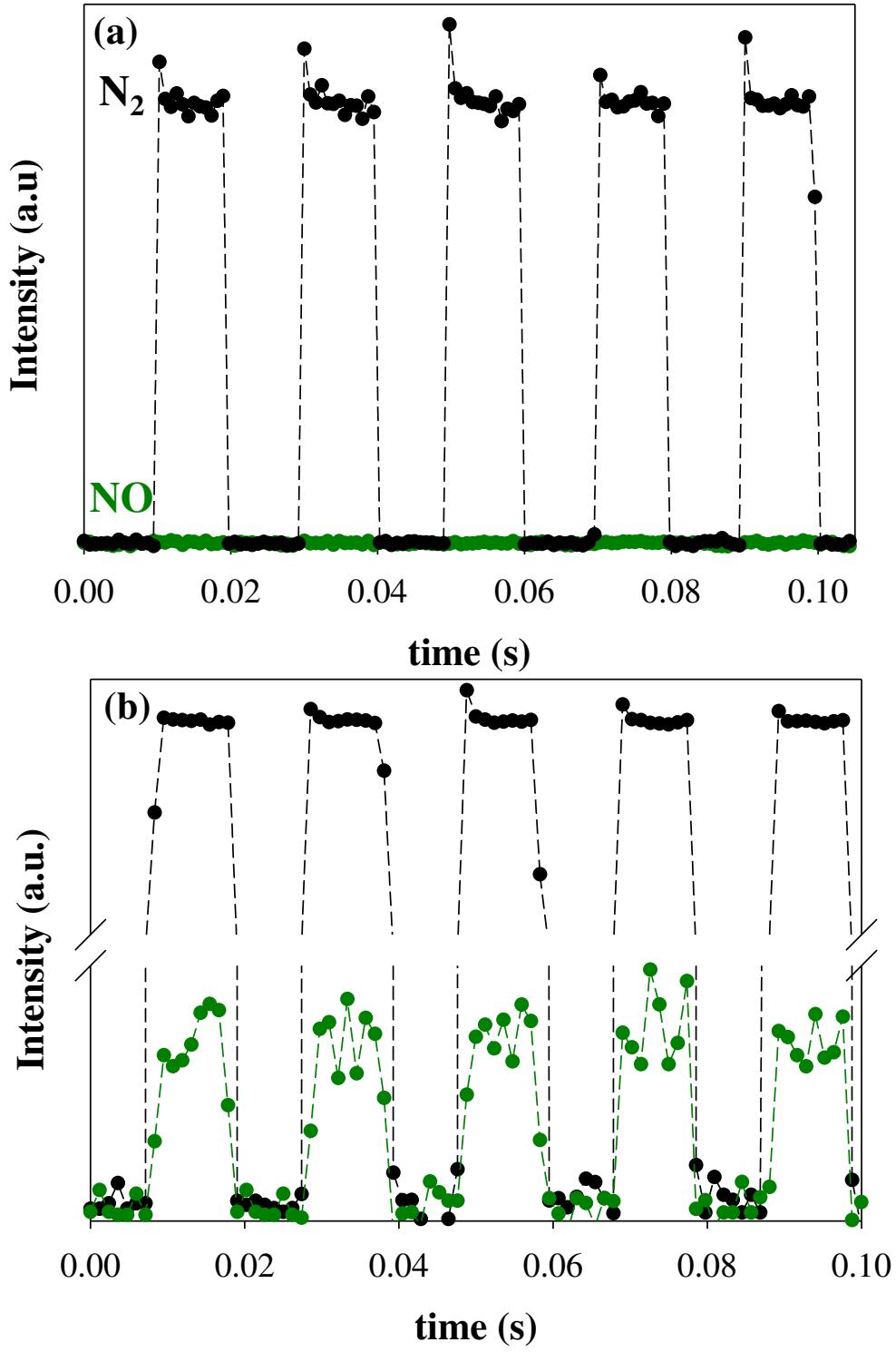

Figure 7.10. Time-resolved intensity of N_2 (black trace) and NO (green trace) with (a) no substrate and (b) a zeolite pellet in the coil region of an N_2 pulsed plasma (p = 100 mTorr, P_{eq} = 175 W, 50 % d.c.)

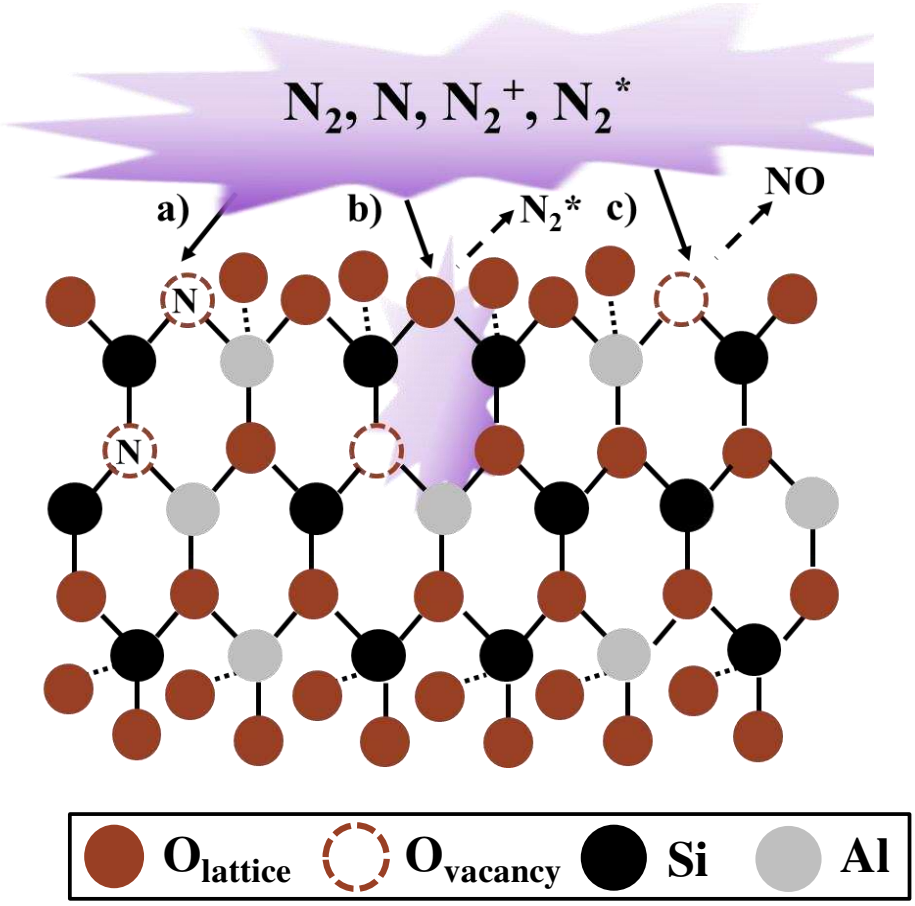

Figure 7.11. Schematic representation of various surface modification processes occurring during N_2 plasma processing: (a) N-doping of the substrate; (b) energetic bombardment resulting in vibrational quenching and possible microdischarge formation; and (c) etching and formation of new gaseous species.

The gas-surface interactions studied herein are schematically depicted in Figure 7.11. Although numerous possible gas-catalyst interactions exist, we believe these four are the most prevalent in our systems. XPS data reveal that under certain operating conditions, N is doped into both the zeolite and TiO_2 substrates. The etching of lattice oxygen in both TiO_2 and zeolite (nominally SiO_2) substrates can occur when excited state nitrogen impinges and reacts to form additional gas-phase species (i.e., NO, OH) as depicted in Figure 7.2 and Reaction 7.2,

$$N_{2\,(g)}^{*} + 2O_{(g)} \rightarrow 2NO_{(g)}^{*} \qquad (7.2)$$

where N_2^* and NO^* represent excited state species. Ultimately, we believe there is still much work to be done to further understand the underlying mechanisms involved in PAC systems. Nevertheless, the data presented herein clearly demonstrate that not only does the plasma alter the surface of catalytic substrates, but the presence of both micro- and nano-structured catalytic materials clearly alter energy partitioning within the gas-phase of the plasma.

7.3 Summary

As evidenced by gas-phase energetics data and resulting materials characterization, there is a synergistic, dynamic interface that arises when a plasma is coupled with catalysts. Regardless of material surface area, the presence of a catalyst in the coil region of a low-pressure rf plasma results in a pronounced decrease in the vibrational temperature of gas-phase species, with no clear or significant impact on rotational cooling pathways. For PAC to become a viable means of pollution control, it is essential that these energetic pathways and plasma-surface interactions be further examined. Notably, all work presented herein characterized excited state species; we have shown previously a significant energetic difference between ground and excited state N_2 and NO molecules.[1,56] As such, additional data on ground-state molecules in the system could provide further insight into energy partitioning within these systems. Finally, employing our

unique Imaging Radicals Interacting with Surfaces (IRIS) technique to determine a molecule's propensity to scatter from both nano- and micro-structured surfaces may provide more direct evidence of how plasma species synergistically interact with catalytic substrates. This holistic experimental approach, combining gas-phase diagnostics, IRIS, and robust material characterization will be essential to realizing the potential of PAC for pollution remediation.

REFERENCES

1. Hanna, A. R.; Blechle, J. M.; Fisher, E. R., Using Fundamental Spectroscopy to Elucidate Kinetic and Energetic Mechanisms within Environmentally Relevant Inductively Coupled Plasma Systems. *J. Phys. Chem. A* **2017**, *121*, 7627-7640.
2. Bacariza, M. C.; Biset-Peiro, M.; Graca, I.; Guilera, J.; Morante, J.; Lopes, J. M.; Andreu, T.; Henriques, C., DBD Plasma-assisted CO_2 Methanation using Zeolite-Based Catalysts: Structure Composition-Reactivity Approach and Effect of Ce as Promoter. *J. CO_2 Util.* **2018**, *26*, 202-211.
3. Feng, X.; Liu, H.; Hi, C.; Shen, Z.; Wang, T., Synergistic Effects and Mechanism of a Non-Thermal Plasma Catalysis System in Volatile Organic Compound Removal: A Review. *Catal. Sci. Technol.* **2018**, *8*, 936-954.
4. Puliyalil, H.; Jurkovic, D. L.; Dasireddy, V. D. B. C.; Likozar, B., A Review of Plasma-Assisted Catalytic Conversion of Gaseous Carbon Dioxide and Methane into Value-Added Platform Chemicals and Fuels. *RSC Adv.* **2018**, *8*, 27481-27508.
5. Neyts, E. C., Plasma-surface Interactions in Plasma Catalysis. *Plasma Chem. Plasma Process.* **2016**, *36*, 185-212.
6. Van Durme, J.; Dewulf, J.; Leys, C.; Van Langenhove, H., Combining Non-thermal Plasma with Heterogeneous Catalysis in Waste Gas Treatment: A Review. *Appl. Catal., B* **2008**, *78*, 324-333.
7. Xu, W.; Lin, K.; Ye, D.; Jiang, X.; Liu, J.; Chen, Y., Performance of Toluene Removal in a Nonthermal Plasma Catalysis System over Flake-Like HZSM-5 Zeolite with Tunable Pore Size and Evaluation of Its Byproducts. *Nanomaterials (Basel, Switzerland)* **2019**, *9*, 290.
8. Mei, D.; Zhu, X.; He, Y.-L.; Yan, J. D.; Tu, X., Plasma-assisted Conversion of CO_2 in a Dielectric Barrier Discharge Reactor: Understanding the Effect of Packing Materials. *Plasma Sources Sci. Technol.* **2014**, *24*, 015011.
9. Chen, G.; Britun, N.; Godfroid, T.; Georgieva, V.; Snyders, R.; Delplancke-Ogletree, M.-P., An Overview of CO_2 Conversion in a Microwave Discharge: the Role of Plasma-Catalysis. *J. Phys. D: Appl. Phys.* **2017**, *50*, 084001.
10. Tu, X.; Whitehead, J. C., Plasma-Catalytic Dry Reforming of Methane in an Atmospheric Dielectric Barrier Discharge: Understanding the Synergistic Effect at Low Temperature. *Appl. Catal., B* **2012**, *125*, 439-448.
11. Mustafa, M. F.; Fu, X.; Liu, Y.; Abbas, Y.; Wang, H.; Lu, W., Volatile Organic compounds (VOCs) Removal in Non-thermal Plasma Double Dielectric Barrier Discharge Reactor. *J. Hazard. Mater.* **2018**, *347*, 317-324.
12. Peng, P.; Chen, P.; Schiappacasse, C.; Zhou, N.; Anderson, E.; Chen, D.; Liu, J.; Cheng, Y.; Hatzenbeller, R.; Addy, M.; Zhang, Y.; Liu, Y.; Ruan, R., A Review on the Non-thermal Plasma-assisted Ammonia Synthesis Technologies. *J. Cleaner Prod.* **2018**, *177*, 597-609.
13. Santhosh, N. M.; Filipič, G.; Tatarova, E.; Baranov, O.; Kondo, H.; Sekine, M.; Hori, M.; Ostrikov, K. K.; Cvelbar, U., Oriented Carbon Nanostructures by Plasma Processing: Recent Advances and Future Challenges. *Micromachines* **2018**, *9*, 565.
14. Taghvaei, H.; Heravi, M.; Rahimpour, M. R., Synthesis of Supported Nanocatalysts via Novel Non-thermal Plasma Methods and its Application in Catalytic Processes. *Plasma Process. Polym.* **2017**, *14*, 1600204.

15. Adamovich, I.; Baalrud, S. D.; Bogaerts, A.; Bruggeman, P. J.; Cappelli, M.; Colombo, V.; Czarnetzki, U.; Ebert, U.; Eden, J. G.; Favia, P.; Graves, D. B.; Hamaguchi, S.; Hieftje, G.; Hori, M.; Kaganovich, I. D.; Kortshagen, U.; Kushner, M. J.; Mason, N. J.; Mazouffre, S.; Thagard, S. M.; Metelmann, H. R.; Mizuno, A.; Moreau, E.; Murphy, A. B.; Niemira, B. A.; Oehrlein, G. S.; Petrovic, Z. L.; Pitchford, L. C.; Pu, Y. K.; Rauf, S.; Sakai, O.; Samukawa, S.; Starikovskaia, S.; Tennyson, J.; Terashima, K.; Turner, M. M.; Sanden, M. C. M. v. d.; Vardelle, A., The 2017 Plasma Roadmap: Low Temperature Plasma Science and Technology. *J. Phys. D: Appl. Phys.* **2017**, *50*, 323001.
16. Whitehead, J. C., Plasma-Catalysis: The Known Knowns, the Known Unknowns, and the Unknown Unknowns. *J. Phys. D: Appl. Phys.* **2016**, *49*, 243001 (243024pp).
17. Malik, M. A.; Minamitani, Y.; Schoenback, K. H., Comparison of Catalytic Activity of Aluminum Oxide and Silica Gel for Decomposition of Volatile Organic Compounds (VOCs) in a Plasmacatalytic Reactor. *IEEE Trans. Plasma Sci.* **2005**, *33*, 50-56.
18. Gong; Zhao, R.; Qin, J.; Wang, H.; Wang, D., Ultra-efficient Removal of NO in a MOFs-NTP Synergistic Process at Ambient Temperature. *Chem. Eng. J.* **2019**, *358*, 291-298.
19. Wu, H.; Xu, C.; Xu, J.; Lu, L.; Fan, Z.; Chen, X.; Song, Y.; Li, D., Enhanced Supercapacitance in Anodic TiO_2 Nanotube Films by Hydrogen Plasma Treatment. *Nanotechnology* **2013**, *24*, 455401.
20. Han, J.-B.; Wang, X.; Wang, N.; Wei, Z.-H.; Yu, G.-P.; Zhou, Z.-G.; Wang, Q.-Q., Effect of Plasma Treatment on Hydrophilic Properties of TiO_2 Thin Films. *Surf. Coat. Technol.* **2006**, *200*, 4876-4878.
21. Porter, R. A.; Harshbarger, W. R., Gas Rotational Temperature in an RF Plasma. *J. Electrochem. Soc.* **1979**, *126*, 460-464.
22. Cernogora, G.; Ferreira, C. M.; Hochard, L.; Touzeau, M.; Loureiro, J., Vibrational Populations of N_2 ($A^3\Sigma_u^+$) in a Pure Nitrogen Glow Discharge. *J. Phys. B: At., Mol. Opt. Phys.* **1984**, *17*, 4429-4437.
23. Zhang, J.; Liu, L.; Ma, T.; Deng, X., Rotational Temperature of Nitrogen Glow Discharge Obtained by Optical Emission Spectroscopy. *Spectrochim. Acta, Part A* **2002**, *58*, 1915-1922.
24. Masoud, N.; Martus, K.; Figus, M.; Becker, K., Rotational and Vibrational Temperature Measurements in a High-Pressure Cylindrical Dielectric Barrier Discharge (C-DBD). *Contrib. Plasma Phys.* **2005**, *45*, 32-39.
25. Britun, N.; Gaillard, M.; Ricard, A.; Kim, Y. M.; Kim, K. S.; Han, J. G., Determination of the Vibrational, Rotational and Electron Temperatures in N_2 and Ar–N_2 rf discharge. *J. Phys. D: Appl. Phys.* **2007**, *40*, 1022-1029.
26. Gangoli, S. P.; Gutsol, A. F.; Fridman, A. A., A Non-equilibrium Plasma Source: Magnetically Stabilized Gliding Arc Discharge: I. Design and Diagnostics. *Plasma Sources Sci. Technol.* **2010**, *19*, 065003.
27. Wu, A. J.; Zhang, H.; Li, X. D.; Lu, S. Y.; Du, C. M.; Yan, J. H., Determination of Spectroscopic Temperatures and Electron Density in Rotating Gliding Arc Discharge. *IEEE Trans. Plasma Sci.* **2015**, *43*, 836-845.
28. Yang, F.; Mu, Z.; Zhang, J., Discharge Modes Suggested by Emission Spectra of Nitrogen Dielectric Barrier Discharge with Wire-Cylinder Electrodes. *Plasma Sci. Technol.* **2016**, *18*, 79-85.
29. Gröger, S.; Ramakers, M.; Hamme, M.; Medrano, J. A.; Bibinov, N.; Gallucci, F.; Bogaerts, A.; Awakowicz, P., Characterization of a Nitrogen Gliding Arc Plasmatron Using

Optical Emission Spectroscopy and High-speed Camera. *J. Phys. D: Appl. Phys.* **2018**, *52*, 065201.
30. Tu, X.; Gallon, J.; Whitehead, J. C., Electrical and Spectroscopic Diagnostics of a Single-Stage Plasma-Catalysis System: Effect of Packing with TiO_2. *J. Phys. D: Appl. Phys.* **2011**, *44*, 482003.
31. Niu, J.; Peng, B.; Yang, Q.; Cong, Y.; Liu, D.; Fan, H., Spectroscopic Diagnostics of Plasma-Assisted Catalytic Systems for NO Removal from $NO/N_2/O_2/C_2H_4$ Mixtures. *Catal. Today* **2013**, *211*, 58-65.
32. Tu, X.; Verheyde, B.; Cofrthais, S.; Paulussen, S.; Sels, B. F., Effect of Packing Solid Material on Characteristics of Helium Dielectric Barrier Discharge at Atmospheric Pressure. *Phys. Plasmas* **2011**, *18*, 080702.
33. Zhang, Y.; Wang, H.-y.; Zhang, Y.-r.; Bogaerts, A., Formation of Microdischarges Inside a Mesoporous Catalyst in Dielectric Barrier Discharge Plasmas. *Plasma Sources Sci. Technol.* **2017**, *26*, 054002.
34. Gu, J.-G.; Zhang, Y.; Gao, M.-X.; Wang, H.-Y.; Zhang, Q.-Z.; Yi, L.; Jiang, W., Enhancement of Surface Discharge in Catalyst Pores in Dielectric Barrier Discharges. *J. Appl. Phys.* **2019**, *125*, 153303.
35. Laux, C. O., Radiation and Nonequilibrium Collisional-Radiative Models. *von Karman Institute Lecture Series* **2002**, *7*.
36. Meichsner, J.; Schmidt, M.; Schneider, R.; Wagner, H. E., *Nonthermal Plasma Chemistry and Physics*. Taylor & Francis: 2012.
37. Dilecce, G., Optical Spectroscopy Diagnostics of Discharges at Atmospheric Pressure. *Plasma Sources Sci. Technol.* **2014**, *23*, 015011.
38. Grill, A., *Cold Plasma Materials Fabrications: From Fundamentals to Applications*. IEEE Press: Piscataway, NJ, 1994.
39. Mehta, P.; Barboun, P.; Go, D. B.; Hicks, J. C.; Schneider, W. F., Catalysis Enabled by Plasma Activation of Strong Chemical Bonds: A Review. *ACS Energy Letters* **2019**, 1115-1133.
40. Wang, W.; Kim, H.-H.; Van Laer, K.; Bogaerts, A., Streamer Propagation in a Packed Bed Plasma Reactor for Plasma Catalysis Applications. *Chem. Eng. J.* **2018**, *334*, 2467-2479.
41. Hanna, A. R.; Cuddy, M. F.; Fisher, E. R., Energy Partitioning and its Influence on Surface Scatter Coefficients within Fluorinated Inductively Coupled Plasmas. *J. Vac. Sci. Technol., A* **2017**, *35*, 05C308.
42. Fridman, A., *Plasma Chemistry*. Cambridge University Press: 2008.
43. Zhang, Y.-R.; Neyts, E. C.; Bogaerts, A., Enhancement of Plasma Generation in Catalyst Pores with Different Shapes. *Plasma Sources Sci. Technol.* **2018**, *27*, 055008.
44. Nasonova, A.; Kim, K.-S., Effects of TiO_2 Coating on Zeolite particles for NO and SO_2 Removal by Dielectric Barrier Discharge Process. *Catal. Today* **2013**, *211*, 90-95.
45. Antonczak, A. J.; Skowronski, L.; Trzcinski, M.; Kinzhybalo, V. V.; Lazarek, L. K.; Abramski, K. M., Laser-induced Oxidation of Titanium Substrate: Analysis of the Physicochemical Structure of the Surface and Sub-surface Layers. *Appl. Surf. Sci.* **2015**, *325*, 217-226.
46. Kollbek, K.; Szkudlarek, A.; Marzec, M. M.; Lyson-Sypien, B.; Cecot, M.; Bernasik, A.; Radecka, M.; Zakrzewska, Optical and Electrical Properties of $Ti(Cr)O_2$:N Thin Films Deposted by Magnetron Co-Sputtering. *Appl. Surf. Sci.* **2016**, *380*, 73-82.

47. Shearer, J. C.; Fisher, M. J.; Hoogeland, D.; Fisher, E. R., Composite SiO_2/TiO_2 and Polymer/TiO_2 Nanoparticles Produced Using Plasma-Enhanced Chemical Vapor Deposition. *Appl. Surf. Sci.* **2010**, *256*, 2081-2091.
48. Cui, X.; Chen, C.; Sun, S.; Zhou, D.; Ndayisenga, F.; Huo, M.; Zhu, S.; Zhang, L.; Crittenden, J. C., Acceleration of Saturated Porous Media Clogging and Silicon Dissolution Due to Low Concentrations of Al(III) in the Recharge of Reclaimed Water. *Water Res.* **2018**, *143*, 136-145.
49. Groening, P.; Biino, G. G., X-ray Photoelectron Spectroscopy (XPS) Used as a Structural and Chemical Surface Probe on Aluminosilicate Minerals. *Eur. J. Mineral.* **1998**, *10*, 423-437.
50. Alexander, M. R.; Short, R. D.; Jones, F. R.; Michaeli, W.; Blomfield, C. J., A Study of HMDSO/O_2 Plasma Deposits Using a High-Sensitivity and -Energy Resolution XPS Instrument: Curve Fitting of the Si_{2p} Core Level. *Appl. Surf. Sci.* **1999**, *137*, 179-183.
51. Rybin, M.; Pereyaslavtsev, A.; Vasilieva, T.; Myasnikov, V.; Sokolov, I.; Pavlova, A.; Obraztsova, E.; Khomich, A.; Ralchenko, V.; Obraztsova, E., Efficient Nitrogen Doping of Graphene by Plasma Treatment. *Carbon* **2016**, *96*, 196-202.
52. Pulsipher, D. J. V.; Martin, I. T.; Fisher, E. R., Controlled Nitrogen Doping and Film Colorimetrics in Porous TiO_2 Materials using Plasma Processing. *ACS Appl. Mater. Interfaces* **2010**, *2*, 1743-1753.
53. Hanna, A. R.; Van Surksum, T. L.; Fisher, E. R., Investigating the Impact of Catalysts on N_2 Rotational and Vibrational Temperatures in Low Pressure Plasmas. *J. Phys. D: Appl. Phys.* **2019**, *52*, 345202.
54. Hanna, A. R.; Fisher, E. R., Investigating Recent Developments and Applications of Optical Plasma Spectroscopy: A Review. *J. Vac. Sci. Technol., A* **2020**.
55. Mackus, A. J. M.; Heil, S. B. S.; Langereis, E.; Knoops, H. C. M.; van de Sanden, M. C. M.; Kessels, W. M. M., Optical Emission Spectroscopy as a Tool for Studying, Optimizing, and Monitoring Plasma-assisted Atomic Layer Deposition Processes. *J. Vac. Sci. Technol., A* **2009**, *28*, 77-87.
56. Blechle, J. M.; Hanna, A. R.; Fisher, E. R., Determination of Internal Temperatures within Nitric Oxide Inductively Coupled Plasmas. *Plasma Process. Polym.* **2017**, 1700041-n/a.

CHAPTER 8

EFFORTS TOWARDS UNRAVELING PLASMA-ASSISTED CATALYSIS: DETERMINATION OF KINETICS AND MOLECULAR TEMPERATURES WITHIN N_2O DISCHARGES[a]

The work presented in this dissertation sought to establish links between the gas-phase, gas-surface interface, and resulting material properties. This chapter utilizes optical emission spectroscopy to examine the impact of Pt and zeolite catalysts on gas-phase species densities, plasma energetics, reaction kinetics, and plasma-catalyst configurations within an N_2O rf plasma. The studies herein exemplify the need for a holistic approach to solving challenges presented in the plasma-catalysis community. This work was supported by the National Science Foundation (NSF CBET – 1803067) and the American Chemical Society Petroleum Research Fund (ACS PRF 59776 – ND6). I would like to thank the staff of the CSU Central Instrument Facility for assistance with the XPS, XRD, and SEM analyses.

[a] This chapter is reproduced from a submitted article to *ACS Catalysis* by Angela R. Hanna and Ellen R. Fisher.

8.1 Introduction

N_2O is a greenhouse gas that contributes to ozone depletion,[1] has a greenhouse warming potential ~300 times that of CO_2 and can remain in the atmosphere an average of 114 years.[2] N_2O is produced through natural processes; however, it is largely emitted from anthropogenic sources, including wastewater management, industrial processes, agriculture, and fuel combustion. The continuous increase of N_2O in the atmosphere, combined with long atmospheric residence times, requires developing efficient solutions for its abatement. Thermal decomposition,[3] selective adsorption,[4,5] catalytic decomposition, and plasma technologies[6,7] have been studied as means to reduce and remove N_2O emissions, including decreased energy requirements and enhanced rate conversions. Prior investigations have shown N_2O decomposes via a first order reaction, where proposed, general reaction schemes for its catalytic decomposition are shown in Reactions 8.1 and 8.2.[8,9]

$$catalyst + N_2O_{(g)} \rightarrow N_{2\,(g)} + O_{(ads)} \qquad (8.1)$$

$$O_{(ads)} + N_2O_{(g)} \rightarrow N_{2\,(g)} + O_{2\,(ads)} \qquad (8.2)$$

Several catalysts have been examined for N_2O decomposition, including noble metals (Pt, Au, and Pd);[10] metal oxides (TiO_2, NiO, Fe_2O_3, ZnO);[8,11] mixed metal oxides;[12,13]zeolites (ZSM-5, ZSM-11, Ferrierite);[4,14,15] and perovskite-type oxides.[16] Although these catalysts show high removal efficiency, they can also require relatively high operating temperatures (> 300 °C). To improve energy efficiency and selectivity of these processes, plasma-assisted catalysis (PAC) has been explored as a promising alternative technology for pollution abatement.[17-19]

Although auspicious, the applicability of PAC is limited due to a paucity of knowledge of the nature of fundamental plasma-catalyst interactions. Currently, there are three PAC techniques actively investigated; including two different configurations of two-stage systems, wherein the

catalyst and plasma are physically separated, as well as single-stage systems wherein the catalyst is placed directly in the discharge.[20,21] Within two-stage systems, the plasma alters the gas-phase composition, either prior to or after interaction with the catalyst; whereas single-stage systems enable all plasma species to interact with the catalyst simultaneously, often resulting in diverse dissociation products and significant alteration to the surface properties of the catalyst. Thus, deciphering possible synergisms within single-stage PAC systems is complex, originating from the discharge-catalyst interdependence.

The principles of PAC can be applied across a wide range of waste treatments, not limited to the oxidation of volatile organic compounds,[22] ammonia synthesis,[23] and methanation of CO_2;[24] however, NO_x emissions are of particular interest. Hur *et al.* studied the decomposition of N_2O in a low-pressure reactor, finding the destruction and removal efficiency (DRE) of N_2O enhanced by increasing applied power from 1.3 to 1.8 kW.[25] Jo *et al.* investigated the decomposition of N_2O over gamma alumina-supported metal oxide catalysts, revealing decomposition efficiency tends to decrease with increasing amounts of O_2 in the feed gas.[12] This result suggests gas-phase species compete for active sites on the catalyst and the adsorption of oxygen onto these active sites could inhibit the decomposition of N_2O.[12] This hypothesis was further supported by the work completed by Fan *et al*., documenting a substantial decrease in N_2O conversion with the concomitant increase of O_2 content in a N_2-O_2 mixture.[26] The type of plasma discharge (e.g., gliding arc, dielectric barrier, radio frequency, etc.), chemical nature, and substrate morphology are all capable of modifying plasma-catalytic processes. Affordable materials (compared to rare-earth metals) with complex morphologies (specifically nano- and micro-structured materials) could have an advantageous impact on PAC processes. Increasing surface-area to volume ratio for a catalyst could initiate additional surface interactions between the plasma species and

material, synergistically combining to result in augmented decomposition of a waste stream. Numerous studies have, therefore, focused on ion-exchanged Zeolite Socony Mobil (ZSM)-5 zeolites. Specifically, Centi *et al.*[4] and Guilemot *et al.*[27] found Ba-ZSM-5 to be a successful material in N_2O treatment applications. The addition of an active material can clearly impact the plasma itself, therefore it is crucial to characterize gas-phase species with and without a catalytic substrate in the system.

We have previously studied emitting and absorbing species in N_2O discharges without a substrate,[28] determining rotational (T_R) and vibrational (T_V) temperatures for both N_2 and NO molecules increase with increasing applied rf power (P) and decrease with increasing system pressure (p), reported in Chapter 6. This suggests as more energy is supplied to the discharge through increasing applied power, this energy is transferred to the gas-phase molecules, thereby populating higher vibrational states. As system pressure increases, the number of collisions within the plasma concomitantly increases, resulting in decreased T_R and T_V values through collisional quenching. Initial time-resolved optical emission spectroscopy (TR-OES) experiments suggested a mechanism of direct, electron-impact excitation of NO from both NO and N_2O precursors.[28] Through the combination of energetic and kinetic information, we can begin to optimize plasma operating conditions for the increased decomposition of N_2O into ambient species (e.g., N_2 and O_2) and decrease the amount of NO formed in a discharge.

In this work, these foundational plasma studies were expanded to investigate the decomposition of N_2O over Pt and zeolite catalysts. By selecting two forms of the same catalyst, Pt in foil and nanopowder form, the influence of material morphology on the discharge can be deduced, nominally without the complication of large differences in chemical identity. In addition to the rare-earth metal catalysts, micro-structured aluminosilicate zeolites were studied

herein. Of burgeoning interest is the correlation between material properties (e.g., chemical identity and pore size) and their potential influence on plasma properties (e.g., species density, energy distributions, formation of microplasmas within pores). Significant research efforts have been focused towards understanding the scaling of microplasmas in porous materials,[17,29] therefore we also sought to characterize the impact of both nano- and micro-scaled materials on plasma thermodynamics and kinetics. By focusing on these plasma properties, the experiments and results herein will produce foundational data for addressing critical intellectual challenges in the field of plasma science.[17] Collectively, this approach can advance globally-relevant technologies by providing pathways to better processes and materials for pollution abatement via PAC.

8.2 Results

A major focus of this work is to explore the potential of Pt and zeolite substrates as catalysts in the plasma-assisted decomposition of N_2O. One key element of these studies examines the impact of substrate morphology on the overall process. Pt foil (Figure 8.1a) shows a relatively smooth morphology; however, scratches and imperfections can be seen at higher (65x) magnification. The Pt powder substrate (Figure 8.1b) displays a random, highly porous network with minimum agglomeration of nanoparticle clusters. Microstructured zeolite pellets (Figure 8.1c) also display an interconnected porous morphology.

Using inert gas actinometry, the relative densities of excited-state plasma species (denoted here with brackets, e.g. "[NO]") observed in N_2O systems, with and without substrates, can be evaluated. Depicted in Figure 8.2, relative densities of N_2 (Figure 8.2a), NO (Figure 8.2b), atomic O (Figure 8.2c), and OH (Figure 8.2d) generated from a 90:10 N_2O/Ar plasma are plotted as a function of power for systems with no substrate, and with substrates in the coil (Figure 2.1a).

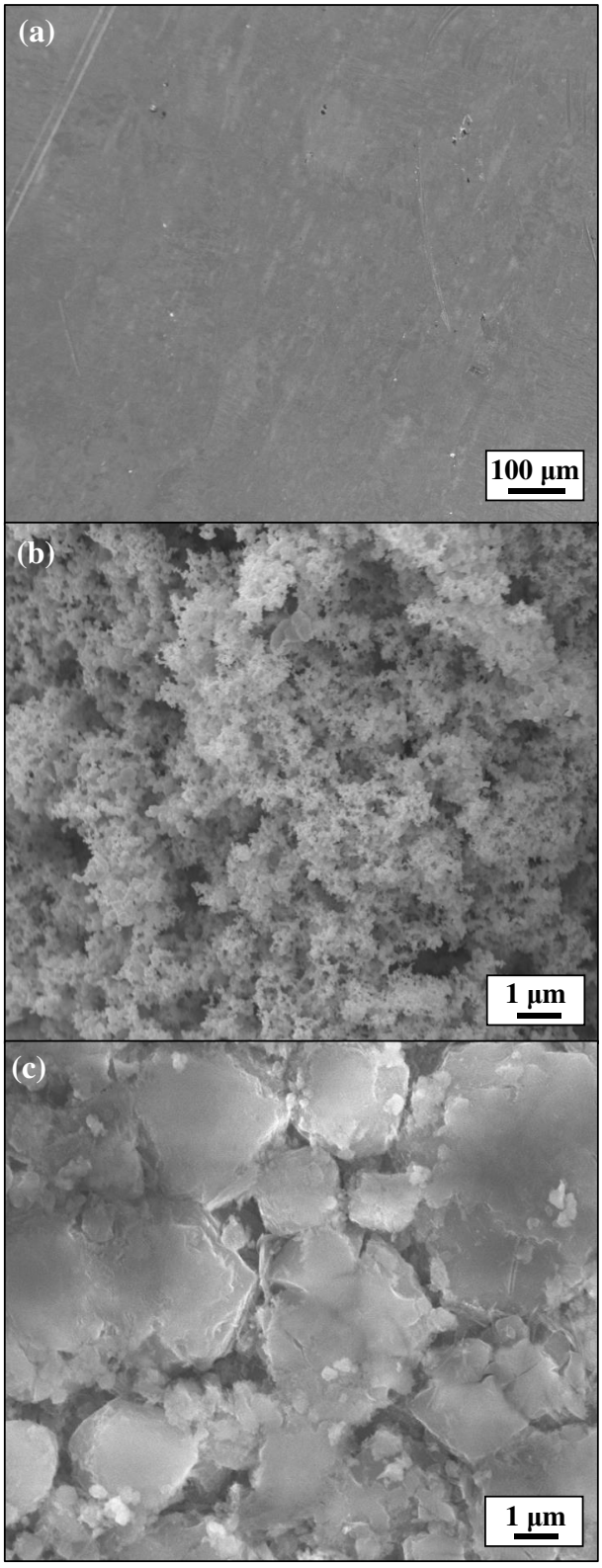

Figure 8.1. SEM images of (a) Pt foil (65x); (b) Pt powder (5000x) and (c) zeolite pellet (5000x).

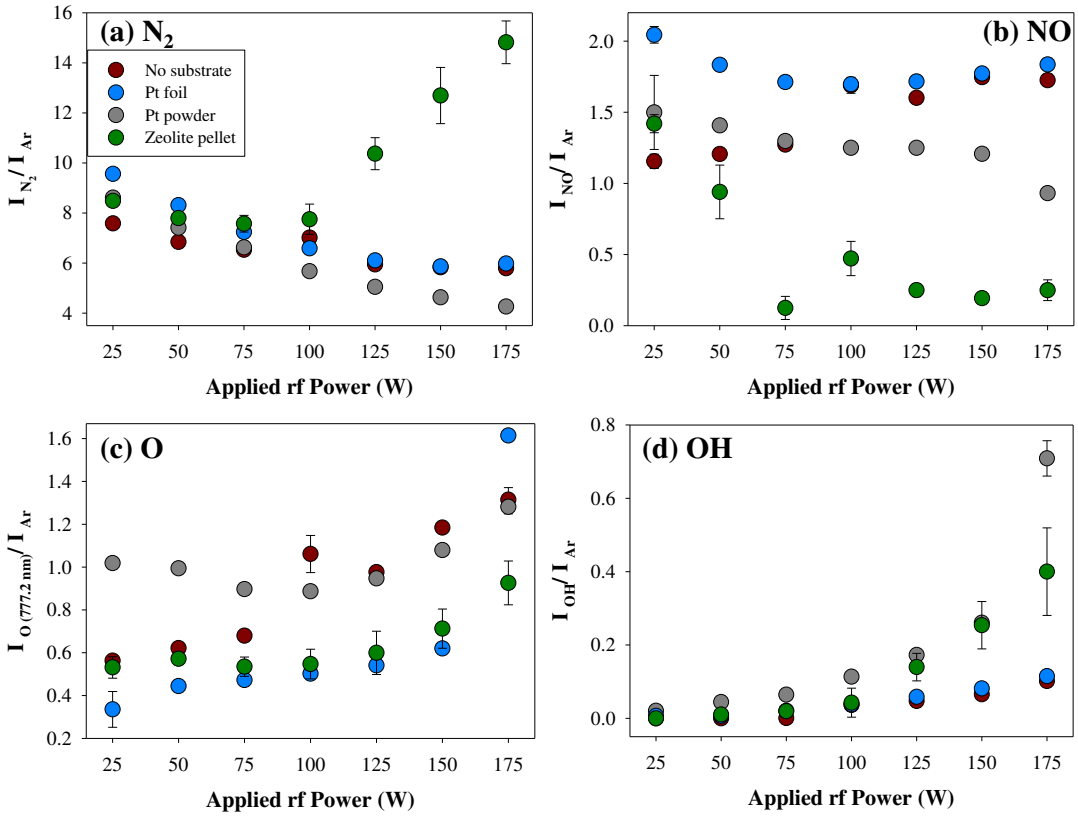

Figure 8.2. Relative density of (a) N_2, (b) NO, (c) O, and (d) OH as a function of *P* in a 100 mTorr, single stage N_2O plasma system. Error bars are plotted for all points and represent one standard deviation from the mean ($n \geq 3$).

With no substrate in the plasma discharge, [N_2] slightly decreases with a concomitant increase of [NO], [O], and [OH] as *P* increases from 25 to 175 W, suggesting additional fragmentation of N_2O at higher power. At 25 – 75 W, the relative densities of N_2 and NO are higher with Pt foil present compared to the substrate-free system, ultimately converging to values within experimental error of each other as *P* increases to 175 W. The Pt foil system also demonstrates an increase in [O] with power, yet more atomic oxygen is present in the substrate-free system at all *P* except 175 W. The nanostructured Pt powder (Figure 8.2b) resulted in a decrease in excited state N_2 and NO with a corresponding increase in atomic O. These data clearly highlight the impact of material morphology; although both substrates are nominally platinum, there is a significant and measurable difference in the resulting gas-phase chemistry. Furthermore, the amount of OH in the discharge is substantially increased at higher *P* with a Pt powder substrate, a trend that continues with the micro-porous zeolite pellet. Unlike the other catalytic materials, a sharp increase in [N_2] and corresponding decrease in [NO] is measured at $P \geq 75$ W with a zeolite pellet in the coil. Notably, all data provided in Figure 8.2 were collected over several minutes, averaging multiple spectra collected with a 50 ms integration time, 150 averages per scan. As such, these effectively steady-state measurements can clearly provide insight into plasma-catalyst interactions. Nevertheless, optical spectroscopy can also be employed to gain temporally-resolved information about these plasma-catalyst systems, discussed in Chapter 3.

The presence of a zeolite pellet in an N_2O plasma resulted in the smallest amount of NO produced in the discharge. As such, actinometric TR-OES data were collected with a zeolite substrate in the system at two *P*, Figure 8.3. Relative intensities of N_2 (orange), NO (blue), O (green), and OH (grey) were monitored via TR-OES as a function of time. At $P = 25$ W, [N_2]

increases as a function of time, reaching an intensity maximum after ~12 s. A subsequent decay to an apparent steady-state density occurred as time increases to 60 s. When *P* is increased to 150 W, [N_2] gradually increases over the 60 s collection time, in contrast to the 25 W data. Figure 8.3b is plotted with a logarithmic y-axis to more easily distinguish species at low concentrations. Note also that there is a gradual decrease in [NO] over time in the 25 W system, whereas in the 150 W system, [NO] signals became erratic and are only slightly above experimental noise after ~35 s. [O] increased throughout the plasma duration at 150 W compared to the 25 W discharge, where an initial increase and slight decay to a steady-state was measured. In contrast, the [OH] in the discharge at 25 W did not change over time, further supporting the observation that there is little to no OH in the system with these conditions (Figure 8.2d). At higher *P*, the [OH] increases significantly with time, exceeding the [O] after ~35 s. Particularly noticeable in the 150 W system, the first few points (< 5 s) are scattered for all species, thus, select species were studied with a higher time resolution to elucidate how they are initially formed and interact within the discharge.

TR-OES was performed without the addition of Ar to study the first 4 s of plasma ignition, employing a 1.5 ms integration time. Described in Chapter 2, a first order exponential was used to fit the onset of OES signals for N_2 and NO species (Figure 2.6). N_2 and NO k_f (s^{-1}) values were determined and are depicted as a function of power in Figure 8.4a and 8.4b, respectively. These k_f values are also reported in Table 8.1; k_d(NO) values are included in Table 8.2. $k_f(N_2)$ values increased with increasing power for the substrate free, Pt powder, and zeolite systems, ranging from 1.484 s^{-1} (zeolite: 25 W) to 17.579 s^{-1} (Pt powder: 150 W). Note, 150 W is the highest applied power examined in the time-resolved studies, compared to 175 W in the steady-state experiments.

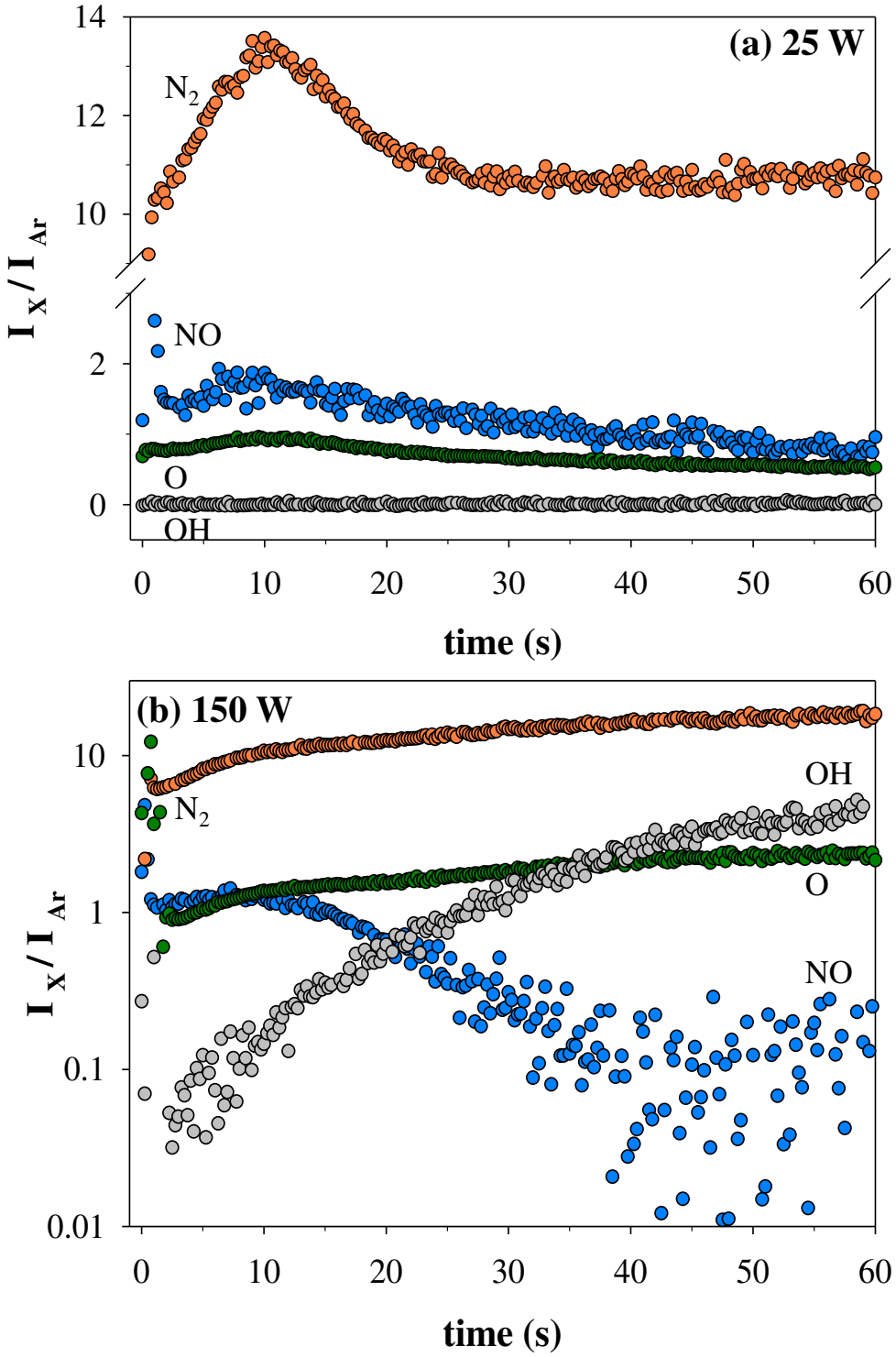

Figure 8.3. Relative intensity of plasma species (X) as a function of time for a 100 mTorr 90/10 N_2O/Ar plasma at (a) 25W and (b) 150 W, with a zeolite pellet present in the coil region of the discharge. Note relative intensities are plotted on a linear (a) and log (b) scale.

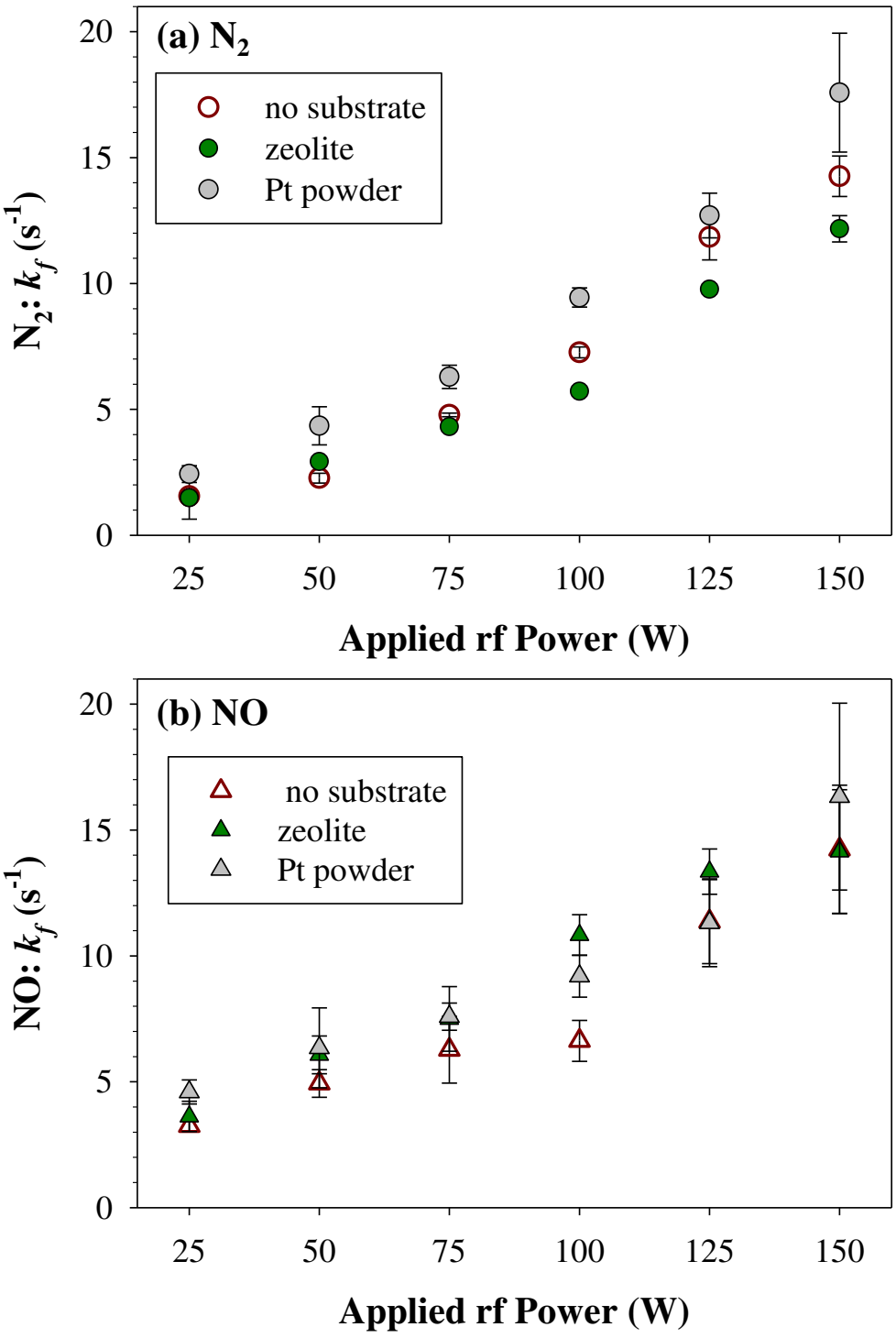

Figure 8.4. k_f (s^{-1}) for (a) N_2 and (b) NO plotted as a function of P and substrate. Error bars represent one standard deviation from the mean ($n \geq 6$).

Table 8.1. k_f (s^{-1}) values in N_2O plasma systems[a]

	***P* (W)**	**No substrate**	**Pt powder**	**Zeolite**
N_2	25	1.551 (0.912)	2.431 (0.332)	1.484 (0.0432)
	50	2.269 (0.195)	4.438 (0.757)	2.925 (0.0523)
	75	4.778 (0.0703)	6.291 (0.460)	4.310 (0.132)
	100	7.264 (0.216)	9.444 (0.381)	5.713 (0.173)
	125	11.845 (0.908)	12.700 (0.889)	9.770 (0.0961)
	150	14.260 (0.803)	17.579 (2.360)	12.171 (0.522)
NO	25	3.249 (0.240)	4.596 (0.478)	3.622 (0.604)
	50	4.933 (0.548)	6.347 (1.586)	6.069 (0.750)
	75	6.273 (1.327)	7.589 (0.540)	7.496 (1.284)
	100	6.625 (0.813)	9.193 (0.833)	10.930 (0.807)
	125	11.362 (1.669)	11.315 (1.741)	13.345 (0.899)
	150	14.229 (2.550)	16.326 (3.714)	14.145 (2.454)

[a]Values in parentheses represent standard deviation calculated from the mean of $n \geq 6$ trials

Table 8.2. k_d (s^{-1}) values in N_2O plasma systems[a]

	***P* (W)**	**No substrate**	**Pt powder**	**Zeolite**
NO	50	4.105 (1.056)	2.780 (0.628)	1.539 (0.459)
	75	6.445 (1.055)	2.937 (1.163)	4.408 (0.888)
	100	7.717 (0.739)	6.038 (1.871)	4.632 (0.545)
	125	11.843 (1.234)	6.533 (0.989)	6.406 (0.343)
	150	9.300 (1.015)	7.289 (0.865)	8.243 (1.146)

[a]Values in parentheses represent standard deviation calculated from the mean of $n \geq 6$ trials

At P = 175 W, plasma ignition was influenced by reflected rf P fluctuations within the first μs; therefore, rate constants could not be reliably quantified. Moreover, [NO] (and therefore NO signal) in the discharge is low at P = 175 W for both Pt powder and zeolite systems. At all P, excluding 125 W, $k_f(N_2)$ with a Pt powder were slightly elevated compared to the substrate free and zeolite systems. At $P \geq 100$ W, $k_f(N_2)$ decreased in the presence of a zeolite pellet. At $P <$ 100 W, k_f(NO) for a given system are higher compared to the N_2 rate constants. Additionally, k_f(NO) values demonstrate little to no dependence on the addition of a substrate. As detailed in Chapter 2 and depicted in Figure 2.4, after reaching a maximum, the intensity of NO follows an exponential decay to a steady-state, denoted as k_d. Due to low signal-to-noise ratios at 25 W, k_d(NO) values are not reported. k_d(NO) values demonstrated a slight dependence on P, however several conditions are within experimental error of each other. Evaluation of plasma kinetics can provide insight into plasma ignition and initial plasma-catalyst interactions; however, illumination of steady-state energetics is also a critical component of a holistic evaluation of PAC systems.

T_R values of excited state N_2 and NO are plotted as a function of applied rf power and substrate, Figures 8.5a and 8.5b, respectively and included in Table 8.3. When no substrate is present, $T_R(N_2)$ values have thermalized to approximately room temperature, with little to no power dependence. The Pt foil system shows a slightly stronger power dependence, $T_R(N_2)$ increases to 340 ± 10 K at P = 175 W. Interestingly, the two porous substrates impact the ability of N_2 molecules to rotationally thermalize, particularly the Pt powder substrates as $T_R(N_2)$ = 405 ± 10 K at P = 175 W. Albeit, this increase in $T_R(N_2)$ values as power increases is significantly smaller compared to the increase in T_R(NO) values, shown in Figure 8.5b.

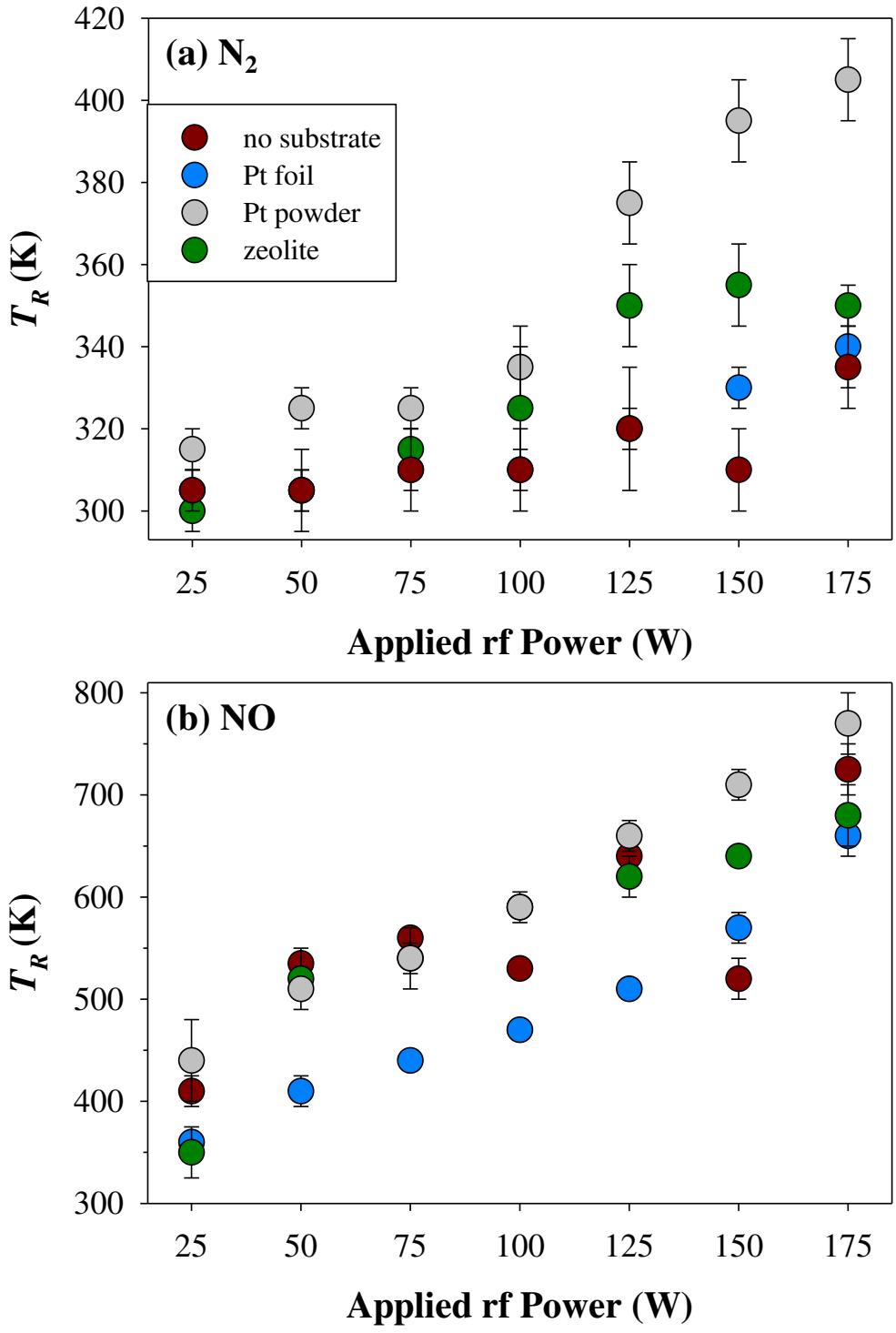

Figure 8.5. T_R (K) values for (a) N_2 and (b) NO molecules, plotted as a function of applied rf power and substrate within p = 100 mTorr N_2O discharge. Error bars represent one standard deviation from the mean ($n \geq 3$).

Table 8.3. T_R (K) for excited state N_2 and NO within N_2O plasmas[a,b]

	***P* (W)**	**No substrate**	**Pt foil**	**Pt powder**	**Zeolite**
N_2	25	305 (5)	305 (5)	315 (5)	300 (5)
	50[b]	305 (10)	305 (5)	325 (5)	305 (5)
	75	310 (10)	310 (5)	325 (5)	315 (5)
	100[b]	310 (5)	310 (10)	335 (10)	325 (15)
	125	320 (15)	320 (5)	375 (10)	350 (10)
	150[b]	310 (10)	330 (5)	395 (10)	355 (10)
	175	335 (10)	340 (10)	405 (10)	350 (5)
NO	25	410 (15)	360 (10)	440 (40)	350 (25)
	50[b]	535 (10)	410 (15)	510 (10)	520 (30)
	75	560 (10)	440 (10)	540 (15)	540 (30)
	100[b]	530 (5)	470 (10)	590 (15)	590 (10)
	125	640 (10)	510 (10)	660 (15)	620 (20)
	150[b]	520 (20)	570 (15)	710 (15)	640 (10)
	175	725 (25)	660 (20)	770 (30)	680 (30)

[a]Values in parentheses represent standard deviation calculated from the mean of $n \geq 3$ trials
[b]Previously reported[28]

Table 8.4. T_V (K) for excited state N_2 and NO within N_2O plasmas[a.b]

	***P* (W)**	**No substrate**	**Pt foil**	**Pt powder**	**Zeolite**
N_2	25	2850 (15)	2500 (20)	2560 (180)	2570 (70)
	50	3450 (80)	3150 (15)	2960 (100)	3010 (160)
	75	3880 (70)	3670 (70)	3380 (70)	3700 (40)
	100	4410 (50)	4150 (15)	3650 (30)	4060 (90)
	125	5290 (90)	4600 (10)	3990 (60)	4830 (10)
	150	6360 (50)	5050 (30)	4210 (70)	5190 (40)
	175	6890 (50)	6380 (70)	4190 (210)	5900 (80)
NO	25	2880 (20)	2760 (20)	2990 (10)	2850 (140)
	50[b]	2870 (60)	2770 (20)	2900 (50)	3300 (160)
	75	2910 (90)	2790 (10)	2910 (20)	3320 (120)
	100[b]	2900 (10)	2780 (20)	2860 (40)	3630 (100)
	125	3080 (50)	2920 (130)	2910 (20)	3550 (120)
	150[b]	3300 (170)	2860 (10)	3160 (50)	4200 (180)
	175	3850 (110)	3500 (30)	3730 (90)	4050 (140)

[a]Values in parentheses represent standard deviation calculated from the mean of $n \geq 3$ trials
[b]Previously reported[28]

A positive correlation between rf P and T_R(NO) was determined, where T_R(NO) values increased by ~300 K as P increased from 25 to 175 W for each system. At 150 W, the addition of a substrate (Pt foil and power, zeolite pellet) resulted in increased T_R(NO) values, yet T_R(NO) values converge within experimental error as P increases to 175 W.

T_V values for excited state N_2 and NO are listed in Table 8.4. Regardless of catalytic substrate, $T_V(N_2)$ increases as a function of rf power. T_V(NO) also displays a power dependence; however, the increase in T_V(NO) between 25 and 175 W is significantly less compared to that observed for N_2 species. When no substrate is present, T_V(NO) values at lower P (25 – 100 W) are all within experimental error of each other. As the rf power is increased from 100 – 175 W, an increase in T_V(NO) is observed. ΔT_V for N_2 (Figure 8.6a) and NO (Figure 8.6b) was determined via Equation 8.4 as a function of power and substrate to probe differences in vibrational energy partitioning upon the addition of a catalyst.

$$\Delta T_V = [T_V(catalyst) - T_V(no\ substrate)] \qquad (8.4)$$

At all conditions herein, vibrational cooling of N_2 molecules, as measured by ΔT_V, was observed upon the addition of catalytic substrates. At 25 and 50 W, vibrational cooling was relatively independent of catalyst type; however, as P is increased to 175 W, the temperature difference between the Pt powder and substrate-free system became more pronounced [$\Delta T_V(N_2)$ = - 2700 ± 210 K]. ΔT_V with zeolite and Pt foil substrates display a similar, limited dependence on P [$\Delta T_V(N_2) \leq$ - 500 K] below P = 125 W. Notably, ΔT_V at 150 and 175 W is significantly larger (-1170 ± 60 K and -990 ± 90 K, respectively) in the presence of a zeolite pellet. Unlike $T_V(N_2)$, vibrational cooling of NO was not observed for all substrates, shown in Figure 8.6b and Table 8.4. At 25 W, the presence of catalysts does not impact the resulting NO vibrational energetics. As P is increased in the zeolite system, T_V (NO) is enhanced, with limited P dependence.

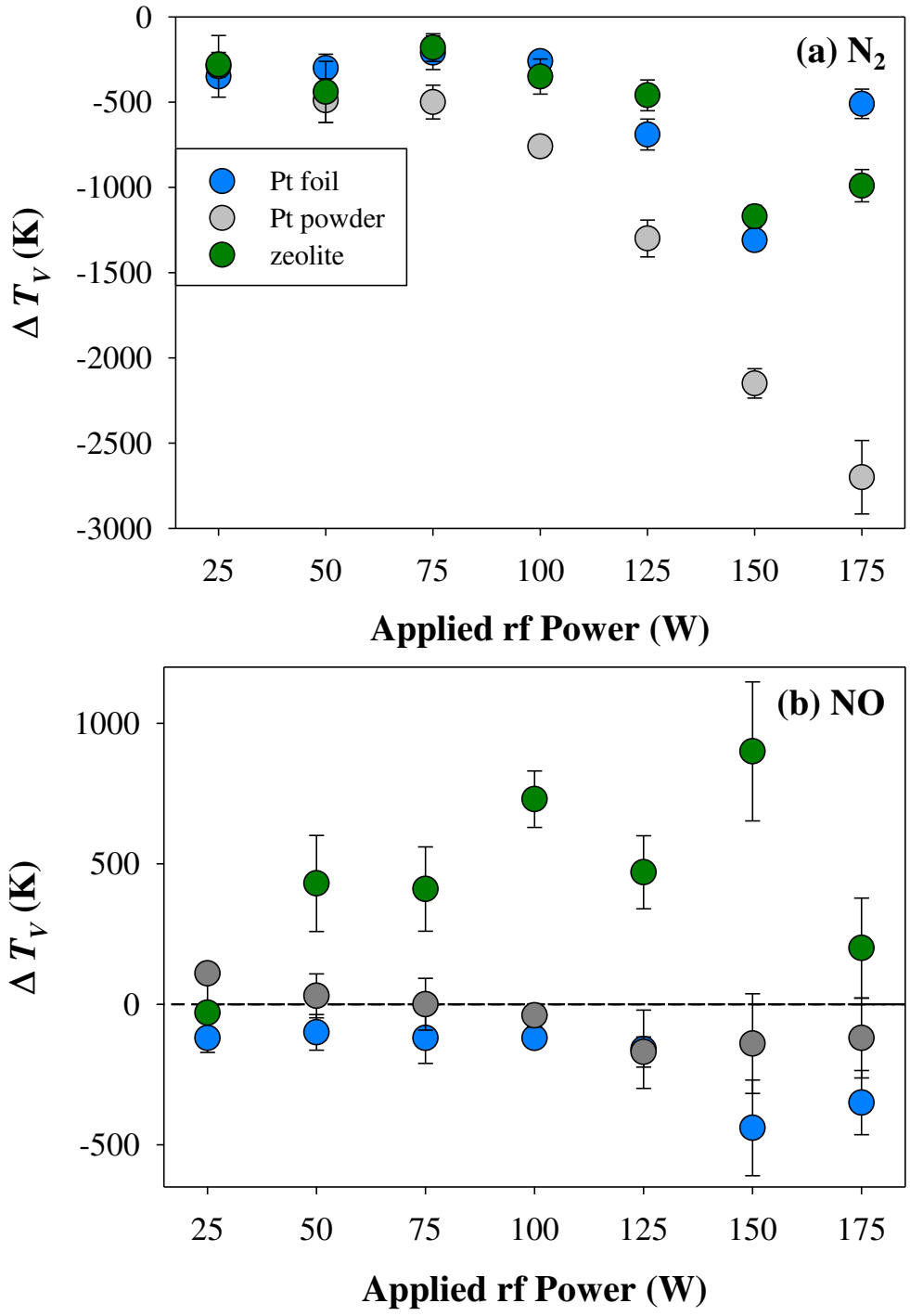

Figure 8.6. ΔT_V for (a) N_2 and (b) NO as a function of applied power and substrate within a 100 mTorr N_2O discharge.

The two Pt substrates studied here do not have a substantial impact on T_V (NO). Indeed, many of the data points calculated here are within experimental error of the substrate-free system. The relative species density, energy partitioning, and kinetic distributions have been measured as a function of operating conditions and catalytic substrate within single-stage PAC systems. Noted in the Introduction, the configuration of the plasma and catalyst may also impact the efficacy of PAC technologies.

Figure 8.7 depicts [N_2], [O], and [NO] density as a function of P and plasma-catalysis configuration for the Pt powder substrates. For comparison, substrate free and single-stage actinometric data are shown in Figure 8.2. At 25 and 50 W, plasma-catalyst orientation does not impact [N_2]. As P increases from 75 to 175 W, [N_2] decreases, with little difference between the no substrate and single-stage configuration. Additional decreases in [N_2] are observed, however, with the two-stage system. Described above, [O] slightly increases with P when no substrate is present. At P < 125 W, less atomic O is formed, with no dependence on single or two-stage configuration. At 175 W, [O] has no apparent dependence on PAC orientation. [NO] decreases substantially at higher P with the addition of Pt nanopowder in the coil region of the plasma and was further diminished in the pre-plasma catalysis orientation.

To better understand these gas-phase trends and to understand the impact of plasma processing on each substrate, the catalysts were studied before and after plasma exposure. PXRD and XPS techniques were used to characterize bulk and surface properties, respectively. The diffraction patterns of Pt foil (Figure 8.8a) and powder (Figure 8.8b) are shown for untreated as well as N_2O plasma-treated substrates. The diffraction peaks at $2\theta = 39.6$, 46.4, and 67.4° in Figures 8.8a and 8.8b correspond to the reflections (111), (200), (220), respectively, consistent with the face centered cubic (fcc) structure of platinum.[30]

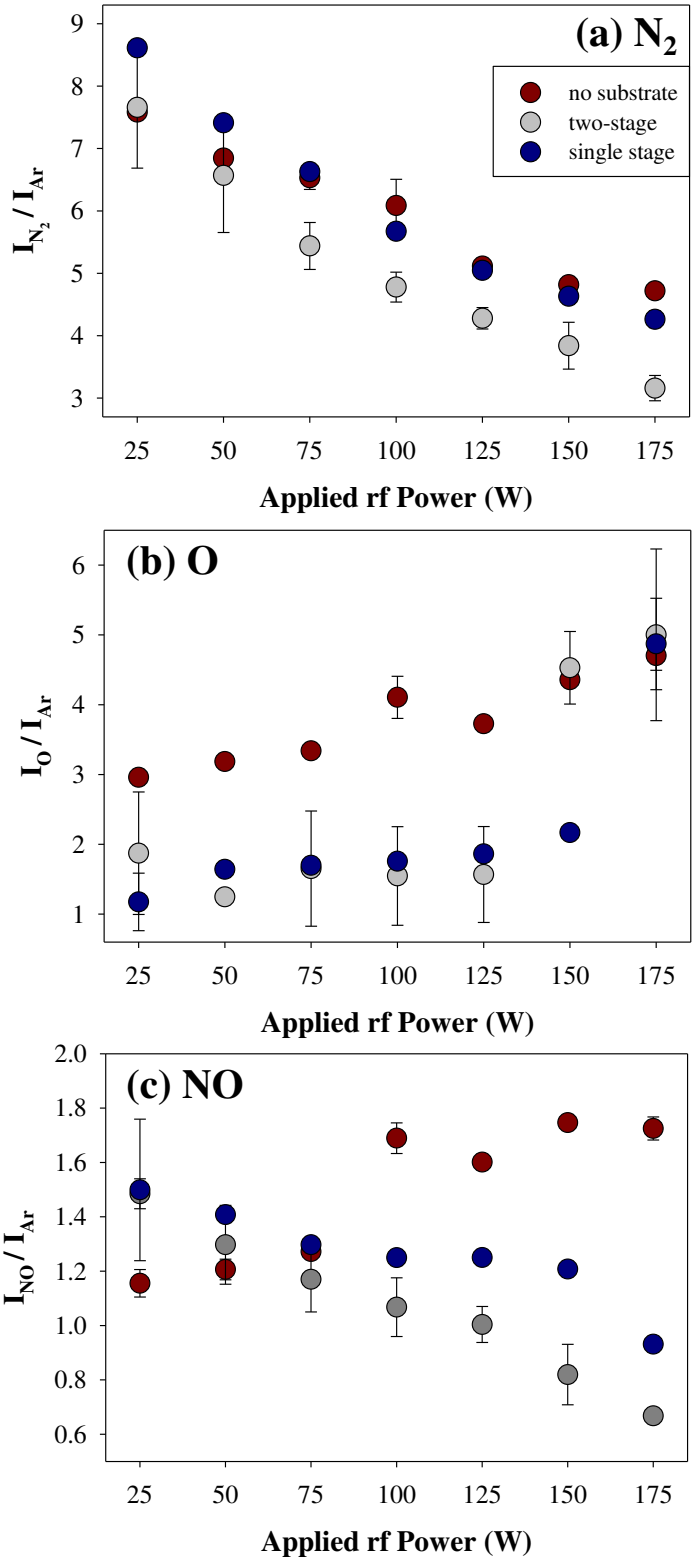

Figure 8.7. Species density as a function of *P* and plasma catalysis set-up, with Pt powder substrates present. Error bars represent one standard deviation from the mean (n = 4).

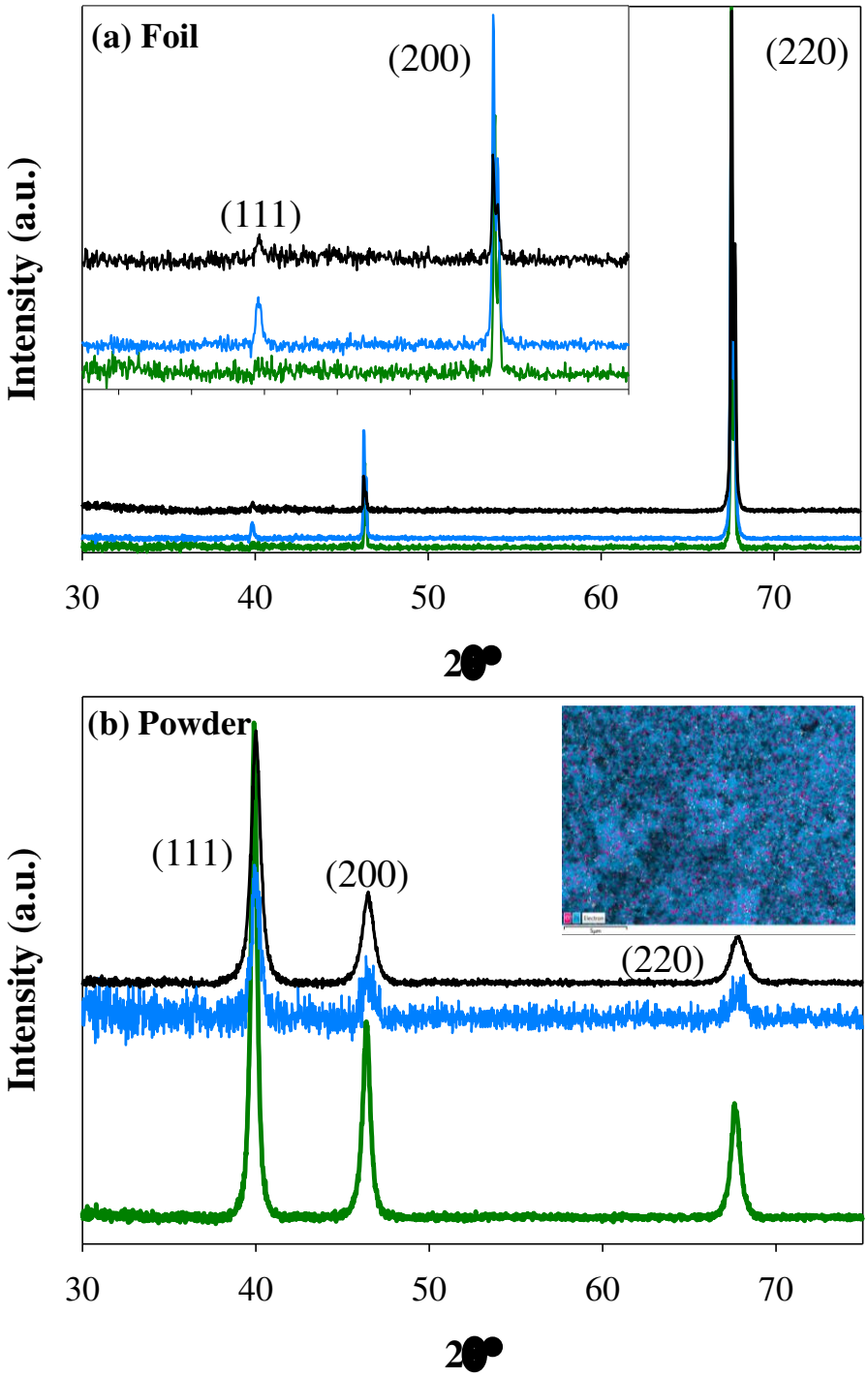

Figure 8.8. PXRD patterns for Pt (a) foil and (b) powder substrates: untreated (black trace) and N_2O treated at p = 100 mTorr, P = 175 W, t = 10 minutes (green trace). Inset in panel (a) highlights the (111) and (200) peaks in the Pt foil diffraction patterns, where the green trace was multiplied by 10 to better compare diffraction intensities. Inset EDS image in panel (b) corresponds to the N_2O treated Pt powder (p = 100 mTorr, P = 175 W, t = 10 minutes).

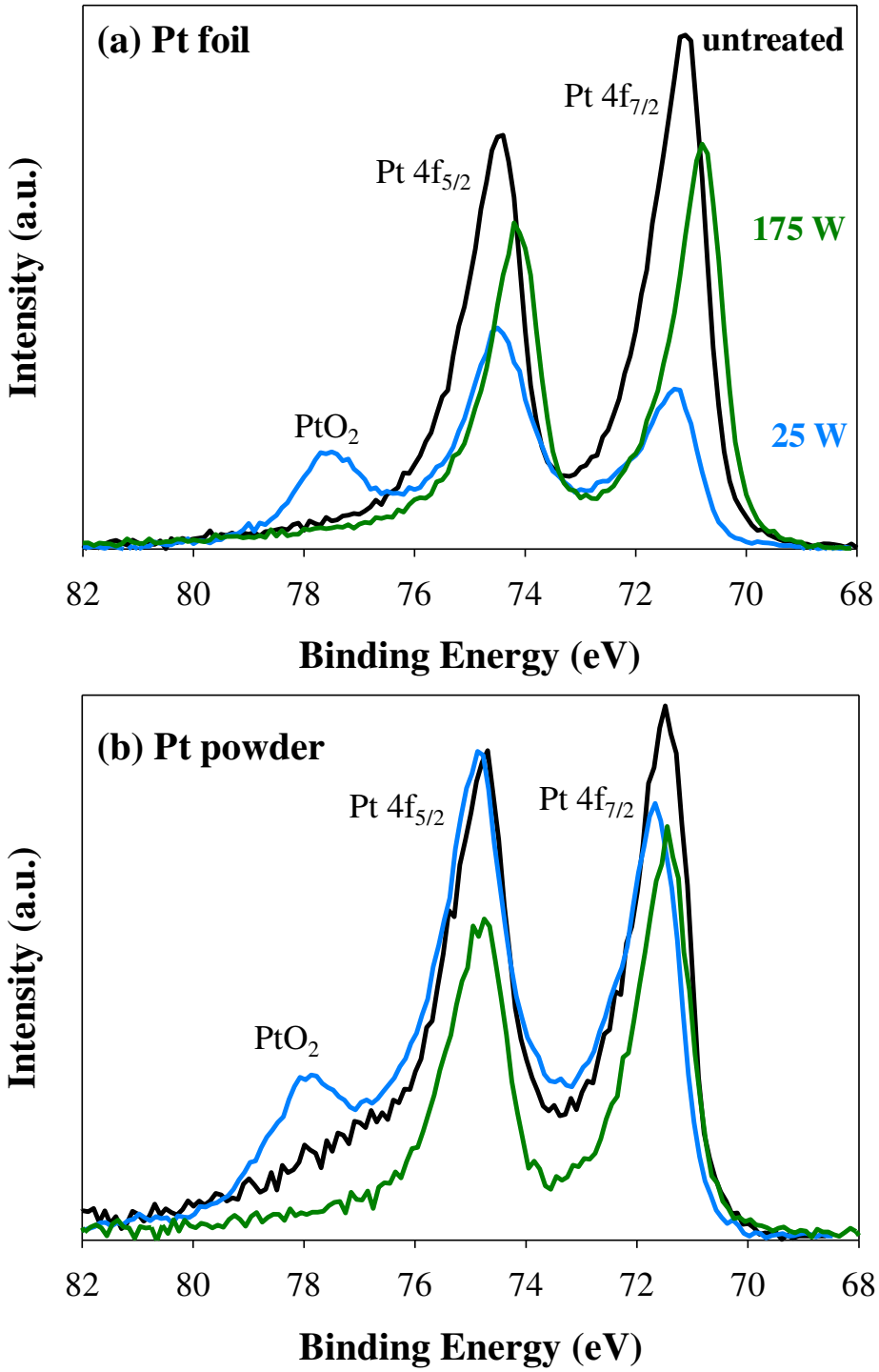

Figure 8.9. High resolution Pt$_{4f}$ XPS spectra for untreated Pt (a) foil and (b) powder (black traces) and N_2O plasma treated substrates at P = 25 W (blue traces) and 175 W (green traces), with p = 100 mTorr and t = 10 min.

The (111) diffraction peak of the Pt foil has nominally disappeared after a 175 W plasma treatment; no substantive changes to the XRD patterns were measured for the Pt powder substrate. The inset EDS image in Figure 8.8b corresponds to Pt powder after exposure to a 100 mTorr, 175 W N_2O plasma for 10 min, revealing the bulk of the material is comprised of platinum, with some oxygen dispersed throughout the material. These data, in conjunction with the PXRD diffraction, highlight the bulk chemistry of these materials is metallic Pt. In XPS spectra, both Pt foil and Pt powder (Figure 8.9a and Figure 8.9b, respectively) show the addition of a peak at 78.0 eV in the Pt_{4f} spectra, corresponding to the oxidation of the Pt substrate.

Atomic compositions for these materials are reported in Table 8.5. Both Pt materials have high concentrations of carbon on the surface. Post plasma exposure at either 25 or 175 W, the amount of oxygen on the Pt foil surface increased compared to the untreated material, with a concomitant decrease in carbon. In some spots on the Pt powder substrates, no carbon was detected in the survey spectra; hence, there is a large error associated with the amount of carbon adsorbed to the surface of the nanopowder. In contrast to the Pt foil, after gas and plasma exposure the carbon content on the Pt powder substrates increased significantly. Although the bulk of these materials are metallic Pt, verified through PXRD and EDS, the surface chemistry is much more complex and clearly affected by plasma exposure. These data exemplify the need for robust material characterization (e.g., bulk and surface properties) in conjunction with gas-phase studies.

The impact of plasma-catalyst configuration on gas-phase species densities was also investigated with a zeolite substrate as the catalyst, Figure 8.10. N_2 density decreases as a function of P for the two-stage and substrate-free systems, converging to the same values at $P \geq 75$ W.

Table 8.5. XPS atomic composition for Pt and zeolite substrates[a,b]

	Pt foil			Pt powder				Zeolite pellet		
	UT	**25 W**	**175 W**	**UT**	**Gas flow**[c]	**25 W**	**175 W**	**UT**[d]	**Gas flow**[c]	**175 W**
Pt(%)	25.3(1.9)	23.8(2.2)	26.0(2.9)	53.4(12.2)	32.3(6.8)	32.5(2.0)	29.6(2.1)	--	--	--
O(%)	18.3(2.6)	53.5(2.5)	39.1(6.2)	37.0(4.1)	29.1(0.8)	45.5(4.2)	31.6(4.2)	57.5(4.0)	57.3(1.2)	60.3(3.5)
C(%)	56.3(3.6)	22.7(3.0)	34.9(4.1)	9.5(13.6)	38.6(6.7)	22.0(4.6)	38.8(7.1)	22.7(7.0)	21.2(0.9)	14.4(5.9)
Si(%)	--	--	--	--	--	--	--	15.5(2.6)	15.7(0.8)	20.9(2.2)
Al(%)	--	--	--	--	--	--	--	4.4(0.6)	5.7(0.4)	4.4(0.4)

[a]Values in parentheses represent one standard deviation for the measurement.

[b]Treatment conditions: p = 100 mTorr, t = 10 min

[c]Substrates were placed in pre-plasma catalysis chamber

[d]Previously reported[31]

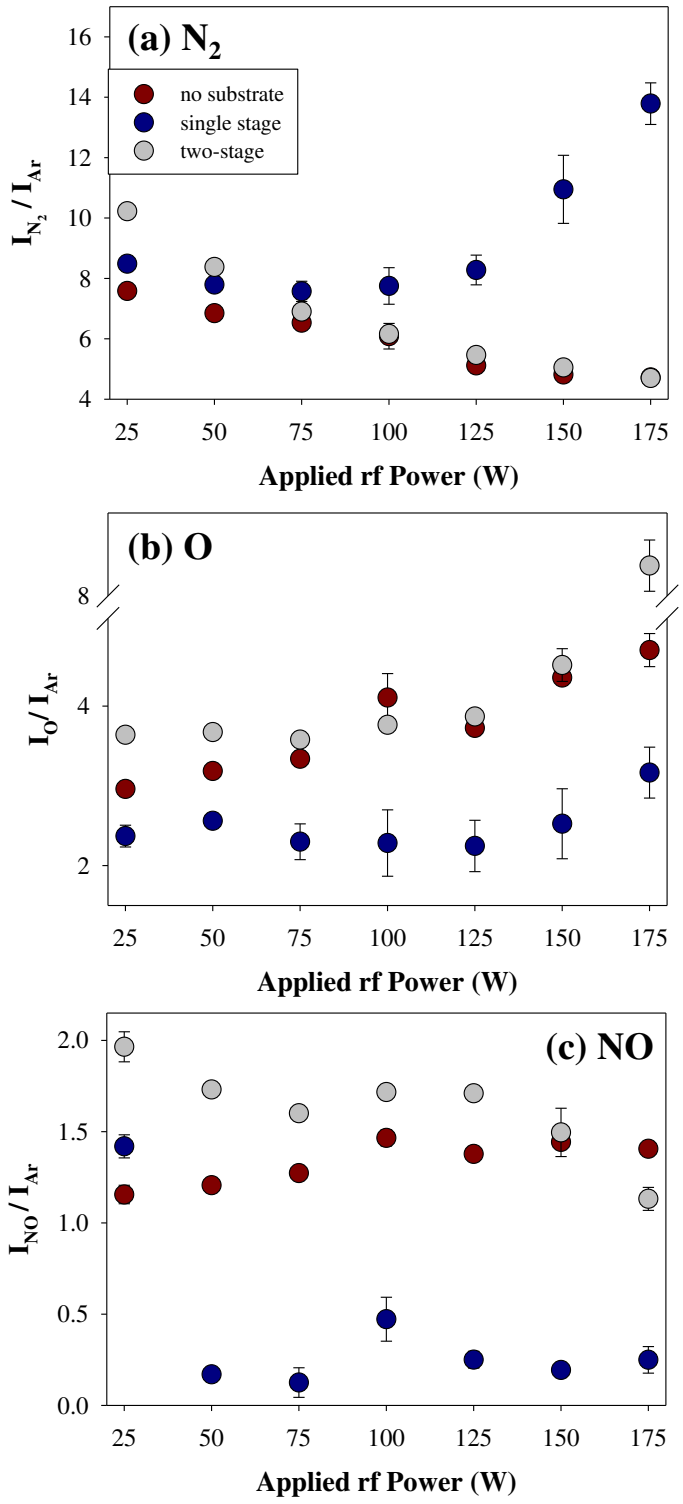

Figure 8.10. Species density as a function of *P* and plasma catalysis set-up, with zeolite pellets present. Error bars represent one standard deviation from the mean (n = 4).

The single-stage system resulted in significantly less atomic O compared to the substrate-free and two-stage systems studied herein, with largely no dependence on *P*. At 175 W, there is substantially more O produced in the two-stage system and a slight decrease in [NO] was detected with this configuration. At $P \leq 125$ W, the two-stage zeolite system produced more NO in the discharge compared to when no catalyst is present, whereas a zeolite placed directly in the discharge enhanced the decomposition of NO at higher power.

The surface and bulk properties of the zeolite materials were also characterized after these plasma exposures. XPS atomic composition is listed in Table 8.5 and Figure 8.11 shows the high resolution Si_{2p} and O_{1s} XPS spectra for untreated (a,d), single-stage (b,e), and two-stage (c,f) N_2O plasma-exposed zeolite pellets. The high-resolution Si_{2p} spectra show two Si binding environments: Si(-O_4) at 103.4 eV and Si(-O_3) at 102.8 eV.(36) The primary oxygen binding environments include the Si-O-Si band at 531.7 eV and Si-O-Al band at 530.8 eV.(31,37) The single-stage system depicts an increase in the Si(-O_4) (Figure 8.11b) and Si-O-Al (Figure 8.11e) binding environments compared to the untreated or two-stage system. This suggests some surface "cleaning" to expose the underlying aluminosilicate bridges is occurring. Although there are slight differences in the surface chemistry of zeolite materials after plasma processing, substrate morphology and bulk properties remained largely unchanged, Figure 8.12.

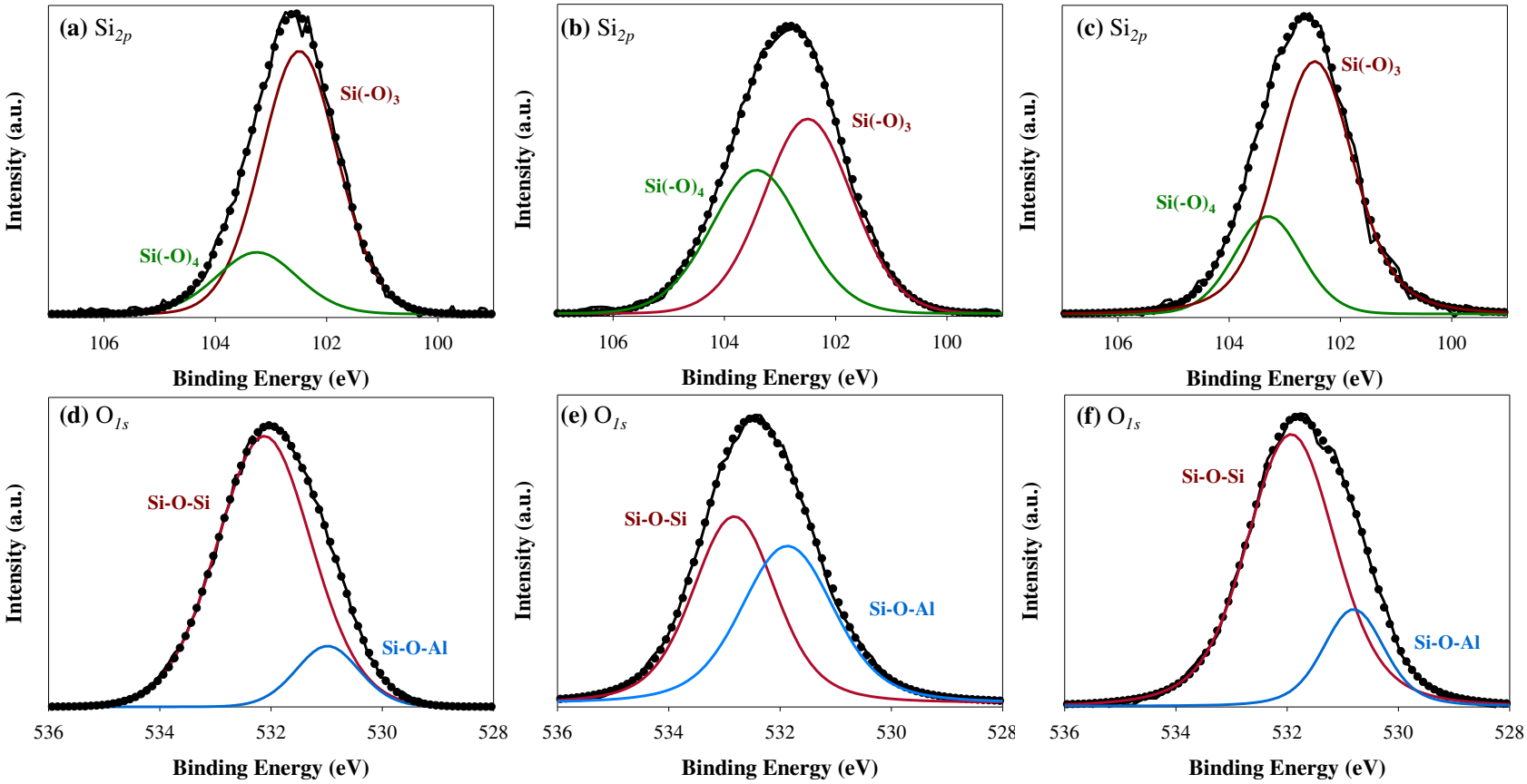

Figure 8.11. High resolution Si_{2p} (top) and O_{1s} (bottom) XPS spectra for untreated (a,d); single-stage (b,e); and two-stage (c,f) N_2O plasma treated zeolite pellet (100 mTorr, 175 W, 10 min).

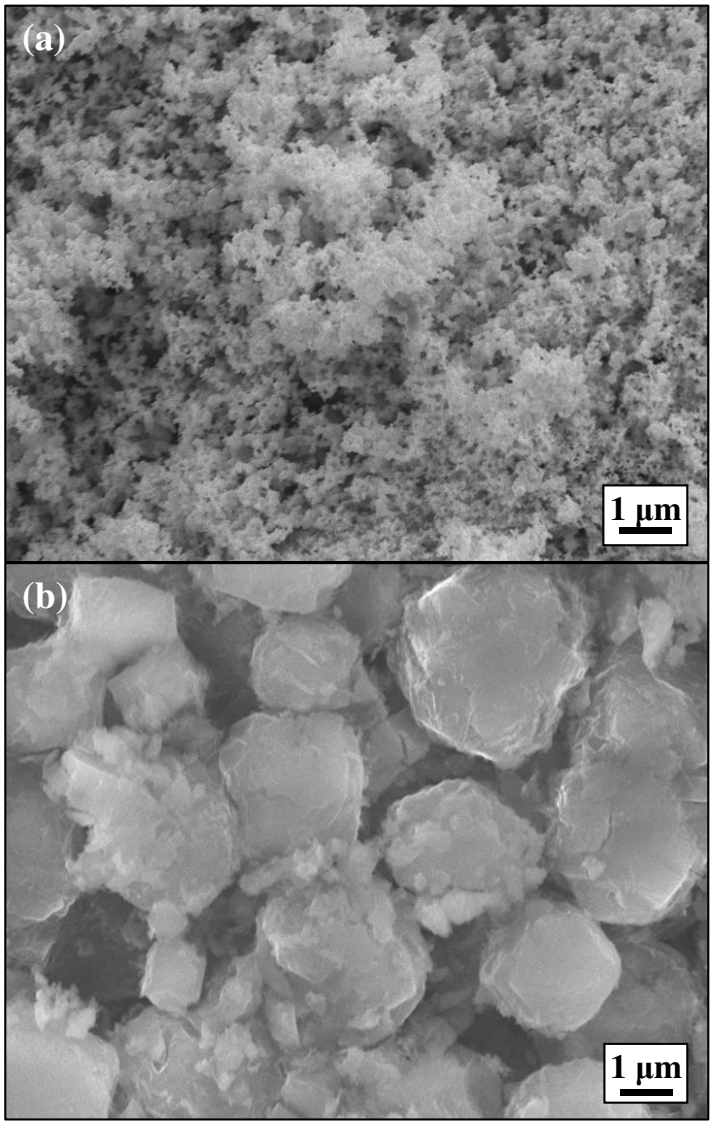

Figure 8.12. SEM images of N_2O treated (100 mTorr, 175 W, 10 minutes) (a) Pt powder and (b) zeolite pellet, collected at 5000x magnification.

8.3 Discussion

Detailed in the Introduction, the applicability of PAC for decomposition of pollutants is inherently hindered by a lack of knowledge regarding plasma-catalyst interactions. This pertains to both the potential modification of the catalyst by the plasma and the ability of the substrate to influence plasma chemistry. Therefore, a holistic experimental approach is necessary to understand relationships between gas-phase species, processes at the gas-surface interface, and resulting catalyst properties. For example, within plasmas (sans substrate), N_2O is hypothesized to decompose primarily through multiple electron-impact dissociation pathways, described briefly in Reactions 8.5 and 8.6.

$$N_2O_{(g)} + e^- \rightarrow N_{2\,(g)} + O_{(g)} + e^- \qquad (8.5)$$

$$N_2O_{(g)} + e^- \rightarrow N_{(g)} + NO_{(g)} + e^- \qquad (8.6)$$

Using inert gas actinometry, the relative density of these reaction products can be elucidated as a function of operating conditions. With no substrate in the plasma discharge, [NO] slightly increases as P increases from 25 to 175 W. This could indicate further fragmentation of the precursor (N_2O) at higher power, or NO could form via additional reactions between O and N. This study sought to abate N_2O via PAC, however, the decomposition of N_2O to NO (Reaction 8.6) is non-ideal as reactions between NO and other environmental byproducts can be detrimental to the atmosphere. Given this type of complexity, the data presented here reveal several major observations regarding the interactions of catalytic substrates with N_2O plasmas.

The first major observation is that the presence of a zeolite substrate dramatically changes the plasma chemistry, ultimately increasing the decomposition of N_2O (and NO) into benign N_2 at rf $P \geq 75$ W, Figure 8.2. Consequently, this sharp decrease in NO in the presence of a zeolite pellet coincides with a sharp increase in N_2 (Figure 8.2a), expressed via Reaction 8.7[25]

$$NO_{(g)} + N_{(g)} \rightarrow N_{2\,(g)} + O_{(g)} \qquad (8.7)$$

Atomic nitrogen emission peaks are not observed in the N_2O emission spectra, further supporting its consumption in Reaction 8.7 to form N_2 and O species. Generally, N_2O and subsequent NO decomposition increased by increasing the applied rf *P* for both Pt powder and zeolite substrates. This likely occurs as a result of more reactive species being generated at a higher power. Upon plasma ignition, a variety of reactive species are created via excitation, ionization, and dissociation, including excited state N_2, N radicals, and N_2^+ ions. Jo *et al.* hypothesize these species nominally decompose N_2O via Reaction 8.8.[12]

$$N_2(A^3\Sigma_u^+)_{(g)} + N_2O_{(g)} \rightarrow 2N_{2\,(g)} + O_{(g)} \qquad (8.8)$$

At 25 W, [NO] in the discharge increased upon the addition of a substrate, suggesting a gas-phase molecule could remove adsorbed O from the surface and undergo reactions to form additional NO. Within the Pt foil system, [NO] is elevated compared to the substrate-free system at $P \leq 75$ W, but as power increases to 175 W these systems are the same within experimental error. The Pt foil seems to have little to no impact on the plasma environment; the densities of N_2, NO, and OH are within experimental error with the substrate-free system at most rf powers studied here. Depicted in Figure 8.2b, both Pt powder and zeolite substrates drastically altered the plasma chemistry, ultimately decreasing the amount of NO in the discharge at $P \geq 50$ W (zeolite) and $P \geq 100$ W (Pt powder). Therefore, it is likely the porous network of these materials impacts the ability of the catalyst to decompose N_2O and NO. Illustrated in Figure 8.1, pore size and shape drastically differ between the Pt nanopowder and micro-structured zeolite. The variability of the porous network could impact the formation of microplasmas within the pores of the catalyst, which is hypothesized to enhance pollutant decomposition.[32]

Zhang *et al.* studied the influence of the material dielectric constant on plasma generation inside catalyst pores using a two-dimensional fluid model of an atmospheric pressure helium discharge.[33] The authors concluded pore size and shape is a crucial variable in the propagation of plasma into catalyst pores. In a 100 μm pore, the electron impact ionization in the pore is greatly enhanced for dielectric constants (ε_r) below 300, however, ferroelectric materials with dielectric constants above 300 did not yield plasma enhancement inside catalyst pores, regardless of pore size. The authors argue common catalysts supports [Al_2O_3 (ε_r =8-11), SiO_2 (ε_r =4.2), and zeolites (ε_r =1.5- 5)] should more easily allow formation of microdischarges within pores, even those of smaller sizes.[33] Aluminosilicate zeolites have a smaller dielectric constant compared to Pt (ε_r = 6.5-7.5) and the zeolites employed in this study have significantly larger pores compared to the nanostructured Pt powder. This suggests microdischarges may form more easily with the zeolite catalyst, hence it is the system with the most NO decomposition. As evidenced by the results depicted in Figure 8.2, chemical nature and morphology (i.e., pore size) can have a substantial impact on the resulting plasma composition. An additional variable is the catalyst placement, which is why the PAC community is actively investigating different plasma-catalyst configurations for pollution abatement, including those where the plasma and catalyst can directly interact (single-stage) or be separated (two-stage).[19] By exploring both single- and two-stage arrangements, synergisms between gas-substrate (two-stage) and plasma-substrate (single-stage) can be separately evaluated.

Within a two-stage, pre-plasma catalysis configuration, gas flows over the catalyst and is further treated by the inductively coupled plasma (Figure 2.2b). As the porous substrates (Pt powder and zeolites) had the greatest impact on the amount of NO in the discharge (Figure 8.2b), they were chosen for the two-stage studies. As noted above, [NO] decreases substantially at

higher powers ($P \geq 100$ W) with the addition of a nano-structured Pt catalyst in the discharge. Thus, a second major observation herein was the further diminished NO density in the system with the pre-plasma catalysis set-up, compared to the substrate-free and single-stage configurations, Figure 8.7c. Within the two-stage system, $N_2O_{(g)}$ likely interacts with the catalyst via Reactions 8.1 and 8.2, wherein the interactions with adsorbed O are hypothesized to be the rate-limiting step.[12] Density functional theory (DFT) studies have shown $N_2O_{(g)}$ can be easily absorbed on metal surfaces, calculating a favorable adsorption energy of N_2O on the top site of Pt(111) surfaces.[34] Using CaS(100) as a catalyst model in DFT calculations, Wu *et al.* computed a 1.228 eV energy requirement for N_2O to decompose to $N_{2(g)}$ and $O_{(ads)}$ (Reaction 8.1). The subsequent removal of $O_{(ads)}$ from the surface is more energy intensive, discussed further below.[35] At low temperatures, there is limited regeneration of active sites due to adsorbed species, hence overall catalytic activity is diminished. In a review article, Konsolakis compiled literature studies of N_2O decomposition on bare oxides, where system temperatures ranged from 300 to 710 °C.[36] In the present study, all results were nominally collected at room temperature,[37] suggesting the combination of the catalyst with a plasma inherently removes the necessity for high reaction temperatures. Within the single-stage discharge, N_2O is mostly fragmented upon ignition (Reactions 8.5 and 8.6), therefore it is unlikely intact N_2O is interacting with the substrate.

To further probe the differences in these configurations and plasma chemistry, the materials were thoroughly characterized before and after plasma exposure. Specifically, PXRD and XPS techniques were used to characterize bulk and surface properties of the materials, respectively. Both Pt catalysts were used as received and contained large amounts of C on the surface. The high experimental error reported for the untreated Pt powder substrates (Table 8.5) resulted from

having some sampling locations containing no measurable carbon. As detailed in Chapter 2, a minimum of three spots on three samples were analyzed for XPS studies to gain a representative view of the surface chemistry. Within the two-stage configuration, flowing 100 mTorr N_2O over the Pt powder substrate for ten minutes does not appear to change the catalyst (Table 8.5), whereas placing the Pt catalysts in the discharge actively changes the chemical identity of the catalysts and hence may hinder catalytic activity. Both Pt materials are clearly modified upon plasma exposure, as an additional binding environment at 75.0 eV, corresponding to PtO_2, appears in the Pt_{4f} XPS spectra (Figure 8.9). Several studies have demonstrated an increase in oxygen negatively influences the ability of Pt to decompose N_2O.[9,12] Surface oxygen on the Pt powder is likely blocking the active sites of the catalyst, hence [NO] is lower in the two-stage system compared to the single-stage configuration.

A two-stage PAC system was also investigated using a zeolite pellet, Figure 8.10. For both the substrate-free and two-stage systems, [N_2] decreases as rf *P* increases from 25 to 175 W. The single-stage system resulted in significantly less O compared to both the substrate-free and two-stage system, with largely no dependence on rf power. Within the two-stage system at $P = 25 – 125$ W, there is more NO in the gas-phase compared to when no catalyst is present. This suggests the decomposition of the N_2O precursor into N_2, NO, and O is occurring, yet further NO decomposition is not. Clearly, in the case of zeolites, a single-stage system is optimal, exemplified in Figure 8.10c. The distinct and exaggerated decrease in NO indicates the plasma is necessary for activation of the catalyst. Furthermore, plasma exposure does not appreciably change the surface or bulk chemistries of the zeolite materials; therefore, the catalyst is not being degraded or damaged by the plasma (Figure 8.12b and Table 8.5). These gas-phase and material

characterization results support the hypotheses proposed in the Introduction; namely, affordable materials (e.g., zeolites) can be utilized in PAC pollution abatement.

As noted in Section 8.1, it is imperative to study both the steady-state plasma, as well as discharge phenomena as a function of time to obtain a comprehensive representation of plasma-surface interactions. As such, TR-OES was used to probe the sharp decrease of [NO] in the single-stage, zeolite system. Shown in Figure 8.3b, [NO] suddenly decreases 10 s after plasma ignition at P = 150 W. Small amounts of Ar (~10 %) were added to the system for actinometric purposes, which could also influence the decomposition and formation of plasma species. Lee and Kim found the application of an Ar plasma in conjunction with alumina-supported Ru catalysts could decompose N_2O bonds to form NO, N, and O species at relatively low substrate temperatures.[38] Using a 245 °C reaction temperature, the authors noted as the N_2O:Ar ratio increased to 3:1, N_2O conversion decreased to 23.8%.[38] These data suggest Ar plays an important role in the dissociation of N_2O. As the atmosphere contains < 1 % Ar, we sought to study plasma kinetics and energetics without the addition of Ar, quantifying rate constants for formation and destruction as a function of plasma operating P and catalytic substrate.

Through TR-OES, the formation profiles of excited state N_2 and NO within an N_2O discharge were measured and differentiated. The intensity of N_2 (337.0 nm) increases as a function of time, ultimately reaching an apparent steady state, where NO emission (235.9 nm) initially increases to a local maximum and subsequently decays. These data suggest that Reactions 8.6 and 8.7 are occurring sequentially in the discharge: NO is initially formed through the dissociation of the N_2O precursor, then a decay in NO intensity is observed as it undergoes further reactions within the plasma. From a thermodynamic perspective,

$\Delta H_{rxn} = 481.1\ kJ/mol$ for Reaction 8.6 and $\Delta H_{rxn} = -122.1\ kJ/mol$ for Reaction 8.7.[39] When no substrate is present, the discharge operating mode also impacts k_f values. Specifically, when the discharge shifts from inductance (E) to capacitance (H) mode operation at 125 and 150 W, there is an increase in both $k_f(N_2)$ and k_f(NO) values.

Additionally, at P > 100 W, $k_f(N_2)$ decreased in the presence of a zeolite pellet, where k_d(NO) appears largely independent of the catalyst. As described above, we hypothesize the structure and surface chemistry of the zeolite pellet promotes formation of microdischarges near or within the pores of the material. Consequently, the formation of N_2 species within the bulk discharge could be impacted by the microdischarges within the material. Collisional quenching of excited state N_2 is another proposed pathway for decreased rate constants at certain conditions. We have previously studied the impact of zeolite catalysts within an N_2 plasma, where a decay to a steady-state emission (similar to the NO within N_2O herein) was documented at 125 and 150 W with zeolite(s) present.[31] To further assess these hypotheses of plasma-material interactions, a third major finding herein was the deciphering of energy partitioning between degrees of freedom and across multiple molecules (i.e., N_2 and NO) formed in N_2O plasmas.

Excited state N_2 and NO T_R values were determined as a function of rf power and substrate, Figures 8.5a and 8.5b. The Pt powder system had the most significant impact on $T_R(N_2)$ values, compared to the substrate-free discharge. As shown in Figure 8.5a and Table 8.3, it appears that that the discharge mode and resulting rotational distributions are interrelated with Pt nanopowder present. $T_R(N_2)$ values increase from 335 ± 10 K (100 W) to 375 ± 10 K (125 W) as the discharge shifts from E to H mode operation. This trend is not prevalent in the zeolite system, $T_R(N_2)$ values at P = 100 W and 125 W are within experimental error, although T_R generally increases within increasing rf power. Rotational energy distributions of absorbing and emitting

N_2 molecules in a variety of discharges (e.g., N_2, N_2O, N_2/O_2) have been previously studied via broadband absorption spectroscopy (BAS) and OES, respectively, where all $T_R(N_2)$ values were less than 440 K.[28] This suggests the rotational populations within N_2 molecules readily thermalize to slightly above room temperature, an observation that holds here, as all calculated $T_R(N_2)$ values are less than 405 K, Figure 8.5a. Rotational temperatures for excited state NO radicals are significantly elevated compared to N_2. When no substrate is present, as P increases from 25 to 175 W, T_R(NO) increases from ~400 to ~725 K. This is not, however, a clear, linear increase as T_R(NO) at 50 and 150 W are within error. At P = 50 – 125 W, a decrease in T_R(NO) of ~50 – 130 K was measured in the presence of Pt foil. This suggest that excited state molecules interact with the flat Pt substrate and scatter with some rotational relaxation at these powers. At 150 W, an increase in T_R (NO) is determined for all catalytic substrates, with Pt powder yielding the highest T_R value (710 K), followed by the zeolite (640 K), Pt foil (570 K), and sans substrate (520 K) systems. These data suggest that material morphology may play a more important role in plasma energetics than material chemistry; the porous materials impact the ability of NO molecules to thermalize rotationally. At the highest power studied (175 W), T_R does not display a strong dependence on the catalytic substrate, even though there is a large difference in the amount of NO in the discharge with no substrate ([NO] = 1.73 ± 0.04) compared to when a zeolite pellet is present ([NO] = 0.25 ± 0.07). Rotational relaxation is a relatively fast process, typically requiring fewer than ten collisions to reach equilibrium. Therefore, on the time scale that both the energetic and actinometric data were collected (i.e., minutes), the NO ($A^2\Sigma^+$) radicals have effectively reached a quasi-rotational equilibrium and substrate effects are negligible, regardless of the amount of NO in the discharge. All T_R values

reported herein are < 800 K, an order of magnitude less than the T_V values for excited state N_2 and NO, listed in Table 8.4.

Regardless of substrate, as applied rf power in the system is increased from 25 to 175 W, there is a clear increase in T_V (N_2), a trend we have previously quantified in N_2 (with and without catalysts),[31] NO (no substrate),[40] and N_2/O_2 (no substrate)[28] rf ICPs. At all power conditions studied herein, a decrease in $T_V(N_2)$ was determined upon the addition of catalytic substrates, where the temperature difference between the Pt powder and substrate-free system increased with increasing power. The discharge mode of the plasma likely contributes to the enhanced vibrational cooling documented in Figure 8.6a; as *P* increases from 125 to 150 W, the rf plasma herein shifts from E (low plasma density) to H mode (higher plasma density). We have previously studied $T_V(N_2)$ within a 100% N_2 plasma, with TiO_2 and zeolite substrates in the discharge and a similar decrease in T_V with catalysts present was measured.[31] N_2 vibrational energy distributions within N_xO_y plasmas are clearly impacted by a catalyst, therefore examining the plasma-material interface could garner additional insight into this phenomena.

Larsson described a selective energy transfer (SET) model to explain catalysts-reactant interactions,[41-43] where the catalyst provides the energy required to populate higher vibrational levels within a molecule. This model suggests vibrationally excited N_2 molecules can interact with a substrate, scatter with some energy loss, potentially through an energy transfer mechanism.[44] Larsson investigated numerous catalytic systems [e.g., hydrocarbon cracking over zeolites,[45] ethane hydrogenolysis over Pt, Ni, Fe and Co catalysts[46]], applying the SET model to probe vibrational resonance processes. In many of the SET systems reported in the literature, little chemisorption of the intact molecule onto the catalyst surface is observed, depending on the catalyst.[43] Therefore, we sought to understand the plasma-material interactions within N_2O

discharges using a SET model. Pt nanopowder was exposed to a P = 175 W N_2O plasma for 10 min, as depicted in Figure 8.9b, the resulting Pt_{4f} XPS spectra did not exhibit the additional PtO_2 peak, documented at P = 25 W. Furthermore, at P = 175 W, the most pronounced decrease in $T_V(N_2)$ values was measured, whereas at P = 25 W, limited vibrational cooling was measured. The combination of these gas-phase and surface chemistry data suggest that at P = 175 W a vibrational energy transfer is occurring with a Pt powder substrate.

Unlike $T_V(N_2)$ values, vibrational cooling of NO did not occur for all catalysts studied herein, Figure 8.6b and Table 8.4. With a zeolite, as power increases, T_V(NO) values also increases. Examining ΔT_V(NO), Figure 8.6b, reveals the zeolite clearly has a very different effect on plasma energetics compared to the Pt substrates. As the applied power is increased, only the zeolite system displays an enhancement in T_V(NO). Interestingly, neither of the Pt substrates have a substantial impact on the energetics of NO radicals in the discharge. There are fewer NO and N_2 molecules in the discharge when a Pt powder substrate is present in the discharge from 100 – 175 W, as well as enhanced N_2 vibrational cooling (Figure 8.6a). The lack of vibrationally excited N_2 under these conditions, suggests N_2 molecules with sufficiently high T_V are likely involved in additional gas-phase reactions to form $NO_{(g)}$, $O_{(g)}$, and $OH_{(g)}$. Note, all data presented herein correspond to excited state, emitting gas-phase species. We have previously reported vast differences in vibrational temperatures of excited and ground state molecules, therefore it will be essential to probe the ground state species in these N_2O-catalyst systems via BAS.[28,40]

As evidenced via energy partitioning and kinetic studies here, it is necessary to consider both thermodynamic and mechanistic implications for the applicability of PAC technologies nominally the fourth major observation herein.

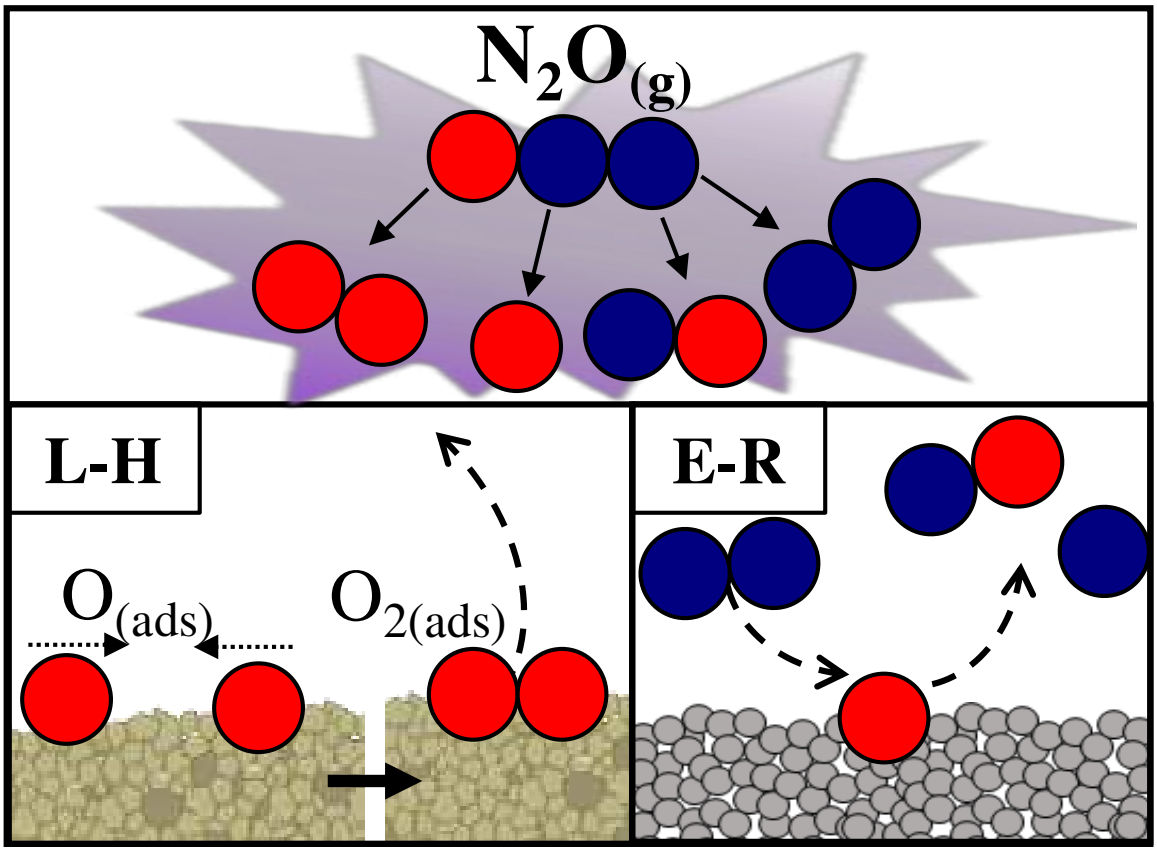

Figure 8.13. Schematic representation of plasma-catalyst interactions; example Langmuir-Hinshelwood (L-H) and Elrey- Rideal (E-R) mechanisms are depicted.

The decomposition of N_2O on metal oxide catalysts is often expressed using Langmuir-Hinshelwood (L-H) or Eley-Rideal (E-R) models, schematically represented in Figure 8.13. Reactions 8.9 and 8.10 depict a possible N_2O decomposition pathway via a L-H mechanism:

$$2N_2O_{(g)} + (*) \rightarrow 2N_{2\,(g)} + 2O^*_{(abs)} \qquad (8.9)$$

$$2O^*_{(abs)} \rightarrow O_{2\,(g)} + (*) \qquad (8.10)$$

where (*) symbolizes an active site on the catalyst surface. Within this mechanism scheme, the adsorbed surface oxygen migrates from one active site to another to form O_2 by recombination, ultimately the rate-determining step in the decomposition of N_2O, described above.[8] As shown in Reactions 8.5 and 8.6, the PAC decomposition of N_2O produces atomic O and NO radicals, which can then potentially regenerate the active sites of the catalyst by recombining on the surface and desorbing. The O_{1s} binding environment for adsorbed oxygen is 532.1 eV, often documented in the evaluation of TiO_2 materials,[47] which overlaps with the Si-O-Al binding environment. Thus, increase in the Si-O-Al peak area in Figure 8.11e is likely the result of the plasma creating oxygen vacancies in the material, lending to a slight increase in the amount of Si at the surface. Although there are slight differences in the surface chemistry of zeolite materials after plasma processing, the substrate morphology remained largely unchanged (Figure 8.12).

Within the E-R mechanism, a chemisorbed molecule or atom interacts with a gas-phase species. The reaction of an $N_2O_{(g)}$ molecule interacting with $O_{(ads)}$ is depicted in Reaction 8.11:

$$O_{(ads)} + N_2O_{(g)} \rightarrow N_2 + O_{2(ads)} \rightarrow N_{2\,(g)} + O_{2\,(g)} \qquad (8.11)$$

The E-R mechanism is considered rare in thermal catalysis because of the timescale of gas-phase surface interactions (picoseconds), reaction orientation, and entropy considerations.[48] Moreover, the E-R mechanism requires that a species from the gas-phase interacts with adsorbed species; thus the probability for such a collision can be low.[48] Using DFT calculations to study N_2O

decomposition over a CaS(100) surface, Wu *et al.* calculated the reaction of $N_2O_{(g)}$ and $O_{(ads)}$ to form $O_{2(ads)}$ (Reaction 8.10) required 1.863 eV, whereas the removal of $O_{(ads)}$ from the surface by binding with neighboring $O_{(ads)}$ via the L-H mechanisms (Reactions 8.9 and 8.10), depicted in Figure 8.3, required 1.877 eV.[35]

Within an N_2O PAC system, $N_{2(g)}$ can react with $O_{(ads)}$, subsequently desorbing to form NO via an E-R pathway, depicted in Figure 8.13. These reaction products can undergo additional pathways (Reaction 8.7) to form gas-phase species measured via optical spectroscopy. Zaharia *et al.* experimentally demonstrated an E-R reaction pathway when an O-covered Ru(0001) crystal was exposed to a molecular beam of nitrogen atoms and molecules. Within the initial stages of exposure, $O_{(ads)}$ interacts with $N_{2(g)}$ or $N_{(g)}$ from the beam, forming $NO_{(g)}$ species. The authors determined as O coverage decreases and the adsorbed N coverage increased, the initial flux of NO is rapidly attenuated and a concomitant increase in $N_{2(g)}$ is documented.[49] The experimental determination of E-R pathways using molecular beams interacting with a material suggest these reaction processes can occur within the PAC systems studied herein. Furthermore, modification of the direct E-R mechanisms proposes an indirect, hot-atom pathway occurs when a gas-phase atom interacts and rebounds from the surface several times before colliding and reacting with an adsorbed species.[48] Regardless of pathway, the removal of adsorbed oxygen to regenerate the active site of the catalyst is a critical step. Within a single-stage system, the zeolite catalysts benefited from direct plasma interactions, resulting in the smallest amount of NO in the discharge. A two-stage, pre-plasma configuration was deemed optimal for the Pt powder constructs, reducing the amount of NO compared to the native system without the detrimental oxidation effects caused by plasma exposure.

By obtaining a fundamental understanding of plasma-catalyst systems; efforts can focus on determining the most effective catalyst in conjunction with optimal design, configuration, and plasma operating conditions.[50] A plethora of variables can dominate these plasma-material interactions, including electron-impact reactions, gas-phase neutral reactions, as well as multitude of surface reactions. These interactions become progressively convoluted as the complexity of the systems increases. Suarez *et al.* studied the influence of a 2 vol. % water vapor addition to an N_2O feed gas, resulting in a decrease in catalytic activity with Rh-γ-Al_2O_3-sepiolite monolithic catalysts.[13] A similar effect was observed upon the addition of NH_3, suggesting that NH_X or OH species tend to adsorb at the same sites as N_2O, reducing the number of active sites available for the decomposition of nitrous oxide, consequently yielding a decrease in catalytic activity.[13] Ultimately, we believe there is still much work to be done to further understand the underlying mechanisms involved in the plasma-catalytic decomposition of N_2O. Nevertheless, the data presented herein clearly demonstrate that not only does the plasma alter the surface of catalytic substrates, but the presence of both micro- and nano-structured catalytic materials clearly alter energy partitioning and reaction dynamics within the gas-phase of the plasma.

8.4 Summary

A comprehensive understanding of plasma-material interactions necessarily must include processes that occur at surfaces. Ultimately, many of our results demonstrate that the presence of a substrate in a plasma can dramatically alter the gas-phase chemistry of the system, from both a kinetics perspective and an energetics perspective. Although this might seem obvious, few studies have appropriately documented these effects. Within an N_2O rf ICP, N_2 emissions rise to an apparent steady state, whereas NO emissions approach a local maximum and a subsequent

decay, where the addition of a catalyst had minimal impact on measured rate constants. Steady-state energetics revealed the addition of Pt and zeolite catalysts results in a pronounced decrease in the vibrational temperature of excited state N_2. The vibrational temperature of NO species seems to depend more on chemical nature compared to morphology; both Pt catalysts had little to some quenching effects on T_V, where the addition of a zeolite pellet yielded an increase in T_V(NO). Moreover, this study epitomized the necessity to examine of each portion of the PAC system (i.e., the plasma, the plasma-surface interface, and corresponding material analyses). Post plasma exposure material characterization revealed the plasma effectively poisons the Pt materials through oxidation, resulting in poorer performance in the single-stage system, whereas the bulk and surface properties of the zeolites were nominally unaffected by the plasma. This line of scientific inquiry should be expanded to more complex mixed-gas systems, ultimately studying systems that resemble exhaust systems and atmospheric pollutants.

REFERENCES

1. Ravishankara, A. R.; Daniel, J. S.; Portmann, R. W., Nitrous Oxide (N_2O): The Dominant Ozone-Depleting Substance Emitted in the 21st Century. *Science* **2009**, *326*, 123.
2. Understanding Global Warming Potentials. https://www.epa.gov/ghgemissions/understanding-global-warming-potentials (accessed June 3 2019).
3. Shimizu, A.; Tanaka, K.; Fujimori, M., Abatement Technologies for N_2O Emissions in the Adipic Acid Industry. *Chemosphere: Global Change Sci.* **2000**, *2*, 425-434.
4. Centi, G.; Generali, P.; dall'Olio, L.; Perathoner, S.; Rak, Z., Removal of N_2O from Industrial Gaseous Streams by Selective Adsorption over Metal-Exchanged Zeolites. *Ind. Eng. Chem. Res.* **2000**, *39*, 131-137.
5. Groen, J. C.; Pérez-Ramírez, J.; Zhu, W., Adsorption of Nitrous Oxide on Silicalite-1. *J. Chem. Eng. Data* **2002**, *47*, 587-589.
6. Wójtowicz, M. A.; Miknis, F. P.; Grimes, R. W.; Smith, W. W.; Serio, M. A., Control of Nitric Oxide, Nitrous Oxide, and Ammonia Emissions Using Microwave Plasmas. *J. Hazard. Mater.* **2000**, *74*, 81-89.
7. Zhao, G.-B.; Hu, X.; Plumb, O. A.; Radosz, M., Energy Consumption and Optimal Reactor Configuration for Nonthermal Plasma Conversion of N_2O in Nitrogen and N_2O in Argon. *Energy Fuels* **2004**, *18*, 1522-1530.
8. Wagner, C., The Mechanism of the Decomposition of Nitrous Oxide on Zinc Oxide as Catalyst. *J. Chem. Phys.* **1950**, *18*, 69-71.
9. Steacie, E. W. R.; McCubbin, J. W., The Decomposition of Nitrous Oxide on the Surface of Platinum. I. The Retarding Effect of Oxygen. *J. Chem. Phys.* **1934**, *2*, 585-589.
10. Ohno, Y.; Kimura, K.; Bi, M.; Matsushima, T., The Translational Energy of Desorbing Products in NO and N_2O Decomposition on Pd (110). *J. Chem. Phys.* **1999**, *110*, 8221-8224.
11. Zhang, F.; Wang, X.; Zhang, X.; Turxun, M.; Yu, H.; Zhao, J., The Catalytic Activity of NiO for N_2O Decomposition Doubly Promoted by Barium and Cerium. *Chem. Eng. J.* **2014**, *256*, 365-371.
12. Jo, J.-O.; Trinh, Q. H.; Kim, S. H.; Mok, Y. S., Plasma-Catalytic Decomposition of Nitrous Oxide over γ-Alumina-Supported Metal Oxides. *Catal. Today* **2018**, *310*, 42-48.
13. Suárez, S.; Saiz, C.; Yates, M.; Martin, J. A.; Avila, P.; Blanco, J., Rh/γ-Al_2O_3–Sepiolite Monolithic Catalysts for Decomposition of N_2O Traces. *Appl. Catal., B* **2005**, *55*, 57-64.
14. Trinh, Q.-H.; Kim, S. H.; Mok, Y. S., Removal of Dilute Nitrous Oxide from Gas Streams Using a Cyclic Zeolite Adsorption–Plasma Decomposition Process. *Chem. Eng. J.* **2016**, *302*, 12-22.
15. Zhang, B.; He, G.; Shan, Y.; He, H., Experimental and DFT Study of the Adsorption of N_2O on Transition Ion-Exchanged ZSM-5. *Catal. Today* **2019**, *327*, 177-181.
16. Russo, N.; Mescia, D.; Fino, D.; Saracco, G.; Specchia, V., N_2O Decomposition over Perovskite Catalysts. *Ind. Eng. Chem. Res.* **2007**, *46*, 4226-4231.
17. Adamovich, I.; Baalrud, S. D.; Bogaerts, A.; Bruggeman, P. J.; Cappelli, M.; Colombo, V.; Czarnetzki, U.; Ebert, U.; Eden, J. G.; Favia, P.; Graves, D. B.; Hamaguchi, S.; Hieftje, G.; Hori, M.; Kaganovich, I. D.; Kortshagen, U.; Kushner, M. J.; Mason, N. J.; Mazouffre, S.; Thagard, S. M.; Metelmann, H. R.; Mizuno, A.; Moreau, E.; Murphy, A. B.; Niemira, B. A.; Oehrlein, G. S.; Petrovic, Z. L.; Pitchford, L. C.; Pu, Y. K.; Rauf, S.; Sakai, O.; Samukawa, S.; Starikovskaia, S.; Tennyson, J.; Terashima, K.; Turner, M. M.; Sanden, M. C. M. v. d.; Vardelle,

A., The 2017 Plasma Roadmap: Low Temperature Plasma Science and Technology. *J. Phys. D: Appl. Phys.* **2017**, *50*, 323001.
18. Fan, X.; Kang, S.; Li, J.; Zhu, T., Formation of Nitrogen Oxides (N_2O, NO, and NO_2) in Typical Plasma and Plasma-Catalytic Processes for Air Pollution Control. *Water, Air, Soil Pollut.* **2018**, *229*, 351.
19. Whitehead, J. C., Plasma-Catalysis: The Known Knowns, the Known Unknowns, and the Unknown Unknowns. *J. Phys. D: Appl. Phys.* **2016**, *49*, 243001 (243024pp).
20. Kim, H.-H.; Teramoto, Y.; Ogata, A.; Takagi, H.; Nanba, T., Plasma Catalysis for Environmental Treatment and Energy Applications. *Plasma Chem. Plasma Process.* **2016**, *36*, 45-72.
21. Whitehead, J. C., Plasma Catalysis: A Solution for Environmental Problems. In *Pure Appl. Chem.*, 2010; Vol. 82, p 1329.
22. Affonso Nóbrega, P. H.; Rohani, V.; Fulcheri, L., Non-Thermal Plasma Treatment of Volatile Organic Compounds: A Predictive Model Based on Experimental Data Analysis. *Chem. Eng. J.* **2019**, *364*, 37-44.
23. Barboun, P.; Mehta, P.; Herrera, F. A.; Go, D. B.; Schneider, W. F.; Hicks, J. C., Distinguishing Plasma Contributions to Catalyst Performance in Plasma-Assisted Ammonia Synthesis. *ACS Sustainable Chem. Eng.* **2019**, *7*, 8621-8630.
24. Dębek, R.; Azzolina-Jury, F.; Travert, A.; Maugé, F., A Review on Plasma-Catalytic Methanation of Carbon Dioxide – Looking for an Efficient Eatalyst. *Renewable Sustainable Energy Rev.* **2019**, *116*, 109427.
25. Hur, M.; Lee, J. O.; Lee, J. Y.; Kang, W. S.; Song, Y. H., Abatement Characteristics of N_2O in Low-Pressure Plasma Reactor. *Plasma Sources Sci. Technol.* **2015**, *25*, 015008.
26. Fan, X.; Kang, S.; Li, J.; Zhu, T., Conversion of Dilute Nitrous Oxide (N_2O) in N_2 and N_2–O_2 Mixtures by Plasma and Plasma-Catalytic Processes. *RSC Adv.* **2018**, *8*, 26998-27007.
27. Guillemot, M.; Castel, B., Workplace Nitrous Oxide Sampling: Alternative Adsorbents. *Ind. Eng. Chem. Res.* **2015**, *54*, 7760-7765.
28. Hanna, A. R.; Blechle, J. M.; Fisher, E. R., Using Fundamental Spectroscopy to Elucidate Kinetic and Energetic Mechanisms within Environmentally Relevant Inductively Coupled Plasma Systems. *J. Phys. Chem. A* **2017**, *121*, 7627-7640.
29. Zhang, Y.-R.; Van Laer, K.; Neyts, E. C.; Bogaerts, A., Can Plasma be Formed in Catalyst Pores? A Modeling Investigation. *Appl. Catal., B* **2016**, *185*, 56-67.
30. Shah, M. A., Growth of Uniform Nanoparticles of Platinum By an Economical Approach at Relatively Low Temperature. *Sci. Iran.* **2012**, *19*, 964-966.
31. Hanna, A. R.; Surksum, T. L. V.; Fisher, E. R., Investigating the Impact of Catalysts on N_2 Rotational and Vibrational Temperatures in Low Pressure Plasmas. *J. Phys. D: Appl. Phys.* **2019**, *52*, 345202.
32. Neyts, E. C.; Ostrikov, K.; Sunkara, M. K.; Bogaerts, A., Plasma Catalysis: Synergistic Effects at the Nanoscale. *Chem. Rev.* **2015**, *115*, 13408-13446.
33. Zhang, Y.-R.; Neyts, E. C.; Bogaerts, A., Influence of the Material Dielectric Constant on Plasma Generation inside Catalyst Pores. *J. Phys. Chem. C* **2016**, *120*, 25923-25934.
34. Chen, H.; Yue, J.; Li, Y.; Yi, C.; Yang, B.; Qi, S., Catalytic Activity Prediction of Different Metal Surfaces for N_2O Catalytic Decomposition by Density Functional Theory. *Comput. Theor. Chem.* **2015**, *1057*, 1-6.
35. Wu, L.; Qin, W.; Hu, X.; Ju, S.; Dong, C.; Yang, Y., Decomposition and Reduction of N_2O on CaS (100) surface: A Theoretical Account. *Surf. Sci.* **2015**, *632*, 83-87.

36. Konsolakis, M., Recent Advances on Nitrous Oxide (N_2O) Decomposition over Non-Noble-Metal Oxide Catalysts: Catalytic Performance, Mechanistic Considerations, and Surface Chemistry Aspects. *ACS Catal.* **2015**, *5*, 6397-6421.
37. Stillahn, J. M.; Trevino, K. J.; Fisher, E. R., Deposition of Amorphous CNx Materials in BrCN Plasmas: Exploring Adhesion Behavior as an Indicator of Film Properties. *ACS Appl. Mater. Interfaces* **2011**, *3*, 1402-1410.
38. Lee, D. H.; Kim, T., N_2O Decomposition by Catalyst-Assisted Cold Plasma. In *20th Int. Symp. Plasma Chem.*, Philadelphia, USA, 2012.
39. Burgess, D. R., Jr., Thermochemical Data. In *NIST Chemistry WebBook, NIST Standard Reference Database Number 69*, Linstrom, P. J.; Mallard, W. G., Eds. National Institute of Standards and Technology: Gaithersburg MD.
40. Blechle, J. M.; Hanna, A. R.; Fisher, E. R., Determination of Internal Temperatures Within Nitric Oxide Inductively Coupled Plasmas. *Plasma Process. Polym.* **2017**, 1700041-n/a.
41. Larsson, R., Propane Dehydrogenation Catalyzed by ZSM-5 Zeolites. A Mechanistic Study Based on the Selective Energy Transfer (SET) Theory. *Molecules (Basel, Switzerland)* **2015**, *20*, 2529-2535.
42. Larsson, R., A Model of Selective Energy Transfer at the Active Site of the Catalyst. *J. Mol. Catal.* **1989**, *55*, 70-83.
43. Larsson, R., Concluding Remarks on the Theory of Selective Energy Transfer and Exemplification on a Zeolite Kinetics Study. *Monatshefte für Chemie - Chemical Monthly* **2013**, *144*, 21-28.
44. Hanna, A. R.; Fisher, E. R., Investigating Recent Developments and Applications of Optical Plasma Spectroscopy: A Review. *J. Vac. Sci. Technol., A* **2020**, *38*, 020806.
45. Larsson, R., Zeolite Catalysis and Molecular Vibrations. *Catal. Today* **1988**, *3*, 387-394.
46. Larsson, R., Isokinetic Effects in Ethane Hydrogenolysis and Their Relation to the Mechanism of the Reaction. *Catal. Lett.* **1991**, *11*, 137-148.
47. Cao, Y.; Meng, Q.; Yang, W.; Yao, J.; Shu, Y.; Wang, W.; Chen, G., Effect of Plasma Treatment on Surface Properties of TiO_2 Nanoparticulate Films. *Colloids Surf., A* **2005**, *262*, 181-186.
48. Prins, R., Eley–Rideal, the Other Mechanism. *Top. Catal.* **2018**, *61*, 714-721.
49. Zaharia, T.; Kleyn, A. W.; Gleeson, M. A., Eley-Rideal Reactions with N Atoms at Ru(0001): Formation of NO and N_2. *Phys. Rev. Lett.* **2014**, *113*, 053201.
50. Whitehead, J. C., Plasma-Catalysis: Is it just a question of scale? *Front. Chem. Sci. Eng.* **2019**, *13*, 264-273.

CHAPTER 9
RESEARCH SUMMARY AND FUTURE DIRECTIONS

This dissertation concludes with a summary of major aspects and themes of the research presented in Chapters 3 – 8, as well as outlooks and implications for future inquiry. The broader impacts of this work are discussed in the context of coupling plasmas with catalysts for enhanced pollution abatement.

9.1 Research Summary

9.1.1 A holistic experimental approach to plasma-substrate interactions

Plasma discharges are an inherently complex environment with a multitude of energetic species, ranging from free electrons, ions, metastables, atoms and molecules.[1,2] As such, a plethora of diagnostic tools have been developed to study gas-phase interactions within these systems. Langmuir probes have been extensively used to measure electron properties (i.e., density, temperatures, and energy distributions) and the electric potential of a discharge.[2] These probes, however, physically perturb the plasma environment and are also susceptible to surface contamination. As such, optical spectroscopies are becoming widely employed as non-intrusive diagnostic tools. The most common uses of OES include species identification and determination of relative densities via inert gas actinometry.[3] Here, a literature review regarding the diagnostic capabilities of OES beyond simplistic species identification was provided (Chapter 3). OES lines were used to elucidate electron temperature (T_e) and electron density (n_e) trends as a function of power and pressure in rf Ar plasmas.[4] Chapter 3 also introduced the framework of this dissertation, where spectroscopic techniques were used to investigate

technologically (C_xF_y) and environmentally (N_xO_y) relevant plasma systems as prime examples of how a holistic approach to the study of plasma chemistry applies to a range of systems.

Plasma energetics, specifically determining how energy is partitioned between rotational and vibrational modes, as well as how vibrational energies can impact interactions at surfaces, is another critical component of plasma chemistry. These key features were investigated within C_xF_y discharges, which have enormous utility in numerous of applications, especially the semiconductor and microelectronics industries. Knowledge of system energetics, as well as gas-substrate interactions, could lead to significant improvements in process development. The culmination of work by several Fisher Group members, especially Dr. M.F. Cuddy, determined a linear relationship between the propensity of CF radicals to scatter from a Si substrate and excited-state CF vibrational temperature (T_V).[5,6] Additionally, the influence of precursor, system pressure, and applied power was elucidated for emitting CF radicals. Previously, BAS characterized emitting and absorbing NO radicals within NO discharges.[7] Here, BAS was employed to investigate more complex systems, specifically to determine rotational temperature (T_R) for ground-state CF_2 radicals within C_xF_y plasmas. CF_2 and other oligomeric species are hypothesized to substantially contribute to FC film formation,[8] therefore the gas-phase insights of Chapter 4 were further applied to the modification of microporous zeolites studies within Chapter 5.

The surface properties (i.e., wettability, composition) of NaX zeolites were tuned via C_xF_y and $H_2O_{(v)}$ plasma exposure. The wettability of solid surfaces is an important material property, governed by chemical composition and the geometrical structure of the surface.[9,10] The net effect of plasma treatment on the zeolite substrates was predominantly assessed via WCA, where C_xF_y precursors with large F/C ratios ($F/C \geq 3$) rendered the surface more hydrophilic via surface

etching processes. Tuning precursor selection, operating conditions, and gas-feed additives (i.e., H_2 and O_2), the surface properties of zeolites ranged from completely wettable to super-hydrophobic (Chapter 5). Regardless of plasma treatment, the bulk crystallinity of the zeolite remained intact. This is an improvement over acid modification strategies that often also result in structural damage to the zeolite framework,[11,12] The zeolites employed in these plasma modification studies also have potential in catalysis applications, therefore were used in subsequent PAC studies.

Before adding the complexity of catalysts to the discharge, the gas-phase chemistry of N_xO_y plasmas was studied with emission and absorbance spectroscopy (Chapter 6). This study confirmed the empirical relationship where electron temperatures are several orders of magnitude elevated compared to vibrational and rotational temperatures. Furthermore, a positive, linear correlation was determined for applied rf power and measured internal temperatures (i.e., T_V and T_R). Increasing system pressure, however, resulted in a concomitant decrease in T_V (NO and N_2), likely due to collisional quenching. After thorough characterization of gas-phase energetics and kinetics within N_xO_y discharges, a homonuclear diatomic (N_2) was selected for an exploratory plasma-assisted catalysis (PAC) system.

The chemistry within N_2 plasmas with the addition of a zeolite was studied via OES as a function of power and system pressure. Interestingly, the addition of a microporous zeolite pellet resulted in dramatically reduced N_2 vibrational temperatures, with little impact on rotational thermalization pathways.[13] These data suggest excited-state N_2 interacts with the micro-structured catalyst and rebounds with some energy loss. The quenching of vibrational energy is hypothesized to arise from the formation of microplasmas within the pores of the material. Numerous theoretical studies have assessed the impact of pore size, shape and composition on

the formation of microdischarges in low- and atmospheric-pressure discharges.[14] To further experimentally investigate this vibrational cooling phenomenon, the plasma reactor was completely lined with zeolite pellets (Figure 2.2a). The resulting N_2 vibrational temperatures were further thermalized, suggesting the interactions between the plasma and catalysts directly impacts gas-phase energetics. Additional gaseous species (i.e., OH and NO) were formed with a zeolite in the system, suggesting surface removal of oxygen into the gas-phase. This hypothesis was verified with X-ray photoelectron spectroscopy, where small amounts of nitrogen were measured on the surface, likely filling oxygen vacancies created upon plasma exposure. PAC studies were expanded to explore the impact of both micro- and nanostructured catalysts on more complex plasma systems.

N_2O is a greenhouse pollutant that is generated from both natural and anthropogenic sources, forming N_2, NO, and O species upon dissociation. Gas-phase (densities, energetics, and kinetics) and material properties (surface chemistry, morphology, crystallinity) were systematically and robustly investigated for platinum and zeolite catalysts within N_2O discharges to understand how the plasma impacts dissociation of N_2O. With a single zeolite in the N_2O plasma, OES revealed an increase in the production of ambient species (i.e., N_2), with little emission from NO peaks at $P \geq 75$ W.s. These data exemplify the potential for energetic plasma species to enhance the catalytic ability of zeolites within a single-stage PAC system. The majority of the work presented in this dissertation explored single-stage systems, however, a two-stage, pre-plasma catalysis configuration was constructed and used to study the catalytic decomposition of N_2O. These preliminary results suggest Pt catalysts are better suited for pre-plasma configurations, as the Pt metal is oxidized when directly interfaced with the plasma (Chapter 8). Future

investigations of environmentally-relevant plasmas systems are needed to yield important information about the nature of plasma-catalysts interactions, discussed in Section 9.2.

9.1.2 Broader impacts and outlook for plasma –assisted catalysis

These studies evaluated the potential effectiveness of non-thermal plasmas, coupled with catalysts, to decompose atmospheric pollutants through an understanding of underlying chemistry of gas-phase energetics and kinetics, as well as gas-surface interactions within N_xO_y plasma systems. This dissertation emphasizes the necessity to employ a host of complementary techniques to study plasma-catalysts synergisms for the design of effective materials and plasma systems. For researchers to fully address PAC limitations, it is imperative not only to understand how the plasma affects the catalyst (i.e., possible degradation and poisoning), but also how catalysts impact the resulting gas-phase chemistry. Furthermore, this holistic approach to PAC can be employed for various material architectures and gas mixtures, discussed in greater detail below.

9.2 Future Directions

9.2.1 A multi-faceted approach to plasma diagnostics

This dissertation sought to employ a wide array of techniques to analyze the gas-phase of various plasma precursors, ranging from noble gases (e.g., Ar) to large, complex fluorocarbons. Energetic electrons are a governing force for the resulting plasma character and thus many studies have sought to understand electron dynamics within a discharge, presented in Chapter 3. Phase-resolved OES (PR-OES) is an additional non-intrusive diagnostic tool that provides access to highly energetic electrons with enhanced spatial and temporal resolution.[15] Fundamental plasma parameters such as electron density, electron temperature, and electron energy

distributions can be determined on the nanosecond time scale. PR-OES is sensitive to high energy electrons (> 10 eV), which is particularly interesting as these electrons dominate ionization processes and are nominally responsible for the non-thermal nature of plasma discharges.[15] The combination of OES line-emission analysis and PR-OES data can provide a thorough description of both low (bulk) and high energy electrons. The current IRIS apparatus could be modified to support this diagnostic tool as the most important requirement for PR-OES is a gated intensified charged coupled device (ICCD) camera (Figure 2.7).[16] Gans *et al.* studied pulsed rf ICPs via PR-OES and time-resolved ion energy analysis, concluding that a pulsed ICP initially ignites capacitively before reaching a stable inductive mode.[17] Additionally, by analyzing the plasma afterglow, they found the boundary sheath does not fully collapse for rf H_2 discharges, which is attributed to electron heating through collisions with vibrationally excited hydrogen molecules.[17] Therefore, the use of PR-OES could allow us to more readily understand plasma-sheath effects when a material is added to the discharge. Limited studies on pulsed-plasma systems are provided herein; thus, characterizing pulse dynamics and the afterglow is an avenue for future exploration. Additional experimental strategies to study PAC systems is discussed in Section 9.2.2.

9.2.2 Expanding pollution abatement strategies

Concentrations of environmental pollutants are continually rising, therefore alternative technologies are needed alleviate the detrimental impact of atmospheric contaminants. Prevalent researchers have identified plasmas utilized in environmental applications as a growing, important area of research within the low-temperature plasma community.[18] The 2017 Plasma Roadmap states:

> "*Solving these challenges requires developing an understanding of the fundamental plasma-surface interactions in an integrated approach that combines new computational strategies and diagnostics techniques.*"[18]

This proposed approach, using a variety of diagnostic techniques to probe plasma-substrate interactions, was a focal point of this dissertation. Optical spectroscopy is, inherently, a comparative strategy to probe the impact of adding a catalyst to the discharge, gas-phase interactions (sans catalysts) must be elucidated first. The IRIS technique, however, provides significant insight into the plasma-surface interface *during* plasma processing through the determination of a radical's propensity to scatter or react at a surface. NO scatter coefficients within N_xO_y plasmas have been determined from Pt and Si surfaces, showing no dependence on the catalytic nature of the substrate.[7,19] These substrates, however, are morphologically similar with a smooth, 2D surface. Therefore, it is necessary to elucidate the propensity of radicals to scatter from micro-and nano-structured catalysts, a set of experiments not performed here. These interactions are likely coupled to plasma species with a variety of internal and translational energies. The IRIS apparatus can also determine translational energies, where kinetic energy distributions (e.g. translational temperatures) of NH_2 within NH_3 discharges,[20] Si and SiF_2 in a SiF_4 molecular beam,[21] and preliminary work on CF_2 within C_2F_6 and C_3F_6 systems[5] have been measured. Connecting plasma energy partitioning data and specific molecule-surface interactions during non-thermal processing is necessary to realize the potential of PAC.

Continuing the work presented in Chapters 6 –8, the gas-phase composition of mixed gas systems should be explored spectroscopically to measure internal temperatures of plasma species such as NO, N_2, OH, H_2, and O_2, and the characterization of electron properties as a function of plasma parameters in the presence of catalytic substrates. Figure 9.1a depicts representative OES spectra of $H_2O_{(v)}$, N_2O: $H_2O_{(v)}$ (50:50), and N_2O plasmas ignited at 100 mTorr, 175 W.

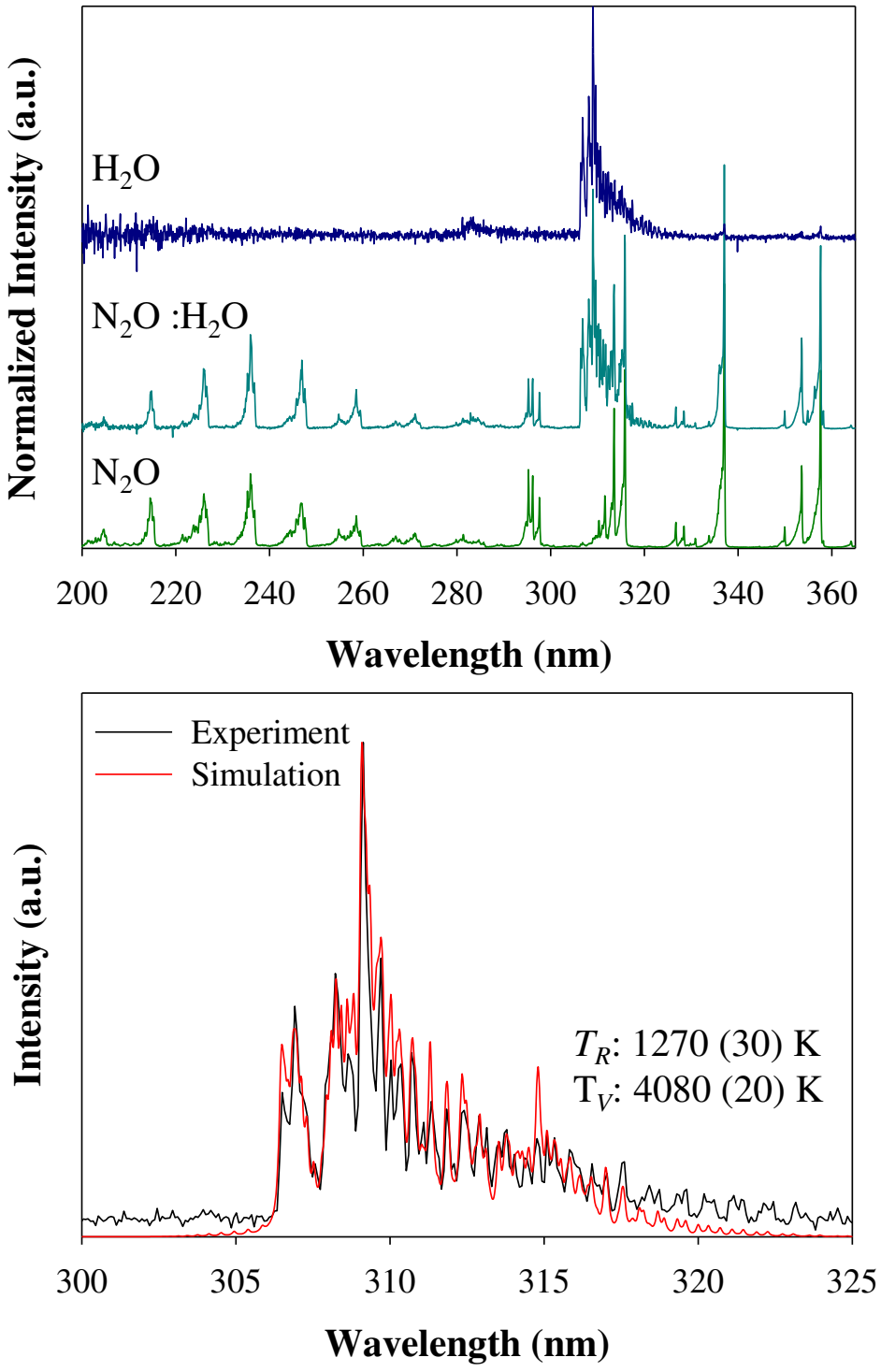

Figure 9.1. (a) Representative OES spectra of N_2O, N_2O: H_2O (50:50), and H_2O plasmas (p = 100 mTorr, P = 175 W) and (b) OH ($A^2\Sigma^+ \rightarrow X^2\Pi$) band within H_2O plasma fit with LIFBASE.

The N_2O emission spectra is populated with NO ($A^2\Sigma^+ \rightarrow X^2\Pi$) and N_2 ($C^3\Pi_u \rightarrow B^3\Pi_g$) transitions. Once H_2O is added to the gas feed, strong emissions from the OH ($A^2\Sigma^+ \rightarrow X^2\Pi$) band are measured. Figure 9.1b depicts the OH ($A^2\Sigma^+ \rightarrow X^2\Pi$) band within an $H_2O_{(v)}$, discharge with the corresponding fit generated in LIFBASE.[22] Notably, the determined T_R(OH) within a $H_2O_{(v)}$ plasma is considerably higher than values reported for NO and N_2, a trend previously documented by Stuckert *et al.*.[23] Spatially- and temporally-resolved spectroscopy should be completed on gaseous mixtures, where gases are systematically added to the feed to understand the role of each component species within the overall chemistry and reactivity within increasingly complex PAC systems. Moreover, it is important to decipher the role of ground state neutrals and ions within PAC systems via BAS and mass spectrometry (MS) techniques. Charged species play critical and dynamic roles in PAC systems, therefore MS is a key analytical tool that can measure ion densities and distributions within the discharge. To deconvolute coupled effects of reactive neutrals and ions bombarding the catalyst surface, two approaches can be taken: (1) the gas-phase environment downstream of the catalysts can be measured spectroscopically and (2) experiments can be performed wherein ions are prevented from interacting with the substrate, such as grounding the substrate via a wire mesh or designing alternative geometry reactors.

Briefly demonstrated in our N_2 PAC study with zeolites (Chapter 7), the amount of catalyst in the discharge can drastically impact the resulting chemistry. Increasing the amount of catalyst present innately reduces the plasma volume, likely to change the discharge character, which could promote exhaust decomposition or non-uniform electric fields in the system (i.e., microdischarges).[24] The multi-substrate experiments detailed in Chapter 7 should be expanded to additional N_xO_y precursors and mixed-gas systems. Furthermore, the investigation of two-

stage PAC systems has been limited,[24] therefore additional system characterization and optimization of plasma-catalyst configurations is warranted. Post-plasma catalysis, Figure 1.1c, has yet to be studied by the Fisher Group. Understanding the resulting gas-phase composition after plasma ignition and subsequent interaction with a catalyst could be accomplished with Fourier Transform infrared spectroscopy or residual gas analyzers, both positioned downstream of the plasma reactor. Although the synergistic coupling of a plasma with a catalyst to access reactions not energetically feasible at thermal conditions is an intrinsic benefit of single-stage systems, the direct interaction of energetic plasma species can negatively impact the catalyst. Hence, two-stage configurations may prevent or postpone degradation of the catalyst over numerous exposures.

Lastly, investigating a range of different nano- and micro-structured catalysts will further elucidate effects of substrate morphology and chemistry on plasma-catalyst interactions. Here, the relative density of NO within an N_2O plasma was greatly diminished in the presence of a microporous NaX zeolite, even compared to the rare earth metal Pt. There are over 40 types of naturally occurring zeolites and these aluminosilicate minerals are significantly less expensive than traditional rare-earth metals, thereby present a sustainable pathway for PAC improvement. Specifically, it would be beneficial to explore the impact of different SiO_2/Al_2O_3 ratios and size distributions on the resulting plasma chemistry. Representative SEM images of untreated ZSM-5 are illustrated in Figure 9.2 at two different magnifications. These nano-structured materials have a manufacturer reported Si/Al ratio of 23, significantly higher than that for the materials utilized in these studies (Si/Al ratio ~3.3). These materials can be used as-received, pressed into pellets, spun into fibers, or doped with additional catalytic materials.

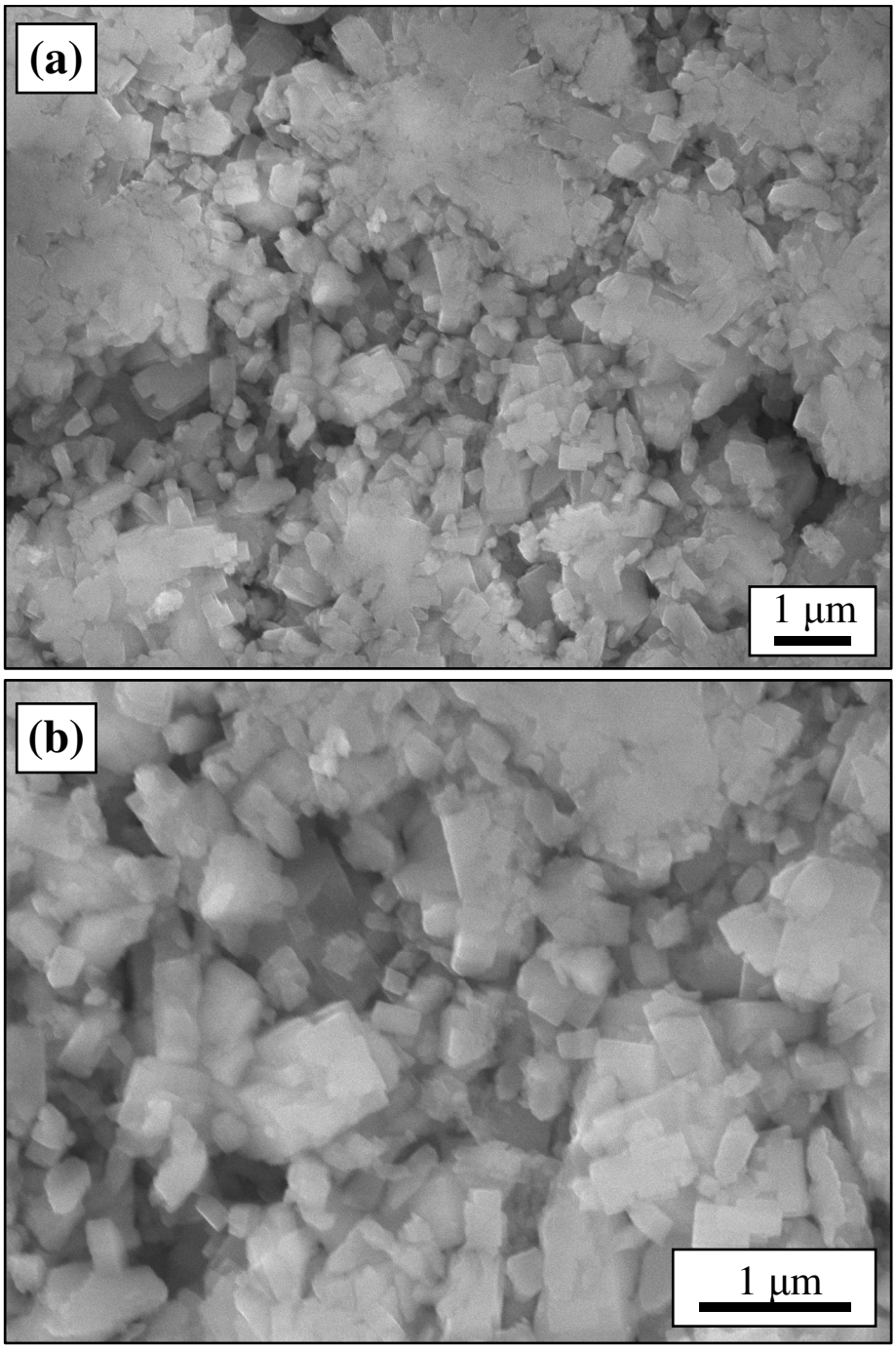

Figure 9.2. Representative SEM image of untreated ZSM-5 zeolite pellet at (a) 10000x and (b) 20000x magnification.

Specifically, Zeolites are commonly used as a support structure and can also be loaded with metal catalysts (i.e., Ni) or metal oxides (i.e., TiO_2[25]and γ-Al_2O_3[26]), therefore the utility of composite or mixed material catalysts to decompose atmospheric pollutants should also be explored. Ultimately, the potential of plasma-assisted catalysis as a means for pollution abatement depends largely on the ability to understand the underlying chemistry and plasma-catalyst interactions within these multifaceted systems.

REFERENCES

1. Fridman, A., *Plasma Chemistry*. Cambridge University Press: 2008.
2. Grill, A., *Cold Plasma Materials Fabrications: From Fundamentals to Applications*. IEEE Press: Piscataway, NJ, 1994.
3. Coburn, J. W.; Chen, M., Optical Emission Spectroscopy of Reactive Plasmas: A Method for Correlating Emission Intensities to Reactive Particle Density. *J. Appl. Phys.* **1980**, *51*, 3134-3136.
4. Hanna, A. R.; Fisher, E. R., Investigating Recent Developments and Applications of Optical Plasma Spectroscopy: A Review. *J. Vac. Sci. Technol., A* **2020**, *38*, 020806.
5. Cuddy, M. F. Contributions of Gas-Phase Plasma Chemisry to Surface Modifications and Gas-Surface Interations: Investigations of Fluorocarbon rf Plasmas. Colorado State University, ProQuest Dissertations Publishing, 2012.
6. Hanna, A. R.; Cuddy, M. F.; Fisher, E. R., Energy Partitioning and its Influence on Surface Scatter Coefficients within Fluorinated Inductively Coupled Plasmas. *J. Vac. Sci. Technol., A* **2017**, *35*, 05C308.
7. Blechle, J. M.; Hanna, A. R.; Fisher, E. R., Determination of Internal Temperatures Within Nitric Oxide Inductively Coupled Plasmas. *Plasma Process. Polym.* **2017**, *14*, 1700041.
8. Cuddy, M. F.; Fisher, E. R., Contributions of CF and CF_2 Species to Fluorocarbon Film Composition and Properties for C_xF_y Plasma-Enhanced Chemical Vapor Deposition. *ACS Appl. Mater. Interfaces* **2012**, *4*, 1733-1741.
9. Feng, L.; Li, S.; Li, Y.; Li, H.; Zhang, L.; Zhai, J.; Song, Y.; Liu, B.; Jiang, L.; Zhu, D., Super-Hydrophobic Surfaces: From Natural to Artificial. *Adv. Mater.* **2002**, *14*, 1857-1860.
10. Jiang, L.; Wang, R.; Yang, B.; Li, T. J.; Tryk, D. A.; Fujishima, A.; Hashimoto, K.; Zhu, D. B., Binary Cooperative Complementary Nanoscale Interfacial Materials. *Pure Appl. Chem.* **2000**, *72*, 73-81.
11. Furukawa, K.; Tian, S. R.; Yamauchi, H.; Yamazaki, S.; Ijiri, H.; Ariga, K.; Muraoka, K., Characterization of H–Y Zeolite Modified by a Radio-Frequency CF_4 Plasma. *Chem. Phys. Lett.* **2000**, *318*, 22-26.
12. Deng, C.; Zhang, J.; Dong, L.; Huang, M.; Bin, L.; Jin, G.; Gao, J.; Zhang, F.; Fan, M.; Zhang, L.; Gong, Y., The Effect of Positioning Cations on Acidity and Stability of the Framework Structure of Y Zeolite. *Sci. Rep.* **2016**, *6*, 23382.
13. Hanna, A. R.; Van Surksum, T. L.; Fisher, E. R., Investigating the Impact of Catalysts on N_2 Rotational and Vibrational Temperatures in Low Pressure Plasmas. *J. Phys. D: Appl. Phys.* **2019**, *52*, 345202.
14. Zhang, Y.; Wang, H.-y.; Zhang, Y.-r.; Bogaerts, A., Formation of Microdischarges Inside a Mesoporous Catalyst in Dielectric Barrier Discharge Plasmas. *Plasma Sources Sci. Technol.* **2017**, *26*, 054002.
15. Schulze, J.; Schüngel, E.; Donkó, Z.; Luggenhölscher, D.; Czarnetzki, U., Phase Resolved Optical Emission Spectroscopy: A Non-Intrusive Diagnostic to Study Electron Dynamics in Capacitive Radio Frequency Discharges. *J. Phys. D: Appl. Phys.* **2010**, *43*, 124016.
16. Benedikt, J.; Hofmann, S.; Knake, N.; Böttner, H.; Reuter, R.; Keudell, A.; Gathen, V., Phase Resolved Optical Emission Spectroscopy of Coaxial Microplasma Jet Operated with He and Ar. *Eur. Phys. J. D* **2010**, *60*, 539-546.
17. Gans, T.; Osiac, M.; O'Connell, D.; Kadetov, V. A.; Czarnetzki, U.; Schwarz-Selinger, T.; Halfmann, H.; Awakowicz, P., Characterization of Stationary and Pulsed Inductively

Coupled RF Discharges for Plasma Sterilization. *Plasma Phys. Controlled Fusion* **2005**, *47*, A353-A360.
18. Adamovich, I.; Baalrud, S. D.; Bogaerts, A.; Bruggeman, P. J.; Cappelli, M.; Colombo, V.; Czarnetzki, U.; Ebert, U.; Eden, J. G.; Favia, P.; Graves, D. B.; Hamaguchi, S.; Hieftje, G.; Hori, M.; Kaganovich, I. D.; Kortshagen, U.; Kushner, M. J.; Mason, N. J.; Mazouffre, S.; Thagard, S. M.; Metelmann, H. R.; Mizuno, A.; Moreau, E.; Murphy, A. B.; Niemira, B. A.; Oehrlein, G. S.; Petrovic, Z. L.; Pitchford, L. C.; Pu, Y. K.; Rauf, S.; Sakai, O.; Samukawa, S.; Starikovskaia, S.; Tennyson, J.; Terashima, K.; Turner, M. M.; van de Sanden, M. C. M.; Vardelle, A., The 2017 Plasma Roadmap: Low Temperature Plasma Science and Technology. *J. Phys. D: Appl. Phys.* **2017**, *50*, 323001.
19. Blechle, J. M.; Cuddy, M. F.; Fisher, E. R., Effect of Ion Energies on the Surface Interactions of NO Formed in Nitrogen Oxide Plasma Systems. *J. Phys. Chem. A* **2013**, *117*, 1204-1215.
20. McCurdy, P. R.; Venturo, V. A.; Fisher, E. R., Velocity distributions of NH_2 radicals in an NH_3 plasma molecular beam. *Chem. Phys. Lett.* **1997**, *274*, 120-126.
21. Zhang, J.; Williams, K. L.; Fisher, E. R., Velocity Distributions of SiF and SiF_2 in an SiF_4 Plasma Molecular Beam. *J. Phys. Chem. A* **2003**, *107*, 593-597.
22. Crosley, J. L. D. R. *LIFBASE: Database and Spectral Simulation Program (Version 1.5)*; 1999.
23. Stuckert, E. P.; Miller, C. J.; Fisher, E. R., Gas-Phase Diagnostics During H_2 and H_2O Plasma Treatment of SnO_2 Nanomaterials: Implications for Surface Modification. *J. Vac. Sci. Technol., B* **2017**, *35*, 021802.
24. Whitehead, J. C., Plasma-Catalysis: The Known Knowns, the Known Unknowns, and the Unknown Unknowns. *J. Phys. D: Appl. Phys.* **2016**, *49*, 243001 (243024pp).
25. Nasonova, A.; Kim, K.-S., Effects of TiO_2 coating on zeolite particles for NO and SO_2 removal by dielectric barrier discharge process. *Cat. Today* **2013**, *211*, 90-95.
26. Jo, J.-O.; Trinh, Q. H.; Kim, S. H.; Mok, Y. S., Plasma-Catalytic Decomposition of Nitrous Oxide over γ-Alumina-Supported Metal Oxides. *Catal. Today* **2018**, *310*, 42-48.

APPENDIX A

A brief description of data pertaining to the fabrication and characterization of zeolite and TiO_2 fibers is provided here. A bench-top electrospinning unit was designed and built by Angela R. Hanna and Dr. M.M. Mann. I would like to thank both Tom Frederick and Ron Costello for their essential advice and assistance in the construction of this apparatus.

Numerous experimental factors can affect fiber morphology, including distance between the collector and the syringe, applied voltage, solution flow rate, choice of polymer, and solution composition (e.g., solvent, concentration). Currently, there are limited studies on the design of zeolites prepared from an electrospun polymer template, therefore preliminary data herein sought to primarily optimize zeolite fiber fabrication. In addition, electrospun polymers with embedded nanoparticles (i.e., TiO_2) fibers were also investigated to test the ability to translate this process to another material system. Morphological variations related to the electrospinning process were investigated, with the potential to open new domains for zeolite and TiO_2 fibers in a wide range of applications.

A.1. Electrospinning Results

Recently, incorporating zeolites into fibrous forms has attracted scientific inquiry for new applications in adsorption, optics, chemical sensors, and petroleum refining.[1-3] Here, microporous NaX zeolites were added to a polyvinylpyrrolidone (PVP) solution to create zeolite:polymer composite fibers, described in Chapter 2. The electrospinning process is illustrated in Figure 2.8b; briefly, voltage is applied to a syringe needle filled with 5 mL of a zeolite:PVP:ethanol (EtOH) solution. During electrospinning, the syringe pump dispenses solution at 5 $mLhr^{-1}$ for 1 hour, where the EtOH solvent evaporates and a composite zeolite:PVP

fiber mat is collected on an Al foil – wrapped disk. The chemical structure of the PVP backbone is depicted in Figure 5.4a.

Prior to adding the complexity of the solid zeolites, the impact of electrospinning distance (i.e., between collector and syringe) on fiber formation was investigated, Figure A.1. When the conductive disk was 10 cm from the needle tip (Figure 2.8), the size distribution of the fibers varied (Figure A.1a) An ImageJ plugin, DiameterJ, was employed for image analysis to measure fiber dimensions.[4] A more uniform size distribution was achieved with a 15 cm electrospinning distance. Anis and Hashaikeh studied the fabrication of zeolite –Y: PVP fibers, reporting an optimal distance of 15 cm.[5] Therefore, the conductor disk was 15 cm away from the needle for all subsequent studies. Anis and Hashaikeh also explored three different concentrations of zeolite: PVP (1:0.7, 0.7:1, and 1:1 by weight) in EtOH via SEM.[5] Preliminary experiments here also investigated three zeolite:PVP concentrations (1:2, 1:1, and 2:1) within EtOH. The solutions with a higher concentration of zeolites generally did not yield uniform electrospun mats; although a homogenous solution was loaded into the syringe-needle, precipitates (presumably zeolites) formed in the needle during the electrospinning process. Zeolite concentration conditions were optimized for our work, where the majority of the results presented in this Appendix were obtained with a 1:2 zeolite:PVP ratio.

Figure A.2. shows as-spun zeolite:PVP fibers at 12, 16, 20, and 24 kV spinning voltages. The fibers fabricated with 12 kV and 16 kV (Figure A.2a and A.2b) appear evenly distributed, where the fibers spun at 20 kV are increasingly random with agglomeration of zeolites (Figure A.2c). Moreover, significant beading is observed when the solution is electrospun at 24 kV. Therefore, lower voltages (e.g., 12 and 16 kV) were used in subsequent parameter optimization.

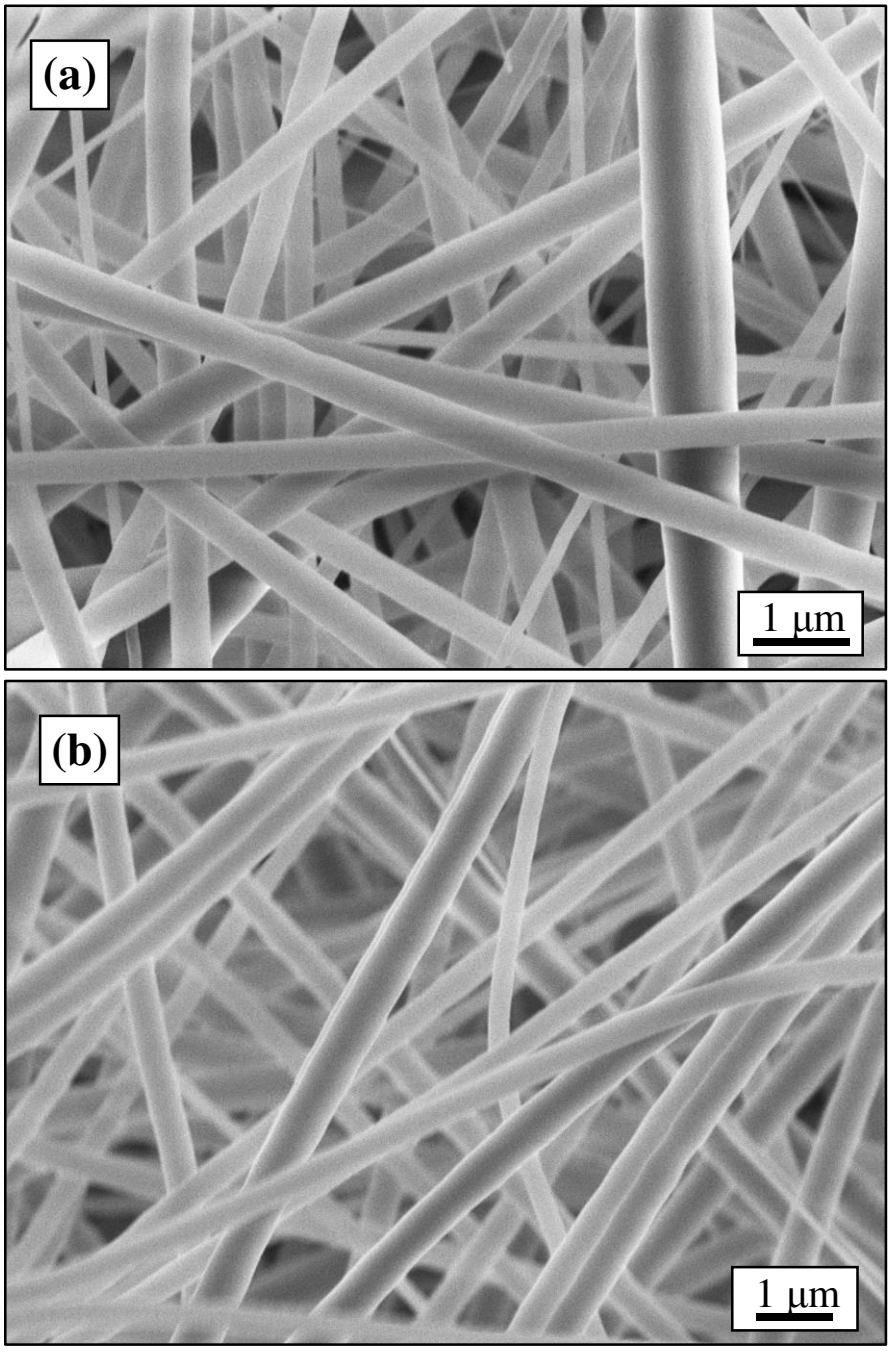

Figure A.1. Representative SEM images of electrospun 100% PVP fibers at16 kV, (a) 10 cm (13000x) and (b) 15 cm (10000x).

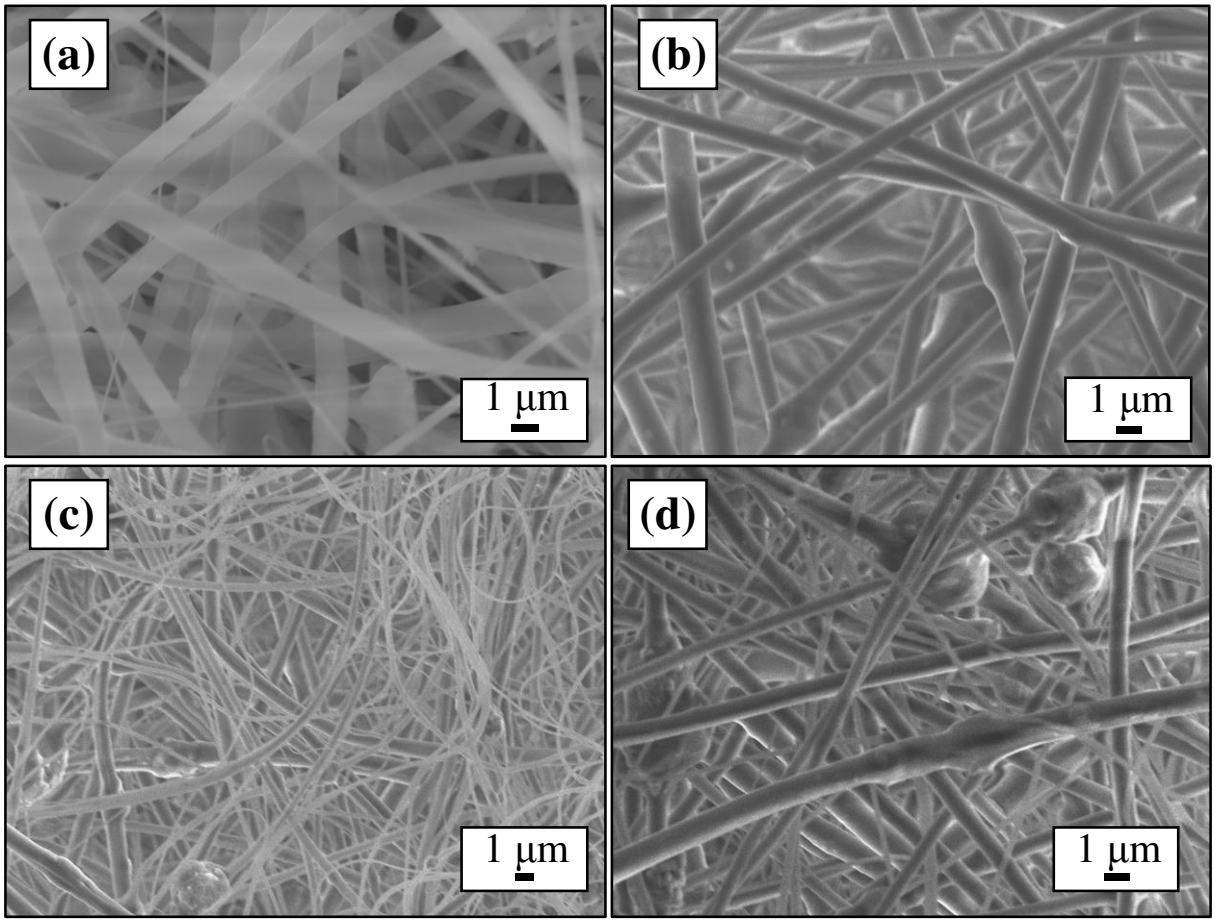

Figure A.2. Representative SEM images of electrospun zeolite: PVP fibers, (1:2 ratio, 15 cm) fibers at (a) 12 kV (5000x), (b) 16 kV (5000x), (c) 20 kV (3500x), and (d) 24 kV (5000x) voltages.

Described in Chapter 5, zeolite: PVP composite fibers require calcination to remove the polymeric phase and form zeolite fibers. Anis and Hashaikeh calcinated zeolite –Y fibers in a furnace at 550 °C for 2 hours, reporting a heating rate of 1 °C/min.[5] Here, the operating temperature of a furnace was slowly increased to 550 °C for 2 hours. The oven calcinated fibers were assessed with SEM and XPS techniques to verify removal of the polymeric phase, Figure A.3. The resulting fiber appears to be morphologically damaged, with consistent fissures along the width of the fiber. An XPS survey scan measured binding environments representative of the zeolite material (i.e., Na, Si, and Al), detailed in Chapter 5. Ultimately, these oven calcination studies served as a proof-of-concept that zeolite fibers could be fabricated with the current apparatus.

Discussed throughout this dissertation, plasmas are used to modify surfaces via thin film formation, functionalization, or etching. The utility of plasma to fabricate new materials, particularly in catalysis, is gaining significant research attention.[6] Here, O_2 and Ar plasmas were employed to remove the polymeric phase in efforts to decrease fabrication time. O_2 is commonly used to etch polymers,[7] where the energetic bombardment of O atoms can readily etch the surface. High resolution C_{1s} and O_{1s} XPS spectra for as –spun and O_2 plasma calcinated fibers are depicted in Figure A.4. Binding environments corresponding to aliphatic carbon (284.8 eV), -C-O-R/C-O-H (~ 286 eV) and C-N (~ 287 eV) were measured, where O is nominally bound to C, with small amounts bound to Si arising from the underlying zeolite material (Figure A.4b). Table A.1. details preliminary XPS atomic compositions for the as-received, native zeolites (discussed in Chapter 5), as–spun zeolite:PVP, and zeolite fibers after O_2 and Ar plasma treatments. These results are preliminary, and a larger sample size is needed to comprehensively characterize these materials.

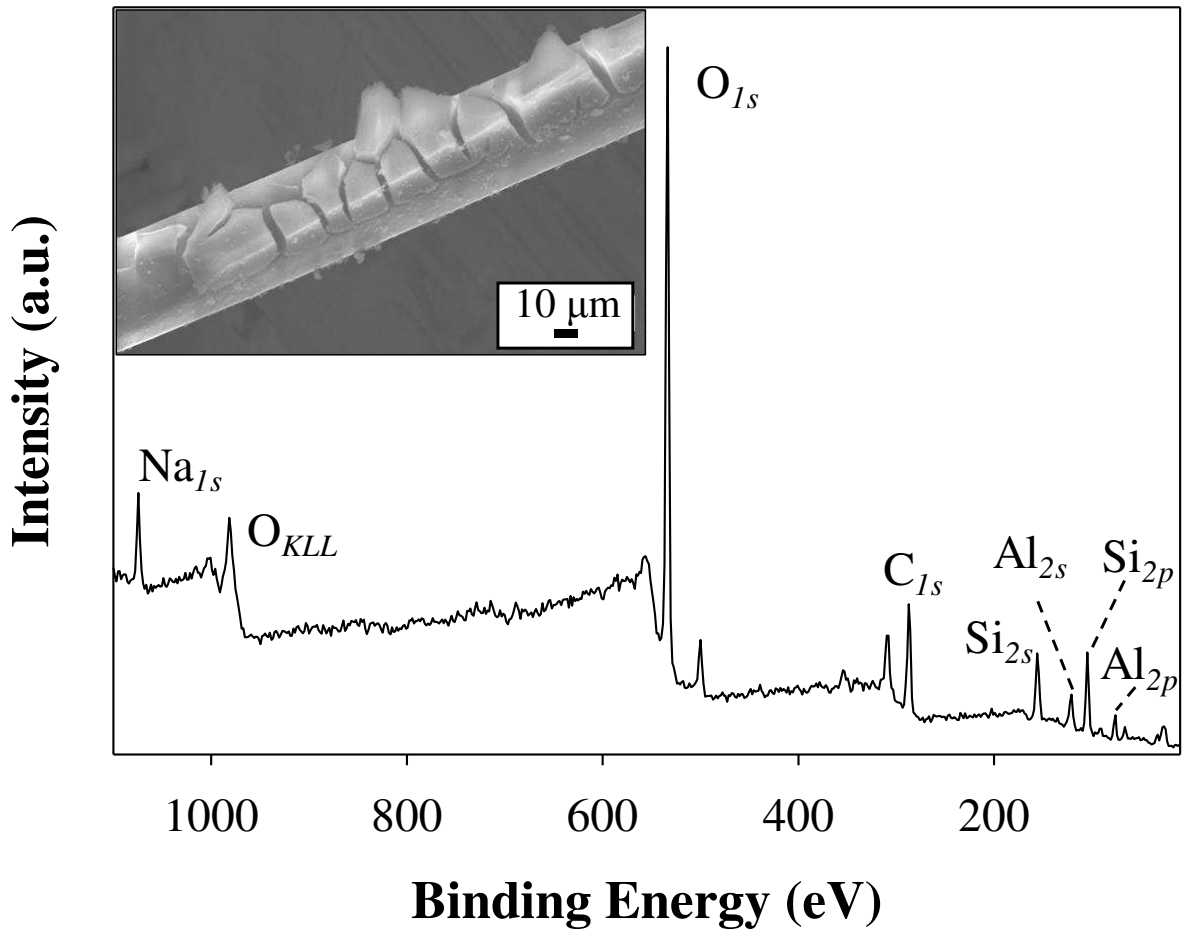

Figure A.3. Representative XPS survey spectrum and SEM image of oven calcinated zeolite fiber (1:2 ratio, 15 cm, 16 kV).

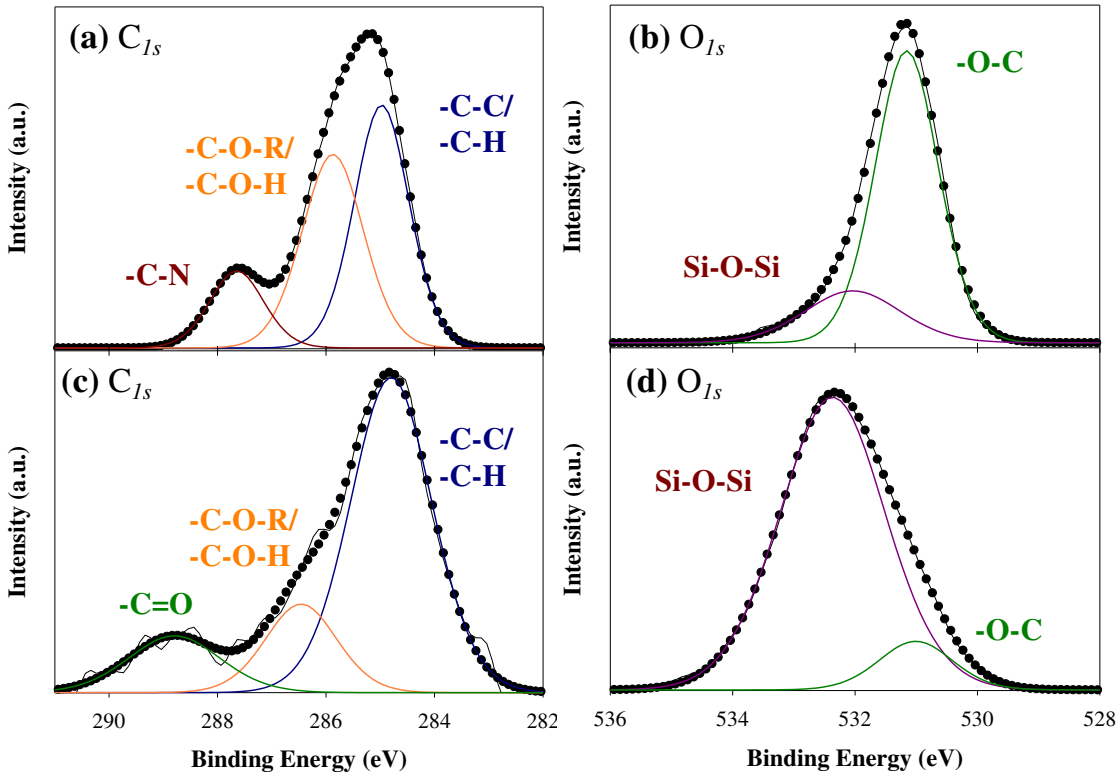

Figure A.4. High resolution (a,c) C_{1s} and (b,d) O_{1s} XPS spectra for (a,b) as-spun zeolite: PVP (1:2 ratio, 15 cm, 16 kV) and (c,d) O_2 plasma calcinated zeolite fibers (100 mTorr, 100 W, 15 min).

Table A.1. XPS atomic compositions for zeolites, zeolite-PVP and zeolite fibers[a,b]

	n	C (%)	O (%)	Si (%)	Al (%)	N (%)
native	9	19.9 (4.8)	58.4 (3.2)	17.5 (1.4)	4.4 (0.6)	--
as–spun	2	78.7 (0.4)	10.7 (0.5)	--	--	10.6 (0.1)
O_2	3	5.9 (0.4)	69.1 (1.1)	20.5 (0.8)	4.6 (0.7)	--
Ar	1	40.6	40.5	10.8	2.5	5.6

[a]Zeolite: PVP fabrication parameters (1:2 ratio, 15 cm, 16 kV)

[b]Treatments were performed at p = 100 mTorr, P = 100 W, t = 15 min in the coil region

Regardless, Si and Al were not measured on the surface of the as-spun (pre-calcinated) materials, suggesting zeolite encapsulation within the polymer. Upon an O_2 plasma treatment (100 mTorr, 100 W, 15 min), the amount of carbon measured on the surface decreased from 78.7 (0.4) % to 5.9 (0.4) %, Table A.1. Additionally, the amount of Si and Al on the surface of the O_2 calcinated fibers is comparable to the native, suggesting removal of the PVP from the fiber. Although XPS provides surface composition, it is important to characterize the morphology of the calcinated fibers. Therefore, EDS compositional maps were collected in conjunction with SEM images to probe morphology and compositional distributions, Figure A.5. This approach exemplifies the need to use a complement of analytical techniques to study these materials. An O_2 plasma calcinated fiber mounted on copper tape is depicted in Figure A.5. The length of the fiber is nominally composed of O and Si, with C and Cu dominating the background. Ar plasmas generate a multitude of excited Ar species and ions, discussed in Chapter 3 and are often used in grafting applications.[8] Detailed in Table A.1, Ar exposure was less efficient removing the PVP compared to O_2 plasmas, nominally N (5.6 %) and a significant amount of carbon (40.6 %) was measured. Notably, this result has yet to be reproduced. Wavhal and Fisher studied Ar plasma treated ultrafiltration membranes, arguing exposure to the atmosphere causes the attachment of oxygen and nitrogen moieties on the polymer.[8] Clearly, more work must be completed to understand the plasma-material interactions within the fabrication of these fibers. The ideal combination of plasma exposure, system pressure, and applied rf power remains unoptimized. Discussed in Chapter 3, optical emission spectroscopy can be employed to monitor the formation of gas-phase etch products to improve plasma calcination processes.

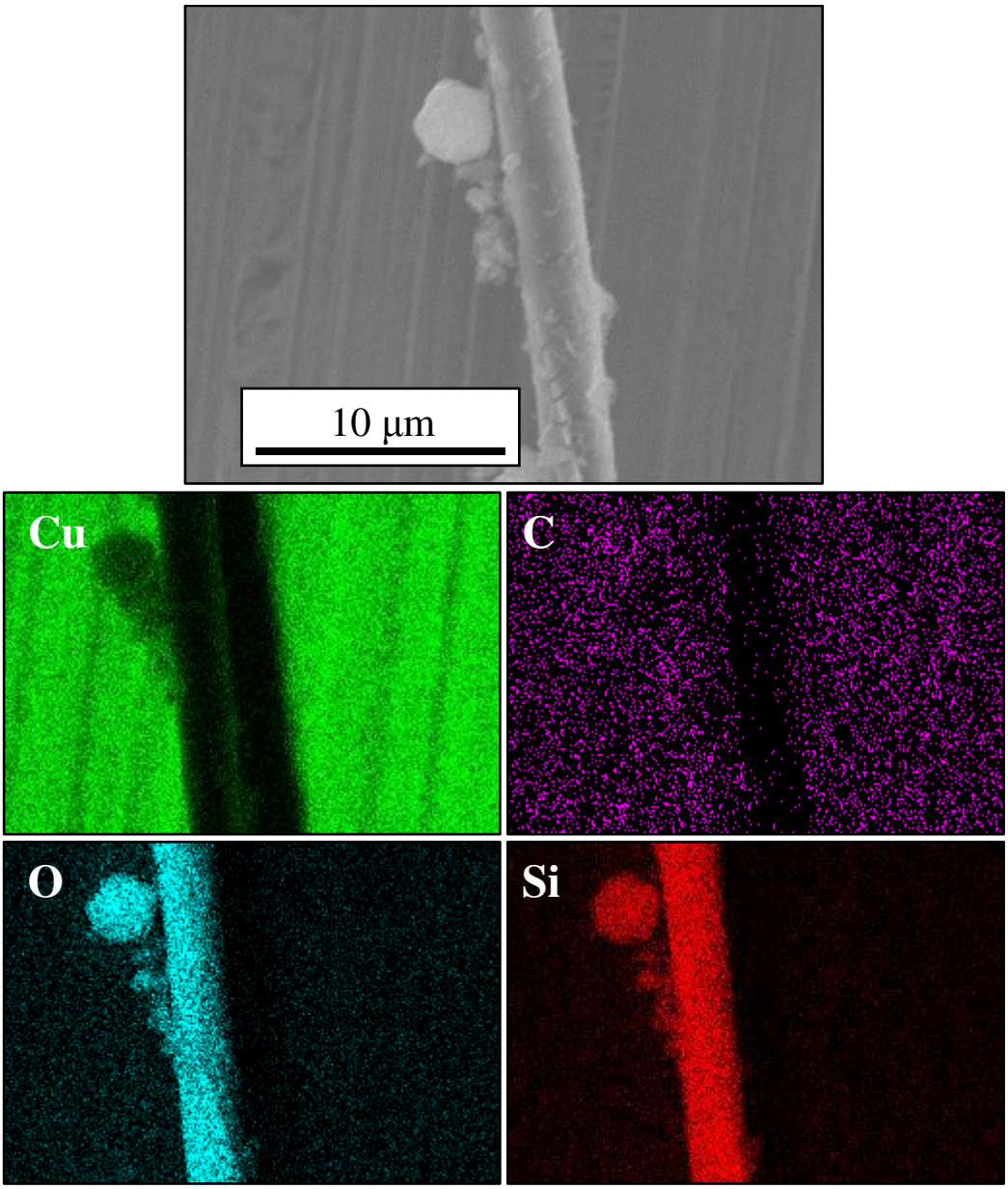

Figure A.5. Representative SEM image and EDS elemental maps of O_2 plasma (100 mTorr, 100 W, 15 min) calcinated zeolite fibers (1:2, 15 cm, 16 kV).

A primary goal of this study was to explore the vast parameter space within this fabrication process. Therefore, the plasma calcination of fibers fabricated at 12 kV were also investigated, shown in Figure A.6. Representative SEM and EDS images were obtained for Ar and O_2 treated fibers. These treatments appear to be less effective than the fiber depicted in Figure A.5, evidenced by the significant presence of C. Please note the color differences identifying Al, Si, and Na between the Ar (Figure A.6a) and O_2 (Figure A.6b) treated constructs, an artifact of the on-board EDS software. These data suggest different fibers require different plasma operating parameter to effectively remove the overlying PVP.

Figure A.7 illustrates representative SEM image and EDS maps for as-spun zeolite:PVP fibers, varying several parameters. Here, the zeolite:PVP ratio was increased to 1:1; flow was decreased to 0.5 $mLhr^{-1}$ for 20 min. These experiments were conducted following the example of Anis and Hashaikeh, who used a constant 0.5 $mLhr^{-1}$ flow for approximately 1–2 minutes.[5] The authors documented if the flow rate is too low, discontinuous jets are produced, where if the flow rate is too excessive, solution droplets are formed instead of a continuous jet.[1,5]

Significant work is necessary to optimize the fabrication of zeolite fibers, particularly for these materials to be used in an application. Anis *et al.* recently published a review article, detailing the synthesis of mirco- and nano-porous zeolite fibers for catalysis.[1] Additionally, zeolite composite materials have been studied for increased pollution abatement. Zhang *et al*. synthesized TiO_2/zeolite composites via hydrolysis desorption and subsequent calcination. The increased photoactivity of these materials was attributed to high surface area and surface -OH groups.[9] Ultimately, this dissertation work sought to improve pollution abatement processes through plasma-assisted catalysis, the coupling of an energetic discharge with catalytic materials.

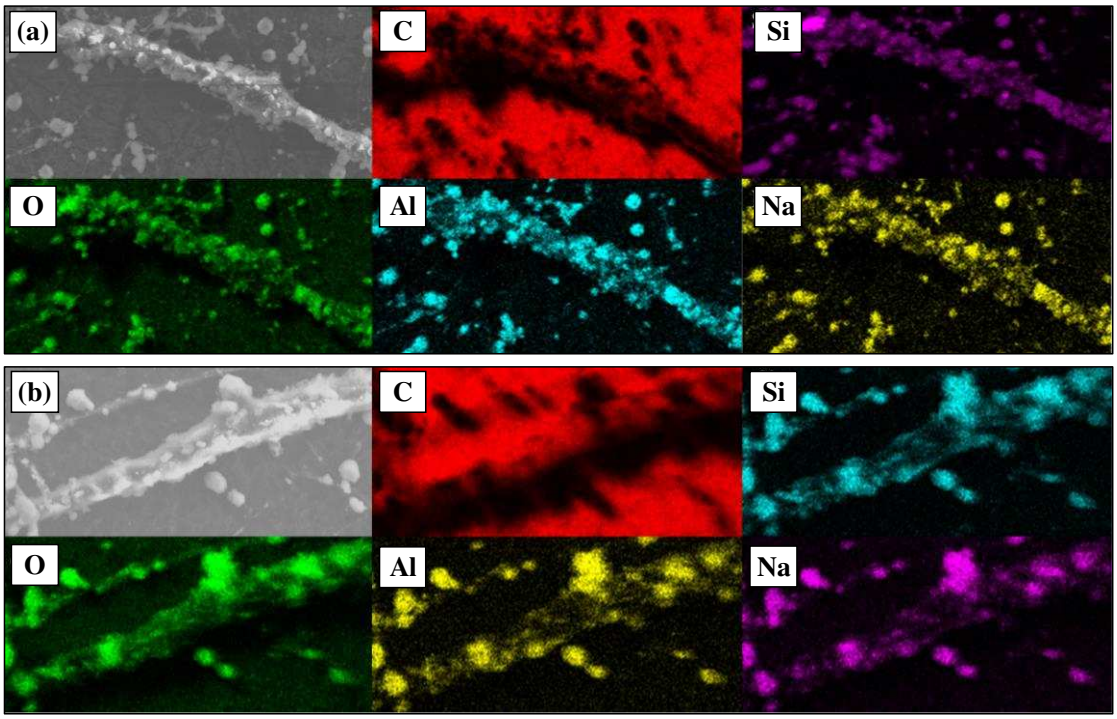

Figure A.6. Representative SEM image and EDS compositional maps for (a) Ar and O_2 plasma (100 mTorr, 100 W, 15 min) treated zeolite fibers (1:2, 15 cm, 12 kV).

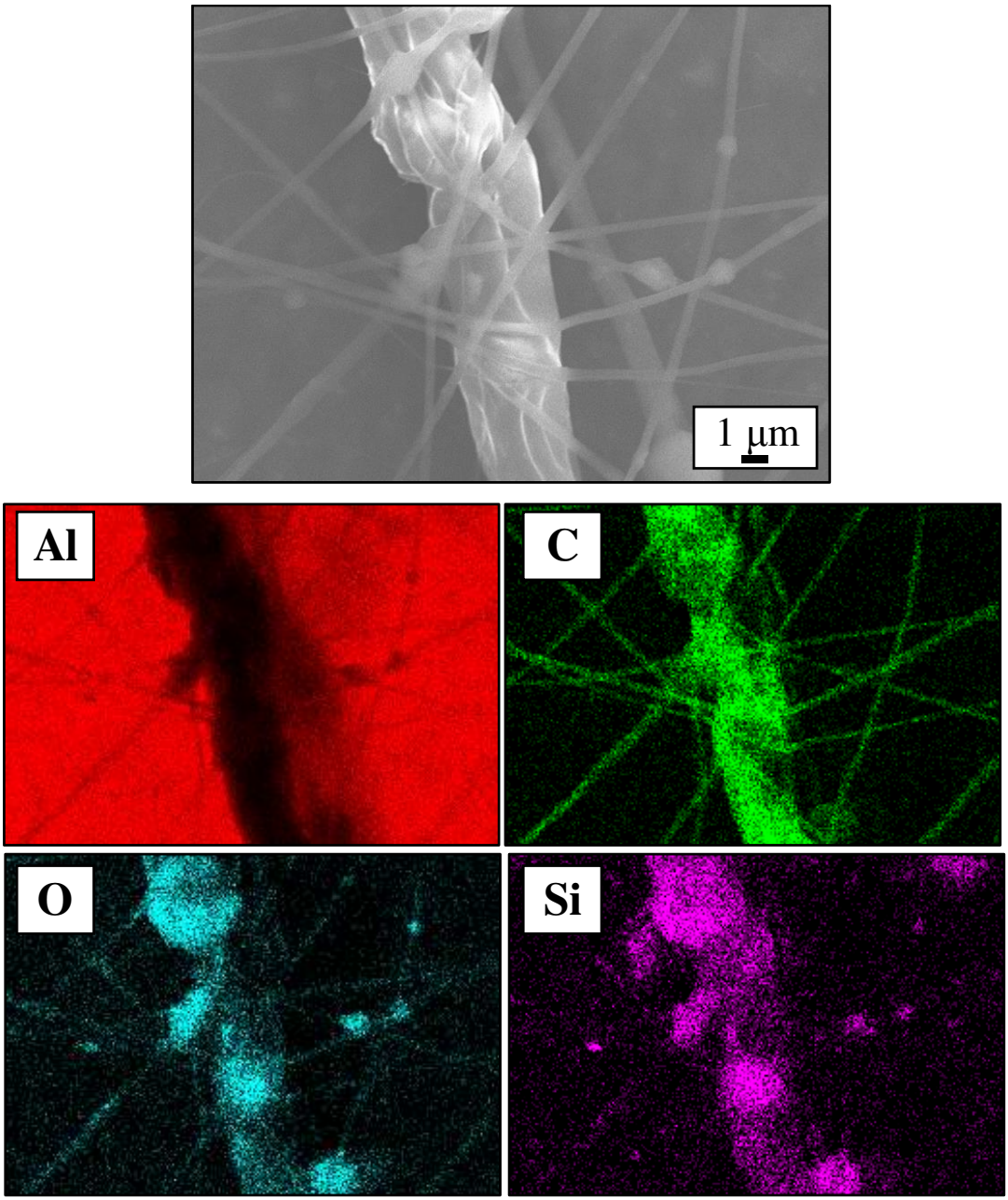

Figure A.7. Representative SEM image and EDS compositional maps for as-spun zeolite: PVP fibers (1:1 ratio, 15 cm, 16 kV, 0.5 $mLhr^{-1}$, 20 min).

The fabrication of morphologically complex catalysts is an additional avenue of exploration. Figure A.8. illustrates the fabrication of TiO_2 nanoparticles: PVP composite fibers (Figure A.8a and A.8d), as well as Ar (Figure A.8b and A.8e) and O_2 (Figure A.8c and A.8f) plasma calcinated fibers at a variety of magnifications. These results represent the first steps to synthesis metal oxide fibers which can be employed in catalysis, biomaterial, or gas-sensing applications.

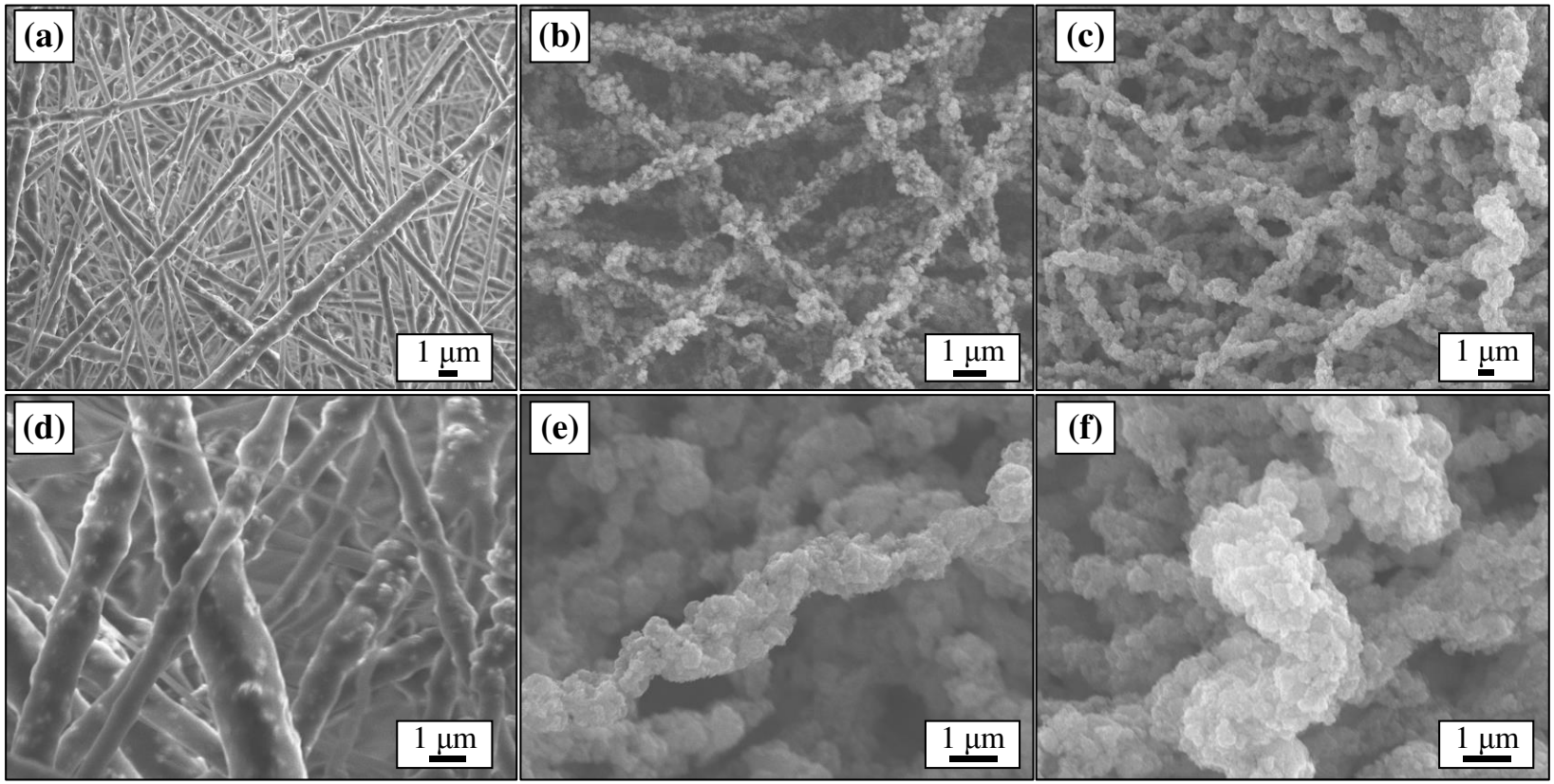

Figure A.8. Representative SEM images of electrospun (a,d) TiO_2: PVP fibers; (b,e) Ar treated (100 mTorr, 100W, 17 min); and (c,f) O_2 treated (100 mTorr, 100, 11 min). A variety of magnifications were used: (a) 3300x, (b) 7000x, (c) 3500x, (d) 9000x, and (e, f) 11000x.

REFERENCES

1. Anis, S. F.; Khalil, A.; Saepurahman; Singaravel, G.; Hashaikeh, R., A Review on the Fabrication of Zeolite and Mesoporous Inorganic Nanofibers Formation for Catalytic Applications. *Microporous Mesoporous Mater.* **2016**, *236*, 176-192.
2. Di, J.; Zhao, Y.; Yu, J., Fabrication of Molecular Sieve Fibers by Electrospinning. *J. Mater. Chem.* **2011**, *21*, 8511-8520.
3. Goergen, S.; Saada, M. A.; Soulard, M.; Rouleau, L.; Patarin, J., Dry Gel Conversion Synthesis of Shape Controlled MFI Type Zeolite Materials. *J. Porous Mater.* **2010**, *17*, 635-641.
4. Hotaling, N. A.; Bharti, K.; Kriel, H.; Simon, C. G., DiameterJ: A Validated Open Source Nanofiber Diameter Measurement Tool. *Biomaterials* **2015**, *61*, 327-338.
5. Anis, S. F.; Hashaikeh, R., Electrospun Zeolite-Y fibers: Fabrication and Morphology Analysis. *Microporous Mesoporous Mater.* **2016**, *233*, 78-86.
6. Wang, Z.; Zhang, Y.; Neyts, E. C.; Cao, X.; Zhang, X.; Jang, B. W. L.; Liu, C.-j., Catalyst Preparation with Plasmas: How Does It Work? *ACS Catal.* **2018**, *8*, 2093-2110.
7. Goldstein, I. S.; Kalk, F., Oxygen Plasma Etching of Thick Polymer Layers. *J. Vac. Sci. Technol.* **1981**, *19*, 743-747.
8. Wavhal, D.; Fisher, E., Hydrophilic Modification of Polyethersulfone Membranes by Low Temperature Plasma-induced Graft Polymerization. *J. Membr. Sci.* **2002**, *209*, 255-269.
9. Zhang, G.; Song, A.; Duan, Y.; Zheng, S., Enhanced Photocatalytic Activity of TiO_2/ Zeolite Composite for Abatement of Pollutants. *Microporous Mesoporous Mater.* **2017**, *255*.

APPENDIX B

As noted in the Introduction to this dissertation, knowledge of internal molecular temperatures within a plasma system will significantly aid plasma modeling efforts. Likewise, combining OES with the LIF-based IRIS technique affords insight into the energetics and kinetics, including gas-substrate interactions. A comprehensive understanding of plasma-material interactions necessarily must include processes that occur at surfaces. Ultimately, many of our results demonstrate that the presence of a substrate in a plasma can dramatically alter the gas-phase chemistry of the system, from both a kinetics perspective and an energetics perspective. Although this might seem obvious, few studies have appropriately documented these effects. IRIS data presented herein were collected by previous Fisher Group members, specifically Dr. M. F. Cuddy and Dr. J. M. Blechle.

B.1. Probing the gas-surface interface

Another feature of our OES-related studies entails *in situ* measurements of steady-state plasma-substrate interactions. Specifically, our unique LIF-based IRIS technique was coupled with OES measurements to investigate potential synergisms between a molecule's propensity to scatter and excited state vibrational energy. As documented in previous studies and shown here (Chapters 7 and 8), the presence of a substrate can have a substantial impact on T_V.[1] Thus, one study examined the relationship between NO scatter [S(NO)] and excited state T_V(NO) values obtained from NO plasmas (p = 50 mTorr; at three P) with either a Si wafer or a Pt foil substrate in the plasma, Figure B.1. Notably, S(NO) values are largely independent of substrate type (Si wafer vs. Pt foil) and increase with increasing P.

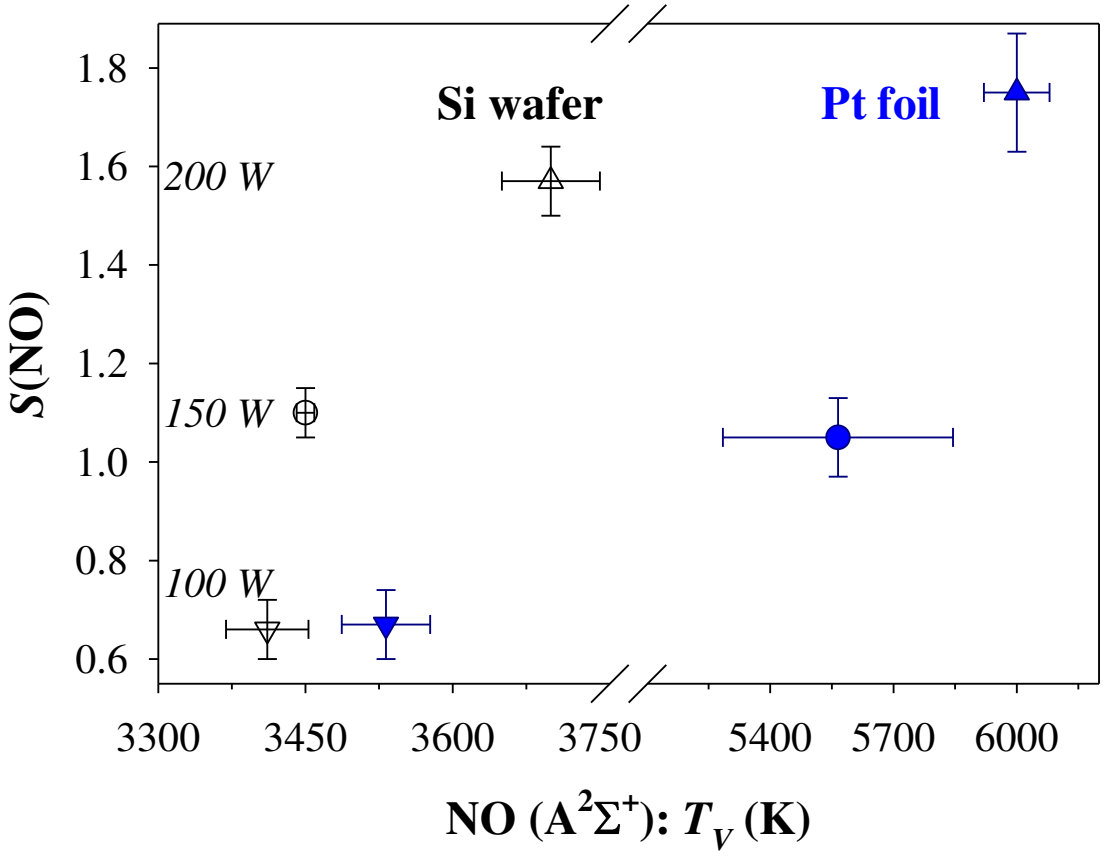

Figure B.1. S(NO) as a function of excited state T_V(NO) values from an NO plasma (p = 50 mTorr) with a Si (black) or Pt foil (blue) substrate present. Bidirectional error bars represent ±1 standard deviation from the mean (n ≥ 3).

Scatter values greater than unity indicate surface production of a molecule; therefore, the Figure B.1 data suggest that as P increases, surface production of NO also increases.

For each substrate, there is a substantial increase in T_V(NO) at P = 200 W, relative to that at 100 W, with that for Pt (~3550 K to ~6000 K) being substantially larger than that for Si (~3450 K to ~3750 K). For Pt, the 150 W data also shows a substantial rise in T_V(NO) (~5550 K) over the 100 W data. One potential hypothesis for this observation is that higher scatter coefficients result from the surface interactions of vibrationally hot molecules. Depicted in Figure B.1, 100 W is the only condition where S(NO) < 1, regardless of substrate, implying surface loss of NO. Notably, this is also the only set of conditions wherein T_V(NO) with a Pt substrate is less than T_V(NO) in the substrate-free system. With a Si substrate in the system, T_V(NO) was lower than T_V(NO) in the substrate-free system under all conditions.[2] As noted above with respect to the selective energy transfer (SET) model (Chapter 8),[3-5] this suggests that vibrationally excited molecules interact with the substrate and scatter, having undergone some energy loss, potentially through a resonant energy transfer mechanism. This phenomenon has been previously documented via OES in N_2 plasmas, with both TiO_2 nanoparticles and micro-structured zeolites (Chapter 7).[1]

To further explore this trend, the plasma reactor, Figure 2.2, was lined from end to end with zeolite substrates and a further vibrational cooling was documented (Chapter 7). Micro-plasma generation near and in the pores of these nano- and micro-structured materials may be heightened, ultimately leading to enhanced vibrational quenching/resonant transfer interactions with the catalyst surface. Notably, within this study, the presence of a catalyst(s) did not have a clear or significant impact on rotational thermalization pathways.[1] Evaluating steady-state OES provides valuable information regarding energy distributions as well plasma-substrate

interactions, however, as noted Chapter 1 and 3, it is also essential to use temporally-resolved spectroscopy to detangle complex plasma dynamics. We also employed TR-OES to study the impact of catalyst(s) on excited-state N_2 kinetics,[1] as the coupling of energetic and temporally-resolved data is essential to holistically understanding the chemistries within PAC systems.

Although S(NO) does not appear to depend substantially on substrate identity, the presence of Pt foil resulted in significantly higher T_V values compared to the substrate-free and Si wafer systems, further evidence that the SET mechanism may be contributing to our experimental observations. At all P, there is substantial scatter of NO off of both substrates, with more than 50% of the molecules desorbing from under all conditions. If we focus on the data from the 200 W systems, however, we observe S(NO) is significantly greater than unity for both substrates, implying surface production of NO. Surface production of NO could be attributed to several different reactions, a few of which are depicted in Reactions B.1 – B.4,

$$NO^*_{(g)} \rightarrow NO_{(ads)} \rightarrow NO_{(g)} \quad \text{(B.1)}$$

$$NO^+_{(g)} \rightarrow NO_{(ads)} \rightarrow NO_{(g)} \quad \text{(B.2)}$$

$$N_{(g)} + O_{(g)} \rightarrow N_{(ads)} + O_{(ads)} \rightarrow NO_{(ads)} \rightarrow NO_{(g)} \quad \text{(B.3)}$$

$$N_2O_{(g)} \rightarrow N_2O_{(ads)} \rightarrow NO_{(ads)} + O_{(ads)} \rightarrow NO_{(g)} + O_{(ads)} \quad \text{(B.4)}$$

where (ads) indicates an adsorbed species, (g) indicates a gas-phase species, and the * indicates an excited state species. Note that in reaction B.1, we depict an excited state NO molecule desorbing as a ground state molecule, which does not fully describe the internal temperatures of either molecule. Assuming $NO_{(ads)}$ species exist on any given substrate, regardless of how they were formed, they must have sufficient energy to overcome the potential energy barrier for desorption for us to observe them in the IRIS system as surface production of NO. The energy required for desorption of NO from either a Si(111)7 x 7 or a Pt(111) substrate is ~14 kcal/mol[6]

and ~25 kcal/mol,[7] respectively. The differences in these desorption energy barriers corroborates the notion that vibrationally hot molecules may contribute significantly to higher *S* values. It also aligns with the observation that a resonant energy transfer mechanism may be at play on the Pt substrate as the SET model allows for a compensation effect whereby vibrational quanta can be added in a stepwise fashion to overcome an activation barrier. Given that it takes more energy for NO radicals to desorb form a Pt surface, we may expect that those molecules may leave the surface vibrationally hotter than ones leaving the Si surface. The data presented here suggest that energy in vibrational modes may preferentially provide a radical with the means to desorb relative to translationally or rotationally hot molecules. Si and Pt substrates were chosen for a non-catalytic and model catalyst system; however, it is important to consider material morphology in addition to chemical identity. Both substrates employed herein are nominally flat and smooth; understanding how radicals scatter from morphologically complex structures may provide more direct evidence of how plasma species synergistically interact with catalytic substrates.[1]

Overall, the combination of the IRIS technique and OES derived data on specific molecules can be employed to study plasma systems with various processing effects on surfaces. Shown in this dissertation are two systems that have very different processing outcomes from a substrate perspective: NO_x plasmas can oxidize (or nitride) surfaces;[8] CF_4 plasmas are largely used as an etchant, and decreasing the F/C ratio using C_xF_y plasmas leads to film deposition (Chapter 4 and 5).[9] Thus, the hypothesis that increasing scatter coefficients result from surface interactions of vibrationally hot molecules was further tested with a variety of FC precursors, shown in Figure 4.8. Vibrational temperatures for excited state CF radicals appear to linearly correlate with measured *S*(CF) values. As the vibrational temperature of excited state CF radicals increases, the

observed *S*(CF) of the ground state species concomitantly grows. This implies that vibrationally hot CF in excited electronic states contributes significantly to the observed scatter of the ground state species. Excited state CF radicals in the molecular beam may electronically quench at the substrate surface, desorb as ground state CF (i.e., the CF equivalent of reaction B.1), yielding a higher scatter value. Energy from this process may be dissipated into the surrounding FC film or passivation layer being deposited on the surface. The already deposited fluorocarbon film is still receiving the full complement of plasma species and as such can be facilely removed, resulting in a high observed scatter coefficient. Thus, highly vibrationally excited CF may act indirectly as an etchant to ablate FC material.

Consideration of species' vibrational temperature when seeking to optimize any plasma process may increase the ability to tailor and tune experimental conditions. This may be especially relevant for precursors and systems that have competing processes, such as the ability to both etch and deposit, depending on experimental conditions. For example, d'Agostino and co-workers documented C_4F_{10} and C_2F_6 can etch or deposit, depending on the bias applied to a substrate, discussed in Chapter 5.[9] By selecting experimental conditions with vibrationally cooler CF, measured by OES, the competition between etching and depositing regimes can be shifted to promote fluorocarbon film formation. The preferential partitioning of energy into vibrational modes correlated with an increased propensity for scatter when a molecule interacts with a substrate, however, does not represent a complete embodiment of the possible surface reactions occurring in these systems. Indeed, as partially depicted in reactions B.1 – B.4, ion, neutral, and radiation bombardment, vibrational relaxation, decomposition, recombination, and charging of the surface via electron or ion bombardment are all occurring simultaneously.[10] The complexity within these systems exemplifies the need for a comprehensive, holistic approach to

plasma diagnostics. Optical spectroscopies can provide insight into how a substrate can modify the plasma discharge itself, ultimately providing means for system optimization, regardless of end application.

REFERENCES

1. Hanna, A. R.; Van Surksum, T. L.; Fisher, E. R., Investigating the Impact of Catalysts on N_2 Rotational and Vibrational Temperatures in Low Pressure Plasmas. *J. Phys. D: Appl. Phys.* **2019**, *52*, 345202.
2. Blechle, J. M.; Hanna, A. R.; Fisher, E. R., Determination of Internal Temperatures Within Nitric Oxide Inductively Coupled Plasmas. *Plasma Process. Polym.* **2017**, 1700041.
3. Larsson, R., A Model of Selective Energy Transfer at the Active Site of the Catalyst. *J. Mol. Catal.* **1989**, *55*, 70-83.
4. Larsson, R., Concluding Remarks on the Theory of Selective Energy Transfer and Exemplification on a Zeolite Kinetics Study. *Monatsh. Chem.* **2013**, *144*, 21-28.
5. Larsson, R., Propane Dehydrogenation Catalyzed by ZSM-5 Zeolites. A Mechanistic Study Based on the Selective Energy Transfer (SET) Theory. *Molecules (Basel, Switzerland)* **2015**, *20*, 2529-2535.
6. Ying, Z. C.; Ho, W., Thermo- and Photo-Induced Reactions of NO on Si(111)7×7. I. Adsorption and Chemical Reactions. *J. Chem. Phys.* **1989**, *91*, 2689-2705.
7. Kruse, N.; Abend, G.; Block, J. H., The Kinetics of Adsorption and Thermal Desorption of NO on Stepped Pt Single Crystal Surfaces. *J. Chem. Phys.* **1988**, *88*, 1307-1312.
8. Morgan, M. M.; Cuddy, M. F.; Fisher, E. R., Gas-Phase Chemistry in Inductively Coupled Plasmas for NO Removal from Mixed Gas Systems. *J. Phys. Chem. A* **2010**, *114*, 1722-1733.
9. d'Agostino, R.; Cramarossa, F.; Fracassi, F.; Illuzzi, F., 2 - Plasma Polymerization of Fluorocarbons. In *Plasma Deposition, Treatment, and Etching of Polymers*, d'Agostino, R., Ed. Academic Press: San Diego, 1990; pp 95-162.
10. Lafleur, T.; Schulze, J.; Donkó, Z., Plasma-Surface Interactions. *Plasma Sources Sci. Technol.* **2019**, *28*, 040201.

APPENDIX C

INDEPENDENT RESEARCH PROPOSAL

The following is the entirety of an independent research proposal, prepared by Angela R. Hanna, in accordance with the doctoral requirements of the Department of Chemistry at Colorado State University. This proposal entitled "*Exploring Fundamental Chemistry in Plasma Aided Ignition and Combustion Systems*," was submitted and recommended for funding by the American Chemical Society Committee on the Petroleum Research Fund for $110,000. A.R.H. would like to thank Dr. Anthony Rappé and Justin Joyce for providing the molecular structure calculations shown herein, as well as Tara L. Van Surksum for providing preliminary methane plasma work.

C.1 Abstract

Over the past decade, there has been significant progress in demonstrating the potential utility of low temperature plasmas for ignition and combustion control. This proposal addresses fundamental issues associated with plasma aided ignition and combustion by examining the steady state energetics and surface reactivity of plasma-generated species on catalysts using a suite of diagnostics tools. Using both emission and absorption spectroscopies, energy partitioning between degrees of freedom (e.g., translational, rotational, and vibrational) will be determined for a variety of diatomic molecules that are critical in combustion processes. Time-resolved spectroscopies will also be utilized to determine rate constants, providing mechanistic insight in molecule formation and decay to steady-state concentrations. Surface reactivities of species of interest (e.g., C_2, CH, OH, NO, NH_x) will be determined as a function of plasma and substrate parameters (e.g., gas composition, plasma power, pressure, catalyst morphology and chemical identity). Phase-resolved optical emission spectroscopy will provide insight on electron heating and energy distributions within the plasma systems. Detailed information about plasma-surface interface reactions will be correlated to internal and kinetic temperature of the species as well as to substrate architecture (e.g., nanowires, nanoparticles, flat films). This combined approach will provide unparalleled insight on the surface interactions of a range of species and chemical mechanisms involved in hydrocarbon combustion and ignition.

C.2 Overview

Combustion of petroleum-based hydrocarbon systems still represents a significant source of global energy.[1-3] Despite extensive studies of combustion, however, the conversion efficiency of most combustion processes remains un-optimized. Plasma aided ignition and combustion (PAIC) is a promising approach to increasing efficiency, that ultimately could contribute to new

engine technology, reduction of harmful emissions, and improved fuel efficiency.[4-7] In addition, PAIC offers an alternative route to the conversion of methane into transportation fuels.[8] Thus, the primary focus of the research proposed herein is to improve understanding of the chemical processes that occur during PAIC, especially in the presence of catalytic surfaces. Molecular-level study of chemical processes provides an in-depth understanding of complex systems, such as low temperature plasmas (LTPs), thereby unlocking extraordinary potential across a wide range of technologies. This research will have profound influence on our ability to design more efficient, high-valued processes for PAIC. Our unique multipronged approach provides unparalleled insight into molecular-level chemistry, affording a more complete understanding not achieved by examining a single aspect of LTP processing. Our approach will include

- developing electronic structure calculations to model formation mechanisms of gas-phase plasma species relevant to PAIC and petroleum technologies;
- illuminating the kinetics and thermodynamics of gas-phase plasma chemistry, including examination of species evolved off catalytic surfaces;
- measuring the steady-state reactivity of plasma-generated species at the surface of catalysts using the imaging of radicals interacting with surfaces (IRIS) technique; and
- elucidating synergistic or coupled plasma interactions via correlation of data derived from all of the above methodologies.

The proposed work combines computational and experimental strategies to measure fundamental properties of LTPs. We seek to create a new direction in our laboratories by incorporating electronic structure calculations, developing a PAIC-specific reactor system, and employing new techniques such as phase-resolved optical emission spectroscopy (PR-OES) to better access the dynamic interplay between the plasma and catalytic materials employed in

hydrocarbon conversion systems. This approach is uniquely suited to provide critically important data for understanding plasma-catalyst surface interactions and much needed insight into chemical mechanisms for PAIC. By focusing on the fundamental properties in complex LTPs, the proposed experiments and calculations will produce foundational data for addressing critical intellectual challenges at the intersection of combustion and ignition chemistry and plasma science.

C.3 Motivation and Background

To understand foundational gas phase and gas-surface interface chemistry, we propose to unravel the complexity of the chemical milieu within plasmas utilized in PAIC. Nonequilibrium LTPs, wherein the electron temperature (T_e) is on the order of a few eV, the ion temperature is substantially higher, and the fraction of gas dissociation is relatively low (<1%),[6,9,10] can initiate processes with a unique selectivity and unmatched energy efficiency, nominally due to their non-equilibrium state.[6] Consequently, plasma-initiated reactions often generate radicals, excited state species, and photons that are simply inaccessible within purely thermal, equilibrium systems. Thus, enormous potential exists for LTPs to have a transformative impact on a wide range of applications. This potential is, however, accompanied by a long list of challenges, including understanding (1) spatial and temporal behavior of plasma species; (2) kinetics of surface reactions; (3) interactions of plasmas with catalytic materials; (4) possible synergistic reactions of various plasma components; and (5) control of plasma chemistry to create specifically tailored materials and chemical environments.[6,9,10] Clearly, no single analysis method or specific plasma system can afford complete understanding of all these aspects. As such, we propose to use a multipronged approach, as depicted in Figure C.1, with an eye toward developing as *in situ* as possible probing of the LTP and characterizing resulting material properties and performance.

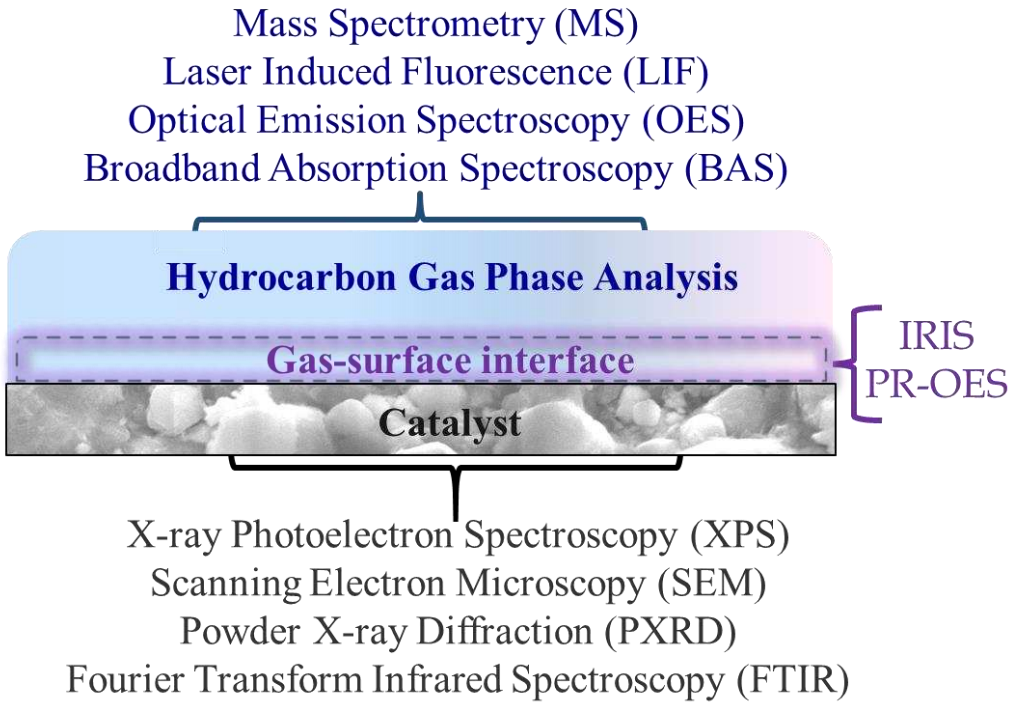

Figure C.1. Conceptual framework of our multipronged approach to characterizing essential components of PAIC

This combination can provide a more complete understanding of LTPs and their potential utility in the petroleum field. Equally as important, such studies generate foundational knowledge and data required for efforts aimed at predictive modeling of these complex systems.

In the context of PAIC, the 2017 Plasma Roadmap[10] suggests a key factor in using plasmas within combustion or conversion processes is the ability to lower environmental impact and improve efficiencies in processes such as exhaust gas recirculation, controlled ignition, and cold startup. The Roadmap[10] clearly indicates that understanding the role of energetics (e.g., rotational/vibrational/translational) as well as reaction kinetics are key factors in realizing the potential of PAIC. Historically, significant efforts have been devoted to the study of elementary process within PAIC systems.[7,11-13] Given that LTPs contain a plethora of reactions occurring simultaneously within the gas phase and at the gas-surface interface, understanding and predicting fundamental processes in these discharges remain complex challenges.

Plasma simulations could theoretically predict PAIC process outcomes, but these rely on the foundational data used to build them, which in many cases must be extrapolated as no reliable data exist. Many experimental studies have focused primarily on collecting gas-phase data in LTPs with relatively low complexity (e.g., rare gas, N_2, and O_2 plasmas).[14-17] There remains, however, a paucity of data for the more complex LTPs, such as those typically used for improved hydrocarbon processing. Thus, we seek to elucidate the kinetics of and synergisms between fundamental chemical processes in the gas phase and at the gas-surface interface in LTPs used for PAIC. We will develop a single plasma-diagnostics platform housing temporally- and spatially-resolved gas-phase diagnostics [optical emission spectroscopy (OES), broadband absorption spectroscopy (BAS), and mass spectrometry (MS)] coupled to a plasma reactor specifically designed for PAIC systems. Molecular-level information will be gleaned from

measuring energy partitioning in gas-phase species, kinetics of species formation and destruction, and molecule-surface interactions *during* PAIC. *By focusing on these fundamental properties in complex LTPs, the proposed calculations and experiments will produce foundational data for addressing critical intellectual challenges in the field of plasma science. Collectively, the comprehensive approach proposed will advance globally-critical petroleum technologies by providing pathways to better processes and materials.*

Background. Within an electrical discharge, collisions of energetic electrons with neutral gas molecules form chemically active species (e.g., ions, excited state species, radicals), thereby initiating additional chemical reactions. Consequently, surface reaction rates can be greatly enhanced via interactions between plasma-generated reactive species and adsorbates on a catalyst surface. Although gas-phase reactions are critical to chemical transformations in these systems, plasma-induced surface reactions on the catalysts must play a key role in PAIC processes. For the decomposition of volatile organic compounds, a synergistic effect between the discharge and catalytic material has been attributed to the availability of short-lived, highly reactive plasma species.[18-21] Although these synergies tend to increase the rate of conversion, different catalysts yield different efficiencies and selectivities.[22] Yet, there has been no systematic exploration of gas-surface interface reactions in these systems under relevant conditions. Likewise, basic properties of LTPs, including species temperatures [e.g., T_e, ion temperature (T_i), vibrational temperature (T_V), rotational temperature (T_R), translational temperature (T_T)], energy transfer to surfaces, gas phase kinetics, and surface reaction probabilities are not well described.

Gas temperature, for example, is considered one of the most important properties of LTPs;[23] yet species temperature within methane plasmas, the simplest hydrocarbon system, have not been

extensively characterized outside a minimal set of conditions, and these primarily focus on a single species, CH radicals.[24-27] Similarly, only a few studies report on energy partitioning trends in CH_4 discharges with catalytic substrates.[19,28] Even less is known about fundamental plasma properties in systems containing larger hydrocarbons (e.g. C_2H_4, C_3H_6, etc.) or more complex gas mixtures (e.g. addition of H_2O, O_2, N_2, etc.).[13,29-31] Understanding how energy is dispersed into different modes of a specific molecule during plasma-induced decomposition in particular, can provide insight into molecule formation mechanisms, decomposition pathways, and overall plasma chemistry.[32,33] For example, one report indicates that NO dimer photodissociation involves excitation into a 3p Rydberg state as well as formation of excited state NO, with associated vibrational excitation of ground state NO upon emission. Formation of NO in a plasma via other routes (e.g. precursor decomposition, interaction with a surface, bimolecular collision) may also involve Rydberg states and associated vibrational signatures.[34] Another study showed a range of highly excited valence and Rydberg states of NO were populated upon photoexcitation.[35] Moreover, insight gained from measurement of both internal (T_V, T_R) and T_T temperatures can elucidate the processes that dictate the overall plasma character. The non-thermal nature of LTPs, however, makes accurate measurements challenging as internal energies often deviate from a Boltzmann population distribution.[36-38] Despite many studies of diatomic species in simple plasma systems (e.g., N_2), *a vast data gap persists for the majority of species found in technologically-relevant plasmas, severely limiting the utility of computational plasma models*.

C.4 Proposed Work

We propose to explore fundamental chemistry within PAIC systems by applying a multipronged approach that combines theoretical calculations with a range of experimental

studies. The proposed work represents new directions for the Fisher group on several fronts, including (a) application of computational studies; (b) creation of a comprehensive diagnostics platform for PAIC systems; and (c) development of a unique phase-resolved OES system for examining electron dynamics and molecule-surface interactions during PAIC. In the following, we describe the different elements of our approach, some preliminary work, and specific tasks we will complete during this study; Section C.4.e describes the timeline for completion.

C.4.1 Electronic Structure Calculations. As the complexity of LTPs can constrain the utility of theoretical methods, several numerical simulations (e.g., molecular dynamics (MD) calculations) have been used to model LTP processes.[39-41] Electronic structure calculations can also be used to investigate gas adsorption properties and the role of coupled nuclear and electronic dynamics on molecule formation mechanisms. Here, in preliminary work with our colleague, Prof. Rappé, electronic structure calculations were performed to determine the direct excitation profile of NO and CH_4, as shown in Figure C.2. The NO ground state was optimized utilizing the aug-cc-pVTZ basis set with a variety of electronic structure methods. Subsequent natural transition orbital determinations were performed using APFD/aug-cc-pVTZ. For example, Figure C.2a depicts the different orbital geometries associated with an electron excited from the 2π orbital in the NO ground state to a large 3s-like orbital in the $^2\Sigma$ state (lowest excited state). The $^2\Sigma$ state is best described as the CO triple bond electronic configuration of NO^+ with the remaining electron in a 3s Rydberg orbital. Thus, emission from this state will be accompanied by significant vibrational excitation. The energy of the $^2\Sigma$ state (5.45 eV) and the relatively low ionization potential of NO (9.26 eV) suggest a nearly 4 eV range for valence excitations and additional Rydberg features of spectroscopic interest. Methane electronic geometry was optimized at APFD and also used the aug-cc-pVTZ basis set.

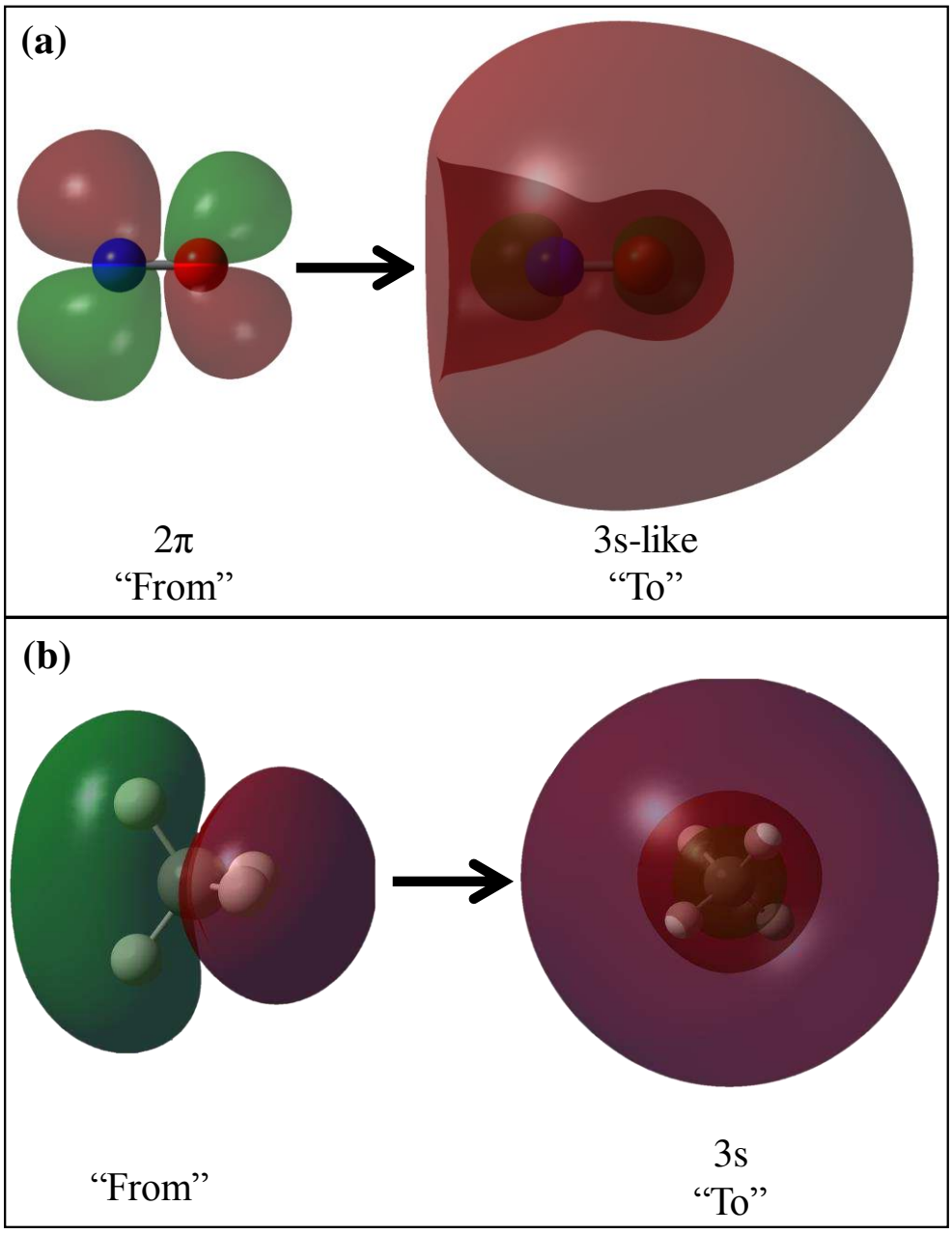

Figure C.2. TD-DFT representation of the natural transition orbitals for excitation of NO from the ground state 2π orbital ("From") to a large 3s-like orbital ("To").

Time-dependent density functional theory (TD – DFT) was performed on the subsequent geometry. The lowest-lying excitations were triply degenerate at 9.94 eV above ground state. Transitions for CH_4, Figure C.2b, are best described as an electron excited from the $2sp^3$ orbital (T_1 state) to a large 3s-like orbital. These calculations showcase our ability to compute electronic geometries of species relevant to PAIC.

The proposed computational work (performed with Gaussian 16) will utilize multi-reference configuration interaction (MR-CI) and TD-DFT electronic structure calculations to characterize the excited state electronic structure and vibrational profile of molecules relevant to our PAIC systems formed via various excitation mechanisms. For example, using DFT methods, Shirazi et al. determined the presence of surface-bound species (e.g., H atoms and hydrocarbon fragments) largely influences catalytic activity.[42] This information will lead to improved interpretation of experimental spectroscopy data and help elucidate excitation pathways within LTPs. Initially, we will perform electronic structure calculations to explore the role of CH and C_2 formation mechanisms on vibrational excitation of various hydrocarbons, focusing on correlating experimental molecular and electron temperatures measured within PAIC systems with structural information gained from these computational studies.

C.4.2 Gas – Phase Analyses. One emerging theme for further exploration evaluates the potential effectiveness of PAIC through understanding energetic distributions and gas phase kinetics in LTPs.[6,43] Applying a range of gas-phase optical diagnostics [laser-induced fluorescence (LIF), OES, BAS] is key to this comprehensive characterization. Species interactions and plasma energetics are intertwined; thus, temporally-resolved data are necessary to accurately probe the intricate dynamics within LTPs. We have developed a customized pilot (alpha) spectrometer/reactor design for OES, BAS, and time-resolved spectroscopy

measurements, Figure C.3a. The spectrometer comprises a broadband light source (deuterium and halogen lamps) collimating and collection optics, and a multichannel detector with a spectral detection range of ~190 – 1015 nm. Notably, we have not addressed adding temporal control (i.e., a shutter and timing system), nor have we formulated the most efficient collection of spatially-resolved BAS, as we must account for logistics of optical element placement. Thus, we propose to build a new (beta) apparatus to house our extant TR-OES/BAS spectrometer, accommodate spatially-resolved spectral analysis, and mass spectrometry capabilities. We aim to build this system from a repurposed vacuum system (i.e., no new capital equipment is required) that can be operated at higher pressures (approaching atmospheric) than our present reactors currently accommodate. As we will be able to operate at both lower (10-200 mTorr) and higher (nominally 0.8-10 Torr) pressures, we can evaluate the impact of a broad pressure range on the discharge kinetics, including transitioning to more efficient processes resulting from hydrodynamic effects that can arise under more process-relevant (higher) pressures.

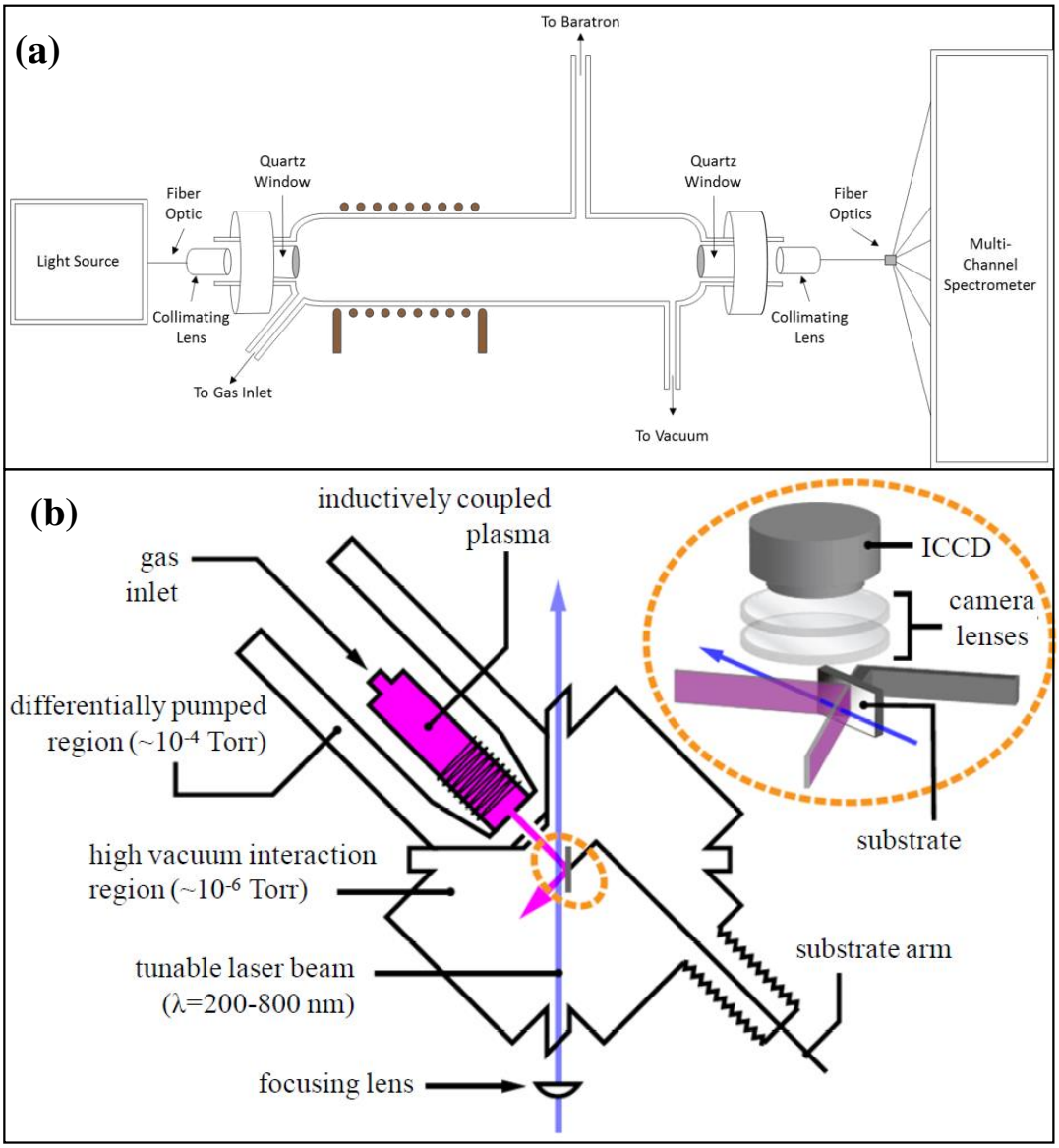

Figure C.3. Schematic of inductively-coupled plasma reactor for a) OES & BAS and b) IRIS apparatus.

As noted above, gas temperature is a central property of LTPs, especially in catalytic processes and understanding how energy partitions into different modes can provide significant insight into fundamental plasma chemistry. To address the data gap for energy partitioning within petroleum-relevant plasmas, we propose to create a library of fundamental energy partitioning data, and kinetic rates, for species relevant to combustion and ignition processes.

Table C.1 lists diatomic species we will analyze as a function of feed gas composition, catalyst, and plasma parameters [e.g., power (P); pressure (p)]. To demonstrate the type of data we can acquire, Figure C.4 shows a raw OES spectrum of a CH_4/Ar plasma with SnO_2 nanoparticles (NP) supported on a glass slide. The spectral region assigned to excited state CH was fit in LIFBASE to elucidate T_V and T_R. Observation of Sn atoms in the gas phase clearly indicates the interdependence between the plasma and materials being processed. Clearly, deeper understanding of LTP interactions with nanomaterials must be obtained to further refine and optimize PAIC processes utilizing catalytic materials. Proposed studies will center on plasma processing of nanomaterials with various morphologies, specifically chosen for their heightened catalytic behavior. Outcomes will focus on understanding how the plasma affects the substrate and how the substrate affects the gas phase of the plasma.

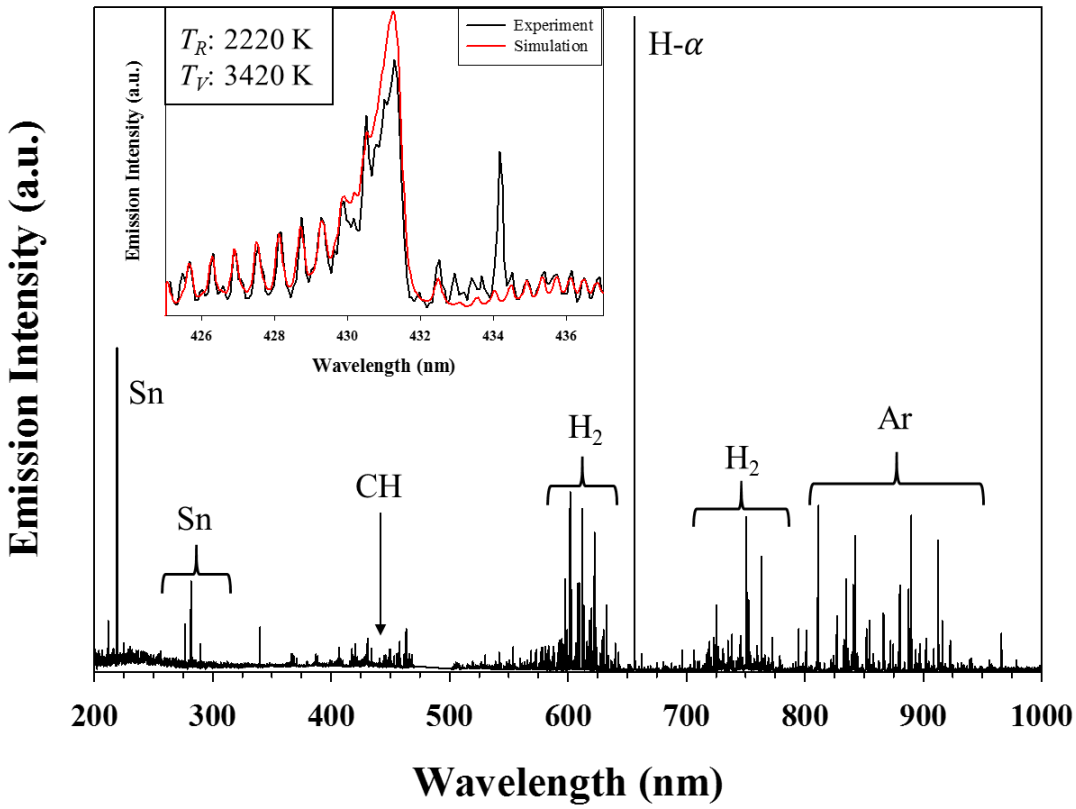

Figure C.4. Raw OES spectra for a 95:5 CH_4:Ar plasma (150 mTorr, 75 W) containing SnO_2 nanoparticles. Peaks are labeled with the corresponding species. Inset highlights the determination of energy partitioning information for CH radicals.

C.4.3 Gas – Surface Interface. A primary challenge to understanding LTP chemistry in the context of PAIC processes lies in deciphering plasma-surface interactions.[6,9,10,22] Thus, it is critical to distinguish effects arising from (a) different types of species bombarding the surface; (b) synergistic or coupled reactions at the surface (e.g., ion bombardment assisting chemical etching[15,44]) and (c) energy partitioning within molecules. All can impact how molecules interact with a surface, especially because the rates of many surface reactions are likely controlled by molecular vibrational and electronic states.[45] Our IRIS technique provides insight into the plasma-surface interface *during* plasma processing by determination of in situ, steady-state radical-surface interactions. In the differentially-pumped IRIS apparatus (Figure C.2b), a collimated, near-effusive molecular beam is produced from an LTP.[46] In the interaction region, the plasma molecular beam (PMB) impinges on a substrate 45º from surface normal and a tunable laser beam propagates in the principal scattering plane, intersecting the PMB, ~3-5 mm upstream from the substrate. The laser is tuned to an absorption frequency of a single PMB species; spatially-resolved LIF signals are collected by a gated, intensified CCD (ICCD) located perpendicular to the PMB and laser beam (above the interaction region). ICCD images are collected with the substrate in the path of the PMB, and with it rotated out of the PMB. As the PMB encompasses effectively all source species (with the likely exception of electrons), IRIS substrates are processed in a nearly identical fashion to those processed directly in our LTPs. Substrates of any type (e.g., both non- and catalytic materials) can be heated or cooled to examine substrate temperature (T_S) dependence on surface reactivity. We can control ion bombardment of IRIS substrates by application of a substrate bias, addition of a grounded mesh screen (removes majority of ionic PMB species), or use of alternate ion-free sources (e.g., a hot filament rector[47]). IRIS data are analyzed by modeling ICCD image cross sectional data with a

numerical simulation.[46,48] The output is a calculated fraction of radicals scattered off the substrate (surface scatter coefficient, S), related to surface reactivity by $R = 1 - S$, where R represents a steady-state surface loss coefficient. As IRIS utilizes LIF, we can also measure T_R by collecting LIF signals as a function of wavelength to yield rotational excitation spectra, and data obtained using different ICCD gate delays yield T_T values.[49] T_T for scattered molecules can also be measured, provided the fluorescence lifetime is sufficiently long.[50,51] Such detailed information for molecule-surface interactions during LTP processes is unobtainable with any other single experimental technique.

We will utilize IRIS to examine plasma-surface interactions of the molecules in Table C.1 on catalytic substrates. Initially, we will use small hydrocarbons and mixtures of hydrocarbons and H_2O, O_2, N_2, and N_xO_y as precursor gases to explore the surface interactions of C_2 and C_3 on control substrates (e.g., Si) as well as on a range of catalytic materials (Table C.1). Although we have employed IRIS previously, we propose several significant modifications to create an apparatus to perform PR-OES studies. PR-OES is a non-intrusive, diagnostic technique to study electron and population dynamics of excited states within LTPs.[52,53] In many plasmas, electron heating and electron dynamics are not fully understood; nevertheless, these energetic electrons have an immense role in influencing plasma chemistry and gas-surface interactions. Using a time-dependent model of excitation dynamics within a given LTP system, PR-OES provides access to fundamental plasma parameters such as T_e, electron density (n_e), and electron energy distribution function (EEDF).[54] Briefly, from an experimental perspective, PR-OES requires a fast, gateable (nanoseconds) ICCD camera and the ability to synchronize the ICCD with the applied RF voltage waveform to measure space and phase-resolved emission. Addition of appropriate optical elements generally yields a spatial resolution of ~0.5 mm and a temporal

resolution of ~5 ns. Given that the key experimental components already exist on our IRIS apparatus, modification to allow PR-OES studies should be straightforward.

As one example of how PR-OES provides critical insight for plasma processes, prior work on energy partitioning within fluorocarbon plasma systems suggests T_e does not have a strong influence on T_V values.[55] Rather, increases in vibrational energy with increasing P for a given molecule are predominantly a consequence of increased n_e. Experimentally determining n_e as a function of plasma conditions (feed gas composition, p, P) with a non-intrusive technique such as PR-OES will provide unique insight into the synergistic relationships between energetic electrons and resulting gas-phase chemistry. Here, we seek to study electron dynamics in hydrocarbon plasmas (CH_4, C_2H_4, etc.) with and without micro- and nanostructured catalysts, elucidating the role of electrons in the plasma sheath formation and in energy partitioning for molecular species such as CH, C_2, and C_3. This element of the proposed work represents a new direction in diagnostics applied to PAIC systems.

C.4.4 Relevant Material Characterization. Particle size significantly influences the overall rate and efficiency of PAIC processes; yet, little is understood about how LTPs interact with micro- and nanostructured materials. Understandably, this has been identified as a major challenge in the field.[10] Although LTPs have been used to synthesize NPs and to modify a range of nanoscale architectures, limited foundational chemical and physical data exist on how reactive plasma species are formed within LTPs and how they interact with nanomaterials. Because the scale of nanostructured materials is intermediate between bulk and molecular, surface interactions of energetic species on NPs and nanowires (NWs) may be fundamentally different than with flat films. A possible explanation is that reactions of energetic plasma species are not limited to the nanomaterial surface, but rather they may rapidly diffuse through particles on the

substrate. The exact mechanisms of how reactive species (e.g., radicals, ions, electrons) interact at particle surfaces is, however, largely unknown. When porous or nanostructured materials are placed in plasmas, spatial inhomogeneity can be created (e.g., microplasmas within pores, localized electric fields) which alters electrical characteristics of the plasma.[56,57] Residence times of reactive species can also lengthen, significantly changing surface chemistries/morphologies, as well as gas-phase densities.[19,22,58] Clearly, plasma-surface interactions across a range of spatial and temporal scales are driving forces in these systems. Figure C.5 demonstrates our ability to fabricate a variety of catalytic materials with different, complex three-dimensional architectures. Here, we will study the Table C.1 catalysts by examining changes within the gas phase and at the gas-surface interface when these substrates are in the plasma, providing insight on how catalysts affect the plasma. We will also perform extensive material characterization before and after plasma exposure to reveal how the plasma affects the catalyst.

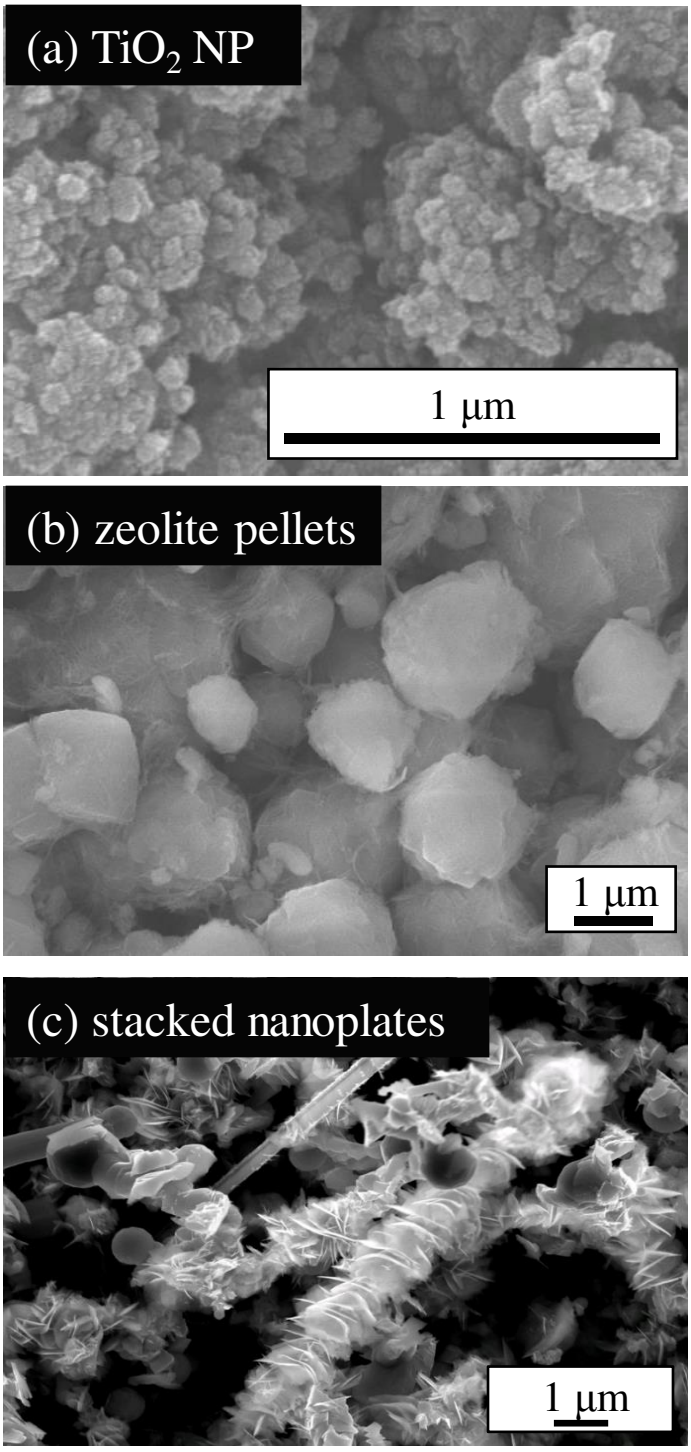

Figure C.5. SEM images of TiO_2 nanoparticles, zeolite pellets, and SnO_2 stacked nanoplates.

Table C.1. Molecules of interest to PAIC processes

Precursor	Molecule	Transition	Excitation Wavelength (λ), nm	Radiative lifetime (ns)	Substrates
C_XH_Y	CH	$A^2\Delta - X^2\Pi$	430	537	Si, Pt, Au nano-structured metal oxides (TiO_2, SnO_2) $Ni/\gamma\text{-}Al_2O_3$ Co-ZSM-5 Zeolites
	C_2	$A^1\Pi - X^1\Sigma^+$	691	1.85×10^4	
	C_3	$A^1\Pi - X^1\Sigma^+$	410	200	
N_XO_Y	NO	$A^2\Sigma^+ - X^2\Pi$	226	215	
	N_2	$C^3\Pi_u - B^3\Pi_g$	315	35 – 40	
H_2O	OH	$A^2\Sigma^+ - X^2\Pi$	308	688	
	O_2	$A^3\Sigma^+ - X^3\Pi_u^+$	249	1.2×10^5	
NH_3	NH	$A^3\Pi - X^3\Sigma^-$	336	440	
	NH_2	$A^2A_1 - X^2B_1$	598	1×10^4	
SO_2	SO	$B^3\Sigma - X^3\Sigma$	235	16.2	
	SO_2	$A^1B_1 - X^1A_1$	300	3×10^4	

C.4.5 Connecting Research Questions. We anticipate the proposed comprehensive approach will provide insight into how a specific molecule (e.g., CH, C_2, OH, etc.) interacts with catalytic substrates and how energy is partitioned within a plasma system. There is a critical need for such a comprehensive approach to address the interdependent relationships and to decouple synergistic effects of coincident plasma-surface interactions.

Table C.2 contains a projected timeline for the proposed work. Year 1 focuses on building the proposed comprehensive diagnostics apparatus along with developing our expertise with electronic structure calculations. A graduate student will work with Prof. Rappé to become proficient with MR-CI and TD-DFT calculations. During construction of the new diagnostics platform, we will perform gas phase CH and C_2 temperature measurements with a range of catalytic substrates using our current system and will characterize those substrates before and after plasma exposure. Depending on how these experiments progress, we will explore surface interactions of other molecules of interest (e.g., OH, CN, and NH formed via addition of gases such as H_2O, NH_3, and nitrogen oxides). Initial Year 1 electronic structure calculations will examine C_2 formation mechanisms, as well as O_2 and CH, within a variety of hydrocarbons. Materials analysis including evaluation of effects of LTP processing on catalytic behavior will be performed throughout the project. From a fundamental science perspective, this holistic experimental and computational approach promises to significantly enhance our overall understanding of LTP chemistry, including deciphering synergistic interactions with the goal of optimizing PAIC processes.

Table C.2. Projected Timeline for Proposed Work

Development of Experimental & Theoretical Approach	Year 1				Year 2			
	Q1	Q2	Q3	Q4	Q1	Q2	Q3	Q4
Diagnostic apparatus construction, troubleshooting								
Development of basis sets, student expertise for calculations, initial calculations								
Plasma Diagnostics for PAIC Systems								
Gas-phase C_2, CH temperature measurements with/without catalytic substrates								
PR-OES, TR-OES, TR-BAS, MS measurements (kinetics/formation mechanisms)								
IRIS studies of CH, C_2, & HS on catalytic substrates								
IRIS studies of OH, NH, and NO in hydrocarbon systems w/ additivities (e.g., H_2O, N_2, O_2, NH_3)								
Materials for PAIC Systems								
Zeolite and metal oxide substrate fabrication								
Plasma treatment (C_XH_Y,H_2O,NH_3) of substrates								
Surface analysis and materials characterization of catalyst substrates								
Catalytic Activity Assessment								
Photocatalytic decomposition studies								
Role of LTPs in catalyst activation								

C.5. Summary

These studies presented here offer a unique opportunity for substantial contributions toward understanding the underlying chemical mechanisms involved in PAIC. We anticipate the proposed comprehensive approach will provide significant insights into how a specific molecule (CH, C_2, OH, etc.) interacts with specific catalytic substrates and how energy is partitioned within a specific plasma. Our studies are designed to elucidate key factors that address critical scientific challenges, including overarching research questions of:

(1) How do molecule formation mechanisms affect energy partitioning and reaction kinetics in LTPs?

(2) On a molecular level, how do LTPs interact with materials, and how does substrate architecture affect those interactions?

(3) What factors govern synergisms between reactions occurring in LTPs, and can we control them to create efficient and selective PAIC processes?

The proposed experiments will provide robust experimental and theoretical data to improve comprehensive plasma simulations of relevant systems that currently rely on either incomplete data or extrapolated information. Our holistic approach will provide fundamental insight into the gas phase, the surface, and most importantly, the gas-surface interface chemistry, which is imperative for significant progress to be made with PAIC, ultimately lowering environmental impact and improve process efficiencies.

REFERENCES

1. Interational Energy Outlook 2017. Administration, U. S. E. I., Ed. 2017.
2. Bayomi, N.; Fernandez, J. E., Trends of Energy Demand in the Middle East: A Sectoral Level Analysis. *Int. J. Energy Res.* **2018**, *42*, 731-753.
3. Bilger, R. W., The Role of Combustion Technology in the 21st Century. In *Turbulent Combustion Modeling: Advances, New Trends and Perspectives*, Echekki, T.; Mastorakos, E., Eds. Springer Netherlands: Dordrecht, 2011; pp 3-18.
4. Starikovskaia, S. M., Plasma-Assisted Ignition and Combustion: Nanosecond Discharges and Development of Kinetic Mechanisms. *J. Phys. D: Appl. Phys.* **2014**, *47*, 353001.
5. Ju, Y.; Sun, W., Plasma Assisted Combustion: Dynamics and Chemistry. *Prog. Energy Combust. Sci.* **2015**, *48*, 21-83.
6. *Science Challenges in Low Temperature Plasma Science and Engineering: Enabling a Future Based on Electricity through Non-Equilibrium Plasma Chemistry*; National Science Foundation: 2017.
7. Starikovskiy, A.; Aleksandrov, N., Plasma-Assisted Ignition and Combustion. *Prog. Energy Combust. Sci.* **2013**, *39*, 61-110.
8. Chen, Q.; Yang, X.; Sun, J.; Zhang, X.; Mao, X.; Ju, Y.; Koel, B. E., Pyrolysis and Oxidation of Methane in a RF Plasma Reactor. *Plasma Chem. Plasma Process.* **2017**, *37*, 1551-1571.
9. *Low Temperature Plasma Science: Not Only the Fourth State of Matter but All of Them*; Report of the Department of Energy Office of Fusion Energy Sciences, Workshop on Low Temperature Plasmas: 2008.
10. Adamovich, I.; Baalrud, S. D.; Bogaerts, A.; Bruggeman, P. J.; Cappelli, M.; Colombo, V.; Czarnetzki, U.; Ebert, U.; Eden, J. G.; Favia, P.; Graves, D. B.; Hamaguchi, S.; Hieftje, G.; Hori, M.; Kaganovich, I. D.; Kortshagen, U.; Kushner, M. J.; Mason, N. J.; Mazouffre, S.; Thagard, S. M.; Metelmann, H. R.; Mizuno, A.; Moreau, E.; Murphy, A. B.; Niemira, B. A.; Oehrlein, G. S.; Petrovic, Z. L.; Pitchford, L. C.; Pu, Y. K.; Rauf, S.; Sakai, O.; Samukawa, S.; Starikovskaia, S.; Tennyson, J.; Terashima, K.; Turner, M. M.; Sanden, M. C. M. v. d.; Vardelle, A., The 2017 Plasma Roadmap: Low Temperature Plasma Science and Technology. *J. Phys. D: Appl. Phys.* **2017**, *50*, 323001.
11. Ju, Y.; Lefkowitz, J. K.; Reuter, C. B.; Won, S. H.; Yang, X.; Yang, S.; Sun, W.; Jiang, Z.; Chen, Q., Plasma Assisted Low Temperature Combustion. *Plasma Chem. Plasma Process.* **2016**, *36*, 85-105.
12. Starikovskii, A. Y., Plasma Supported Combustion. *Proc. Combust. Inst.* **2005**, *30*, 2405-2417.
13. Igor, V. A.; Walter, R. L., Challenges in Understanding and Predictive Model Development of Plasma-Assisted Combustion. *Plasma Phys. Controlled Fusion* **2015**, *57*, 014001.
14. Britun, N.; Gaillard, M.; Ricard, A.; Kim, Y. M.; Kim, K. S.; Han, J. G., Determination of the Vibrational, Rotational, and Electron Temperatures in N_2 and N_2/Ar rf Discharge. *J. Phys. D: Appl. Phys.* **2007**, *40*, 1022.
15. Van Laer, K.; Tinck, S.; Samara, V.; de Marneffe, J. F.; Bogaerts, A., Etching of Low-k Materials for Microelectronics Applications by Means fo a N_2/H_2 Plasma: Modeling and Eperimental Investigation. *Plasma Sources Sci. Technol.* **2013**, *22*, 025011.

16. Ambrico, P. F.; Bektursunova, R.; Dilecce, G.; De Benedictis, S., Nitrogen Vibrational Excitation in a N_2/He Pulsed Planar-ICP RF Discharge. *Plasma Sources Sci. Technol.* **2005**, *14*, 676-685.
17. Pintassilgo, C. D.; Guerra, V.; Guaitella, O.; Rousseau, A., Study of Gas Heating Mechanisms in Millisecond Pulsed Dicharges and Afterglows in Air at Low Pressures. *Plasma Sources Sci. Technol.* **2014**, *23*, 025006.
18. Holzer, F.; Roland, U.; Kopinke, F.-D., Combination of Non-thermal Plasma and Heterogeneous Catalysis for Oxidation of Volatile Organic Compounds. Part 1. Accessibility of the Intra-particle Volume. *Appl. Catal., B* **2002**, *38*, 163-181.
19. Kim, J.; Go, D. B.; Hicks, J. C., Synergistic Effects of Plasma-Catalyst Interactions for CH_4 Activation. *Phys. Chem. Chem. Phys.* **2017**, *19*, 13010-13021.
20. Roland, U.; Holzer, F.; Kopinke, F.-D., Combination of Non-thermal Plasma and Heterogeneous Catalysis for Oxidation of Volatile Organic Compounds. Part 2. Ozone Decomposition and Deactivation of γ–Al_2O_3. *Appl. Catal., B* **2005**, *58*, 217-226.
21. Roland, U.; Holzer, F.; Poppl, A.; Kopinke, F.-D., Combination of Non-thermal Plasma and Heterogeneous Catalysis for Oxidation of Volatile Organic Compounds. Part 3. Electron Paramagnetic Resonance (EPR) Studies of Plasma-Treated Porous Alumina. *Appl. Catal., B* **2005**, *58*, 227-234.
22. Neyts, E. C., Plasma-Surface Interactions in Plasma Catalysis. *Plasma Chem. Plasma Process.* **2016**, *36*, 185-212.
23. Bruggeman, P.; Sadeghi, N.; Schram, D. C.; Linss, V., Gas Temperature Determination from Rotational Lines in Non-Equilibrium Plasmas: A Review. *Plasma Sources Sci. Technol.* **2014**, *23*, 023001.
24. Heintze, M.; Magureanu, M.; Kettlitz, M., Mechanism of C_2 Hydrocarbon Formation From Methane in a Pulsed Microwave Plasma. *J. Appl. Phys.* **2002**, *92*, 7022-7031.
25. Jonsson, M.; Borggren, J.; Aldén, M.; Bood, J., Time-resolved Spectroscopic Study of Photofragment Fluorescence in Methane/Air Mixtures and its Diagnostic Implications. *Appl. Phys. B* **2015**, *120*, 587-599.
26. Hiroyuki, K.; Shinichiro, K.; Bingjia, X.; Satoru, T., Measurement of Rotational Populations of CH Radicals in Low-Temperature Plasmas. *Jpn. J. Appl. Phys.* **2003**, *42*, 1776.
27. Moon, S. Y.; Kim, D. B.; Gweon, B.; Choe, W., Spectroscopic Characterization of Rovibrational Temperatures in Atmospheric Pressure He⁄CH_4 Plasmas. *Phys. Plasmas* **2008**, *15*, 103504.
28. Bozorgzadeh, H. R., Catalytic and Non-catalytic Conversion of Methane to C_2 Hydrocarbons in a Low Temperature Plasma. *J. Pet. Sci. Technol.* **2015**, *5*, 69-78.
29. Stagni, A.; Brignoli, D.; Cinquanta, M.; Cuoci, A.; Frassoldati, A.; Ranzi, E.; Faravelli, T., The Influence of Low-Temperature Chemistry on Partially-Premixed Counterflow n-heptane/air Flames. *Combust. Flame* **2018**, *188*, 440-452.
30. Kosarev, I. N.; Belov, S. O.; Kindysheva, S. V.; Starikovskiy, A. Y.; Aleksandrov, N. L., Inhibition of Plasma-assisted Ignition in Hydrogen–oxygen Mixtures by Hydrocarbons. *Combust. Flame* **2018**, *189*, 163-172.
31. Jo, J.-O.; Trinh, H. Q.; Kim, S. H.; Mok, Y. S., Simultaneous Removal of Hydrocarbon and CO Using a Nonthermal Plasma-Catalytic Hybrid Reactor System. *Chem. Eng. J.* **2016**, *299*, 93-103.
32. Shimada, M.; Tynan, G. R.; Cattolica, R., Rotational and Translational Temperature Equilibrium in an Inductively Coupled Plasma. *J. Vac. Sci. Technol., A* **2006**, *24*, 1878-1883.

33. Staack, D.; Farouk, B.; Gutsol, A. F.; Fridman, A., Spatially Resolved Temperature Measurements of Atmospheric-Pressure Normal Glow Microplasmas in Ar. *IEEE Trans. Plasma Sci.* **2007**, *35*, 1448.
34. Gessner, O.; Lee, A. M. D.; Shaffer, J. P.; Reisler, H.; Levchenko, S. V.; Krylov, A. I.; Underwood, J. G.; Shi, H.; East, A. L. L.; Wardlaw, D. M.; Chrysostom, E. T. H.; Hayden, C. C.; Stolow, A., Femtosecond Multidimensional Imaging of a Molecular Disscociation. *Science* **2006**, *311*, 219-222.
35. Trabs, P.; Buchner, F.; Ghotbi, M.; Lubcke, A.; Ritze, H.-H.; Vrakking, M. J. J.; Rouzee, A., Time-, Angle- and Kinetic-Energy-Resolved Photoelectron Spectroscopy of Highly Excited States of NO. *J. Phys. B: At., Mol. Opt. Phys.* **2014**, *47*, 124016 (124014 pp).
36. Hrycak, B.; Jasinski, M.; Mizeraczyk, J., Spectroscopic Study of CO_2 Plasma in Microwave Source Desgned for Hydrogen Production via Hydrocarbons Decomposition. *Acta Phys. Pol., A* **2014**, *125*, 1326-1328.
37. Niu, J.; Peng, B.; Yang, Q.; Cong, Y.; Liu, D.; Fan, H., Spectroscopic Diagnostics of Plasma-Assisted Catalytic Systems for NO Removal from $NO/N_2/O_2/C_2H_4$. *Catal. Today* **2013**, *211*, 58-65.
38. Zhao, T.-L.; Xu, Y.; Song, Y.-H.; Li, X.-S.; Liu, J.-L.; Liu, J.-B.; Zhu, A.-M., Determination of Vibrational and Rotational Temperatures in a Gliding Arc Discharge by Using Overlapped Molecular Emission Spectra. *J. Phys. D: Appl. Phys.* **2013**, *46*, 345201.
39. Graves, D. B.; Brault, P., Molecular Dynamics for Low Temperature Plasma-Surface Interaction Studies. *J. Phys. D: Appl. Phys.* **2009**, *42*, 194011.
40. Jimenez-Redondo, M.; Carrasco, E.; Herrero, V. J.; Tanarro, I., Chemistry in Glow Discharges of H_2/O_2 Mixtures: Diagnostics and Modeling. *Plasma Sources Sci. Technol.* **2015**, *24*, 015029.
41. Capitelli, M.; Celiberto, R.; Esposito, F.; Laricchiuta, A., Molecular Dynamics of State-to-State Kinetics of Non-Equilibrium Molecular Plasmas: State of Art and Perspectives. *Plasma Process. Polym.* **2009**, *6*, 279-294.
42. Shirazi, M.; Neyts, E. C.; Bogaerts, A., DFT study of Ni-Catalyzed Plasma Dry Reforming of Methane. *Appl. Catal., B* **2017**, *205*, 605-614.
43. Popov, N. A., Kinetics of Plasma-assisted Combustion: Effect of Non-equilibrium Excitation on the Ignition and Oxidation of Combustible Mixtures. *Plasma Sources Sci. Technol.* **2016**, *25*, 043002.
44. Lee, C. G. N.; Kanarik, K. J.; Gottscho, R. A., The Grand Challenges of Plasma Etching: A Manufacturing Pespective. *J. Phys. D: Appl. Phys.* **2014**, *47*, 273001.
45. Meichsner, J.; Schmidt, M.; Schneider, R.; Wagner, H.-E., *Nonthermal Plasma Chemistry and Physcis*. CRC Press, Taylor & Francis Group: Boca Raton, FL, 2013.
46. McCurdy, P. R.; Bogart, K. H. A.; Dalleska, N. F.; Fisher, E. R., A Modified Molecular Beam Instrument for the Imaging of Radicals Interacting with Surfaces during Plasma Processing. *Rev. Sci. Instrum.* **1997**, *68*, 1684-1693.
47. Liu, D.; Martin, I. T.; Fisher, E. R., CF_2 Surface Reactivity During Hot Filament and Plasma-enhanced Chemical Vapor Deposition of Fluorocarbon Films. *Chem. Phys. Lett.* **2006**, *430*, 113-116.
48. McCurdy, P. R.; Butoi, C. I.; Williams, K. L.; Fisher, E. R., Surface Interactions of NH_2 Radicals in NH_3 Plasmas. *J. Phys. Chem. B* **1999**, *103*, 6919-6929.
49. Zhang, J.; Williams, K. L.; Fisher, E. R., Velocity Distributions of SiF and SiF_2 in an SiF_4 Plasma Molecular Beam. *J. Phys. Chem. A* **2003**, *107*, 593-597.

50. Butoi, C. I.; Steen, M. L.; Peers, J. R. D.; Fisher, E. R., Mechanisms and Energy Transfer for Surface Generation of NH_2 Radicals During NH_3 Plasma Processing of Metal and Polymer Substrates. *J. Phys. Chem. B* **2001**, *105*, 5957-5967.
51. McCurdy, P. R.; Venturo, V. A.; Fisher, E. R., Velocity Distributions of NH_2 Radicals in an NH_3 Plasma Molecular Beam. *Chem. Phys. Lett.* **1997**, *274*, 120-126.
52. Gans, T.; Schulz-von der Gathen, V.; Döbele, H. F., Prospects of Phase Resolved Optical Emission Spectroscopy as a Powerful Diagnostic Tool for RF-Discharges. *Contrib. Plasma Phys.* **2004**, *44*, 523-528.
53. Schulze, J.; Schüngel, E.; Donkó, Z.; Luggenhölscher, D.; Czarnetzki, U., Phase Resolved Optical Emission Spectroscopy: A Non-intrusive Diagnostic to Study Electron Dynamics in Capacitive Radio Frequency Discharges. *J. Phys. D: Appl. Phys.* **2010**, *43*, 124016.
54. John, B. B.; Jung, R. O.; Chun, C. L.; Wendt, A. E., Optical Emission Measurements of Electron Energy Distributions in Low-Pressure Argon Inductively Coupled Plasmas. *Plasma Sources Sci. Technol.* **2010**, *19*, 065001.
55. Hanna, A. R.; Cuddy, M. F.; Fisher, E. R., Energy Partitioning and its Influence on Surface Scatter Coefficients within Fluorinated Inductively Coupled Plasmas. *J. Vac. Sci. Technol., A* **2017**, *35*, 05C308.
56. Tu, X.; Verheyde, B.; Cofrthais, S.; Paulussen, S.; Sels, B. F., Effect of Packing Solid Material on Characteristics of Helium Dielectric Barrier Discharge at Atmospheric Pressure. *Phys. Plasmas* **2011**, *18*, 080702.
57. Tu, X.; Whitehead, J. C., Plasma-Catalytic Dry Reforming of Methane in an Atmospheric Dielectric Barrier Discharge: Understanding the Synergistic Effect at Low Temperature. *Appl. Catal., B* **2012**, *125*, 439-448.
58. Kim, T.; Jo, S.; Song, Y.-H.; Lee, D. H., Synergetic Mechanism of Methanol-Steam Reforming Reaction in a Catalytic Reactor with Electric Discharges. *Appl. Energy* **2014**, *113*, 1692-1699.

LIST OF ABBREVIATIONS

ads	adsorbed
Al_{2p}	aluminum 2p (XPS spectrum)
Ar	argon
BAS	broadband absorbance spectroscopy
B.E.	binding energy
C_{1s}	carbon 1s (XPS spectrum)
CR	collisional radiative
CW	continuous wave
DC	direct current
DFT	density functional theory
DBD	dielectric barrier discharge
e^-	electron
EDS	energy dispersive spectroscopy
EEDF	electron energy distribution function
E mode	inductance or electrostatic mode
E-R	Eley-Rideal
EtOH	ethanol
F/C	fluorine-to-carbon ratio
FC	fluorocarbon
fps	frames per second
FTIR	Fourier transform infrared spectroscopy

FWHM	full width at half maximum
H_2	diatomic hydrogen
H_2O	water
HFPO	hexafluoropropylene oxide
H mode	conductance or electromagnetic mode
ICCD	intensified charge-coupled device
IRIS	imaging of radicals interacting with surfaces
ICP	inductively coupled plasma
k_B	Boltzmann's constant
k_f	rate constant of formation
k_d	rate constant of destruction
L-H	Langmuir-Hinshelwood
LIF	laser-induced fluorescence
LTP	low temperature plasma
MeOH	methanol
min	minute
N_2	diatomic nitrogen
n_e	electron density
NO	nitric oxide
N_2O	nitrous oxide
O_{1s}	oxygen 1s (XPS spectrum)
OES	optical emission spectroscopy
OH	hydroxide radical

P	applied rf power
p	total system pressure
PAC	plasma-assisted catalysis
PAIC	plasma aided ignition and combustion
PECVD	plasma-enhanced chemical vapor deposition
Pt_{4f}	platinum 4f (XPS spectrum)
PXRD	powder X-ray diffraction
PVP	polyvinvlypyrrodine
rf	radio frequency
s	second
S	surface scatter coefficient
sccm	standard cubic centimeters per minute
SEM	Scanning electron microscopy
Si_{2p}	silicon 2p (XPS spectrum)
t	time
T_e	electron temperature
T_{exc}	excitation temperature
T_g	gas temperature
T_i	ion temperature
T_R	rotational temperature
TR-OES	time-resolved optical emission spectroscopy
T_T	translational temperature
T_V	vibrational temperature

UT	untreated or no plasma treatment
WCA	water contact angle
XPS	X-ray photoelectron spectroscopy
ZSM	Zeolite Socony Mobil